Modélisation in-silico des effets hémodynamiques des prothèses endovasculaires dans le traitement des anévrismes cérébraux : application à l'estimation des chances de succès

Alain Berod

THÈSE POUR OBTENIR LE GRADE DE DOCTEUR
DE L'UNIVERSITE DE MONTPELLIER

En Mathématiques et Modélisation

École doctorale : Information, Structures, Systèmes

Unité de recherche : Institut Montpelliérain Alexander Grothendieck

Modélisation in-silico des effets hémodynamiques des prothèses endovasculaires dans le traitement des anévrismes cérébraux: application à l'estimation des chances de succès

Présentée par Alain Berod

Le 19/05/2021

Sous la direction de Franck Nicoud et Simon Mendez

Devant le jury composé de

Franck Nicoud	Professeur, IMAG, Univ. Montpellier	Directeur
Simon Mendez	Chargé de recherche, CNRS, Univ. Montpellier	Co-directeur
Umberto Morbiducci	Professeur, Politecnico di Torino	Rapporteur
Alejandro F. Frangi	Professeur, University of Leeds	Rapporteur
Irene Vignon-Clementel	Directrice de recherche, Inria, Paris	Présidente
Vincent Costalat	Professeur, CHU Gui de Chauliac, Univ. Montpellier	Examinateur
Christophe Chnafa	Vice Président Technologie & Stratégie, Sim&Cure	Co-encadrant

UNIVERSITÉ DE MONTPELLIER

Remerciements

Écrire ses remerciements n'est pas chose aisée, du moins en ce qui me concerne, et ce d'autant plus lorsque l'on sait que c'est la partie de la thèse qui sera probablement la plus lue. Au travers ces quelques paragraphes, je souhaite remercier toutes les personnes qui ont contribué, de près ou de loin, à la réussite de ce travail de longue haleine. Je m'excuse par avance pour les potentiels oublis et je m'engage à me faire pardonner autour d'un verre lors du pot de thèse ou dans d'autres circonstances.

I would like to express my sincere gratitude to the members of the commitee who kindly accepted to review my work: Umberto Morbiducci, Alejandro F. Frangi, Irene Vignon-Clementel and Vincent Costalat. I am truly honoured by your presence and by your stimulating thoughts and remarks.

I would also like to thank Professor Juan Cebral and Dr. Fernando Mut from the Center for Computational Fluid Dynamics of the George Mason University for accepting to collaborate with us with the patient-specific validations presented in Chapter 3 and for stimulating discussions. I hope that this collaboration was as interesting for you as it was for me.

Je souhaite vivement remercier mes directeurs de thèse, Franck Nicoud et Simon Mendez. Votre constante positivité ainsi que vos précieux conseils ont grandement contrebalancé mon manque de confiance en moi et ont contribué à construire la personne que je suis actuellement. J'ai appris énormément de choses à vos côtés: la persévérance, le pragmatisme, la rigueur scientifique et j'en passe. Merci pour ces réunions à rallonges durant lesquelles je ressortais lessivé, pour ces petites perles percutantes et hilarantes (Franck), pour ces remontages de moral (Simon) et pour votre bienveillance.

Mes remerciements vont ensuite à la deuxième facette de ma thèse, Sim&Cure, chez qui l'aventure continue. Je suis reconnaissant envers Mathieu Sanchez de m'avoir accordé sa confiance alors que l'entreprise n'était qu'une petite start-up cachée en embuscade mais avec de grands rêves. Aujourd'hui, petite start-up est devenue grande et donne le vertige: il y a autant de nouvelles personnes qui arrivent chaque mois que le nombre de salariés lorsque j'ai commencé ma thèse. J'espère apporter ma modeste pierre à l'édifice pour les prochaines années et je te

remercie d'avoir renouvelé cette confiance que tu as placée en moi il y a bientôt quatre ans.

Ne t'inquiète pas Christophe, je ne t'ai pas remplacé au profit de Mathieu. Et oui, ce template de thèse est vraiment superbe, je me demande bien où j'ai pu trouver un si beau modèle (chose promise, chose due). Trêve de plaisanteries, parlons sérieusement un peu. On dit souvent que nous sommes des nains sur des épaules de géant. Je trouve que cette expression est tout à fait appropriée pour décrire à quel point tu as été important durant cette thèse, et pourquoi tu l'es encore aujourd'hui. La pertinence de tes réflexions, ta patience à décrypter mes explications et raisonnements (pas toujours très clairs je l'avoue) et ton immense bienveillance ont largement contribué au bon déroulement de cette thèse. Merci d'avoir toujours su me montrer le verre à moitié plein lorsque je le voyais à moitié vide (et je ne parle pas de bières bien sûr, si tu crois que je ne te connais pas). L'aventure continue et j'espère que tu m'autorisera à occuper ton épaule encore un moment.

Je souhaite aussi remercier Julien Sigüenza pour ses encouragements durant la dernière ligne droite et pour ces splendides déploiements de flow-diverter qui m'ont permis de tester la validité du modèle. Team bioméca forever ! Merci à Nathan, Alexis, Sonia et Lucile pour ces parties de belote endiablées qui, je l'espère, pourront reprendre très prochainement. Je souhaite aussi remercier mon informaticien barbu préféré, aka Monsieur Kévin Fissot, aka Richard Stallamn en plus beau, aka Linus Torvalds en plus drôle, pour tout ces petits mots doux, son professionnalisme, sa patience à répondre à mes questions attisées par ma curiosité insatiable et ses magnifiques autocollants vim et git.

J'adresse tous mes remerciements à Daniel Mantilla pour cette fructueuse collaboration présentée dans le Chapitre 4 ainsi que pour ta pédagogie et tes explications médicales lors de nos échanges, notamment au RA. Merci pour ce délicieux café et bon courage pour la suite de ta thèse.

Que serait une thèse sans une équipe soudée dans laquelle bonne humeur, entraide et blagues à foison sont les maîtres mots !

Premièrement, merci à mes co-bureaux qui ont partagé cette tranche de vie avec moi. Rodrigo, aka Monsieur thrombose, aka le Luis Fonsi de la coagulation, aka "Vous êtes champions du monde !!": merci pour ces merveilleux moments et fous rires. Merci à toi Gauthier, pour ta patience et ta pédagogie à tenter de nous expliquer, à Pascal et moi, que trouver une application CR harmonique non triviale c'est tellement facile qu'ont pourrait le faire sous la douche avant le petit déjeuner. Ton incroyable capacité à rester stoïque durant toutes nos discussions bruyantes entre Pascal et moi me fascinera toujours, même si je sais qu'une

petite réplique d'OSS bien placée peut te sortir très facilement de ton stoïcisme. Zaineb, Zainouba, 3azouza, merci pour tout les cadeaux que tu as fait à Lucie, je te souhaite le meilleur pour toi en cette fin de thèse. Pascal, Pascal Pascal, par où commencer ... Le responsable ambiance de l'IMAG et du bureau 109 (aka 130), le ciment de l'équipe sang, que dis-je, des doctorants du labo, la justesse incarnée, la retenue et la demie mesure, le punchliner de l'extrême, le Bear Grylls de la blague douteuse, le critique de musique impartial et objectif, l'encyclopédie Scorsesienne, fan modéré et discret des Affranchis (je vais m'arrêter là sinon les remerciements vont être plus long qu'un chapitre du manuscrit). Cette thèse n'aurait sûrement pas été la même sans ta présence, tes remontages de bretelles et tes précieux conseils durant nos discussions "Hits chocolat" sur le banc dehors. Je sais exactement ce que tu vas dire quand tu liras ces lignes donc j'anticipe: non, je n'exagère pas, je pèse mes mots, je persiste et je signe. Je te remercie sincèrement pour tout ce que tu m'as apporté durant ces quatre années de thèse et te souhaite force et honneur pour la fin de la tienne (n'oublies pas: tu es carré mon gars sûr).

Merci à toute l'équipe sang pour ces super moments ensemble. Thomas, pour ces matchs de badminton endiablés (oui, tu as gagné le dernier en date, pas la peine de me le rappeler) et de m'avoir initié aux joies de vtk, notre amour pythonesque. Bon remplissage de l'espace-k à toi et à très bientôt ! Midou, aka Monsieur surface_set, aka Monsieur couleurs dans les scripts shell: merci pour tes pétages de plombs réguliers à 13h45 sur le canapé en salle de pause, tu es un génie. Pierre, merci à toi pour ta bonne humeur communicative et tes blagues douteuses. Agathe, quand tu veux tu remets ton titre en jeu au lancer de petits cochons, on s'est entraînés comme des dingues avec Pascal pour espérer te battre un jour. Monsieur Robert Rapadamnaba, le seul et vrai mathématicien de l'équipe sang. Merci pour tout tes bons conseils et les bons moments passés ensemble (et j'espère que tu nous fera goûter ton fameux gigot très prochainement). Et pour finir, les petits nouveaux, la relève. C'est étrange de se dire que j'étais à votre place il n'y a pas si longtemps encore. Morgane, je te souhaite bon courage pour ta thèse, je suis convaincu que ça va bien se passer, tu es bien entourée et Lucie pourra t'aider si tu n'arrives pas à remplir l'espace-k, c'est sa spécialité. Bart, fais-nous de la belle FSI, tu régales. Bon courage à toi.

Merci aux doctorants de l'IMAG pour ces quatre années passées à vos côtés: Alan (aka Gauthier en mieux), GodinT(ocard) (passe le bonjour à ta Lucie et Guinness !), Thiziri, Meriem, Radia, Nathan, Julien, Tiffany, Tom, Steven, Abel, Louis, Iro, Gwnenael, André, Abdoulrahim, Emmanuel (t'es le meilleur au basket, pas de doutes la dessus, je supportais Pascal parce qu'il m'avait forcé) et Sonia. Désolé d'avance si j'ai oublié quelqu'un (cf. début des remerciements).

Je souhaite aussi remercier tout le personnel administratif de l'IMAG, à savoir Bernadette Lacan, Nathalie Collain, Carmela Madonia, Sophie Cazanave, Brigitte Labric et Laurence Roux. Merci pour votre aide précieuse et votre bonne humeur constante.

Merci aussi à tout ceux qui m'accompagnent depuis quelques années déjà et qui comptent beaucoup pour moi: Nico (aka Butabiche, le navigateur chevronné), Prapoutelle Tagliatelle (sistah bestah), Le Bouuuusse (enfin une belle personne qui sait apprécier l'humour douteux à sa juste valeur), NufNuf (c'est le bon orthographe ?), Ronron, Martim (mon Portugais préféré), Vialaaa (mon sudiste préféré) et Chambaaard (Monsieur stochastique qui aime la compagnie de gros lasers puissants).

Je souhaite te remercier Cathy pour tes relectures attentives des paragraphes de la thèse en français, n'ayant aucune pitié pour un tiret mal placé. Merci Adrien de m'avoir toujours encouragé et d'avoir montré de l'intérêt pour mon sujet de thèse lors de nos nombreuses discussions.

J'aimerai adresser tous mes remerciements à ma famille, qui m'a soutenu sans relâche durant toutes mes études et sans qui je ne serai pas la personne qui présente cette thèse aujourd'hui. Vos encouragements et les précieux moments de déconnexion totale que nous avons partagé ensemble ont grandement contribué à la réussite de la thèse. Une pensée très particulière à Claude, à qui j'aimerai dédier ce travail en sa mémoire.

Pour finir, Mélodie, je te suis éternellement reconnaissant d'avoir toujours été là pour me soutenir dans les moments difficiles et d'avoir été une épaule solide sur laquelle j'ai pu m'appuyer en toute confiance avant et durant toute la durée de la thèse (et après bien sûr). Merci d'avoir toujours cru en moi.

À Lucie et au futur ...

Résumé

Parmi les différents types d'accidents vasculaires cérébraux (AVC), environ 15% sont qualifiés d'hémorragiques car ils se manifestent par un épanchement de sang dans le cerveau, causant des dommages importants et potentiellement irréversibles dans des régions cruciales au bon fonctionnement de ce dernier. Ces épanchements peuvent avoir lieu dans une zone appelée espace sous-arachnoïdien, situé à la frontière entre le cortex cérébral et l'os du crâne: on parle alors d'hémorragie sous-arachnoïdienne (SAH en anglais). Lors d'une hémorragie de ce type, du sang vient se mélanger au liquide céphalo-rachidien (LCR), dont le rôle principal est de protéger le système nerveux des traumatismes. Ce mélange produit des effets dévastateurs sur le cerveau: des inflammations due à cette présence de sang qui commence à coaguler peuvent détruire ou endommager les cellules du cerveau et des lésions cérébrales peuvent apparaître au cause d'une augmentation de la pression intracrânienne due au blocage de l'écoulement normal du LCR (hydrocéphalie). De plus, le risque d'AVC ischémique[1] provoqué par des constrictions erratiques d'artères (vasospasmes) est élevé à la suite d'une SAH. Il est estimé que 85% des SAH sont causées par la rupture d'un anévrisme cérébral [144], provoquant des symptômes tels qu'un brutal et intense mal de tête accompagné parfois de nausées, d'une rigidité nucale et de perte de conscience. Pour tous les patients atteints par une SAH non prise en charge, un tiers retournent à une vie normale, un tiers perdent leur autonomie fonctionnelle et un tiers ne survivent pas au delà de deux semaines après la rupture [121].

Un anévrisme intracrânien est une déformation pathologique de quelques millimètres à plusieurs centimètres d'une des artères principales irriguant le cerveau et localisées dans une zone appelée polygone de Willis à la base du crâne, comme illustré sur la Figure 1a. 90 % des anévrismes intracrâniens possèdent une forme sphérique dite sacculaire [52] et la plupart se forment et grandissent de manière asymptomatique, rendant leur détection difficile avant la rupture. Il est estimé qu'environ 3% de la population mondiale possède un anévrisme non rompu [148]. La dernière décennie a vu l'apparition de différents traitements, qualifiés de non-invasifs, pour la prise en charge d'anévrismes à la fois rompus et non-rompus, principalement sous la forme de prothèses endovasculaires[2]. Via l'insertion d'un cathéter au niveau de l'aine, le chirurgien navigue jusqu'à la zone artérielle d'intérêt contenant l'anévrisme. Comprimé à l'intérieur du cathéter lors de la

[1] Absence d'irrigation en sang oxygéné dans certaines parties du cerveau
[2] Relatif à l'intérieur des vaisseaux

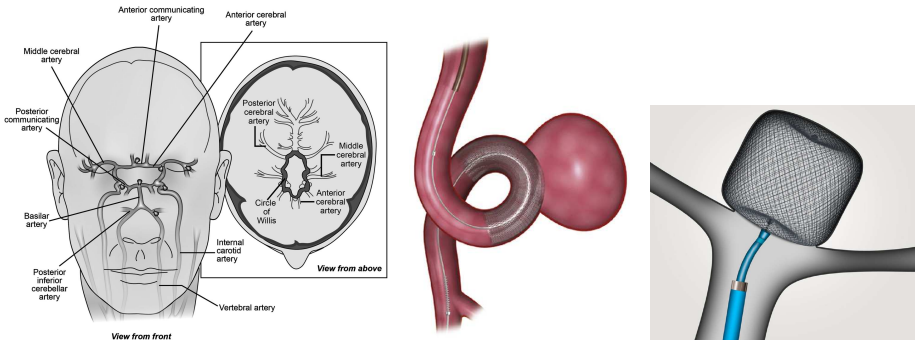

(a) (b) (c)

Figure 1: **a:** Localisation et artères principales composant le polygone de Willis. **b:** Dispositif endoluminale à diversion de flux (Flow-Diverter en anglais). **c:** Dispositif intra-sacculaire (WEB). Images provenant successivement de [53, 117] et [51].

phase de navigation, un dispositif médical est déployé par le chirurgien soit au niveau de l'entrée du sac anévrismal, on parle alors de dispositif endoluminal de type diverteur de flux (flow-diverter en anglais) représenté sur la Figure 1b, soit directement à l'intérieur de l'anévrisme sous la forme d'une cage, comme montré sur la Figure 1c pour un dispositif de type WEB (Woven EndoBridge en anglais). Ces dispositifs formés par un tressage de fils métalliques d'une dizaine de micromètres de diamètre environ se déclinent sous différents modèles en fonction du fabricant, avec des variations sur le nombre de fils, les matériaux (traitements de surface des fils), l'angle de tressage ... La variabilité inter-patient de la forme du sac anévrismal et des artères environnantes induit que chaque modèle est décliné en dizaines de tailles. Cela induit une décision complexe pour le chirurgien qui doit choisir la taille la plus adaptée durant l'opération pour les anévrismes rompus ou pendant une phase de préparation en amont pour les cas électifs non-rompus.

Le but principal de ces dispositifs endovasculaires est de créer une zone de stagnation du sang à l'intérieur du sac anévrismal, favorisant l'apparition d'un thrombus stabilisant ce dernier et conduisant à une potentielle cicatrisation de la lésion [71]. Comprendre les mécanismes d'action impactant le succès ou l'échec d'un tel type de traitement est essentiel. Cela se traduit notamment par la réalisation d'études rétrospectives sur une grande quantité d'anévrismes déjà traités et dont l'issue est connue afin de déterminer des critères significativement différents permettant de discriminer échec et succès de traitement. En utilisant ces critères en amont de l'acte chirurgical, lorsque cela est possible pour un traitement électif, le pourcentage de chances de succès pour chaque type et taille de dispositif est mis à disposition du chirurgien, fournissant des informations cruciales à un traitement effectif de la pathologie. Connaître ces mécanismes est aussi crucial

pour les fabricants en amont du geste chirurgical, lors de la création de nouveaux dispositifs ou l'amélioration de ceux existants déjà.

De part son lien étroit avec la formation et la croissance d'anévrismes [78, 161], l'hémodynamique, la manière dont le sang coule, est considérée par la communauté médicale comme un facteur primordial pour prédire le succès opératoire d'un dispositif médical [113]. Dans le but d'accéder à l'hémodynamique anévrismale avant et après traitement de manière non-invasive et rétrospective, la mécanique des fluides numériques (MFN ou CFD en anglais) a été utilisée massivement durant les dernière années [102, 110]. Résolvant numériquement les équations qui régissent l'écoulement du sang dans des géométries discrétisées réelles de patients traités de manière virtuelle, cette technique permet d'avoir accès à une grande variété d'indices pertinents tels que le frottement pariétal sur le sac (wall shear stress en anglais), le débit traversant le collet anévrismal, la vitesse moyenne dans le sac ...

Afin de prendre en compte l'impact hémodynamique d'un dispositif endovasculaire, une approche classique offerte par la MFN consiste à soustraire du maillage fluide les régions contenues à l'intérieur des fils, ainsi qu'illustré sur la Figure 2. Des conditions aux limites de type mur fixe (à vitesse nulle) à la frontière des fils sont appliquées: on parle alors de méthodes dites *conformes*. Bien que capturant les détails fins de l'écoulement au niveau des fils qui pilotent l'hémodynamique aval dans le sac, l'approche conforme possède un coût numérique non-négligeable principalement du à la différence d'échelles entre les fils (environ 10 µm) et l'artère parente (environ 5 mm). Cette différence induit une complexité dans la génération de maillage ainsi qu'une grande quantité de mailles, rendant la réalisation d'études rétrospectives contenant un grand nombre de cas difficile. Afin de pallier à ces problématiques, une approche développée récemment consiste à remplacer l'effet dissipatif individuel de chaque fils par un effet global se traduisant par une perte de charge au travers de la surface du dispositif [7, 124]. Ainsi, le dispositif n'influe plus localement sur l'écoulement mais de manière globale dans une région entourant la surface de la prothèse (en grise sur la Figure 2): cette approche est qualifiée *d'homogène*. Malgré des réductions importantes de coût numériques, les différents modèles issus de cette famille sont basés sur des hypothèses non compatibles avec la structure fine des prothèses endovasculaires [80]. De plus, ils ne permettent pas de représenter des effets fluidiques complexes tels que la redirection de l'écoulement au niveau des fils, l'hétérogénéité potentielle de densité de fils au niveau du collet ainsi que les contraintes de cisaillement appliquées dans le voisinage du dispositif, effets primordiaux car impactant l'écoulement aval dans le sac [42, 70, 155, 159]. **A cet égard, l'objectif principal de cette thèse est de développer une approche intermédiaire en termes d'erreurs de modélisation et de coûts**

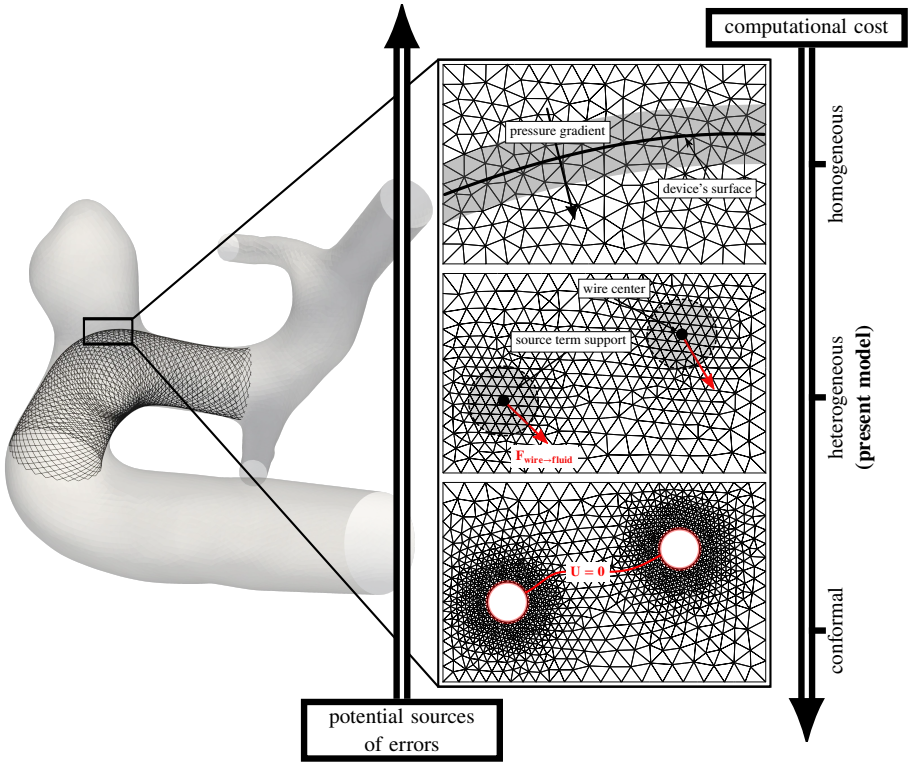

Figure 2: Classification des différentes méthodes développées en MFN (à droite) afin de prendre en compte l'impact d'un dispositif endovasculaire implanté (à gauche). L'approche proposée dans cette thèse vise à minimiser les erreurs de modélisation tout en gardant un coût de calcul raisonnable, se plaçant de-facto entre les deux méthodes classiques conforme et homogène.

de calculs permettant d'avoir accès aux hétérogénéités causées par la présence de fils au collet anévrismal.

Cette approche, schématisée sur la Figure 2, consiste à appliquer une force de traînée (en rouge) sur une région localisée (en grise) autour de chaque fil, région pouvant être plus grande que le diamètre original des fils. Ainsi, la forte dépendance du maillage fluide vis-à-vis de la géométrie du dispositif est éliminée, de même que pour les méthode homogènes, tandis que les hétérogénéités locales de l'écoulement sont en partie conservées, se rapprochant ainsi de l'approche conforme. La description du modèle de force de traînée ainsi que le couplage fluide-structure principalement inspiré de la méthode des frontières immergées [116], IBM en anglais, sont donnés dans le Chapitre 2. L'implémentation de ce modèle dans le code de calcul YALES2BIO hébergé à l'IMAG a été validée sur des configurations simplifiées mais réalistes d'écoulements à travers un dispositif médical idéalisé en considérant les résultats conformes comme étant la référence. Les erreurs sur les profils de vitesse en aval des fils sont de l'ordre de 20% en

moyenne et les hétérogénéités spatiales sont bien reproduites.

Le Chapitre 3 présente une validation du modèle sur des configurations réelles d'anévrismes contenant des prothèses endovasculaires. Une des données nécessaire au fonctionnement du modèle est la connaissance de la vitesse de l'écoulement amont à l'infini, afin d'en déduire des forces de traînées à appliquer ensuite. Prescrite de manière artificielle dans la validation présentée au Chapitre 2 car entièrement contrôlée par les conditions aux limites, cette information n'est plus disponible dans des géométries complexes où l'écoulement est dicté par la forme de l'artère et les interactions locales inter-fils. Une première étape consiste donc à reconstruire à partir d'informations locales le champ de vitesse amont à "l'infini". Cette reconstruction s'effectue en utilisant la conservation du débit entre les fils ainsi que des corrélations entre l'angle local du vecteur vitesse et celui à l'infini. Ces corrélations ont été obtenues avec des simulations 2D. Par la suite, une géométrie réelle d'anévrisme traitée par un diverteur de flux a été étudiée en comparant conforme et approche IBM. Les hétérogénéités sont reproduites, la forme globale de l'écoulement est similaire au conforme et l'erreur sur la vitesse moyenne dans le sac atteint 20%. Cette erreur est considérée comme acceptable au regard des gains drastiques en coûts numériques: diminution de la mémoire utilisée d'un facteur 20 ainsi que du temps de calcul d'un facteur 5000, cette dernière étant principalement causée par l'augmentation du pas de temps entre conforme et IBM. Afin de proposer une validation plus détaillée avec d'autres géométries anévrismales, une collaboration a été mise en place avec une équipe scientifique américaine de l'université Georges Mason[3], spécialisée dans la modélisation en MFN des prothèses endovasculaires et dirigée par le Professeur J.R. Cebral[4]. Cette collaboration a permis de comparer le modèle introduit dans cette thèse avec leurs résultats conformes de référence. De plus, trois modèles homogènes ont été implémentés dans YALES2BIO et utilisés sur ces mêmes géométries afin de démontrer l'apport de la présente modélisation. Pour 1 des 6 cas de flow-diverters étudiés, le modèle IBM induit une erreur sur la vitesse dans le sac légèrement plus grande que pour 2/3 modèles homogènes (30% versus 25%), due à une redirection trop prononcée de l'écoulement au niveau des fils. Néanmoins, l'erreur moyenne constatée pour les autres cas atteint 15% et le modèle a démontré sa polyvalence sur des cas "complexes" dans lesquels le dispositif n'est pas correctement apposé en amont de l'anévrisme, contrairement aux modèles homogènes qui ne parviennent pas à reproduire les résultats conformes pour ces cas et obtiennent des erreurs supérieures à 100%, ainsi qu'illustré sur la Figure 3. De plus, le modèle a prouvé qu'il pouvait être utilisé en l'état sur d'autres formes de dispositifs endovasculaires tressés de type WEB avec 4 cas provenant aussi de la base de don-

[3]https://cfd.gmu.edu/comphemolab/
[4]https://cfd.gmu.edu/~jcebral/

née du Professeur J.R. Cebral, accentuant de fait la polyvalence de l'approche proposée.

Le dernier chapitre de cette thèse s'attache à l'application du modèle au monde médical dans une étude rétrospective sur 27 cas de type WEB traités au sein du service de neuroradiologie de l'hôpital Gui de Chauliac à Montpellier, collaboration réalisée en partenariat avec le Dr. Daniel Mantilla. Des outils numériques semi-automatisés de préparation et de post-traitement des calculs ont été mis en place afin de faciliter l'utilisation de YALES2BIO auprès d'utilisateurs non experts en MFN. Différents aspects liant l'hémodynamique avec la déformation du dispositif sont discutés, et des mécanismes d'actions promouvant les chances de succès sont proposés.

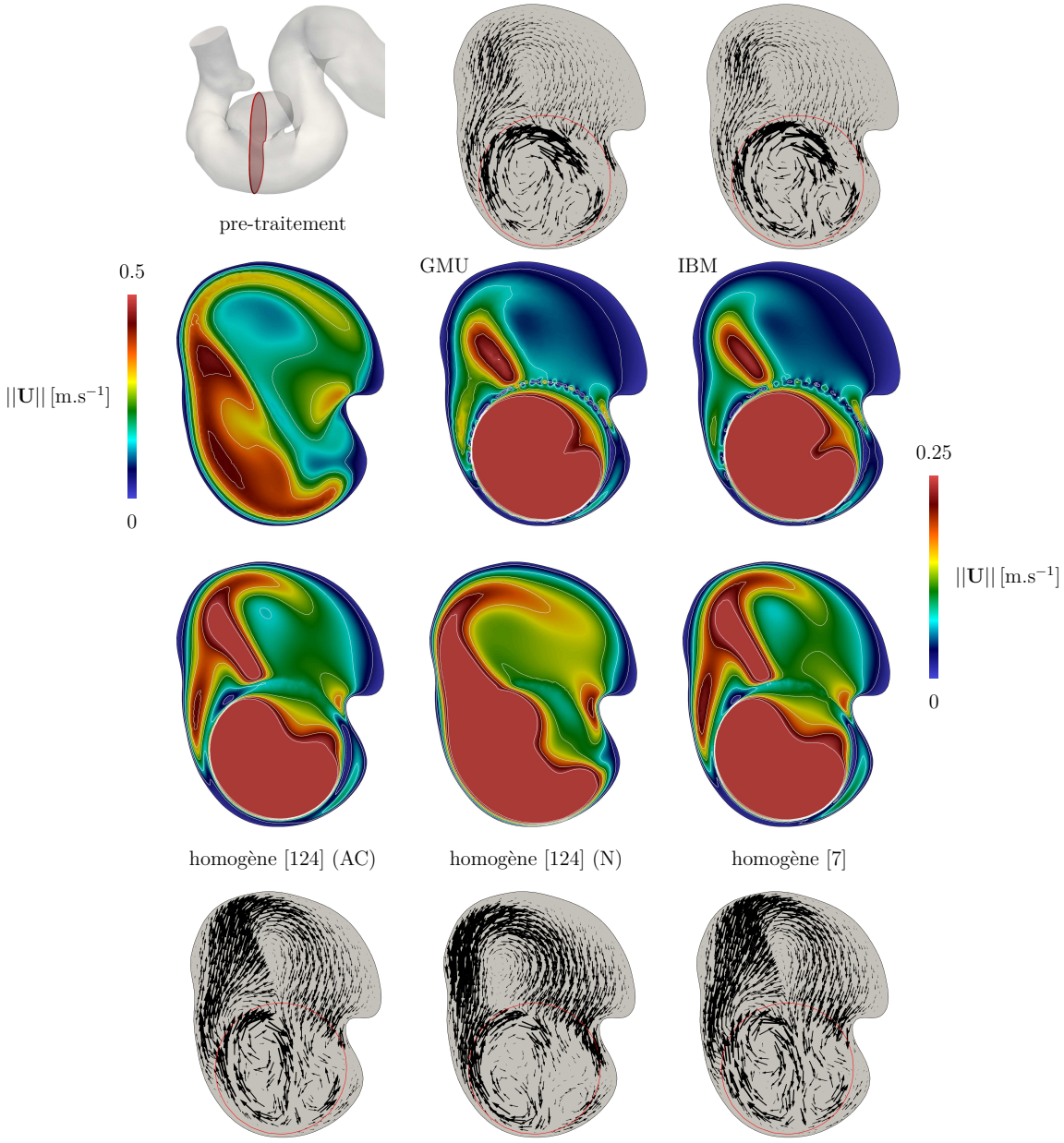

Figure 3: Résultats qualitatifs pour un cas de flow-diverter parmi six pour chaque modèle implémenté, GMU étant la référence conforme provenant de l'équipe de J.R. Cebral et IBM étant le modèle développé durant la présente thèse. Une coupe réalisée au travers du sac permet de visualiser la magnitude du vecteur vitesse ainsi que la direction de ce dernier projeté dans le plan de coupe. La ligne rouge représente la frontière du flow-diverter et la localisation 3D du plan de coupe est disponible en haut à gauche pour aider à la visualisation.

Contents

Chapter 1

Introduction

Chapter contents

1.1 Motivations

Cardiovascular diseases are major health concerns according to the World Health Organization, as they are responsible of 31% of deaths worldwide in 2016[1]. One of these diseases is the rupture of intracranial aneurysms (IAs), which are local dilation of arteries in the brain. The rupture event leads to a leakage of blood in the space surrounding the brain, which is referred to as Subarachnoid Haemorrhage (SAH). SAH carries very high mortality and morbidity rates [108]. When patients suffering from a ruptured aneurysm are taken care on time, physicians need to rapidly choose which medical device (detailed later in Section 1.3) to use depending on the age of the patient, geometric characteristics of the aneurysm such as size, shape, location in the brain and the availability of treatment options in their center. Retrospectively studying these cases contributes to gain knowledge regarding devices working principles and derive indices that could predict treatment efficacy prior to the surgical act. Therefore, there is a need for non-

[1]https://www.who.int/news-room/fact-sheets/detail/cardiovascular-diseases-(cvds)

invasive tools which could give detailed access to the alterations caused by these devices in a retrospective manner.

Additionally, there has been an increase of unruptured intracranial aneurysms being accidentally detected thanks to major advances in medical imaging used during routine scans or examinations for other conditions [126, 135, 154]. Once the decision of treating these unruptured aneurysms has been taken, physicians plan the intervention and study each treatment option to elect the one that will increase the chances of success of the intervention. Therefore, the need previously identified is still relevant, since these innovative tools could guide the decision making process using indices that have been proven retrospectively to significantly predict treatment efficacy.

Furthermore, enhancing success rates of existing devices requires a thorough understanding of their working principles of these devices. Additionally, creating innovative designs requires the manufacturers to perform costly parametric studies on various geometries in order to determine the impact of device design onto performances [112]. This reinforces the need to have access to tools evaluating devices efficacy at minimal costs and at the design level.

Through its intimate relationship with aneurysm formation, growth and rupture, hemodynamics has been proven to be of great interest to fully understand these phenomena [5, 65, 78]. Moreover, quantifying the degree of intra-saccular flow stasis induced by the presence of these devices is crucial to predict potential aneurysm stabilization via the formation of a thrombus [106, 130].

Image-based Computational Fluid Dynamics (CFD) is intended to numerically solve blood flow equations in patient-specific geometries. Used in conjunction with numerical deployment of endovascular devices, CFD fulfils all the aforementioned characteristics. Therefore, it has been chosen to use this framework to address the previously identified needs. As this will be detailed in the following sections, the general objective of the current work is to build a CFD model capable of reliably measuring blood-flow alterations caused by implanted devices in IAs and subsequently perform numerical computations to predict treatment efficacy via hemodynamic indices.

1.2 Cardiovascular system components

Through its multiple interactions with other body systems, the cardiovascular system (CS) ensures human body correct functioning. It delivers oxygen and nutrients needed by muscles for contraction and absorbs nutrients and water inside the digestive system. It also carries clotting components such as platelets for repairing purposes and maintains health by transporting white blood cells and antibodies at infection sites. These transports phenomena are made possi-

ble thanks to the combined action of three components: blood, heart and the circulatory system, which are now going to be described.

Blood Containing cells such as platelets, red and white blood cells (RBCs and WBCs) suspended inside plasma, blood is the medium of transport of the cardiovascular system. These cells represents a mean volume concentration of 45% and are primarly composed of RBCs (99%), as showed in Figure 1.1. One micro litre of blood contains approximately 5 million RBCs. Plasma is made of water (92%) as well as many proteins such as albumin, globulins, fibrinogen and coagulation factors.

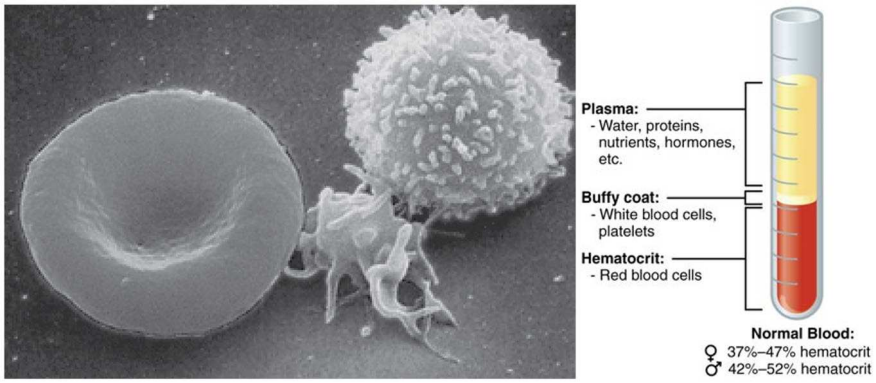

(a) (b)

Figure 1.1: **a:** Elementary cells present in blood, from left to right: red blood cell, platelet and white blood cell. Cells have been isolated from a scanning electron micrograph. **b:** Overall composition of blood with volume percentages for each phase. Images taken and adapted from [11].

Heart The heart, depicted in Figure 1.2, is the central element of the cardiovascular system as it regularly pumps blood into the circulatory system. It is composed of two non-communicating sides, left and right, that contain oxygenated and de-oxygenated blood, respectively (red and blue in Figure 1.2). Each side contains an atrium and a ventricle separated from each other by a valve: tricuspid and mitral (right and left).

During one heart-beat that last approximately one second for healthy subjects at rest, blood pumping includes two phases: diastole and systole. During diastole, blood in the two atria is pushed through opened mitral and tricuspid valves to fill respective ventricles, while aortic and pulmonary valves are closed to prevent backflow. Then, systolic phase is characterized by a contraction of both ventricles, thereby expelling blood into pulmonary arteries and aorta for left and

right sides, respectively. As for diastole, backflow into atria is prevented by mitral and tricuspid valves closing. Correct valves closing is ensured by a connection with heart walls through chordae tendineae that are loose during diastole and tight during systole.

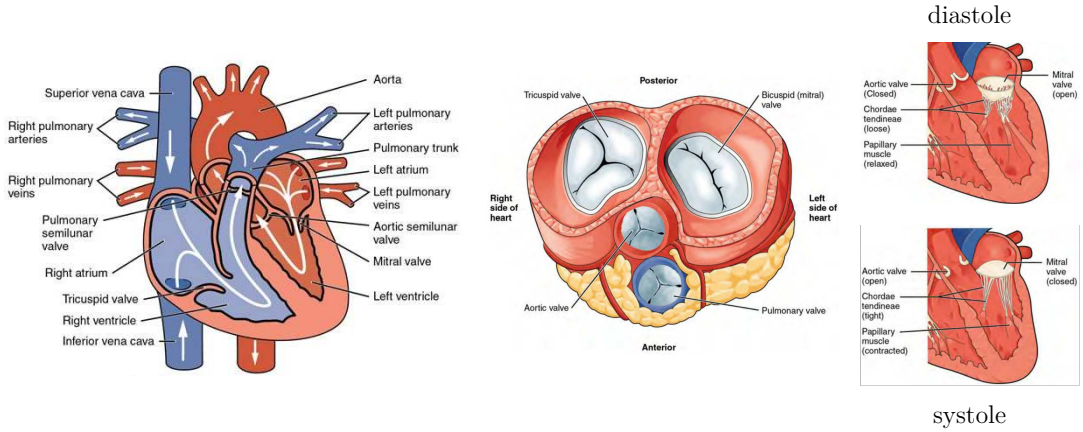

Figure 1.2: **Left:** sketch of a human heart showing blood pathways inside all cavities. **Middle:** different valves involved in correct heart functioning. **Right:** diastolic and systolic phases valves configurations for the left side. Taken from and modified from [11].

Circulatory system The circulatory system is a closed-loop of vessels which can be divided into two parts: systemic and pulmonary. As sketched in Figure 1.3, the systemic circulation transports oxygenated blood (in red) from the left ventricle of the heart to most body organs successively through arteries, arterioles and capillaries, where gas exchanges occurs. These exchanges remove oxygen and add carbon dioxide to the blood, which is send back to the right ventricle of the heart through the veins (in blue).

In contrary, the pulmonary system is fed with de-oxygenated blood coming from the right ventricle of the heart via pulmonary arteries. By diffusion of oxygen through the alveoli in the lungs, blood is re-oxygenated and goes back to the left ventricle to repeat the cycle. It should be noted that pulmonary arteries are the only arteries in the circulatory system that carry relatively de-oxygenated blood, and vice-versa for pulmonary veins.

Arteries and veins are defined as vessels that transports blood away and back to the heart, respectively. As depicted by Figure 1.4, arteries are more circular and thicker than veins of comparable sizes. Focus is now laid onto arteries since it is the only type of vessels considered in this work. They are composed of three layers, also called tunics: externa, media and intima. Depending on the position of the artery with respect to the heart, the relative width of each layer

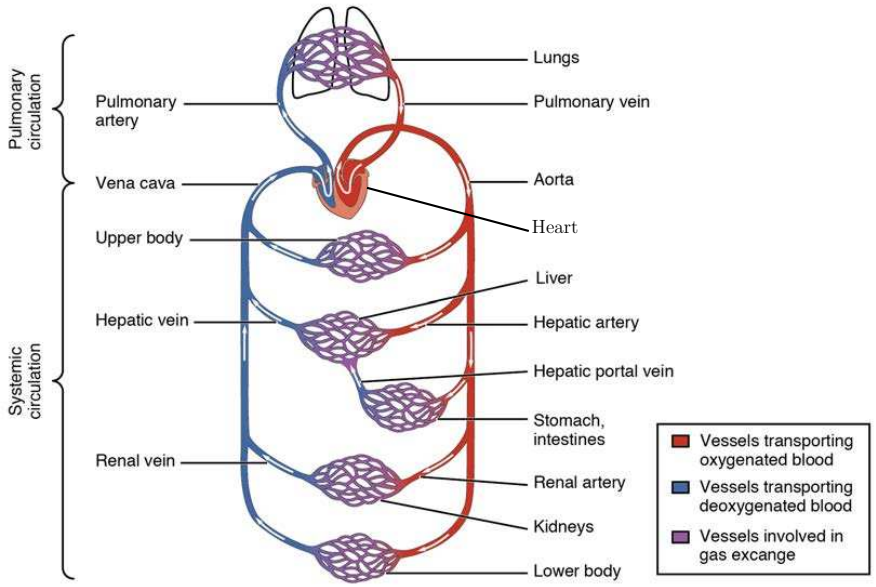

Figure 1.3: Skecth of the circulatory system. Taken and adapted from [11].

and the amount of elastic fibers differ. These fibers are responsible for the elastic behaviour of the artery: the pressure wave coming from heart contraction expands the arterial wall, which stores elastics energy. This energy is then transferred to the blood when the artery returns to its normal size via an elastic recoiling. This helps maintaining the pressure gradient needed to distribute blood through the circulatory system.

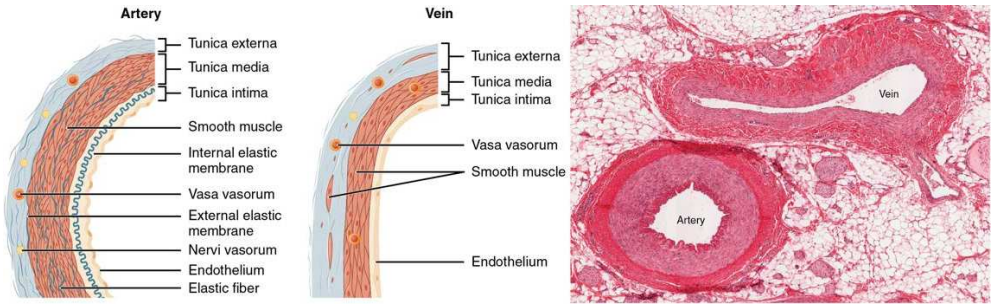

Figure 1.4: Arteries and veins walls layers (top) and a micrograph view (bottom). Taken and adpated from [11].

Endothelial cells present in the intima layer are in direct contact with blood flow and play a major role in wall response to injuries and onset of intracranial aneurysms (detailed later).

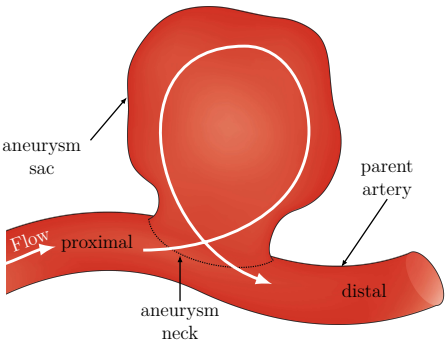

Figure 1.5: Description of saccular aneurysm with related glossary. Typical flow patterns are exhibited with white arrows. Taken and adapted from [115].

1.3 Intracranial aneurysms

In an attempt to fully understand major challenges arisen by IAs, this section addresses very basic but important questions regarding general aspects related to this pathology.

What is an intracranial aneurysm? Intracranial aneurysm are local deformation of arterial arteries that consists of a sac filled with circulating blood. Saccular shapes account for 90% of all aneurysms [52] and grow on the side of their parent artery, as showed in Figure 1.5. Almost 80% of aneurysms have a size between 2 to 12 mm [152]. For comparison purposes, the diameter of cerebral arteries where most aneurysms occur ranges from approximately 5 to 1 mm [3, 74, 122, 123]. The limit between aneurysm sac and its parent artery is referred to as the aneurysm neck, which is a closed contour on the arterial surface. The neck plane is the surface that can be defined using this loop and is the location where blood both enters and exits aneurysm sac.

The Circle of Willis (CoW) is the favoured site of appearance of intracranial aneurysms. This arterial network is intended to supply blood to both hemispheres of the brain by connecting two circulations: anterior and posterior (green and red in Figure 1.6b respectively). The two internal carotid arteries (ICA) on each side of the brain starts the anterior circulation and subdivide to middle and anterior cerebral arteries, MCA and ACA respectively, the latter ending the anterior circulation loop via the anterior communicating artery (ACOM). The posterior circulation consists of the merging of the two vertebral arteries into the basilar one. Connection to the anterior circulation is ensured by the posterior communicating artery (PCOM), thus closing the loop forming the Circle of Willis. According to the International Study of Unruptured Intracranial Aneurysm (ISUIA) [152], 88% of aneurysms are found on the anterior circulation

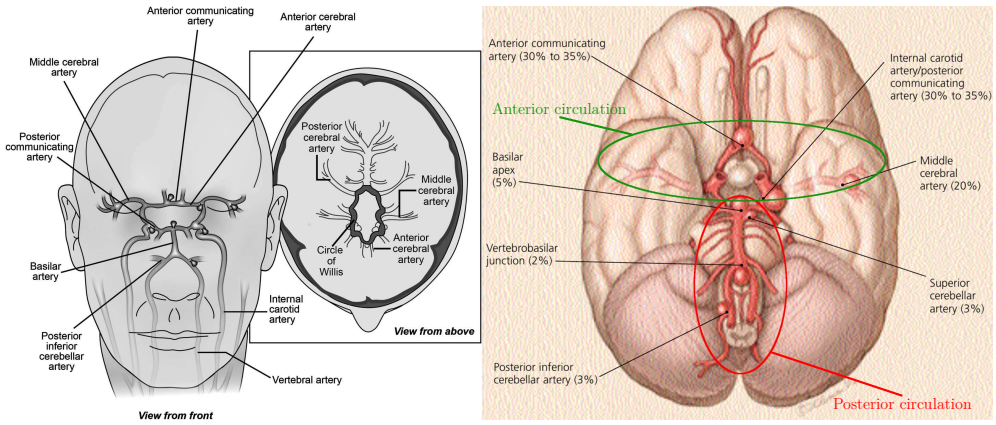

(a) (b)

Figure 1.6: **a:** Main intracranial arteries names and location of the Circle of Willis. Taken from [153]. **b:** Spatial rates of intracranial aneurysm occurrence in the Circle of Willis, viewed from below. View orientation is different between **a** and **b**. Taken and modified from [146].

(green circle in Figure 1.6b) and among patients included in ISUIA, 35% were harbouring more than one aneurysm. It has been estimated by Vlak et al. [148] that IAs have a worldwide prevalence of approximately 3%.

Most aneurysms initiate and grow without presenting any symptoms, which make them very difficult to detect. Common associated symptoms for IAs are headaches, seizure, cranial nerves palsies, focal neurological deficits due to mass effect, *i.e.* when the aneurysm sac is compressing areas of the brain. The most catastrophic event related to aneurysm is the inability of the arterial wall to sustain further growth and thus ruptures, causing blood to leak into regions of the brain. Fortunately, the rates of aneurysm rupture are relatively low. Indeed, given that almost 6-10/100 000 persons experience IA rupture per year [47, 144] and that global prevalence is estimated at 2-3%, this means that approximately 0.3% of all unruptured aneurysms will eventually rupture each year.

What mechanisms drive the formation, growth and rupture of IAs? Aneurysm initiation formation, growth and rupture are closely linked to interactions between hemodynamics and arterial wall inflammatory response.

The structural composition of a non-pathologic cerebral arterial wall, given on the top of Figure 1.7, consists of a stacking of various components. Endothelial cells (ECs), which are in direct contact with blood, are able to "sense" mechanical shear stresses and tend to align with flow direction [64, 78]. Through a phenomenon referred to as "mechanotransduction", ECs can send biochemical signals through the arterial wall, initiating structural remodelling to decrease

vessel diameter due to decreased flow-rate or repair injured arterial regions for example [64].

Via a combination of risk factors and increased hemodynamic stresses typically found at bifurcations in the CoW, ECs initiate an inflammatory response that degrades wall structure rather than repairing it. Degradation subsequently weakens other vessel constituents and results in an outward wall growth aimed at reducing these stresses: the aneurysm is initiated (see the bottom of Figure 1.7).

Then, aneurysm sac evolution pathway, either growth or stabilization, results from a delicate balance between wall remodelling that causes arterial deformations, the latter directly influencing local flow stresses that are transmitted to endothelial cells which finally loops back to wall remodelling via mechanotransduction (see the bottom of Figure 1.7). This cycle can either stop because wall remodelling repair has overcome destruction, thereby inducing a stabilization of the aneurysm wall, or continue until internal pressure becomes higher than the weakened wall strength, causing aneurysm rupture. Interestingly, aneurysm rupture is triggered by blood pressure increase events such as startling and nose blowing [54].

It is thought that the higher predispositions for aneurysms to occur inside intracranial arteries are linked to lower thickness of tunica externa (see Figure 1.4) compared to extracranial vessels [54].

It should be noted that the crucial role of hemodynamics in cardiovascular pathologies is not limited to intracranial aneurysms, as the presence of disturbed shear at the carotid bifurcation is responsible of the initiation and progression of atherosclerosis [98], those disturbances being linked to vortical flow structures encountered near the bifurcation site [57].

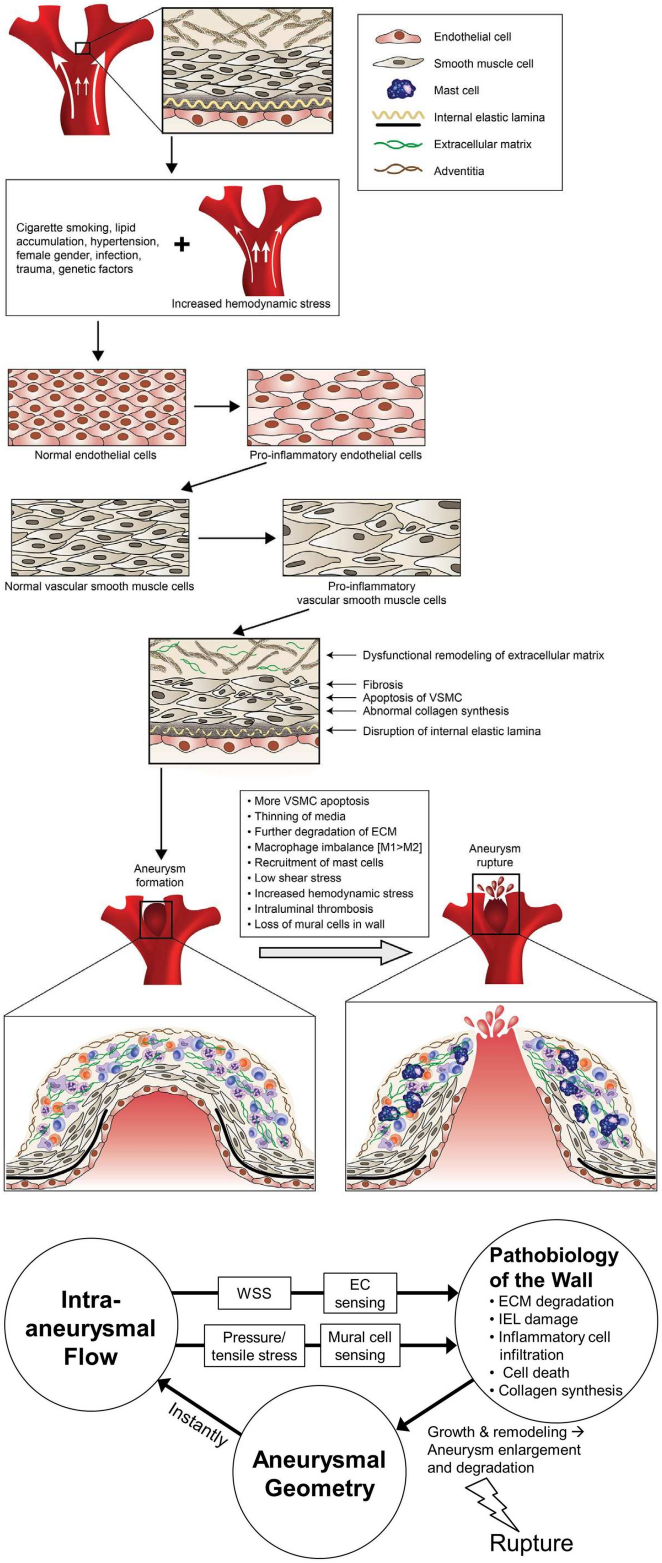

Figure 1.7: Inflammatory response mechanisms responsible for aneurysm initiation, growth and rupture. The continuous loop between hemodynamics, wall-remodelling and aneurysm shape modifications, that ultimately leads to rupture or stabilization, is given at the bottom. Taken and modified from [33, 96].

What are the risks factors for the formation of IAs? Smoking and hypertension have been correlated with the formation of intracranial aneurysms [149]. Furthermore, Vlak et al. [149] demonstrated that when these two factors are combined, the resulting risk factor is even greater than the direct sum of each factor taken separately.

The likelihood for an intracranial aneurysm to initiate has been proven to correlate with a positive family history, which is referred to as familial intracranial aneurysms (FIAs). Indeed, the prevalence of UIAs in people having one first-degree relative (parent, child, sibling) who experienced either an UIA or SAH is equal to 4%, which is sligthly greater than in the general population [127]. This further increases to 8-10% when 2 or more first-degree relatives have been affected by IAs [127]. For FIAs, several factors such as female sex, hypertension and smoking can accumulate and thus increase the formation risk [19].

Age and sex also impacts the formation of aneurysms since UIAs are more prevalent in women than men, with a ratio reaching 2 above 50 years, and more UIAs are discovered for people over 30 years of age [148].

Among inherited diseases, it has been demonstrated that patients suffering of Autosomal Dominant Polycystic Kidney Disease (ADPKD) have an increase of aneurysmal prevalence by a factor of 4 (12.4%) compared to the general population [156]. In addition, patients who survived to an earlier aneurysm rupture have a substantial risk for another aneurysm to develop at other locations [151].

What are the risks factors for IAs rupture? In a large meta-analysis, Greving et al. [61] developed the PHASES score for the prediction of aneurysmal rupture risk which is based upon 6 independent risk factors:

- Population
- Hypertension
- Age $\geq$ 70 years
- Aneurysm size
- Earlier SAH from another aneurysm
- Aneurysm location

Investigators of the PHASES study demonstrated that geographical region plays a role: populations from Finland and Japan tend to have 3.6 and 2.8-times increased risks of experiencing aneurysmal rupture in comparison to other parts of the world. Hypertension, a risk factor already identified in the formation of aneurysms, is also predictive of aneurysm rupture. However, it remains unclear

if blood pressure returning to physiological ranges decreases the rupture risk for patients already harbouring an UIA.

The risk of rupture is also related to the aneurysm itself, as depicted in Figure 1.8. Among all these risks, aneurysm size is a powerful and consistent predictor of aneurysm rupture. Greving et al. [61] demonstrated that there is a rupture risk increase by a factor of 20 for aneurysms bigger than 20 mm compared to those being under 5 mm of size. Additionally, aneurysm location is playing a key role in the rupture risk. Interestingly, despite 88% of unruptured aneurysms are found on the anterior circulation, the rupture risk is more elevated for aneurysms in the posterior circulation, especially those located in the posterior communicating artery (PCOM, h location in Figure 1.8). To this respect, the ISUIA study [152] showed that the 5-year cumulative risk of rupture is systematically greater for aneurysms located in the posterior circulation than those found in anterior one, irrespectively of aneurysm size but only for patients who did not experienced an earlier rupture from a different aneurysm. This fact was further confirmed by Greving et al. [61].

Several aneurysm-related factors not included in the PHASES study that influence aneurysm rupture risk are the presence of irregularities on the aneurysmal sac, such as blebs and daughter sac [73, 99, 140]. Aneurysm growth between two clinical evaluations is also an independent predictor of rupture, with a risk increased by a factor of 12 compared to non-growing aneurysms [147].

Positive familial history was also not studied in the PHASES study. Broderick et al. [18] demonstrated that for aneurysms smaller than 6 mm in the anterior circulation, which have an annual risk of rupture of 0.069% in the general population according to the ISUIA study [152], the rupture risk is multiplied by 17 for patients having a familial intracranial aneurysm (FIA). Therefore, these types of aneurysm can shift treatment decision, since the annual risk of rupture for these persons surpasses preventive treatment risks, which is the inverse for the general population who would have not been treated and be under medical management and observation. Symptomatic aneurysms are also more prone to rupture [150].

What are the consequences of an aneurysm rupture? When aneurysm rupture occurs, the structural integrity of the sac wall is compromised and blood leaks into the space containing brain spinal fluid, referred to as subarachnoid space, thereby causing a so-called Subarachnoid Haemorrhage (SAH) illustrated in Figure 1.9 (see the red $*$ symbol). A wide majority (85%) of SAH found in the population are caused by aneurysm rupture [144].

Symptoms induced by SAH are a sudden and strong headache, which is the only symptom in one third of patients [144], often described as being "the worst headache of my life". Nausea, vomiting, nuchal rigidity and loss of consciousness

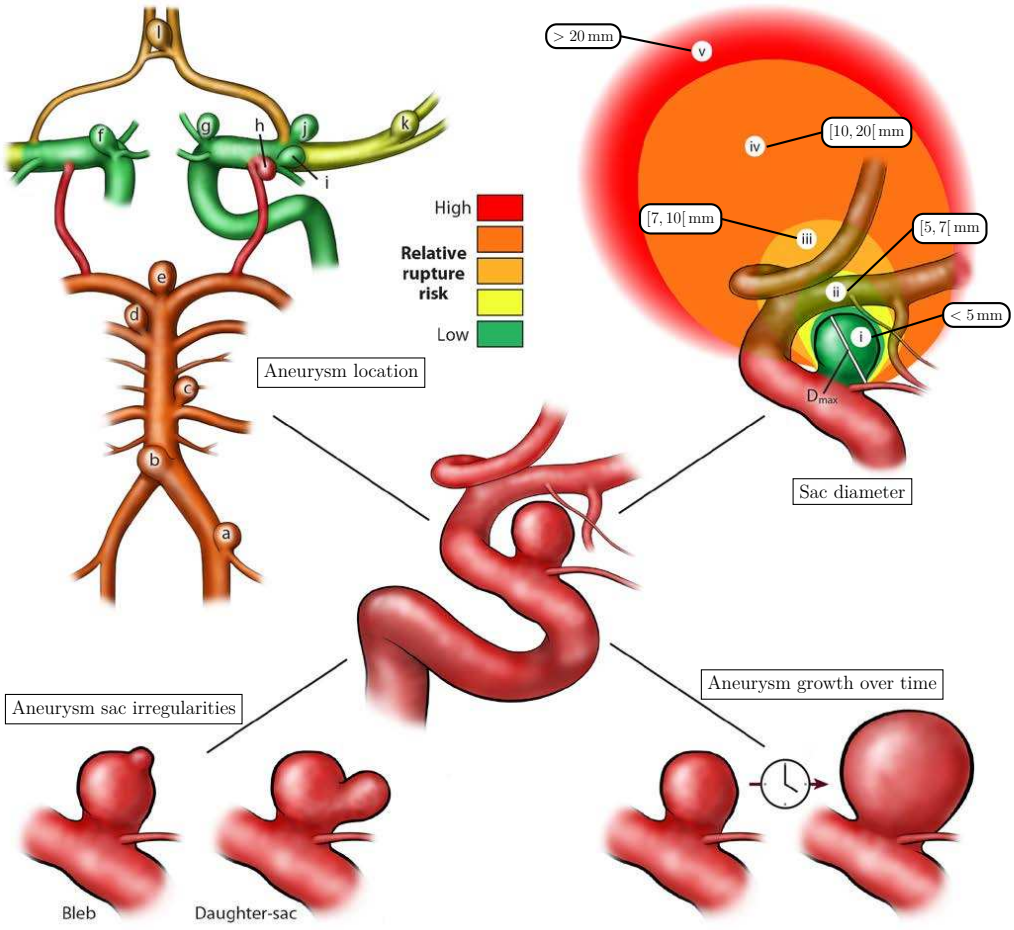

Figure 1.8: Established rupture risk factors related to the aneurysm itself. Taken and modified from [63].

can also be present for patients suffering from SAH. Due to individual differences in symptoms, misdiagnosis is possible and can happen in 12% of patients [1]. The gold standard for providing reliable SAH diagnosis is Computed Tomography (CT) scan (see Figure 1.9). Preceding symptoms are reported in one fourth of patients suffering from SAH and take the form of sentinel headaches weeks before rupture caused by minor leaks and aneurysm sudden expansion [121].

Consequences and complications of SAH are substantial: brain cells damaging, increase of pressure on brain tissue due to excessive amounts of blood (hydrocephalus) and erratic narrowing of arteries impeding blood to flow in vital regions of the brain (vasospasm), which is by far the most severe complication. Consequently, SAH prognosis[2] is very low: among patients with an untreated SAH, one third return to normal life, one third are functionally dependent and

[2]Predicting the likelihood of a person's survival

one third do not survive two weeks after rupture [121].

When detected on time, which is not achieved in 12-15% of patients who either die at home or during transportation to the hospital [1], there exists a non negligible risk of re-rupture that peaks during the first 48 hours after SAH onset. Therefore, rapidly treating the lesion is crucial since prognosis of a second rupture is poor, with a 80% rate of morbidity and mortality [144].

Figure 1.9: Computed Tomography (CT) scan which enables SAH diagnosis with high sensitivity/specificity. The red $*$ symbol identifies the brain region containing blood. Taken and modified from [121].

Which treatments are available? When an IA is discovered, either after of before it ruptures, several treatment strategies developed over the last decades are available. All these strategies are devoted to aneurysm exclusion from parent artery blood flow circulation.

The first treatment was introduced in 1937 by Walter Dandy and revolutionized medical handling of intracranial aneurysms [43]. By placing a silver clip across the aneurysm neck, he successfully managed to isolate a posterior communicating aneurysm in a 43 year-old patient, as illustrated in the left of Figure 1.10. This surgical procedure involves an open craniotomy to reach the aneurysm neck, which is a heavy surgical act (see the right of Figure 1.10). Since the aneurysm is completely excluded and free of hemodynamic stresses, it is considered to be at a low but not null risk of re-rupture [17]. Micro-surgical clipping has been the gold standard in the second half of the 20th century and has seen many improvements, notably in clip designs.

In 1991, the introduction of the Guglielmi detachment coils offered physicians a less invasive procedure compared to clipping since no craniotomy is required. Instead, a micro-catheter is introduced at the patient groin and subsequently navigated until reaching aneurysm location, as depicted in the left of Figure 1.11. Coils are long filaments of platinum/tungsten alloy that are distributed inside

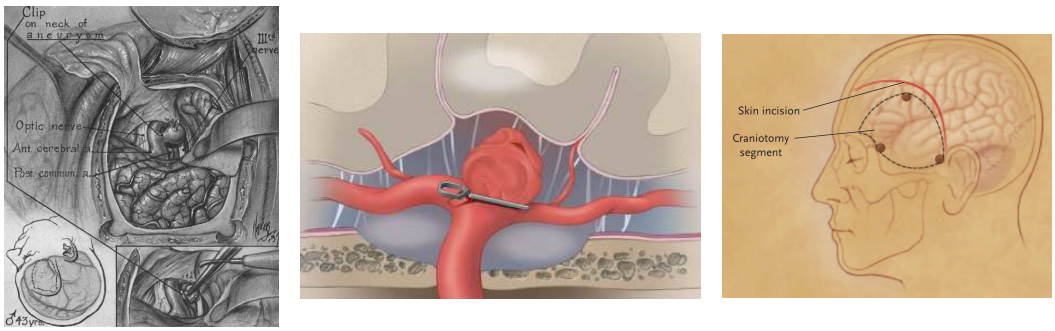

Figure 1.10: Clipping treatment and craniotomy details. From left to right, taken and modified from [17, 43, 53].

the aneurysm sac via the previously inserted micro-catheter. In order to achieve aneurysm filling, three coils shapes, depicted in the middle of Figure 1.11, can be successively inserted:

- Framing coils which are stiff and exert a radial force to achieve positioning stability. Their final position is crucial for treatment success and stability, as they are the foundation on which other more flexible coils rest upon.
- Filling coils: as their name suggests, they are intended to fill the cavity previously created by the framing coils.
- Finishing coils: they are usually smaller in diameter and length compared to previous ones and are used to improve packing density

Unassisted aneurysm coiling, illustrated in the left of Figure 1.11, is however restricted to certain favourable aneurysm morphologies that have a high dome-to-neck ratio to prevent coils from protruding inside the parent-artery, causing vascular puncture or stroke. Therefore, the last decades have seen the appearance of many adjunctive techniques which are depicted in the right of Figure 1.11. For example, a balloon can be inflated at the aneurysm neck during coil filling in order to support framing coils. Once the sac is densely packed with coils, the balloon is deflated and coiling interlocking prevents protrusion inside the parent-artery. The same mechanisms are involved for stent-assisted coiling, on the difference that the stent is not withdrawn after coil filling. For bifurcating aneurysms, a Y-shape stent can be deployed in the two arising arteries and aneurysm filling is performed similarly to previous techniques.

Flow diverting stents (FDs) were introduced in the late 2000's as another endovascular treatment option for aneurysms that harbour complex characteristics such as large sized (giant) and wide-necked [21]. Their design consists of a low-porosity (approximately 30%) stent deployed across the aneurysm neck and

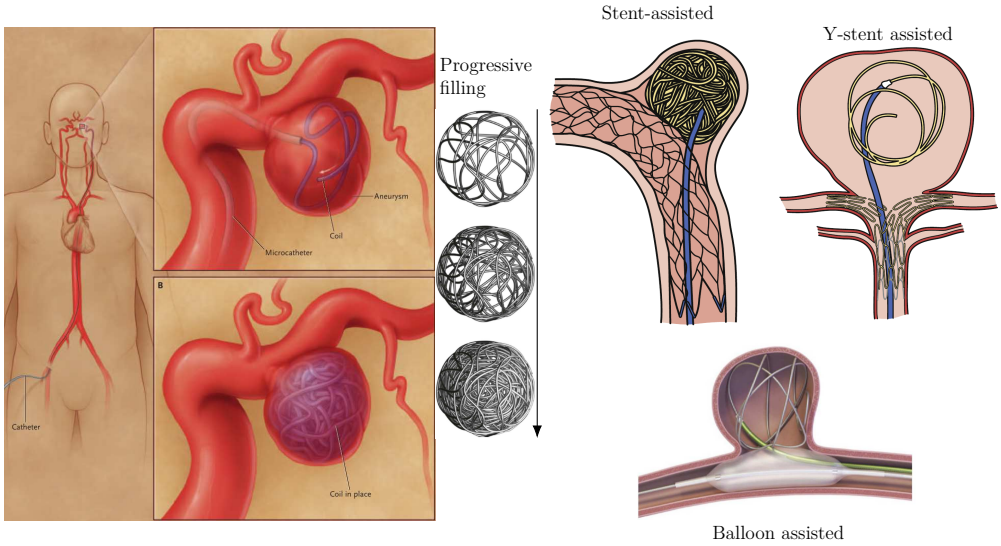

Figure 1.11: Endovascular coiling treatment technique with variants for wide-neck and bifurcating aneurysms. Complete aneurysm filling is performed progressively with 3 types of coils: frame, fill and finish (top to bottom). Taken and modified from [1, 17, 121].

undergoing expansion inside the parent artery (see the left of Figure 1.12). Similarly to coils, aneurysm exclusion from parent artery blood circulation is pursued but mechanisms of actions follow a different pathway. Indeed, FDs are designed to both redirect blood into the parent artery to promote aneurysmal flow stagnation and thrombosis (see top-right in Figure 1.12) and provide a scaffold on which neo-endothelisation coming from apposed device sections is favoured (see bottom line in Figure 1.12) [71, 125]. Pore sizes are designed to be large enough so as to prevent occlusion of perforators arising from parent artery. Due to the fact that they are deployed externally to the aneurysm, no manipulation of the sac is performed, thereby reducing the likelihood of procedural complications compared to coils [121].

One major advantage of such devices is their potential in reducing mass effect, *i.e.* when the aneurysm sac compresses the optic nerve, thanks to intra-saccular scavenger cell-mediated processes [1], which is not achievable with coils. High occlusion and low morbidity and mortality rates for FDs are reported in the literature [9] and consensus is growing among physicians that these devices might be successfully used for other aneurysms shapes they were not firstly intended for.

Due to an increase of available FD designs and references, and more generally of braided device types [21], evaluating device performances and improving them is crucial for both physicians and manufacturers. Therefore, this thesis is intended

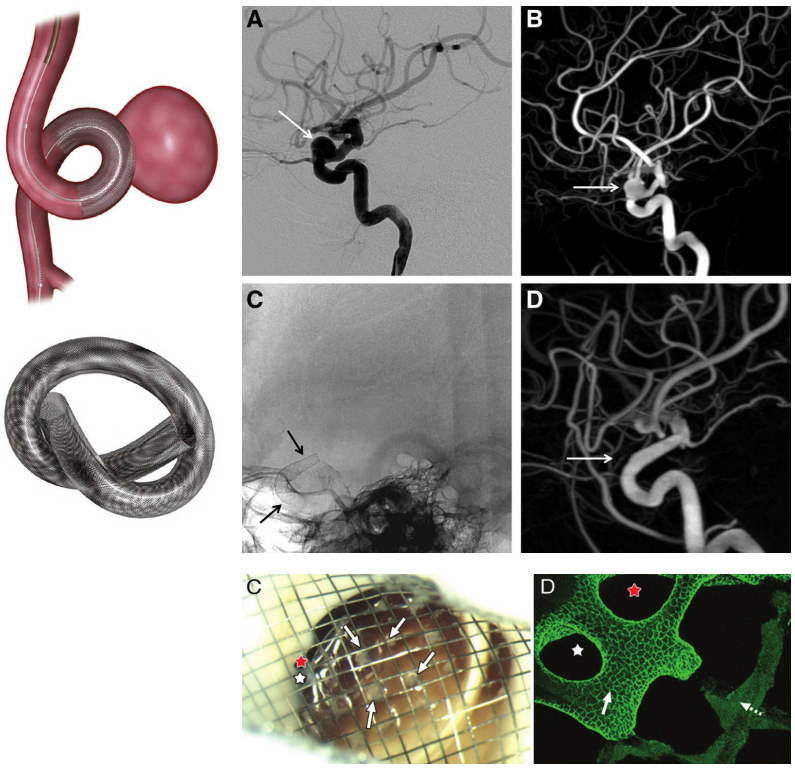

Figure 1.12: Flow diverting deployment and design (left) with successful medical outcome images (top right). Bottom line shows progressive endothelial cells growing from parent artery (solid white arrow on D) along device struts. Taken and modified from [71, 117, 121].

to focus on low porosity endovascular braided device only, meaning that coils and stents are not tackled herein. For the interested reader, an innovative CFD strategy intended to reproduce coils effect onto blood flow can be found in the PhD thesis of Barbour [8], which can be considered as the "coils mirror" of this thesis since pursued objectives are very similar to the present ones.

Why and how CFD has been used in the FD treatment of IAs? Despite high occlusion and low morbidity and mortality rates [9], unexpected delayed ruptures sometimes occur in approximately 3% of FD treated patients [16, 75]. Therefore, there is a need to understand all the key mechanisms that can predict chances of success. To this end, intra-saccular hemodynamics has been thought as one of the essential measures that could enhance success predictions [110]. Additionally, hemodynamic information could also be used to minimize the quantity of metal inside patients by studying flow alterations for different devices characteristics. This could help reducing anti-coagulant quantities for patients who underwent endovascular surgical procedures.

To this end, Computational Fluid Dynamics (CFD) has proven to be an invaluable tool enabling to study the effect of device implantation on the blood flow inside patient-specific geometries [69, 77, 102, 110]. To account for deployed braided devices inside arteries, the most "natural" approach used in most CFD computations is herein referred to as *conformal*, which removes devices struts from the arterial volume via boolean operations. Conformal methods enable to capture the full complexity of flow-patterns induced by the device presence such as wakes, jetting-flow between wires and wake interactions for very densely packed configurations. Although being considered as a ground-truth approach, this method carries significant drawbacks, mainly due to the large difference of length scales between the wires ($\approx 30\,\mu m$) and the arterial ($\approx 5\,mm$) diameters. This scale difference implies a high manual meshing cost in order to produce a grid with sufficient quality around the wires. Additionally, these meshes contain a tremendous number of elements, which requires heavy computational resources. These drawbacks are at odds with short time frames needed by both clinicians for treatment planning and manufacturers for new device numerical experiments with many sizes and geometries [112].

To circumvent these issues, a few techniques have emerged over the last decade, which will be herein referred to as *homogeneous*. The underlying assumption for all these models is that the source of dissipation caused by each device struts produces a collective effect, taking the form of a pressure loss across the surface of the device. Therefore, the sum of local flow dissipations due to the wires can be replaced by a global homogeneous pressure drop to mimic the effect of the device on the fluid. The porous method originally developed by Augsburger et al. [7] and later enhanced by Raschi et al. [124] was the first kind of such homogeneous models. It approximates the device as a porous layer that imposes calibrated pressure losses across its surface via a volume source terms added to the fluid equations. The calibration process of the model was performed by Augsburger et al. [7] thanks to numerical computations on simplified geometries, and was further refined by Raschi et al. [124] who used porous laws through braided meshes. Despite reducing computational costs, Li et al. [80] pointed out that porous model assumptions are not compatible with the very thin structure of endovascular devices. Li et al. [80] went a step further in the modelling of devices by introducing the so-called *screen method*. This technique aims at faithfully reproducing the flow redirection when passing the device while not taking into account each wire individually [81]. Nevertheless, the screen approach remains a homogeneous method inherently unable to capture the full complexity of flows around the device struts.

Representing the flow impact of each individual wire at the neck enables to better predict the intra-saccular hemodynamic environment. In this view, several

previous CFD studies [42, 70, 155, 159] using a conformal approach showed on one hand that local device compaction, and thus struts placement and proximity, is strongly impacting downstream intra-saccular velocities, and on the other hand that device wire density can be optimized to ease treatment decisions for a given case. This strong impact on intra-saccular velocities has been recently confirmed in vitro by Chodzyǹski et al. [38] who found that by deploying the same FD reference (length and diameter) inside a given idealized geometry three times with the same operator, local pore density changes occurred and caused significant differences in aneurysm filling over the cardiac cycle. One may also anticipate that representing the velocity gradient and associated shear stress at the struts is useful to better represent the platelet activation and thus the capability of the device to promote thrombosis, as described in [155]. Nevertheless, these gradients produced by the wires presence are not accessible via homogeneous methods due to both their assumptions and the spatial discretization levels used.

1.4 Thesis outline and objectives

The first objective of this work, presented in **Chapter 2**, is twofold: increase CFD fidelity for endovascularly treated aneurysms and decrease associated computational costs such as mesh-sizes and simulation running time. For this purpose, a novel heterogeneous model aiming at reproducing both flow redirection when passing through the device and struts wakes is introduced. Modifying the well-known Immersed Boundary Method (IBM) [116] to cope with the braided nature of endovascular devices, device local effect onto the flow is modelled by drag forces that are applied on fluid elements lying in wires vicinity. In order to build drag forces models, several working hypotheses are made and numerical computations are performed to calibrate model constants which are specifically designed for endovascular device configurations. Extensive heterogeneous model validation is performed for a simplified device geometry under various representative flow conditions, with conformal results being considered as the ground truth to compare with.

Building on the correct qualitative and quantitative agreement presented in Chapter 2, model validation is extended towards patient-specific geometries using realistic numerical deployment of endovascular devices in **Chapter 3**. Specific issues related to these patient-specific configurations emerged, notably regarding the drag force models that require knowledge of an unperturbed upstream velocity field to compute drag forces, a concept which is not intuitive in "real" finite geometries such as aneurysms. To ensure model operability in these cases, a strategy relying on both conservation principles and fit of an empirical law with numerical computations is developed. Then, model results are compared to

conformal computations originating from our team (1 FD case) and from a collaboration with Professor J.R. Cebral from George Mason University (GMU)[3] for 10 cases: 6 FDs and 4 WEBs. This high number of validation cases aims at measuring model versatility for both various geometries, but more importantly, for different types of endovascular devices (FDs and WEBs). To further illustrate the added value of the proposed model compared to homogeneous strategies, three of the latter were implemented and used on the same geometries. Both qualitative and quantitative analysis are performed using multiple relevant measures to eliminate potential bias and error misses. Computational costs reductions offered by the heterogeneous framework are also assessed in **Chapter 3**.

Chapter 4 is dedicated to model usage in a "real-world" problematic. Preliminary results of a retrospective study are presented, involving 27 WEB-treated aneurysms coming from a database of patients for which access was granted by a collaboration with Dr. Daniel Eduardo Mantilla, interventional neuroradiologist at FOSCAL Clinic, Bucaramanga, Colombia. Starting from medical images and numerical device deployment provided by the Sim&Size® software[4], semi-automatic surface and device pre-processing algorithms are detailed and were used by Dr. Mantilla to autonomously launch CFD computations using the present heterogeneous model. Resulting pre and post-treatment hemodynamic environments are described in details, along with potentially relevant classifications and answers to specific concerns related to WEBs. Finally, a preliminary statistical analysis aiming at linking treatment outcome with both geometrical and hemodynamic indices is presented. Several limitations are raised, which paves the way for deeper analysis and supplementary sensitivity studies.

In the last chapter, results obtained during this thesis are retrospectively analysed and general conclusions are given. Future research directions are finally drawn.

[3]https://cfd.gmu.edu/~jcebral/
[4]https://sim-and-cure.com/product

Chapter 2

Heterogeneous modelling of endovascular devices

Chapter contents

This chapter is based on a recently scientific article under favourable review.[1]

[1] A Heterogeneous Model of Endovascular Devices for the Treatment of Intracranial Aneurysms, *International Journal For Numerical Methods in Biomechanical Engineering*, March 2021

2.1 Introduction

2.1.1 Generalities

When being used for CFD computations of endovascularly treated aneurysms, the conformal approach has proven to be robust thanks to the application of no-slip boundary conditions on the nodes of the struts, as depicted in the bottom of Figure 2.1. Nevertheless, in order to faithfully capture the geometrical and flow complexities induced by the intertwined wires, the mesh has to be sufficiently refined locally, which introduces at least two major costs: manual-meshing and computational.

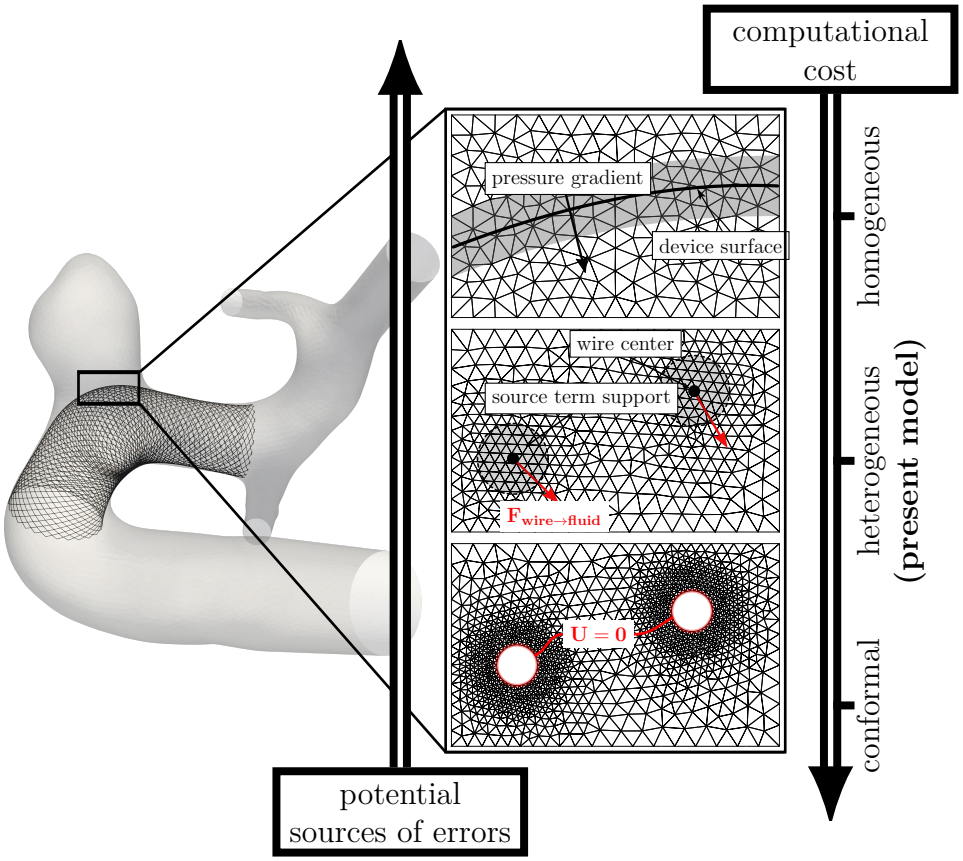

Figure 2.1: Overview of CFD modelling strategies for FD-treated aneurysms. When considering costs and potential sources of errors, the proposed method is lying between homogeneous paradigms such as porous models [7] or the screen approach [81] and more classical techniques herein referred to as conformal [110]. It aims at reproducing the impact of the wires on the flow via a hydrodynamic force $\mathbf{F}_{\mathbf{wire\to fluid}}$ (in red) regularized onto a localized volume source term region (in grey) on the fluid mesh.

To circumvent these issues, homogeneous methods intend to reproduce the

local strut dissipation by a global effect in the form of a pressure loss across the device, which is therefore considered as a porous surface as highlighted in the top of Figure 2.1. This enables to both remove the strong dependence of the fluid mesh on the local struts geometries and coarsen the mesh to reduce computational costs. Nevertheless, this class of methods carries potential sources of errors due to their underlying assumptions and cannot represent the local flow heterogeneities produced by the wires.

We propose here a heterogeneous model of flow diversion, which is an intermediate approach in terms of computational costs and potential sources of errors, as highlighted in Figure 2.1. In this heterogeneous model, the wires forming the endovascular device are replaced by their equivalent 1D neutral fibre. Then, the device is modelled as a collection of linear drag forces $\mathbf{F}$ (force density per unit of length) mimicking the effect of each individual strut on the fluid flow. In this view, the computational mesh is not restricted by the struts, which provides a drastic reduction of both meshing and computational costs. Moreover, each strut is modelled by its corresponding drag force, so that the flow heterogeneities downstream of the device (wakes and jet-like regions) are conserved. These drag forces are applied on fluid regions, highlighted in grey in the middle of Figure 2.1, which can be larger than the struts.

To faithfully mimic the local effect of the struts on the flow without meshing them, the proposed heterogenous model relies upon the paradigm of Immersed Boundary Method (IBM) [116]. IBM is used to represent fluid-structure interactions without explicitly meshing the interface between the fluid and solid domains. Instead, the fluid-structure coupling is performed via a volume source term added to the Navier-Stokes equations so that the fluid flow can feel the presence of the solid domain. This writes:

$$\rho\left(\frac{\partial \mathbf{u}}{\partial t} + \boldsymbol{\nabla}\cdot(\mathbf{u}\otimes\mathbf{u})\right) = -\nabla p + \boldsymbol{\nabla}\cdot\bar{\bar{\tau}} + \mathbf{f} \tag{2.1.1a}$$

$$\boldsymbol{\nabla}\cdot\mathbf{u} = 0 \tag{2.1.1b}$$

with $\mathbf{u}$ the fluid velocity, ρ the density, p the pressure and $\bar{\bar{\tau}}$ the shear stress tensor. In the current approach, $\mathbf{f}$ stands for the volume source term intended to mimic the impact of the device on the flow. Its value is zero everywhere except in the vicinity of the solid parts, *i.e.* the wires of the endovascular device.

Figure 2.2 presents the main ingredients of the Immersed Boundary Method [116] which is the foundation of the proposed model. Starting from a fluid velocity field, the velocity reconstruction step enables to give to the solid parts local velocity information which in turns is used to model the force generated by the solid onto the fluid. Then, in order for the flow to feel the presence of those

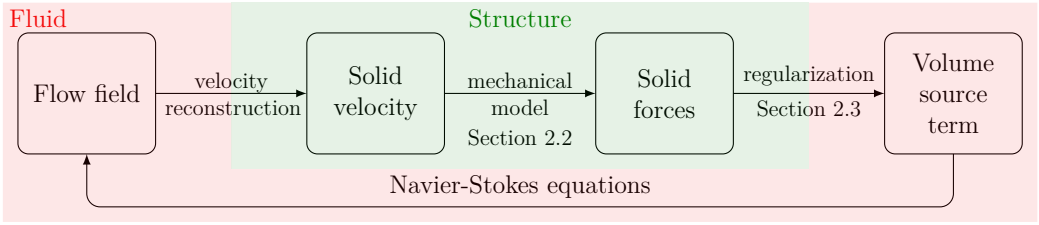

Figure 2.2: Main principles of the Immersed Boundary Method (IBM). Steps involving fluid and solid parts are highlighted in red and green, respectively. The sections involving the main developments are indicated for the ease of comprehension.

forces, a regularization step adds a volume source term in the fluid Navier-Stokes equations. Solving these equations with this newly added source term finally impacts the original velocity field, therefore providing a coupling between fluid and solid.

For the purpose of the intended applications presented herein, only the key steps associated with the most important development efforts will be described in dedicated sections (see Figure 2.2). The remaining steps do not have specific sections associated with them but are still tackled in the present manuscript.

2.1.2 Numerical solver

Aforementioned developments based upon IBM were implemented in the in-house finite-volume YALES2BIO[2] CFD solver. Inheriting massive parallel capabilities from the YALES2 software [100], YALES2BIO intends to solve blood related problems at both microscopic [68, 76, 92, 93, 134, 138] and macroscopic scales [34, 35, 119, 163]. Extensive validations have been performed over the years, as demonstrated in aforementioned references.

In order to be highly scalable, YALES2BIO integrates the concept of Double Domain Decomposition depicted by Figure 2.3a. This supplementary level of decomposition, compared to "classical" parallel codes, is motivated by the idea of localizing the data in parts of the memory which have a faster access speed to the processor, due to the reduced size of manipulated arrays. Therefore, there exists two type of communications: inside each processor and between processors. Both decompositions are carried out by the METIS library. A pressure-projection method is used to handle the incompressibility constraint Equation 2.1.1b, which leads to solving a Poisson equation for the pressure using a Deflated Preconditioned Conjugated Gradient solver [90]. Minimally dissipative fourth-order spatial and time discretization schemes are used to explicitly advance the velocity

[2]https://imag.umontpellier.fr/~yales2bio/index.html

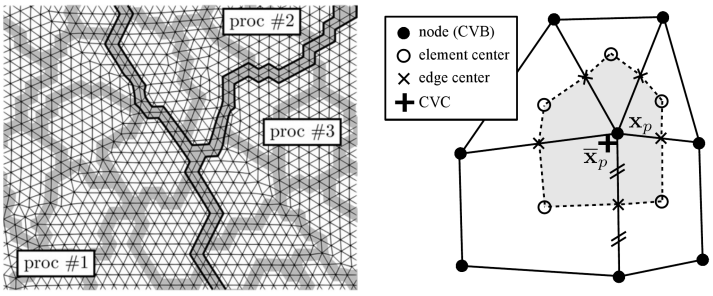

(a) (b)

Figure 2.3: **a:** Double Domain Decomposition found in YALES2 code. Grey and black elements represents cells that are involved in internal and external communication types, respectively. Taken from [100]. **b:** Finite-volume cell-centered notations, taken from [62].

field. A cell-centered finite-volume discretization of Navier-Stokes equations is used in YALES2 and makes uses of control-volumes depicted in Figure 2.3b. More details on the numerical method of YALES2 can be found in [100] and in the PhD thesis of Vantieghem [145], Puiseux [120] and Taraconat [139].

2.2 Cylinders forces

As already stated, the current model replaces the struts volumes by their 1D neutral fibre, which is equivalent to using the beam theory in the field of solid mechanics. Therefore, it is considered that each of these 1D struts applies drag forces $\mathbf{F}$ onto the fluid in their close vicinity while being static with respect to the flow. Focus is now made on the computation of these forces for each edge of the endovascular device.

2.2.1 Working assumptions

This study focuses on braided endovascular devices consisting in two families of crossing struts (see Figure 2.4). Three parameters depicted in Figure 2.4 are used to fully characterize the device geometry: the inter-wire distance W, the strut diameter D and the acute angle formed at the intersections between the struts, α. Typical values of those parameters encountered for Pipeline Embolization Device (PED) flow-diverters are available in [14]. Attached to each cylinder, a local basis can be built as depicted in the right of Figure 2.4. It consists of normal, tangential and longitudinal unit vectors, denoted $\mathbf{n}$, $\mathbf{t}$ and $\mathbf{l}$, respectively. $\mathbf{n}$ is normal to the device, $\mathbf{l}$ is aligned with the strut and $\mathbf{t}$ is tangential to the device (not the strut) and normal to $\mathbf{n}$ and $\mathbf{l}$.

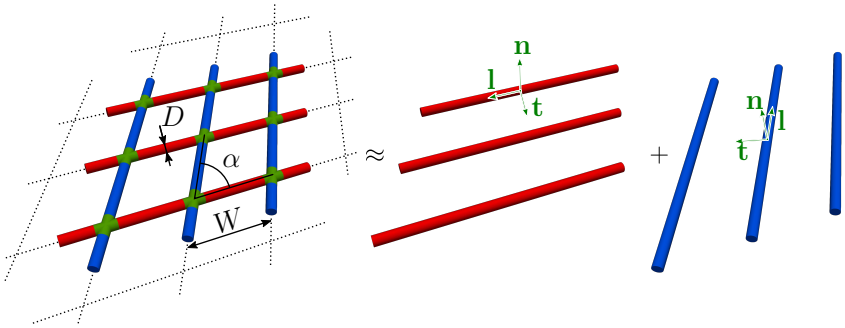

Figure 2.4: The device is assumed to consist of a superposition of two independent families of infinite parallel cylinders (red and blue), which entails that the blue wires are not affected by the flow redirection due to the red ones, and vice-versa. Crossings parts (in green) are also neglected. The device is fully parametrized by the inter-wire distance W, the wire diameter D and the small inner angle α. Attached to each cylinder, a local basis (in green) is used to decompose drag forces into normal $\mathbf{n}$, tangential $\mathbf{t}$ and longitudinal $\mathbf{l}$ directions. It should be noted that the $\mathbf{t}$ unit vector is located in the plane built by all the wires.

In order to build the drag model needed to obtain the force $\mathbf{F_m}$ for each m^{th} edge of the device, the following assumptions have been made:

H1 The local curvature of the wires, as well as the intertwining are neglected. This amounts to considering straight merged cylinders as schematized to the left of Figure 2.4.

H2 It will prove useful to restrict to situations where the inter-wire distance W is much larger than the strut diameter ($W/D > 5$, say). This assumption is not very restrictive and is reasonably met by flow-diverters and intra-saccular types of devices extensively listed in [21].

H3 The inter-wire distance W is assumed to be very small compared to the typical size of the aneurysm neck so that edge effects do not control the flow over the major part of the device. Therefore, from a modeling point of view, the device is considered to be immersed within an infinite fluid domain. Note that edge effects are partly accounted for, as the flow velocity near the edges of the neck is strongly slowed down by the presence of the walls of the artery and of the aneurysm.

H4 The device struts are divided into two distinct "families" made of parallel infinite cylinders, as described to the right of Figure 2.4. Interactions between cylinders are restricted to their parallel family members, which means, using the color code of Figure 2.4, that the flow deviation caused by blue wires is not taken into account when computing drag forces applied by

red wires onto the fluid, and vice versa. Parallel family interactions will be further referred to as "intra-familial" interactions in the remaining of the thesis, as opposed to "extra-familial" ones.

H5 The locations where cylinders merge together (in green) herein referred to as "crossings" are represented by the superposition of the drag forces related to the two families of struts, without further modelling effort.

Hypotheses from H1 to H3 are "geometrical" since they only depend on the geometric characteristics of endovascular devices. H4 and H5 are "modelling" hypotheses because they are used to construct the drag forces models at the struts. In view of these hypotheses, it is assumed that intra-familial interactions between cylinders are negligible in the longitudinal direction $\mathbf{l}$ when compared to the ones present in the normal-tangential plane $(\mathbf{n}, \mathbf{t})$. It is equivalent to state that there is an invariance with respect to the longitudinal direction. This means that the problem reduces to a 2D problem: how does one array of aligned 2D cylinders interact with each other and what is the resulting drag force applied on the fluid ? Even though the longitudinal direction $\mathbf{l}$ is not taken into account in cylinders interactions, drag forces are still present in this direction and will be described later.

In the remainder of this section, it is assumed that cylinders are immersed in a known, uniform velocity field denoted $\mathbf{U}_\infty$. Given this upstream velocity $\mathbf{U}_\infty$, we propose a model for the drag forces in the directions $\mathbf{n}$, $\mathbf{t}$ and $\mathbf{l}$, on the basis of the assumptions H1-H5, which is a classical way of building drag models. The upstream Reynolds number defined by $\mathrm{Re} = \frac{||\mathbf{U}_\infty|| D}{\nu}$ with ν the fluid kinematic viscosity and D the diameter of the wires is sufficient to characterize the drag force experienced by an isolated 2D cylinder. For an array of 2D parallel cylinders, another non-dimensionalized parameter measuring the closeness of cylinders, the $\tilde{W}/D = \frac{W \sin\alpha}{D}$ ratio, say, has to be introduced (see Figure 2.4).

Relevant ranges for Re and $\tilde{W}/D$ have to be considered to make sure that the outcome of the modelling effort will indeed be useful to biomedical applications. From previous observations and computations, the highest Re values encountered in FD-treated intracranial aneurysms is approximately $\mathrm{Re} = 20$. This is confirmed by Raschi et al. [124] who states that the highest Re is usually "*around* $Re = 20$*, hardly exceeding 60 but still falling in the transition zone between low and intermediate Re*". During the whole cardiac cycle, endovascular wires can experience both low and high Reynolds numbers depending on their position at the neck. The high Reynolds regimes mainly drive the most important intra-saccular flow features such as large recirculation regions and incoming jets. Since the ability of endovascular devices to reduce intra-saccular velocities and increase residence time is critical for high Reynolds flow regimes, *i.e.*

when convective effects are dominant, the current modelling effort focuses on these regimes. A heterogeneous model which would include both low and high Reynolds is of course very desirable and could be obtained by combining a model for the diffusive regime with the one proposed in this work. For the remainder of the chapter, we are concerned with modelling the flow through a weaving of wires in the high Reynolds regimes, *i.e.* when convection effects dominate. The performances of the model when the Reynolds number gets small will be assessed for the sake of completeness in Section 2.4.2. Regarding the $\tilde{W}/D$ ratio, its values range approximately from 6 to 10 for PEDs flow-diverters according to the data available in [14].

From the local basis defined in Figure 2.4, the drag force $\mathbf{F_m}$ exerted by the fluid on each cylinder is decomposed into its normal F_n, tangential F_t and longitudinal F_l components:

$$\mathbf{F_m} = F_t\mathbf{t} + F_n\mathbf{n} + F_l\mathbf{l}\,. \tag{2.2.1}$$

As a note of caution regarding units, it should be noted that forces per unit of length are considered for drag forces $\mathbf{F_m}$, since only 2D cylinders are studied. The local orthonormal basis $(\mathbf{n}, \mathbf{t}, \mathbf{l})$ is built to ensure that the scalar product of each unit vector with $\mathbf{U}_\infty$ is positive. Reynolds numbers associated with each velocity components are then computed as:

$$\begin{cases} \mathrm{Re}_n = & \dfrac{(\mathbf{U}_\infty \cdot \mathbf{n})\, D}{\nu}\,, \\ \mathrm{Re}_t = & \dfrac{(\mathbf{U}_\infty \cdot \mathbf{t})\, D}{\nu}\,, \\ \mathrm{Re}_l = & \dfrac{(\mathbf{U}_\infty \cdot \mathbf{l})\, D}{\nu}\,. \end{cases} \tag{2.2.2}$$

As previously stated, the drag force is assumed to be invariant in the longitudinal direction, so that the 3D problem is equivalent to that of an infinite series of cylinders aligned with the tangential direction as schematized in Figure 2.5.

2.2.2 Normal term F_n

The normal component of the force applied by an array of cylinders subjected to a purely normal incoming flow has already been studied by Müller et al. [104], who proposed an empirical fit using a combination of existing analytical drag models and numerical computations. When compared with CFD results, this model provides a maximum error below 4% for the ranges $0 < \mathrm{Re}_n < 20$ and

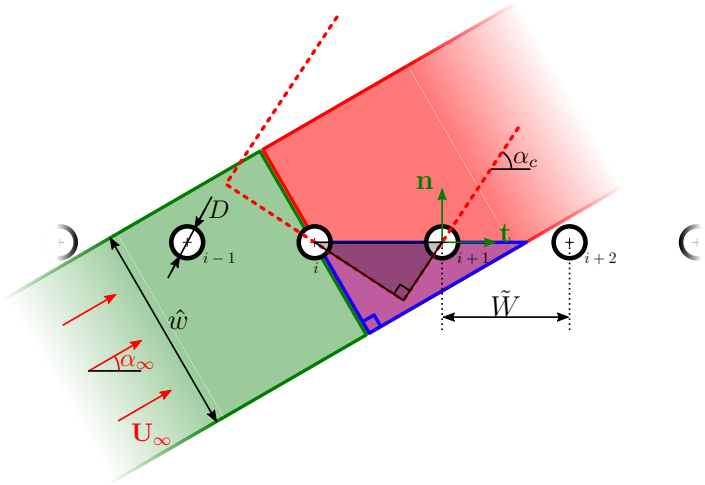

Figure 2.5: An infinite single array of aligned cylinders of diameter D and inter-wire distance $\tilde{W}$ is submitted to an upstream undisturbed velocity field $\mathbf{U}_\infty$; the angle of attack is α_∞. The total force exerted on each cylinder by the fluid can be decomposed in the normal-tangential basis (in green) denoted by $(\mathbf{n}, \mathbf{t})$. Green and red regions of width $\hat{w}$ aim to represent portions of the fluid influencing and being influenced by the i$^{\text{th}}$ cylinder, respectively. In the case displayed here, it is considered that the i$^{\text{th}}$ cylinder only influences one cylinder in its downstream wake, the (i+1)$^{\text{th}}$ cylinder and that it is directly influenced by the wake of a single cylinder, the (i-1)$^{\text{th}}$ one. Additionally, the critical angle α_c which corresponds to the case where the regions edges lie in the middle of the following and preceding cylinders is depicted with red dotted lines. It is considered that the condition $\alpha_\infty < \alpha_c$ entails cylinders wake interactions and thus drag forces modifications compared to the isolated cylinder case.

$2 < \tilde{W}/D < 20$, which encompasses our intended ranges of interest. Following Müller et al. [104], the normal component F_n is given by:

$$F_n(\mathrm{Re}_n, \tilde{W}/D) = C_D \frac{\rho \left(\mathbf{U}_\infty \cdot \mathbf{n}\right)^2 D}{2}, \tag{2.2.3}$$

with ρ the fluid density and C_D the so-called dimensionless drag coefficient that depends on the normal Reynolds number Re_n and the $\tilde{W}/D$ ratio. Following Müller et al. [104], its expression writes:

$$C_D = C_{D,M} \left(1 + 1.966 \mathrm{Re}_n^{0.4193} \times \exp\left[-8.774 \left(\frac{\tilde{W}}{D}\right)^{-0.3143} \mathrm{Re}_n^{-0.4688}\right]\right), \tag{2.2.4}$$

with $C_{D,M}$ being the drag coefficient analytically derived by Miyagi [97] for Stokes flow regime ($\mathrm{Re} \to 0$) and $1.43 < \tilde{W}/D < 100$ ranges. Its expression is

given by:

$$\begin{cases} C_{D,M} &= \dfrac{16\pi a_0}{\mathrm{Re}_n}\,, \\ a_0 &= \left[1 - 2\ln(2\kappa) + \frac{2}{3}\kappa^2 - \frac{1}{9}\kappa^4 + \frac{8}{135}\kappa^6 - \frac{53}{1350}\kappa^8 + \frac{1112}{42525}\kappa^{10} - \frac{241643}{13395375}\kappa^{12} + \frac{18776}{1488375}\kappa^{14}\right]^{-1}\,, \\ \kappa &= \dfrac{\pi D}{2\tilde{W}}\,. \end{cases} \tag{2.2.5}$$

It should be noted that this expression induces that for a given Reynolds number, the drag force increases when the $\tilde{W}/D$ ratio decreases. Moreover, it is worth mentioning that this component only depends on the normal Reynolds Re_n.

2.2.3 Tangential term F_t

General expression To the best of the authors' knowledge, no modelling effort dedicated to tangential drag forces for an array of equally-spaced cylinders is reported in the literature, at least for the ranges of Reynolds number and $\tilde{W}/D$ ratio of interest. For example, Crowdy [41] focused on an inviscid and irrotational flow, which is not relevant to our configuration. This led us to build such a tangential drag model using both CFD computations and existing drag models.

Considering an infinite series of cylinders as depicted in Figure 2.5, the first step is to consider the case where $\tilde{W}/D \to \infty$, meaning that cylinders are isolated and do not interact with each other. We also consider a purely tangential incoming flow. Then, the drag force in the tangential direction can be computed using the so-called *universal drag model* derived by Marheineke and Wegener [91], applicable to any Reynolds number and incident flow angle, except for purely longitudinal configuration. Marheineke and Wegener [91] fitted CFD results with existing drag laws at various Reynolds regimes to obtain their continuous model.

Note that the normal unit vector $\mathbf{n}$ in [91] corresponds in our case to the tangential one $\mathbf{t}$. By using our notation convention, the tangential drag force term for a unique isolated cylinder denoted in the following by F_t^0 is given by:

$$F_t^0 = \frac{\rho\nu^2}{D}\mathrm{Re}_t^2 C_t(\mathrm{Re}_t) \tag{2.2.6}$$

with C_t being the dimensionless drag coefficient in the tangential direction. It should be noted that it only depends on the tangential Reynolds number Re_t and is given by:

$$C_t(\mathrm{Re}_t) = \exp\left[\sum_{j=0}^{3}\left(p_{t,j}\,(\ln \mathrm{Re}_t)^j\right)\right] \tag{2.2.7}$$

with $p_{t,0} = 1.6911$, $p_{t,1} = -6.722 \times 10^{-1}$, $p_{t,2} = 3.3287 \times 10^{-2}$ and $p_{t,3} = 3.5015 \times 10^{-3}$. Equation 2.2.7 is valid in the interval $\mathrm{Re}_t = [0.1, 100]$, which encompasses the intended range of interest relevant to the proposed heterogeneous model. It should be noted that the normal force given by Equation 2.2.3 approaches Equation 2.2.6 on the conditions that $\tilde{W}/D \to \infty$ and that the corresponding Reynolds numbers are equal.

The second step aims at taking into account the interactions between cylinders. The main idea is that due to the angle of attack α_∞, the flow seen by a cylinder may result from the interaction with a different number of cylinders. We first consider a finite series of N_c cylinders aligned in the tangential direction. Each of them is labelled with an index i going from 0 to $N_c - 1$, following the order defined by the direction of the tangential velocity as in Figure 2.5. They are separated by an inter-wire distance $\tilde{W}$ and it is hypothesized that they are subjected to a purely tangential incoming flow. Since the infinite assumption is no more relevant in this case (due to the proximity of the cylinders), each cylinder experiences a drag force which is different than its neighbours. More specifically, it is postulated that the wakes of the cylinder induce a reduction of the drag forces downstream, that is $F_t^{i+1}/F_t^i < 1$. Additionally, it is assumed that the rate of decrease is constant for each cylinder, implying that $F_t^{i+1} = qF_t^i$, $\forall i \in [0, N_c - 1]$ with $0 < q < 1$. Consequently, this amounts to considering that the force exerted by each cylinder on the fluid follows a geometric sequence with a common ratio q to be determined later. In order to homogenise the global effect of those N_c cylinders onto the fluid, one can consider that each cylinder applies a force F_t equals to the average of the total force exerted by all the interacting cylinders such that:

$$F_t = \frac{1}{N_c}\left(\sum_{j=0}^{N_c-1} F_t^j\right) = \frac{1}{N_c}\left(\frac{F_t^0\left(1-q^{N_c}\right)}{1-q}\right), \tag{2.2.8}$$

where F_t^0 is the drag force experienced by the first cylinder. Since it does not have any upstream counterpart, it is considered to be isolated and thus, its drag force expression is given by Equation 2.2.6.

The last step aims at obtaining an expression of the drag force exerted by one cylinder in a infinite array when the incoming flow is not purely tangential, as depicted by Figure 2.5. Starting from Equation 2.2.8, the number of cylinders that are interacting N_c and the geometric common term q are the two main unknowns. To derive an expression for N_c, two areas coloured in green and red in Figure 2.5 are defined and are oriented by the angle of attack α_∞. Since $\mathbf{n}$ and $\mathbf{t}$ are oriented according to $\mathbf{U}_\infty$, α_∞ lies in the $[0, \pi/2]$ range. The red/green areas correspond to the domain of influence of the i$^{\text{th}}$ cylinder and the zone influencing the drag at the same obstacle, respectively. They extend up to infinity parallel to the

incoming flow direction and have a finite perpendicular width $\hat{w}$, expressed as a linear function of the wire diameter D such that $\hat{w} = N_w D$, N_w being the number of cylinder diameter across the influencing region (see Figure 2.5). When reaching a critical angle of attack α_c, the edge of the green region intersects the center of (i-1)$^{\text{th}}$ cylinder, as shown in Figure 2.5 (see the red dotted line). Therefore, the condition $\alpha_\infty > \alpha_c$ entails no cylinder interactions and thus $N_c = 1$ since the coloured regions do not overlap downstream and upstream cylinders. On the other hand, $\alpha_\infty \leq \alpha_c$ implies that the i$^{\text{th}}$ cylinder is influenced and influences $N_c > 1$ cylinders upstream and downstream respectively. It is expected that N_c should increase with decreasing α_∞ to reflect that interactions are getting stronger as more cylinders are added in the influenced region.

Following previous considerations, N_c can be computed such that:

$$N_c = \begin{cases} 1 & \text{if } \alpha_\infty > \alpha_c\,, \\ \dfrac{\sin \alpha_c}{\sin \alpha_\infty} & \text{otherwise.} \end{cases} \tag{2.2.9}$$

The expression on the second line of Equation 2.2.9 has been chosen so as to obtain $N_c = 1$ if the edge of the influencing region touches the (i+1)$^{\text{th}}$ cylinder center, *i.e.* when $\alpha_\infty = \alpha_c$. For smaller α_∞ angles, this expression compares the length of the hypotenuses of the black and blue rectangular triangles in Figure 2.5. It should be noted that N_c is no more an integer when cylinders interact due to the previous definition and that it is a function of both α_∞ and $\tilde{W}/D$. Plugging Equation 2.2.9 into Equation 2.2.8 entails that without cylinder interactions, i.e. $N_c = 1$, the drag force exerted by the i$^{\text{th}}$ cylinder is equal to an isolated one F_t^0, which is the expected behaviour of the model.

Accordingly, the critical angle α_c is defined as:

$$\alpha_c = \begin{cases} \pi/2 & \text{if } \hat{w} > 2\tilde{W}\,, \\ \arcsin\left(\frac{\hat{w}}{2\tilde{W}}\right) & \text{otherwise}\,. \end{cases} \tag{2.2.10}$$

The first line in Equation 2.2.10 represents the case where interactions between cylinders are occurring for any angle of attack α_∞ since the influencing region always overlaps downstream cylinders.

Focus in now made on the expression of the common ratio q. To assess this quantity, it is hypothesized that when cylinders interact, q obeys to a linear relation with respect to the angle of attack α_∞. Otherwise, a constant value of is specified. Therefore,

$$q = \begin{cases} 1 & \text{if } \alpha_\infty > \alpha_c\,, \\ \left(\dfrac{1 - q_p}{\alpha_c}\right)\alpha_\infty + q_p & \text{otherwise.} \end{cases} \tag{2.2.11}$$

with q_p being the common term when the incoming flow is purely parallel to the tangential direction.

All the previous steps are summarized in the following pseudo Algorithm 1 used to compute the tangential force F_t from flow and geometry inputs:

Algorithm 1 Computation of the tangential drag force F_t

Inputs: α_∞, $\tilde{W}$, D, Re_t, ρ, ν
Output: F_t

$F_t^0 = \dfrac{\rho\nu^2}{D}\mathrm{Re}_t^2 C_t(\mathrm{Re}_t)$
C_t given by Equation 2.2.7
$\hat{w} = N_w D$

if $\hat{w} > 2\tilde{W}$ **then**
  $\alpha_c = \frac{\pi}{2}$
else
  $\alpha_c = \arcsin\left(\dfrac{\hat{w}}{2\tilde{W}}\right)$
end if
if $\alpha_\infty < \alpha_c$ **then**
  $N_c = \dfrac{\sin\alpha_c}{\sin\alpha_\infty}$
  $q = \left(\dfrac{1-q_p}{\alpha_c}\right)\alpha_\infty + q_p$
  $F_t = \dfrac{1}{N_c}\left(\dfrac{F_t^0\left(1-q^{N_c}\right)}{1-q}\right)$
else
  $F_t = F_t^0$
end if

It should be noted that the division by zero induced by $q = 1$ in Equation 2.2.8 when cylinders do not interact is circumvented in Algorithm 1 by replacing Equation 2.2.8 by F_t^0 directly. For the tangential model to be fully complete, there remain two unknowns in the previous expressions: the width of the interaction area depending on N_w and the common ratio q_p. Values for these parameters are determined by optimizing the agreement between the modelled tangential drag force given by Algorithm 1 with numerical values obtained from conformal CFD computations.

Numerical fitting of coefficients N_w and q_p Despite being built using 2-dimensional reasoning, it has been decided to perform 3D computations to calibrate the presented tangential model so as to partly account for the complex

intra and extra-familial interactions between cylinders. An idealized configuration consisting of an infinite planar device with two sets of parallel straight wires intersecting at an inner angle $\alpha = \pi/2$ and subjected to an incident velocity $\mathbf{U}_\infty$ was considered. $\mathbf{U}_\infty$ is varied, as well as the spacing between the struts, with the constraint that $\tilde{W}/D = W/D \gg 1$. To compute such a flow, a reduced computational domain is used (see Figure 2.6), with periodic boundary conditions enforced at the left-right and front-bottom faces. At the inlet, the uniform velocity field $\mathbf{U}_\infty$ is applied (see the red section in Figure 2.6). The outlet section (black section in Figure 2.6) was placed further downstream to prevent any interference with wires wakes. A convective outflow condition was applied at the outlet.

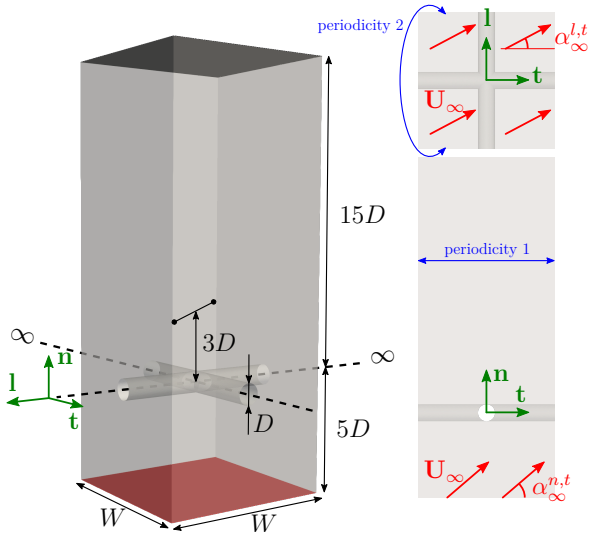

Figure 2.6: 3D bi-periodic domain of width W. No-slip boundary conditions are applied on the struts surfaces. The angle between the wires is $\pi/2$. Inlet and outlet sections are highlighted in red and black, respectively. Periodic boundary conditions are enforced at the left-right and front-bottom faces. The probing line which is latter used to compute the error defined by Equation 3.4.7 is also depicted downstream of the cylinders (line with • symbols).

Compared to the 2D configuration depicted in Figure 2.5, the imposed unperturbed velocity is now free to be outside the $(\mathbf{n}, \mathbf{t})$ plane. The definition of α_∞ in the $(\mathbf{n}, \mathbf{t})$ plane still holds and is now denoted by $\alpha_\infty^{n,t}$; the second angle necessary to define the orientation of the unperturbed velocity is denoted by $\alpha_\infty^{l,t}$ and lies in the $(\mathbf{l}, \mathbf{t})$ plane. Specifying the vector magnitude (using Reynolds number) as well as these two angles enable to fully compute the $\mathbf{U}_\infty$ value at the inlet, as schematized in the right of Figure 2.6. In the following, two values of $\alpha_\infty^{l,t}$ have been considered: 0 and $\pi/3$, the latter being chosen to study the situation where the flow is not aligned with any of the wires family, which is

the general case in real flow conditions. The following ranges have been considered for the other varying parameters: $W/D \in [6, 20]$, $\alpha_\infty^{n,t} \in [\pi/20, \pi/2]$ and $\mathrm{Re} = \frac{\|\mathbf{U}_\infty\| D}{\nu} \in [2.5, 20]$. Computations at $\mathrm{Re} = 2.5$ were performed so as to assess the behaviour of the model when being used outside its working range, *i.e.* at low Reynolds numbers. In other words, this flow condition was not used during the fitting procedure of tangential drag model. For each operating point defined by values of $(\mathrm{Re}, \frac{W}{D}, \alpha_\infty^{n,t}, \alpha_\infty^{l,t})$, a conformal simulation was performed, resulting in 290 numerical computations in total. For all conformal computations, no-slip boundary conditions were applied at the strut surface.

Meshes have been built using Gmsh [59] and smooth mesh size coarsening when moving away from cylinders locations has been specified (see one mesh example in Figure 2.9). At the cylinders surface, a mesh size h was enforced to be a function of the perimeter such that $h = \frac{\pi D}{N_h^c}$ with $N_h^c = 40$. The larger conformal mesh that has been built for $W/D = 20$ computations consists of 19M tetrahedral elements in total. Table 2.1 summarizes the 3D simulation parameters used to fit the proposed tangential model.

Re	W/D	$\alpha_\infty^{n,t}$	$\alpha_\infty^{l,t}$	Mesh size h
$\{2.5^*, 5, 10, 15, 20\}$	$\{6, 8, 10, 20\}$	$\frac{\pi}{20} \to \frac{\pi}{2}$	$\{0, \frac{\pi}{3}\}$	$\frac{\pi D}{40}$

Table 2.1: 3D conformal computation parameters.

For each simulation identified by a single operating point $(\mathrm{Re}, \frac{W}{D}, \alpha_\infty^{n,t}, \alpha_\infty^{l,t})$, numerical computation of the total force $\mathbf{F}$ exerted by the fluid onto each wire family was performed such that:

$$\mathbf{F} = \int_{\partial\Omega} \left(-p\mathbf{n} + \bar{\bar{\tau}}\mathbf{n}\right) \mathrm{d}S \tag{2.2.12}$$

with $\mathbf{n}$ the outward unit normal vector on each considered cylinder $\partial\Omega$. Then, the tangential drag component F_t was obtained via projection onto each wire family basis, which is depicted in green for one family in Figure 2.6. Finally, a least-square fitting procedure minimizing the errors between the aforementioned numerical F_t values and F_t expression given in Algorithm 1 by adjusting both N_w and q_p parameters was performed.

Comparison of the fitted tangential model with CFD data is shown in Figure 2.7 for all the studied Reynolds numbers and for only one cylinder family (the one that corresponds to the green basis in Figure 2.6). The least square fitting yielded values close to $N_w = 12$ and $q_p = 0.5$, which produce a behaviour similar to 3D CFD data (exact values are $N_w = 11.977$ and $q_p = 0.5254$). More precisely, once properly tuned, the model reproduces both the increase and the decrease

of drag force when the incoming flow goes from purely normal ($\alpha_\infty^{n,t} = \pi/2$) to tangential ($\alpha_\infty^{n,t} = 0$), this for various W/D ratios and $\alpha_\infty^{l,t}$ values. It has been found that in general, the fitted tangential model goes from overestimating to underestimating forces when the flow becomes purely normal. This underestimation is even more pronounced when $\alpha_\infty^{l,t} = \pi/3$.

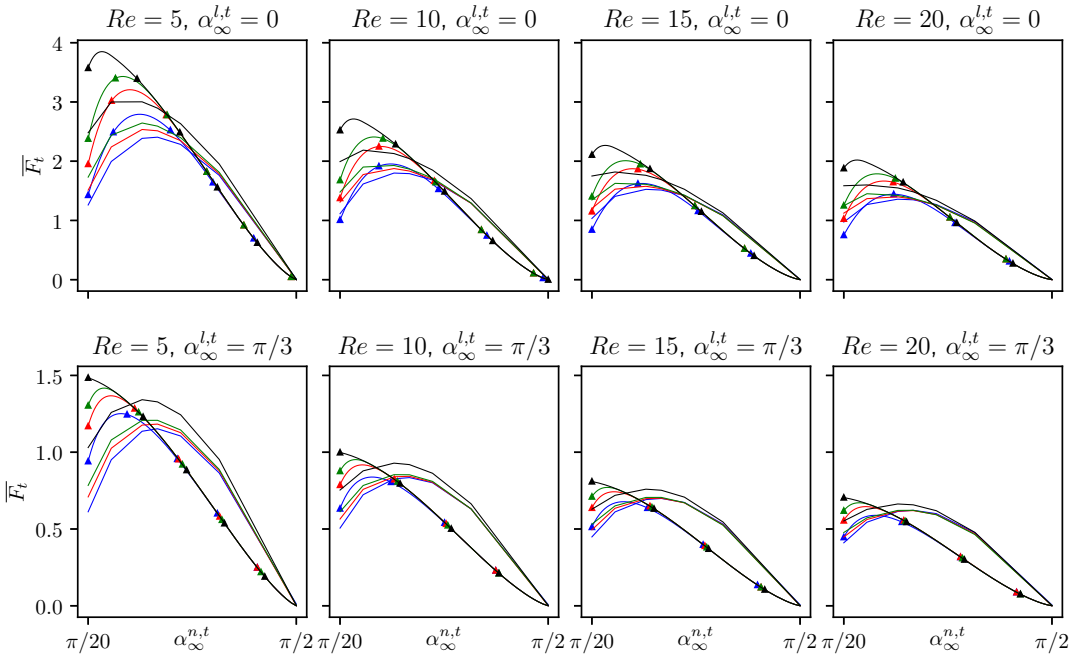

Figure 2.7: Tangential drag force model Algorithm 1 (▲ symbols) and CFD 3D datas (solid lines) when incoming flow angles are $\alpha_\infty^{n,t} \in [\pi/20, \pi/2]$, $\alpha_\infty^{l,t} = 0$ (top row) and $\alpha_\infty^{l,t} = \pi/3$ (bottom row). Several W/D ratios are depicted: 6.0 (—), 8.0 (—), 10.0 (—) and 20.0 (—). $\overline{F_t}$ is defined as $\overline{F_t} = \frac{\mathbf{F}\cdot\mathbf{t}}{0.5\rho||\mathbf{U}_\infty||^2 D}$

2.2.4 Longitudinal term F_l

Though it is not depicted in Figure 2.5, the longitudinal direction also experiences drag force from the fluid flow. Due to translational invariance in the longitudinal direction, it is hypothesized that cylinders are infinite and do not interact with each other longitudinally. Consequently, F_l is independent of the $\tilde{W}/D$ ratio and only depends on the total Reynolds number Re *a priori*. This amounts to considering an isolated infinite cylinder subjected to an angle-oriented flow, a situation which has already been studied by Marheineke and Wegener [91]. Note that the longitudinal direction $\mathbf{l}$ notation in the present work corresponds to the tangential one $\boldsymbol{\tau}$ in [91].

As opposed to the previous normal F_n term, the F_l does not only depend on the longitudinal Reynolds number Re_l. More specifically, Marheineke and Wegener [91] have proposed:

$$F_l(\mathrm{Re}) = F_l(\mathrm{Re}_n, \mathrm{Re}_l) = \frac{\rho\nu^2}{D}\mathrm{Re}_n\mathrm{Re}_l C_l(\mathrm{Re}_n) \tag{2.2.13}$$

with C_l being the dimensionless drag coefficient in the longitudinal direction. It should be noted that it depends only on the normal Reynolds number Re_n and is given by

$$C_l(\mathrm{Re}_n) = \exp\left[\sum_{j=0}^{3}\left(p_{l,j}\,(\ln \mathrm{Re}_n)^j\right)\right] \tag{2.2.14}$$

with $p_{l,0} = 1.1552$, $p_{l,1} = -6.8479 \times 10^{-1}$, $p_{l,2} = 1.4884 \times 10^{-2}$ and $p_{l,3} = 7.4966 \times 10^{-4}$. Equation 2.2.14 is valid in the interval $\mathrm{Re}_n = [0.1, 100]$, which encompasses the intended range of interest relevant to the proposed heterogeneous model.

2.2.5 Summary

For each wire of the endovascular device, the normal, tangential and longitudinal components are computed thanks to Equation 2.2.3, Algorithm 1 and Equation 2.2.13, respectively. These formulae are applied for each family of wires (blue and red in Figure 2.4) and then added up. As a note of caution, it should be mentioned that the total force $\mathbf{F_m}$ given by Equation 2.2.1 stands for drag force experienced by each wire. Due to the reciprocity principle, $-\mathbf{F_m}$ is regularized by the IBM procedure to mimic the force applied by the struts onto the fluid.

2.3 Edge-based IBM regularization

2.3.1 Generalities

Now that the linear force relevant to each wire segment is known, it must be regularized onto the fluid mesh, as illustrated in Figure 2.8. It should be noted that for the proposed model to be applicable, the solid part must have 2 dimensions less than the fluid, *i.e.* 1D struts for 3D fluid. Nevertheless, and for the sake of simplicity and explanations, Figure 2.8 represents 1D wires immersed in a 2D view, which can be seen as a slice through a 3D domain, passing through device wires.

The underlying notations and principles of the proposed *edge-based* IBM are now introduced. Solid and fluid domains are denoted by Ω_s and Ω_f respectively.

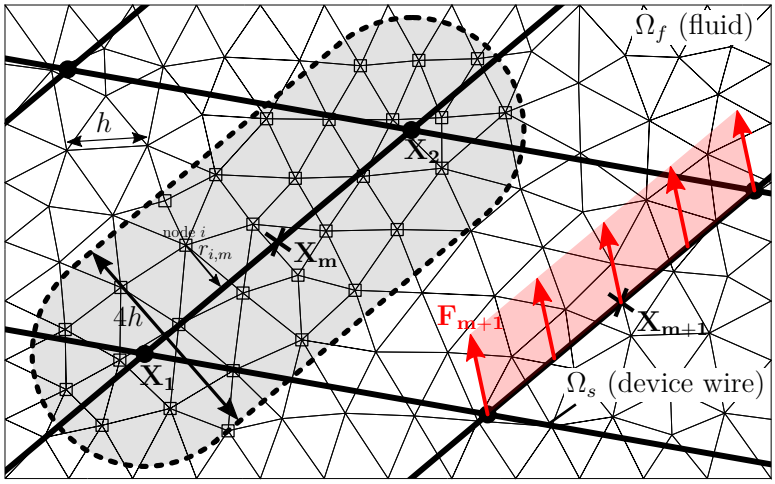

Figure 2.8: Edge-based IBM main components and notations. The support of the modified window function $\overline{w}(r_{i,m})$ Equation 2.3.2 is depicted in grey. It has an ovoid shape around the m$^{\text{th}}$ edge. The square points represents the fluid nodes which are affected by the constant linear density of force $\mathbf{F_m}$ exerted by the m$^{\text{th}}$ edge.

In Figure 2.8, they correspond to the 1D solid wires (thick black lines) and the fluid mesh (thin black triangles) respectively. Capital letters are relevant to the solid domain while lower case denote fluid quantities. The force $\mathbf{f_i}$ at the i$^{\text{th}}$ fluid node is given by:

$$\mathbf{f_i} = \sum_{m=1}^{M} \mathbf{F_m} \overline{w}(r_{i,m}) \,, \tag{2.3.1}$$

with M the total number of wire segments in the neighbourhood of the i$^{\text{th}}$ node and $\mathbf{F_m}$ the linear density of force at the m$^{\text{th}}$ solid edge (see the red vectors in Figure 2.8). In the following, it will be assumed that this density is constant for each edge, reflecting the fact that the wire diameter D is smaller than the inter-wire distance (hypothesis H2 described in Section 2.2.1). In Equation 2.3.1, the $\overline{w}$ coefficients are collectively referred to as the modified regularization window; the way they are computed will be detailed in the remaining of this section.

The edge-based methodology developed to compute the $\overline{w}$ coefficients builds heavily on the work of Pinelli et al. [118] and the RKPM principle introduced by Liu et al. [86]. Following the notations used by Sigüenza et al. [133] and for a

second-order RKPM, the coefficients $\overline{w}$ in Equation 2.3.1 write:

$$\begin{aligned}\overline{w}(r_{i,m}) = w(r_{i,m}) \times \Bigg[&\beta_0 + \beta_1 \left(\frac{x_i - X_m}{h}\right) + \beta_2 \left(\frac{y_i - Y_m}{h}\right) + \beta_3 \left(\frac{z_i - Z_m}{h}\right) \\ &+\beta_4 \left(\frac{x_i - X_m}{h}\right)\left(\frac{y_i - Y_m}{h}\right) + \beta_5 \left(\frac{x_i - X_m}{h}\right)\left(\frac{z_i - Z_m}{h}\right) + \beta_6 \left(\frac{y_i - Y_m}{h}\right)\left(\frac{z_i - Z_m}{h}\right) \\ &+ \beta_7 \left(\frac{x_i - X_m}{h}\right)^2 + \beta_8 \left(\frac{y_i - Y_m}{h}\right)^2 + \beta_9 \left(\frac{z_i - Z_m}{h}\right)^2\Bigg] ,\end{aligned} \tag{2.3.2}$$

with $\mathbf{x_i} = (x_i, y_i, z_i)$ and $\mathbf{X_m} = (X_m, Y_m, Z_m)$ the coordinates of the i$^{\text{th}}$ fluid node and the middle of the m$^{\text{th}}$ solid edge, respectively. $r_{i,m}$ stands for the distance between the i$^{\text{th}}$ fluid node and the point projected onto the m$^{\text{th}}$ solid edge, as depicted in Figure 2.8. The original window function $w(r_{i,m})$ appearing in Equation 2.3.2 is written as:

$$w(r_{i,m}) = \begin{cases} 1 + \cos\left(\dfrac{\pi r_{i,m}}{2h}\right) & \text{if } r_{i,m} < 2h\,, \\ 0 & \text{otherwise,} \end{cases} \tag{2.3.3}$$

with h the characteristic length scale of the fluid mesh (see Figure 2.8). The expression for $w(r_{i,m})$ ensures that the volume source term added to the Navier-Stokes equations is zero everywhere except in the vicinity of solid edges, *i.e.* inside the $4h$ ovoid grey region in Figure 2.8. In other words, it enables to restrict the extent to which the fluid can feel the solid parts and increases as approaching the wires. The $4h$ width of the window function support for edge-based IBM is a classical value in node-based IBM [93, 133], but it is actually a free parameter. More precisely, it has been found in our tests that a width of $6h$ offers a good compromise between errors and numerical stability while properly representing on the fluid mesh the jetting-flow taking place between consecutive struts.

The RKPM coefficients β_k in Equation 2.3.2 stand for the 10 unknowns coefficients of the correction polynomial which are calculated to ensure conservation of solid quantities when regularized onto the fluid. Specific details on how these coefficients are obtained for each edge are now detailed.

2.3.2 RKPM coefficients

To simplify the following derivations, the reasoning is made for one edge only since overall conservation is ensured by the summation over all edges given by Equation 2.3.1.

The main objective of the regularization step is to generate a volume source term $\mathbf{f}$ that faithfully represents the constant linear density of force $\mathbf{F_m}$ along the m$^{\text{th}}$ edge. Being inspired from nodal IBM considerations stated by Pinelli et al. [118] and Mendez et al. [93] who used the RKPM principle introduced by Liu et al. [86], the main constraint for the source term is that the mathematical moments of $\mathbf{F_m}$ are conserved up to a given order. For a second order method, this constraint is given by:

$$\begin{bmatrix} \int_{\Omega_f} \mathbf{f} \mathrm{d}v \\ \int_{\Omega_f} \mathbf{f} \left[\frac{(x-X_m)}{h}\right] \mathrm{d}v \\ \int_{\Omega_f} \mathbf{f} \left[\frac{(y-Y_m)}{h}\right] \mathrm{d}v \\ \int_{\Omega_f} \mathbf{f} \left[\frac{(z-Z_m)}{h}\right] \mathrm{d}v \\ \int_{\Omega_f} \mathbf{f} \left[\frac{(x-X_m)(y-Y_m)}{h^2}\right] \mathrm{d}v \\ \int_{\Omega_f} \mathbf{f} \left[\frac{(y-Y_m)(z-Z_m)}{h^2}\right] \mathrm{d}v \\ \int_{\Omega_f} \mathbf{f} \left[\frac{(x-X_m)(z-Z_m)}{h^2}\right] \mathrm{d}v \\ \int_{\Omega_f} \mathbf{f} \left[\frac{(x-X_m)^2}{h^2}\right] \mathrm{d}v \\ \int_{\Omega_f} \mathbf{f} \left[\frac{(y-Y_m)^2}{h^2}\right] \mathrm{d}v \\ \int_{\Omega_f} \mathbf{f} \left[\frac{(z-Z_m)^2}{h^2}\right] \mathrm{d}v \end{bmatrix} = \begin{bmatrix} \int_{\Omega_s} \mathbf{F_m} \mathrm{d}s \\ \int_{\Omega_s} \mathbf{F_m} \left[\frac{(X(s)-X_m)}{h}\right] \mathrm{d}s \\ \int_{\Omega_s} \mathbf{F_m} \left[\frac{(Y(s)-Y_m)}{h}\right] \mathrm{d}s \\ \int_{\Omega_s} \mathbf{F_m} \left[\frac{(Z(s)-Z_m)}{h}\right] \mathrm{d}s \\ \int_{\Omega_s} \mathbf{F_m} \left[\frac{(X(s)-X_m)(Y(s)-Y_m)}{h^2}\right] \mathrm{d}s \\ \int_{\Omega_s} \mathbf{F_m} \left[\frac{(Y(s)-Y_m)(Z(s)-Z_m)}{h^2}\right] \mathrm{d}s \\ \int_{\Omega_s} \mathbf{F_m} \left[\frac{(X(s)-X_m)(Z(s)-Z_m)}{h^2}\right] \mathrm{d}s \\ \int_{\Omega_s} \mathbf{F_m} \left[\frac{(X(s)-X_m)^2}{h^2}\right] \mathrm{d}s \\ \int_{\Omega_s} \mathbf{F_m} \left[\frac{(Y(s)-Y_m)^2}{h^2}\right] \mathrm{d}s \\ \int_{\Omega_s} \mathbf{F_m} \left[\frac{(Z(s)-Z_m)^2}{h^2}\right] \mathrm{d}s \end{bmatrix}, \quad (2.3.4)$$

with $\mathbf{X_m} = (X_m, Y_m, Z_m)$ the coordinates of the center of the m$^{\text{th}}$ edge, $\mathbf{X(s)} = (X(s), Y(s), Z(s))$ the m$^{\text{th}}$ edge coordinates parametrized by the curvilinear coordinate s and $\mathbf{x} = (x, y, z)$ the coordinates of the mesh fluid node. The right-hand side of Equation 2.3.4 represents the solid moments $\mathbf{M_s}$, while the left-hand side stands for the fluid moments $\mathbf{m_f}$. The first component of $\mathbf{M_s}$ states that regularization must conserve the integral of the force over the edge. The next three components are linked to the mechanical moment of the force on the edge, which is zero by definition when being computed on the edge center $\mathbf{X_m}$.

Since the force density per unit of length $\mathbf{F_m}$ is constant along the m$^{\text{th}}$ edge, it can be taken out from the integral in Equation 2.3.4. Therefore, $\mathbf{M_s}$ only depends

on the geometry of the edge and can be computed analytically such that:

$$\mathbf{M_s} = \mathbf{F_m} \times \begin{bmatrix} L \\ 0 \\ 0 \\ 0 \\ \frac{L}{h^2}\left(\frac{(X_2-X_1)(Y_2-Y_1)}{3} + \frac{X_1Y_2+Y_1X_2}{2} - X_mY_m\right) \\ \frac{L}{h^2}\left(\frac{(Y_2-Y_1)(Z_2-Z_1)}{3} + \frac{Y_1Z_2+Z_1Y_2}{2} - Y_mZ_m\right) \\ \frac{L}{h^2}\left(\frac{(X_2-X_1)(Z_2-Z_1)}{3} + \frac{X_1Z_2+Z_1X_2}{2} - X_mZ_m\right) \\ \frac{L}{h^2}\left(\frac{(X_2-X_1)^2}{3} + X_1X_2 - X_m^2\right) \\ \frac{L}{h^2}\left(\frac{(Y_2-Y_1)^2}{3} + Y_1Y_2 - Y_m^2\right) \\ \frac{L}{h^2}\left(\frac{(Z_2-Z_1)^2}{3} + Z_1Z_2 - Z_m^2\right) \end{bmatrix}. \tag{2.3.5}$$

$\mathbf{X_{1,2}} = (X_{1,2}, Y_{1,2}, Z_{1,2})$ are the end coordinates of the edge of length L (see Figure 2.8).

Using the definition of the fluid source term given by Equation 2.3.1 with only one solid edge and simplifying on both sides by $\mathbf{F_m}$, the equality of moments given by Equation 2.3.4 can be expressed as:

$$\begin{bmatrix} \int_{\Omega_f} \overline{w}(r_{*,m})\mathrm{d}v \\ \int_{\Omega_f} \overline{w}(r_{*,m})\left[\frac{(x-X_m)}{h}\right]\mathrm{d}v \\ \int_{\Omega_f} \overline{w}(r_{*,m})\left[\frac{(y-Y_m)}{h}\right]\mathrm{d}v \\ \int_{\Omega_f} \overline{w}(r_{*,m})\left[\frac{(z-Z_m)}{h}\right]\mathrm{d}v \\ \int_{\Omega_f} \overline{w}(r_{*,m})\left[\frac{(x-X_m)(y-Y_m)}{h^2}\right]\mathrm{d}v \\ \int_{\Omega_f} \overline{w}(r_{*,m})\left[\frac{(y-Y_m)(z-Z_m)}{h^2}\right]\mathrm{d}v \\ \int_{\Omega_f} \overline{w}(r_{*,m})\left[\frac{(x-X_m)(z-Z_m)}{h^2}\right]\mathrm{d}v \\ \int_{\Omega_f} \overline{w}(r_{*,m})\left[\frac{(x-X_m)^2}{h^2}\right]\mathrm{d}v \\ \int_{\Omega_f} \overline{w}(r_{*,m})\left[\frac{(y-Y_m)^2}{h^2}\right]\mathrm{d}v \\ \int_{\Omega_f} \overline{w}(r_{*,m})\left[\frac{(z-Z_m)^2}{h^2}\right]\mathrm{d}v \end{bmatrix} = \begin{bmatrix} L \\ 0 \\ 0 \\ 0 \\ \frac{L}{h^2}\left(\frac{(X_2-X_1)(Y_2-Y_1)}{3} + \frac{X_1Y_2+Y_1X_2}{2} - X_mY_m\right) \\ \frac{L}{h^2}\left(\frac{(Y_2-Y_1)(Z_2-Z_1)}{3} + \frac{Y_1Z_2+Z_1Y_2}{2} - Y_mZ_m\right) \\ \frac{L}{h^2}\left(\frac{(X_2-X_1)(Z_2-Z_1)}{3} + \frac{X_1Z_2+Z_1X_2}{2} - X_mZ_m\right) \\ \frac{L}{h^2}\left(\frac{(X_2-X_1)^2}{3} + X_1X_2 - X_m^2\right) \\ \frac{L}{h^2}\left(\frac{(Y_2-Y_1)^2}{3} + Y_1Y_2 - Y_m^2\right) \\ \frac{L}{h^2}\left(\frac{(Z_2-Z_1)^2}{3} + Z_1Z_2 - Z_m^2\right) \end{bmatrix}. \tag{2.3.6}$$

For the equality Equation 2.3.6 to be satisfied on unstructured meshes, as intended here, we now write $\overline{w}(r_{*,m})$ as a polynomial correction of the original window function $w(r_{*,m})$ following the RKPM principle of Liu et al. [86]:

$$\begin{aligned}\overline{w}(r_{*,m}) = w(r_{*,m}) \times \Bigg[&\beta_0 + \beta_1\left(\frac{x-X_m}{h}\right) + \beta_2\left(\frac{y-Y_m}{h}\right) + \beta_3\left(\frac{z-Z_m}{h}\right) \\ &+\beta_4\left(\frac{x-X_m}{h}\right)\left(\frac{y-Y_m}{h}\right) + \beta_5\left(\frac{x-X_m}{h}\right)\left(\frac{z-Z_m}{h}\right) + \beta_6\left(\frac{y-Y_m}{h}\right)\left(\frac{z-Z_m}{h}\right) \\ &+ \beta_7\left(\frac{x-X_m}{h}\right)^2 + \beta_8\left(\frac{y-Y_m}{h}\right)^2 + \beta_9\left(\frac{z-Z_m}{h}\right)^2\Bigg],\end{aligned} \tag{2.3.7}$$

with β_k the 10 unknowns coefficients of the correction polynomial. They are computed to satisfy the moments equality Equation 2.3.6. For the next steps, it is convenient to introduce the moments $m_{a,b,c}$ of the original window function defined as:

$$m_{a,b,c} = \int_{\Omega_f}\left(\frac{x-X_m}{h}\right)^a\left(\frac{y-Y_m}{h}\right)^b\left(\frac{z-Z_m}{h}\right)^c \times w(r_{*,m})\mathrm{d}v\,. \tag{2.3.8}$$

Using the linearity of the integral operator and the definition of $m_{a,b,c}$ given by Equation 2.3.8, we end up with:

$$\mathcal{M}\boldsymbol{\beta} = \overline{\mathbf{M_s}}\,, \tag{2.3.9}$$

with:

$$\mathcal{M} = \begin{bmatrix} m_{0,0,0} & m_{1,0,0} & m_{0,1,0} & m_{0,0,1} & m_{1,1,0} & m_{1,0,1} & m_{0,1,1} & m_{2,0,0} & m_{0,2,0} & m_{0,0,2} \\ m_{1,0,0} & m_{2,0,0} & m_{1,0,1} & m_{1,1,0} & m_{2,1,0} & m_{2,0,1} & m_{1,1,1} & m_{3,0,0} & m_{1,2,0} & m_{1,0,2} \\ m_{0,1,0} & m_{1,1,0} & m_{0,2,0} & m_{0,1,1} & m_{1,2,0} & m_{1,1,1} & m_{0,2,1} & m_{2,1,0} & m_{0,3,0} & m_{0,1,2} \\ m_{0,0,1} & m_{1,0,1} & m_{0,1,1} & m_{0,0,2} & m_{1,1,1} & m_{1,0,2} & m_{0,1,2} & m_{2,0,1} & m_{0,2,1} & m_{0,0,3} \\ m_{1,1,0} & m_{2,1,0} & m_{1,2,0} & m_{1,1,1} & m_{2,2,0} & m_{2,1,1} & m_{1,2,1} & m_{3,1,0} & m_{1,3,0} & m_{1,1,2} \\ m_{0,1,1} & m_{1,1,1} & m_{0,2,1} & m_{0,1,2} & m_{1,2,2} & m_{1,1,2} & m_{0,2,2} & m_{2,1,1} & m_{0,3,1} & m_{0,1,3} \\ m_{1,0,1} & m_{2,0,1} & m_{1,1,1} & m_{1,0,2} & m_{2,1,1} & m_{2,0,2} & m_{1,1,2} & m_{3,0,1} & m_{1,2,1} & m_{1,0,3} \\ m_{2,0,0} & m_{3,0,0} & m_{2,1,0} & m_{2,0,1} & m_{3,1,0} & m_{3,0,1} & m_{2,1,1} & m_{4,0,0} & m_{2,2,0} & m_{2,0,2} \\ m_{0,2,0} & m_{1,2,0} & m_{0,3,0} & m_{0,2,1} & m_{1,3,0} & m_{1,2,1} & m_{0,3,1} & m_{2,2,0} & m_{0,4,0} & m_{0,2,2} \\ m_{0,0,2} & m_{1,0,2} & m_{0,1,2} & m_{0,0,3} & m_{1,1,2} & m_{1,0,3} & m_{0,1,3} & m_{2,0,2} & m_{0,2,2} & m_{0,0,4} \end{bmatrix}, \boldsymbol{\beta} = \begin{bmatrix} \beta_0 \\ \beta_1 \\ \beta_2 \\ \beta_3 \\ \beta_4 \\ \beta_5 \\ \beta_6 \\ \beta_7 \\ \beta_8 \\ \beta_9 \end{bmatrix}, \tag{2.3.10}$$

and $\overline{\mathbf{M_s}}$ the right hand side of Equation 2.3.6. Inverting matrix $\mathcal{M}$, one can find all the β_k coefficients as:

$$\boldsymbol{\beta} = \mathcal{M}^{-1}\overline{\mathbf{M_s}}\,. \tag{2.3.11}$$

Since solid and fluid domains do not change over time, *i.e.* the device is fixed and the grid is not re-meshed, Equation 2.3.11 is solved once for all at the start of the computation and the β_k coefficients are stored to be used for the regularization step, enabling a low computational cost. It should be kept in mind that the β_k

coefficients are computed for each edge using Equation 2.3.11. Concerning units, the components of $\boldsymbol{\beta}$ are equivalent to $[\mathrm{m}^{-2}]$ so as to be compatible with the ones in Equation 2.3.1 which are $[\mathrm{N.m}^{-3}]$, $[\mathrm{N.m}^{-1}]$ and [1] for $\mathbf{f_i}$, $\mathbf{F_m}$ and $w(r_{*,m})$ respectively. Using these coefficients, the modified window $\overline{w}$ is used to compute the regularized volume source term $\mathbf{f_i}$ at each i^{th} point of the fluid mesh as:

$$\mathbf{f_i} = \sum_{m=1}^{M} \mathbf{F_m} \overline{w}(r_{i,m}) \,. \tag{2.3.12}$$

Due to the summation, a fluid mesh point that lies within the support function of multiple edges receives contributions from all these edges. This is notably the case near the intersection points of the edges (see Figure 2.8).

2.4 Validation

2.4.1 Numerical set-up

Conformal computations using the idealized configuration already described in Figure 2.6 were re-used in order to validate the full whole heterogeneous methodology, *i.e.* drag models and edge-based IBM. In this view, the undisturbed velocity $\mathbf{U}_\infty$ was artificially given as an input to the drag models since it is fully known at the inlet section. For each operating point defined by values of $(\mathrm{Re}, \frac{W}{D}, \alpha_\infty^{n,t}, \alpha_\infty^{l,t})$, an edge-based IBM simulation was performed so as to be compared with its conformal counterpart. The exact same parameters ranges already given in Table 2.1 were used for these IBM simulations. Computations at $\mathrm{Re} = 2.5$ were performed so as to assess the behaviour of the model when being used outside its working range, *i.e.* at low Reynolds numbers. In other words, this flow condition cannot be used to validate the model, similarly to the tangential drag model calibration.

For edge-based IBM grids, the mesh size h was given as a function of the inter-wire distance W such that $h = \frac{W}{N_h^{\mathrm{IBM}}}$ with $N_h^{\mathrm{IBM}} = 20$. Several IBM computations have also been performed for $N_h^{\mathrm{IBM}} = 10$ to demonstrate the independence of the results with respect to the grid discretization. Conformal and IBM mesh sizes are depicted for $W/D = 6$ in Figure 2.9. Since YALES2BIO solves the unsteady Navier-Stokes equations, temporal convergence of the simulations was assessed by measuring the forces integrated over the cylinders walls for conformal simulations, thus enabling to obtain a physical steady time for each operating point. Edge-based IBM computations were ran until the conformal physical steady time was reached.

Conformal and IBM results were compared qualitatively using velocity magnitude contours on specific slices. Quantitative errors were also computed on downstream velocity profiles. More precisely, a probing line of length L diag-

onal to the numerical domain and located three diameters downstream of the device was used to get velocity profiles for both IBM and conformal results (see Figure 2.6). Then, the relative error E in % was computed as:

$$E = 100 \times \frac{1}{L} \int_0^L \frac{||\mathbf{U}_{\text{IBM}} - \mathbf{U_c}||}{||\mathbf{U}_\infty||} \mathrm{d}l \,, \tag{2.4.1}$$

with $\mathbf{U}_{\text{IBM}}$ and $\mathbf{U_c}$ being the IBM and conformal velocity vectors along the probing line, respectively.

All post-processing steps were conducted using the Visualization Toolkit (VTK) library [131] and Paraview [141] software. Each parallel computation has been performed using one processing unit every approximately $100,000$ tetrahedra, which yields a good balance between communication and computation costs for current applications. The number of processors ranged from 28 to 196, the latter being reached for $W/D = 20$ conformal meshes.

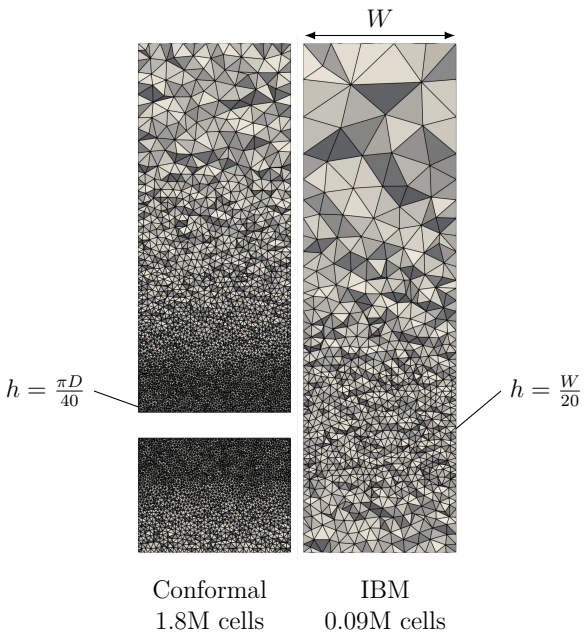

Figure 2.9: Mesh sizes examples for the $W/D = 6$ geometry.

2.4.2 Results

Figure 2.10 gives a qualitative insight into velocity fields on a slice placed diagonally to the 3D domain for both conformal and IBM modalities when the angle $\alpha_\infty^{n,t}$ decreases, for the typical operating point $(\text{Re}, \tilde{W}/D, \alpha_\infty^{l,t}) = (5, 8, 0)$. Very good trends are obtained with the heterogeneous model, whatever the inclination angle of the incident velocity. However, it appears that edge-based IBM

downstream velocities are systematically underestimated compared to conformal ones when $\alpha_\infty^{n,t} > \pi/2$, which is particularly visible when the incoming velocity is close to being purely tangential. Conversely, it is not the case when $\alpha_\infty^{n,t} = \pi/2$ since the recirculation region appears to be longer for conformal computations. These trends have also been found for other $(\mathrm{Re}, \tilde{W}/D, \alpha_\infty^{l,t})$ operating points (not showed here). This suggests that for non-normal incoming flow situations, the drag forces applied on the fluid are too high and overestimate the incoming flow blockage. This overestimation increases with the tangential component of the incoming flow. Nevertheless, the current model correctly reproduces relevant velocity patterns such as redirection due to the cylinders presence, downstream wakes and jetting-flow between the wires compared to conformal fields, using grid sizes h coarser by a factor of 6 approximately.

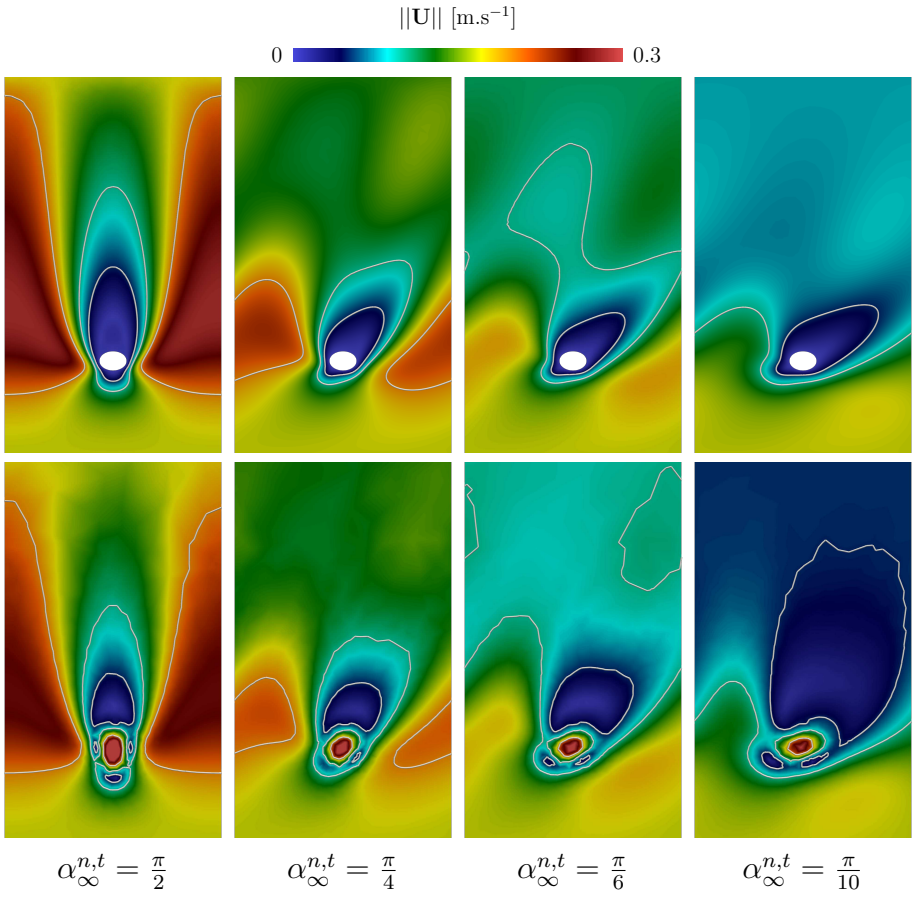

Figure 2.10: Velocity fields and contours for conformal (first line) and edge-based IBM (second line) approaches on a plane placed diagonally to the 3D domain for various $\alpha_\infty^{n,t}$ angle of attack. The operating point is $(\mathrm{Re}, \tilde{W}/D, \alpha_\infty^{l,t}) = (5, 8, 0)$. A good qualitative agreement is reached by the current model when being compared to conformal velocity fields.

Quantitative comparisons between IBM and conformal approaches can be found in Figure 2.11 for all the parameters ranges given in Table 2.1. For each value of $\alpha_\infty^{n,t}$, the solid line represents the mean error and the opaque filling goes from the minimum to the maximum error for all the $\tilde{W}/D$ ratios studied.

As expected, the computations performed outside the intended range of applicability of the model, *i.e.* at a diffusive flow regime where $\mathrm{Re} = 2.5$, exhibit very high errors, reaching almost 140% for tangential inflow conditions. As already stated, these computations were performed to demonstrate that the model cannot be used for diffusive regimes. Therefore, the results presented in the following section only focus on computations performed for $\mathrm{Re} > 2.5$.

The overall agreement is very good: errors above 25% were attained by only 11% of all computations. Among all the operating points, the maximum error reached 59% and was obtained for $(\mathrm{Re}, \tilde{W}/D, \alpha_\infty^{n,t}, \alpha_\infty^{l,t}) = (5, 6, \pi/20, \pi/3)$. Studying each Re individually, it appears that the mean and min-max errors are increasing with decreasing $\alpha_\infty^{n,t}$ for $\mathrm{Re} \in [5, 10]$, which is the opposite for $\mathrm{Re} = 20$. For $\mathrm{Re} = 15$, the errors seem to be constant for all geometric and flow conditions.

Despite not depicted in Figure 2.11, it has been noticed that the maximum errors are obtained for low $\tilde{W}/D$ and low $\alpha_\infty^{n,t}$ values, *i.e.* when cylinders are close to each others and when the incoming flow is close to being purely tangential, which implies strong interactions between cylinders. This indicates that both the tangential and longitudinal components of the force model, which are higher than the normal one for these situations, do not capture sufficiently well intra-familial interactions between cylinders and that additional mechanisms such as extra-familial interactions and crossing effects, which have not been modelled in this work, might be at stake and important to take into account.

The "real-flow condition" where the incident flow is not aligned with the cylinders ($\alpha_\infty^{l,t} = \pi/3$) yield similar results as the case ($\alpha_\infty^{l,t} = 0$), albeit with a small increase in the mean and min-max errors. Nevertheless, these errors were considered to be acceptable, thus demonstrating the robustness of the current model when being used in any incoming flow-conditions.

No significant differences on the obtained errors were noticed when increasing the mesh size by a factor of two (green line in Figure 2.11), which indicates that the current model can be used with such discretization.

2.5 Conclusion

This chapter introduced a novel heterogeneous approach intended to numerically solve blood flow for intracranial aneurysms treated with endovascular devices such as flow-diverters. Mimicking the struts effects on the flow via drag forces regularized on the fluid mesh, this model endeavours to balance computational costs and

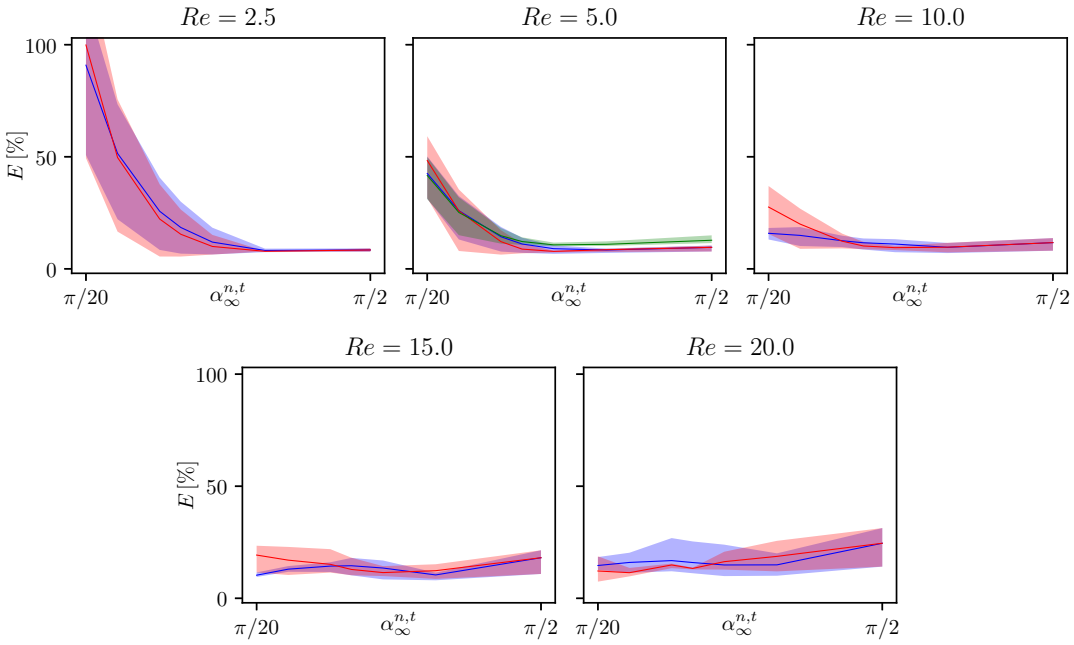

Figure 2.11: Errors given by Equation 2.4.1 for $\alpha_\infty^{l,t} = 0$ (—) and $\alpha_\infty^{l,t} = \pi/3$ (—) at $h = \frac{W}{20}$ and $\alpha_\infty^{l,t} = 0$ (—) at $h = \frac{W}{10}$. The solid line and the opaque filling represent the mean and min-max errors for all the $\tilde{W}/D$ ratios at a given angle $\alpha_\infty^{n,t}$ respectively.

low potential sources of errors while reproducing complex flow patterns near the wires. Several hypotheses regarding geometrical aspects and drag interactions between struts are formulated in order to build the model. More specifically, it is hypothesized that the overall device effect on the flow stems from the independent superposition of drag forces generated by two sets of infinite parallel wires forming the device. Each set of wires is treated independently and interactions between wires are only modelled inside each set. Additionally, the sections where the two sets of cylinders merge together, herein referred to as "crossings", are implicitly modelled as the sum of forces coming from each set. This means that the model is not adapted to very dense weaves, in which crossings cannot be neglected. The drag force is decomposed into several directions as a function of the geometry. For each component, drag force model either comes directly from the literature or is inspired by existing drag laws, modified and calibrated with 3D CFD computations.

The proposed heterogeneous model is validated for a 3D idealized configuration, conformal approach being considered as ground truth. Providing a good qualitative comparison of velocity fields and correctly representing the flow heterogeneities near the wires, it is found that the maximum error reaches 59%.

These error can be explained by an underestimation of downstream velocities in this situation, suggesting that drag forces coming from planar models (tangential and longitudinal) are overestimated in comparison to the normal one.

The present approach has demonstrated its capability to capture very detailed flow gradients near the device wires, which is impossible to obtain with other homogeneous approaches. This makes the model highly versatile and capable of studying in details how wires compaction at the neck influences the intra-saccular environment. Compared to homogeneous frameworks such as porous [7, 124], another advantage is that the heterogeneous model results from well-identified assumptions and sub-models which can be revisited and improved.

The proposed model could first be enhanced by taking into account more complex phenomena such as crossings effects and longitudinal interactions between struts. In particular, one could envision that the 3D conformal CFD computations used to calibrate the tangential component could be performed with more geometric and flow conditions, thereby enabling to parametrically study in details drag interactions for all three components of the forces on the cylinders. This introduces at least two additional parameters on which the drag forces could depend, namely the $\alpha_\infty^{l,t}$ angle and the inter-wire α angle, which has been fixed to $\pi/2$ in this study. Therefore, this would bring the total number of relevant parameters to six, namely $(Re, w, D, \alpha, \alpha_\infty^{n,t}, \alpha_\infty^{l,t})$, which entails a high computational burden. Additionally, performing this kind of 3D parametric study would give insights into the force exerted by the crossings sections and how they could be embedded into the edge-based IBM modelling. Another major improvement of the current edge-based model concerns the diffusive flow regime, which was intentionally not tackled in this work since it was considered to be critical for endovascular devices to reduce the strongest flow features coming from the parent artery. Specifically, designing such a diffusive model would require to revisit the notion of wakes and to study long-range interactions between closely-packed cylinders, especially for tangential and longitudinal components of the force. Combining such a model with the one presented in this work would be of course very desirable and could be useful to account for all flow conditions encountered by endovascular devices.

The next chapter is intended to extend the model validation to patient-specific geometries in order to further prove the capability of the model to account for complex flows and its potential usage for occlusion prediction based on hemodynamic indices.

Chapter 3

Patient-specific model validation

Chapter contents

The heterogeneous model was introduced and validated in the previous chapter for simplified configurations under realistic flow conditions. Despite providing

convincing results, validations with patient-specific geometries are compulsory to ensure model operability for in silico predictions of treatment outcome. To reach this objective, one mandatory input of the proposed method is the upstream velocity $\mathbf{U}_\infty$. As simplified geometries considered in the previous chapter were well-controlled, $\mathbf{U}_\infty$ value was available at the inlet and was given as an input to the drag models. This was done to validate the IBM methodology separately from others building blocks, *i.e.* drag models producing forces which are regularized onto the fluid. Since the concept of upstream and unperturbed flow is quite fuzzy for patient-specific configurations, this chapter begins by introducing a methodology intended to reconstruct the upstream velocity $\mathbf{U}_\infty$.

To illustrate and compare differences between existing porous models and the proposed approach, this chapter also details implementations of such models coming from the literature, namely Raschi et al. [124] and Augsburger et al. [7].

Then, extensive validations with patient-specific geometries treated by endovascular devices are performed in subsequent sections. Evaluation of models performances, either IBM or porous, is done by assessing relevant indices and comparing them to the values from the brute force conformal approach, which is considered as being the reference gold standard.

3.1 Undisturbed velocity reconstruction

As already stressed in Section 2.2, each drag model component need the knowledge of the unperturbed upstream velocity denoted as $\mathbf{U}_\infty$. Nevertheless, when dealing with complex geometries and incident flows such as the ones found in patient-specific cases, the concept of unperturbed upstream velocity is not clear: the flow interacting with the device is not uniform and its structure is dictated by the shape of the parent artery as well as the corresponding time-dependent flow rate. The only option to ensure model operability in situations relevant to intracranial aneurysms is to reconstruct $\mathbf{U}_\infty$ from local and instantaneous information available in the device region.

One first approach would consists in interpolating at each time-step velocities at fluid mesh locations which intersect the wires and consider this interpolated velocity as the unperturbed one. Despite being very simple to implement, this technique suffers from one major drawback: since drag forces are regularized onto the fluid via a source term in the vicinity of the cylinders, the velocity field is strongly impacted at those locations. Therefore, it cannot be considered as being unperturbed due to this coupling.

The approach developed in this thesis to reconstruct $\mathbf{U}_\infty$ takes advantage of both geometrical properties of braided endovascular devices and conservation principles. It can be divided into two parts: interpolation and correction.

3.1.1 Interpolation

As showed in Figure 3.1b, the wires of any device are not completely isolated from each others and form a network of parallel crossing cylinders which creates diamond-shaped cells. Fluid velocities inside theses cells are less impacted by the device than those in the close vicinity of the wires. Therefore, they provide a first approximation of the infinity velocity $\mathbf{U}_\infty$ and can be interpolated from the fluid mesh at every time-step.

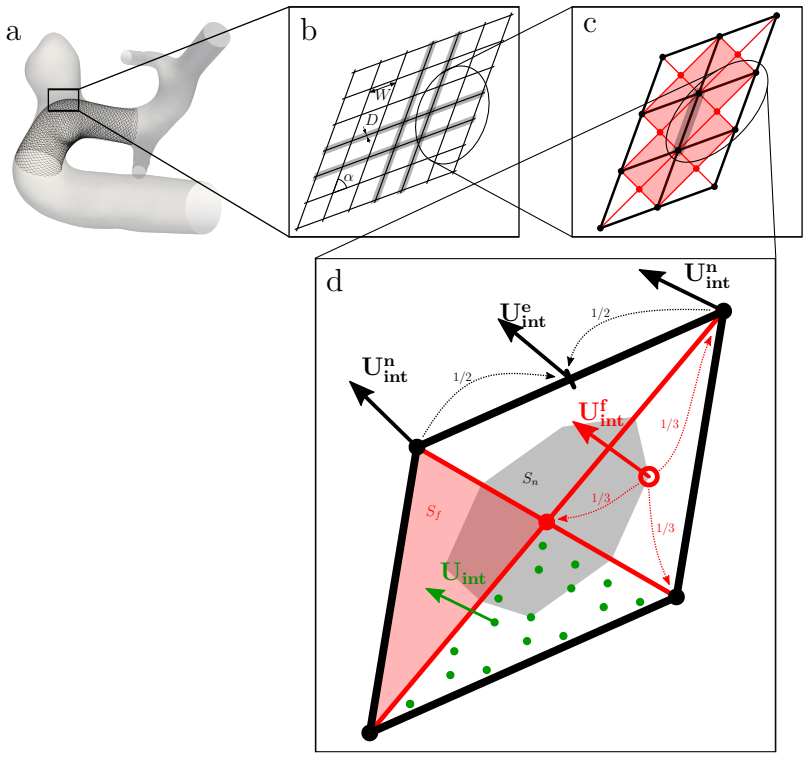

Figure 3.1: Device data structure. **a:** Aneurysm with deployed endovascular flow-diverter. **b:** Wires neutral fibre representation output from mechanical deployment. Only a few cylinders envelopes of diameter D have been coloured in grey for illustration purposes. **c:** Triangles are constructed using original wire-wire intersection points (in black) and the inserted barycentric points (in red). Cells in transparent red are involved in the velocity interpolation for the edge highlighted in grey. Only real cylinders locations (black edges) are used to apply volume forces on the fluid to mimic wires impact on the flow. **d:** Points used to interpolate velocities for one triangle cell are represented in green. Cell-to-points and points-to-edge redistributions are also indicated by dotted arrows with the corresponding coefficients.

To do so, recall that the device data structure output by the mechanical solver consists of only wires 1D neutral fiber, as depicted in Figure 3.1b. To ease the velocity interpolation step, it is converted into a triangulated surface by adding

nodes (in red in Figure 3.1c) at the barycentric coordinates of each diamond-shaped cell and connecting them with the original nodes (in black). Consequently, edges making up the original wires used to apply drag forces (in black) can be differentiated from added ones (in red) using the number of connected neighbours, as showed in Figure 3.1c. Then, a 2-level triangular subdivision is performed on each triangle by connecting edges centres. This produces a total of 16 smaller triangles of equal area with barycentres drawn in green in Figure 3.1d. Although theoretically possible, higher level of subdivision was not considered. Finally, the fluid cells containing each barycentric point (in green) are identified on the mesh and linear interpolation of velocities located at the nodes of these fluid cells is performed. We end-up with a velocity denoted $\mathbf{U_{int}}$, in green in Figure 3.1d, for each barycentric point.

These velocities are then surface-averaged, which produces a unique value per triangle denoted $\mathbf{U^f_{int}}$ (in red). Since drag forces are computed at each original edge (black), interpolated velocities must be redistributed onto each edge. To do so, nodal values of velocities $\mathbf{U^n_{int}}$ are computed from face values $\mathbf{U^f_{int}}$ as follows:

$$\mathbf{U^n_{int}} = \frac{1}{S_n} \sum_{f \in \Omega^n_f} \frac{S_f}{3} \mathbf{U^f_{int}} \,, \tag{3.1.1}$$

with Ω^n_f containing all the triangles connected to the n^{th} node, S_f the f^{th} triangular surface and S_n the nodal surface computed such that:

$$S_n = \sum_{f \in \Omega^n_f} \frac{S_f}{3} \,. \tag{3.1.2}$$

These surfaces are in grey and transparent red in Figure 3.1d, respectively. Finally, interpolated velocity at each edge $\mathbf{U^e_{int}}$ is obtained by averaging the $\mathbf{U^n_{int}}$ values at the nodes. This entail that each edge applying drag forces onto the fluid receives interpolated velocity contributions from 14 connected faces, as exemplified for one edge highlighted in grey in Figure 3.1c with its connected faces in transparent red.

To lighten computational costs, the ids of the fluid elements involved in the interpolation step are searched and stored once for all at the first iteration. This is made possible due to the fact that the wires and fluid mesh are static during the computation.

The interpolated velocity $\mathbf{U^e_{int}}$ previously obtained only provides a first approximation of the "true" unperturbed velocity $\mathbf{U}_\infty$. Indeed, its norm and direction are impacted by the drag forces regularized onto the grid. Therefore, a correction step is needed in order to fully reconstruct $\mathbf{U}_\infty$.

3.1.2 Correction of the direction

Direction correction is mandatory since $\mathbf{U}^{\mathbf{e}}_{\mathbf{int}}$ is expected to be more normal to the device compared to the unperturbed velocity direction since wires force the flow to go trough the diamond-shaped cells via the conservation of mass, thereby producing jet-inflow patterns which are intended to be reproduced by the heterogeneous model. In order to reconstruct the unperturbed velocity direction, several hypotheses have been made, which have been labelled for further references:

HU1 Recall that the network of wires showed in Figure 3.1b is considered to extend to infinity in every direction since boundary effects have been neglected when modelling the effects of the device on the fluid flow, hypothesis H3 (see Section 2.2.1) is reused here. H1 hypothesis (see Section 2.2.1)), which states that extra-familial interactions are neglected, is also reused here. This amounts to study how one family of infinite parallel cylinders redirects an upstream uniform velocity.

HU2 As depicted by Figure 3.2a, one can draw planes going through these cylinders built by the $(\mathbf{U}_\infty, \mathbf{n})$ vectors (red and green arrows). The situation schematized in Figure 3.2a does not represent a physical behaviour, in particular at the intersection of the green and red planes, and is used for illustration purposes only. It is hypothesized that the out-of-plane velocity redirection caused by the wires can be neglected. This means that the path of a fluid particle starting upstream to the wires stays on a given plane. More specifically, this hypothesis states that $\mathbf{U}_\infty$ and $\mathbf{U}^{\mathbf{e}}_{\mathbf{int}}$ are coplanar.

HU3 The complexity stems now from the fact that there exists an infinite number of planes to study, since $\mathbf{U}_\infty$ and $\mathbf{n}$ do not have preferential directions in complex patient-specific geometries. To reduce this complexity, it is considered that in-plane velocity redirection is invariant by rotation around the $\mathbf{n}$ axis. In other words, it means that flow redirection has the same magnitude for any planes. Therefore, it has been chosen to focus on the $(\mathbf{n}, \mathbf{t})$ plane.

From HU1-HU3, the redirection phenomenon can be characterized by studying how one array of 2D cylinders regularly spaced redirects the upstream velocity field, as schematized by green arrows in Figure 3.2b. In particular, we seek to determine a law linking the angle α_∞ from both local flow information and geometrical quantities, such that $\alpha_\infty = f(\text{local flow}, \text{geometry})$. Knowing α_∞ enables to correct the interpolated velocity by applying a rotation to $\mathbf{U}^{\mathbf{e}}_{\mathbf{int}}$ in the $(\mathbf{U}^{\mathbf{e}}_{\mathbf{int}}, \mathbf{n})$ plane, due to hypothesis **HU3**. The following parts detail the relevant inputs to this law and how it has been obtained.

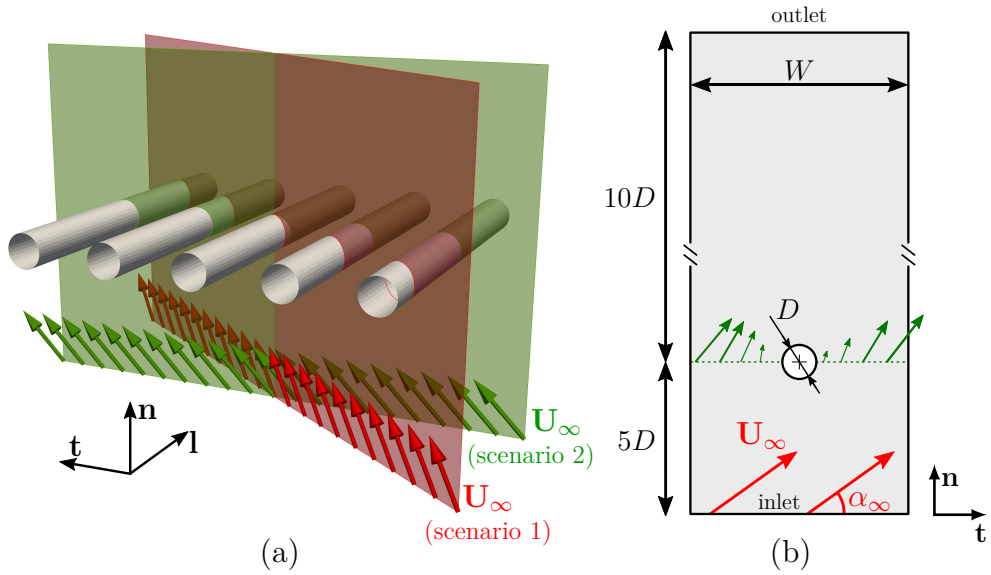

Figure 3.2: **a:** A family of parallel infinite wires being subjected to an upstream infinity velocity. The red and green planes represent two possible scenarios, depending on the relative orientation of $\mathbf{U}_\infty$ with respect to the local basis associated to this family of wires (in black at the bottom-left corner). **b:** 2-dimensional equivalent of the green plane in (a). It consists of a single cylinder with diameter D subtracted from a rectangle of width W. An upstream undisturbed infinity velocity $\mathbf{U}_\infty$ rotated by α_∞ and no slip boundary condition are applied at the inlet section (bottom) and the cylinder wall respectively. Periodicity is enforced on right and left sides of the domain ($\nwarrow$ signs) to mimic an infinite array of aligned wires in the tangential-axis direction. The outlet section extends further than the inlet one to prevent any interference with cylinder wakes. In the close vicinity of the cylinder (green dotted line), a flow redirection is occurring and is schematized by green arrows.

Starting with local flow inputs, the difficulty comes from the fact that the flow deflection angles at the section where the wires stand are not homogeneous as they may reflect all the complexity of the flow structure at this location, as illustrated in Figure 3.2b (see green arrows). To quantitatively measure the local flow diversion using a single variable, let us introduce the mean flow angle $\overline{\alpha}$ over the wires section defined as:

$$\overline{\alpha} = \arctan\left(\frac{\overline{\mathbf{U}} \cdot \mathbf{n}}{\overline{\mathbf{U}} \cdot \mathbf{t}}\right), \tag{3.1.3}$$

with $\overline{\mathbf{U}}$ the mean velocity vector along the line located where the wire stands:

$$\overline{\mathbf{U}} = \frac{1}{W} \int_0^W \mathbf{U} \mathrm{d}l \,. \tag{3.1.4}$$

It should be noted that $\mathbf{U}^{\mathbf{e}}_{\mathbf{int}}$ approaches $\overline{\mathbf{U}}$ when the number of interpolation points goes to infinity (green points in Figure 3.1d). Additionally, it is expected that the upstream Reynolds number Re plays a role in the velocity redirection. Concerning geometrical inputs, the W/D ratio is the only one which is relevant to the configuration showed in Figure 3.2b. Indeed, flow redirection is expected to increase as cylinders are packed more densely, *i.e.* when $W/D \to 0$.

We end-up with a law in the form $\alpha_\infty = f(\overline{\alpha}, W/D, \mathrm{Re})$, which has been obtained from the analysis of a set of 2D conformal computations performed using the domain described in Figure 3.2b. According to the intended ranges of applicability of the model given in Section 2.2.1, the following bounds have been considered: $\mathrm{Re} \in [1, 20]$, $W/D \in [6, 20]$ and $\alpha_\infty \in]0, \pi/2]$, which induces a total of 340 computations. Table 3.1 summarizes the simulation parameters.

	Re	W/D	α_∞
$\alpha_\infty = f(\overline{\alpha}, W/D, \mathrm{Re})$ law	$\{1, 5, 10, 20\}$	$\{6, 8, 10, 20\}$	$0 \to \frac{\pi}{2}$

Table 3.1: 2D conformal computation parameters.

Periodic boundary conditions were enforced in the tangential direction to mimic an infinite array of cylinders. No-slip boundary condition was applied at the cylinders wall. Mesh size was specified to smoothly decrease when approaching the cylinder in order to reach the spatial resolution $h = \frac{\pi D}{45}$. The number of triangular cells ranged from $33,000$ to $110,000$ for the $W/D = 6$ and $W/D = 20$ cases, respectively. Fluid properties were chosen to produce the intended Reynolds number Re. Flow convergence to a steady state was assessed by means of temporal signal of the integrated force exerted over the cylinder.

It is worth mentioning that the $\alpha_\infty = f(\overline{\alpha}, W/D, \mathrm{Re})$ law has been chosen to be fully explicit, which means that all the arguments of the law are considered to be known and measurable. Nevertheless, this property is not fulfilled by the Re input, which is the quantity to be reconstructed in fine. Thus, the aforementioned law has been built for $\mathrm{Re} = 5$ only, which has been considered as the most common flow condition encountered by wires. Computations performed for other Re numbers enable to study how the $\alpha_\infty = f(\overline{\alpha}, W/D, \mathrm{Re})$ law behaves in comparison to the one given by $\mathrm{Re} = 5$. As a refinement of the proposed procedure, a family of laws $\alpha_\infty = f(\overline{\alpha}, W/D, \mathrm{Re})$ could be generated; this is however not presented in the present thesis as it proves not necessary to achieve fair results.

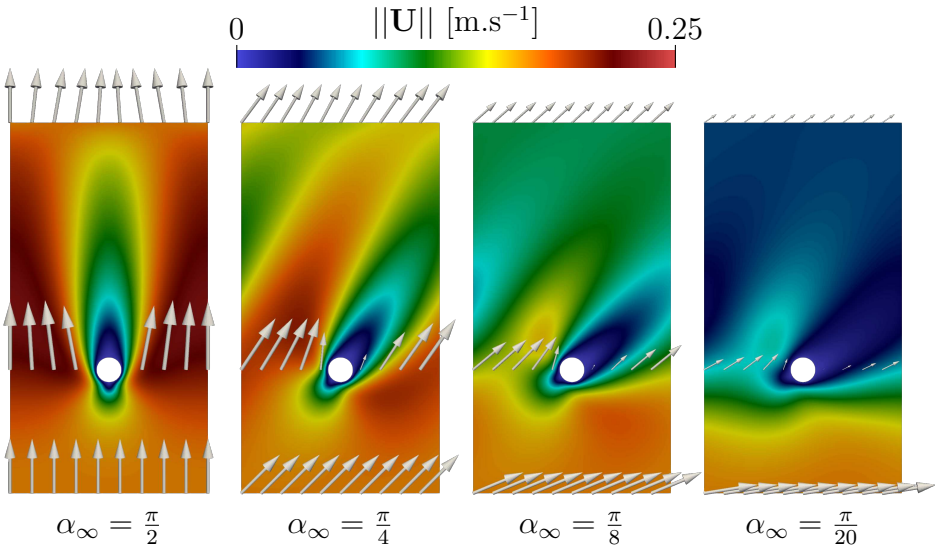

Figure 3.3: Velocity fields of the 2D computations for several α_∞ values at Re = 5 and $W/D = 8$. Velocity vectors have been added to ease flow redirection visualization.

Figure 3.3 depicts numerical velocity fields for a set of representative operating conditions. As the upstream flow goes from being purely normal to tangential, *i.e.* α_∞ decreases, cylinder interactions induce a more pronounced velocity redirection near the wire.

For each computation, the continuous spatial integral in Equation 3.1.4 was discretized using a line at $y = 5D$ (the origin is at the inlet) with 200 discretization points where velocity was interpolated thanks to the VTK library [131]. $\overline{\alpha}$ was then computed following Equation 3.1.3 in order to build the $\alpha_\infty = f(\overline{\alpha}, W/D, \mathrm{Re})$ law. Focusing only on the numerical results in Figure 3.4 (lines with no symbols), one can appreciate that for a given W/D ratio, increasing the upstream Reynolds number induces a less pronounced velocity redirection, *i.e.* the lines approach the $y = x$ curve. This behaviour can be explained by a narrowing of cylinders wakes due an increase of Re. For a given Reynolds number, flow redirection increases as W/D decreases due to conservation of mass.

To build the $\alpha_\infty = f(\overline{\alpha}, W/D, \mathrm{Re})$ law, it proved convenient to express $\overline{\alpha}$ as a function of α_∞ with a piece-wise linear function such that:

$$\overline{\alpha} = \begin{cases} a_1\alpha_\infty + b_1 & \text{if } \alpha_\infty > \frac{\pi}{20}\,, \\ a_2\alpha_\infty & \text{otherwise.} \end{cases} \tag{3.1.5}$$

Values of a_1, b_1 and a_2 depends on the W/D ratio and are given by:

$$\begin{cases} b_1 &= 1.915 \times \exp\left(-0.155\dfrac{W}{D}\right) , \\ a_1 &= 1 - \frac{2}{\pi} b_1 , \\ a_2 &= a_1 + \frac{20}{\pi} b_1 \end{cases} \tag{3.1.6}$$

Coefficients inside these functions have been obtained by fitting Equation 3.1.5 with the numerical results given by the 2D computations at $\mathrm{Re} = 5$, as depicted in the top-right corner of Figure 3.4. Results for other Reynolds numbers are also displayed to appreciate how Equation 3.1.5 behaves when being used at flow conditions for which it was not built for. It should be noted that since Equation 3.1.5 is linear, one can find α_∞ by simply inverting the terms.

Finally, a rotation of axis $(\mathbf{U}^{\mathbf{e}}_{\mathbf{int}} \times \mathbf{n})$ by an angle $(\overline{\alpha} - \alpha_\infty)$ is applied to $\mathbf{U}^{\mathbf{e}}_{\mathbf{int}}$ so as to obtain a vector whose direction is supposed to be collinear to $\mathbf{U}_\infty$.

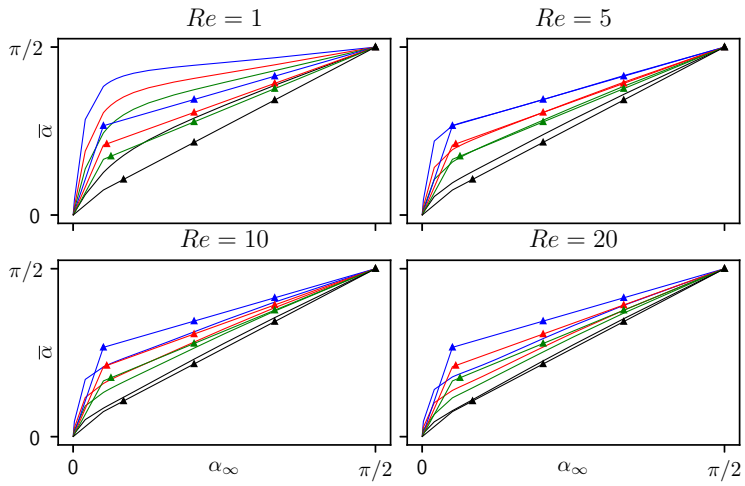

Figure 3.4: $\alpha_\infty = f(\overline{\alpha}, W/D, \mathrm{Re})$ law (▲) and CFD 2D datas (lines without symbols) for various W/D ratios: 6.0 (—), 8.0 (—), 10.0 (—) and 20.0 (—).

3.1.3 Correction of the norm

Now that $\mathbf{U}^{\mathbf{e}}_{\mathbf{int}}$ has been corrected so as to be aligned with $\mathbf{U}_\infty$, the last step aims at correcting its norm. It then proves useful to consider a bi-periodic domain as depicted in Figure 3.5, which is the same as the one used in Chapter 2 to validate the heterogeneous model (see Figure 2.6). The size of this unit cell domain (W) coincides with the inter-wire distance in the two homogeneous directions while it is large enough in the normal direction to consider that the perturbations induced

by the wires do not interact with the inlet and outlet boundaries. Notably, the fluid flow imposed at the bottom section is uniform and equals $\mathbf{U}_\infty$.

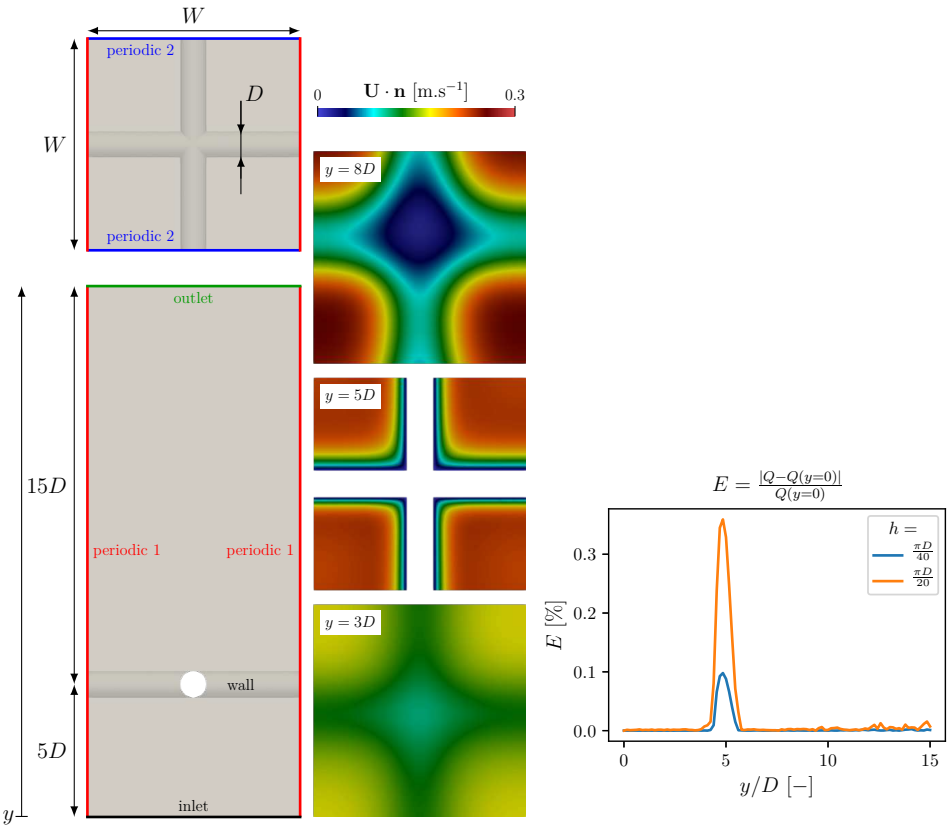

Figure 3.5: Example of numerical results for computations using the 3D bi-periodic domain of width W already depicted in Figure 2.6. The operating point is $(Re, \frac{W}{D}, \alpha_\infty^{n,t}, \alpha_\infty^{l,t}) = (5, 8, \frac{\pi}{4}, 0)$. Due to mass conservation, the flow rate at the inlet produced by the unperturbed velocity $\mathbf{U}_\infty$ is maintained thorough the domain. This is demonstrated by the $\mathbf{U}\cdot\mathbf{n}$ slices on the middle part, and also by the plot on the bottom-right corner, which shows the flow rate error with respect to the inlet for slices (of normal $\mathbf{y}$) placed along the domain height y. The effect of mesh size h is also given. Mass conservation induces that the normal component of $\mathbf{U}_\infty$ can be reconstructed where the wires stand ($y = 5D$ slice).

Because lateral conditions are periodic, mass conservation imposes that the flow rate is the same whatever the horizontal control plane considered, as showed on the middle of Figure 3.5 with plots of $\mathbf{U} \cdot \mathbf{n}$ for several slices and on the plot in the bottom-right corner. The latter depicts the flow rate relative error in percentage with respect to the inlet value thorough the domain height y. The peak at $y = 5D$ is caused by the wires presence and is highly dependent on spatial discretization levels, as a decrease of mesh size by a factor 2 decreases the error by a factor 3. Nevertheless, error values are very low (0.1%), inducing that flow-rate

can be considered to be conserved numerically. Local mass conservation yields that the normal component of $\mathbf{U}_\infty$ can be obtained from the flow rate through the section where the wires stand ($y = 5D$ in Figure 3.5). Benefiting from the data structure already described by Figure 3.1, the flow rate going through the wires is computed on the triangles using the interpolated velocities (schematized in red in Figure 3.1c,d). Flow rate at the triangles is then redistributed to the edges similarly to the interpolated velocities (Section 3.1.1).

Finally, $\mathbf{U}^{\mathbf{e}}_{\mathbf{int}}$ is corrected such that its normal component produces a local flow rate equals to the interpolated one.

3.2 Porous models

To put in perspective the advantages of the heterogeneous framework presented in this thesis, it is mandatory to compare it to previously existing models found in the literature. Therefore, two porous models were implemented in the YALES2BIO solver: the one presented by Augsburger et al. [7], which can be considered as the first of its kind, and the one proposed by Raschi et al. [124]. The exact implementation as well as the underlying hypothesis for each porous modelling are now detailed. Model characteristics common to both models are described in a first part and their specificities in dedicated sections. Limitations inherent to each model, as well as comparisons, are finally presented.

3.2.1 Common characteristics

As for the heterogeneous model, porous models mimic the device effect on the flow via a source term $\mathbf{f}$ added to the Navier-Stokes equations such that:

$$\rho\left(\frac{\partial \mathbf{u}}{\partial t} + \boldsymbol{\nabla}\cdot(\mathbf{u}\otimes\mathbf{u})\right) = -\nabla p + \boldsymbol{\nabla}\cdot\bar{\bar{\tau}} + \mathbf{f} \tag{3.2.1a}$$

$$\boldsymbol{\nabla}\cdot\mathbf{u} = 0\ . \tag{3.2.1b}$$

The value of $\mathbf{f}$ is zero everywhere in the fluid except in a region that will be further referred to as the porous region (PR). To define this region, the device is not considered as a collection of 1D wires immersed in a 3D fluid as for IBM, but rather as a 2D surface (see the black solid line and the grey surface in Figure 3.6a). Using this surface, all grid fluid nodes for which the distance to the device is smaller than the PR width ΔL are identified (red squares in Figure 3.6a) and the source term $\mathbf{f}$ is imposed only at these locations.

A value of $\Delta L = 0.02\,\text{cm}$ was used by Raschi et al. [124] irrespectively of the device struts size since it was prescribed to model both wires of 100 µm and 48 µm

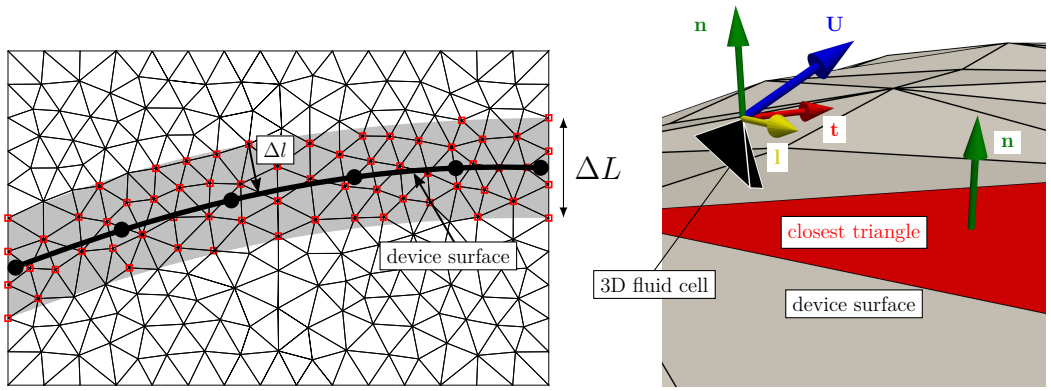

Figure 3.6: Porous modelling key elements. **a:** A two-dimensional representation was chosen to ease visualization, but implementations were performed in 3D. The black solid line represent the discretized device surface, which is the same as the one used in IBM computations (see Figure 3.1 and on the right). Red squares correspond to fluid nodes being at a distance Δl smaller than the PR width ΔL. These nodes harbour a source term $\mathbf{f} \neq 0$, on the contrary to exterior nodes. **b:** Local unit basis for one grid point of a cell (in black) inside the PR region near the device discretized surface (in grey). The basis is built from the closest triangle normal (in green) and the fluid velocity (in blue), as described in the text. Tangential $\mathbf{t}$ and longitudinal $\mathbf{l}$ unit vectors used by the Augsburger et al.'s model are in red and yellow, respectively.

in diameter. We used this PR width for all subsequent computations using Raschi et al. [124] porous model. The exact value for PR width used by Augsburger et al. [7] is not explicitly reported in their article but we found by inverting their porous coefficient equations that it was set to approximately $\Delta L \approx 2D$ with $D = 30\,\mu\text{m}$. We hypothesized that it was not perfectly equal to $2D$ as they attempted to take into account the local curvature of the device that was used to calibrate their normal porous coefficients. Nevertheless, as device curvature is not supposed to be homogeneous across the neck for real cases, we chose to fix $\Delta L = 2D$ for all subsequent computations using Augsburger et al. [7] porous model. No recommendation regarding PR width for wires with different diameters of $30\,\mu\text{m}$ is given by Augsburger et al. [7]. The mesh resolution inside the PR region is recommended by Raschi et al. [124] to be of 4 fluid nodes minimum, whereas nothing is explicitly stated by Augsburger et al. [7]. Therefore, it has been decided to prescribe the 4 nodes recommendation of Raschi et al. [124] for subsequent computations using Augsburger et al. [7] model.

In practice, both porous models implementations in the YALES2BIO CFD code used the device surface data structure already described in Section 3.1 and needed by the IBM model to perform local flow-rate computations. This ensures

that device location and extents are strictly equivalent between porous models and IBM computations, guaranteeing that model comparisons are appropriate.

In the present implementation on YALES2BIO, the fluid nodes belonging to the porous width ΔL and for which the velocity source term $\mathbf{f}$ must be different to zero are identified once for all at the start of porous computations in the following way for each fluid grid node:

1. The closest triangle on the device surface is identified using the ClosestPoint method in the vtkCellLocator vtk class[1]. Its normal $\mathbf{n}$ is also saved into a nodal vector field on the fluid for further use, especially for the Augsburger et al.'s model (green vector in Figure 3.6b).

2. The distance Δl between the fluid grid node and the closest point on the triangle, which does not have to be one of the vertices of the closest triangle (see Figure 3.6a), is computed and saved into a nodal scalar field on the fluid.

These steps were performed at the first iteration only in order to save computational resources, which is made possible by the absence of re-meshing during the computations and by the fact that the position and shape of the device are static.

3.2.2 Model of Augsburger et al. [7]

The main difference between porous models lies inside the expression of the source term $\mathbf{f}$. In [7], it is composed of a viscous loss and an inertial one, such that:

$$\mathbf{f} = -\left(\frac{\mu}{\alpha}\mathbf{u} + C_2\frac{1}{2}\rho||\mathbf{u}||\mathbf{u}\right) \tag{3.2.2}$$

with μ and ρ the dynamic viscosity and density respectively and $\mathbf{u}$ the fluid velocity. The coefficients α and C_2 are referred to as permeability and inertial resistance factor, respectively. To obtain relevant values for these parameters when dealing with endovascular devices, Augsburger et al. [7] performed numerical computations using two idealized configurations depicted in Figure 3.7: normal (left) and tangential (right). The choice made by Augsburger et al. to use these two configurations was motivated by the intent to represent the pressure drop dependency on the orientation of the impacting velocity. Geometrical characteristics for the device implanted in these configurations were chosen following the design of the SILK commercially available flow-diverter (Balt International, Montmorency, France), which mostly consists of wires of 30 µm in diameter.

[1] https://vtk.org/doc/nightly/html/classvtkCellLocator.html

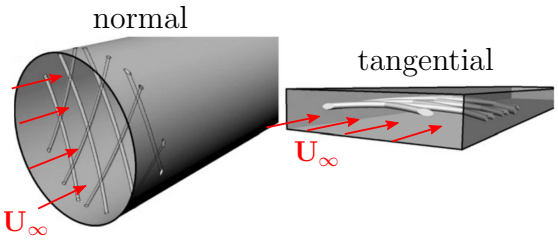

Figure 3.7: Augsburger normal (left) and tangential (right) configurations. Upstream velocity are represented in red at the inlet sections of each case. Taken and modified from [7]

For each configuration, the velocity vector is set to be normal to the inlet of the computational domain ($\mathbf{U}_\infty$ red arrows in Figure 3.7). Its magnitude is then varied inside a range of representative flow conditions encountered by endovascular devices. By measuring the variation of pressure drop across the device as a function of the upstream velocity $\mathbf{U}_\infty$, values for α and C_2 are thus numerically obtained. At the end, four coefficients are assessed in the porous model: (α^n, C_2^n) and (α^t, C_2^t) for normal and tangential configurations, respectively. More details regarding the identification procedure and the values used in the present implementation can be found in [7], the latter being reported in Table 3.2.

	C_2 [m^{-1}]	$1/\alpha$ [m^{-2}]
Normal	8703	8.9×10^8
Tangential	4697	1.7×10^9

Table 3.2: Porous coefficient values taken from Augsburger et al. [7].

In the remaining of this manuscript, Augsburger et al.'s model implementation in YALES2BIO will be referred to as "porous A". In practice, the following steps were implemented. At each fluid iteration, before solving the discrete version of Navier-Stokes equations, and for each fluid grid node:

1. If $\Delta l < \Delta L$, the normal of the closest triangle on the device $\mathbf{n}$ as well as the local fluid velocity vector $\mathbf{u}$ are gathered.

2. The tangential unit vector $\mathbf{t}$ is computed such that it is co-planar to the $(\mathbf{u}, \mathbf{n})$ basis and forms an orthonormal basis with vector $\mathbf{n}$. In practice, this is done by first computing the $(\mathbf{u}, \mathbf{n})$ plane normal, herein referred to as the longitudinal unit vector $\mathbf{l} = \frac{\mathbf{u} \times \mathbf{n}}{||\mathbf{u}||}$. Then, $\mathbf{t}$ is obtained such that $\mathbf{t} = \mathbf{n} \times \mathbf{l}$. These unit vectors are depicted in Figure 3.6b.

3. Velocity vector $\mathbf{u}$ is decomposed into its normal u_n and tangential u_t components such that $u_n = \mathbf{u} \cdot \mathbf{n}$ and $u_t = \mathbf{u} \cdot \mathbf{t}$. Unit vectors of the $(\mathbf{t}, \mathbf{n})$ basis are then reoriented such that $u_n > 0, u_t > 0$. This is done to ensure that the subsequent source term computation using these vectors points in the opposite direction to the velocity (due to the negative sign in Equation 3.2.2).

4. Normal f_n and tangential f_t components of $\mathbf{f}$ are computed following the general expression given by Equation 3.2.2 such that $f_n = \frac{\mu}{\alpha_n} u_n + C_2^n \frac{1}{2} \rho ||\mathbf{u}|| u_n$ and $f_t = \frac{\mu}{\alpha_t} u_t + C_2^t \frac{1}{2} \rho ||\mathbf{u}|| u_t$.

5. The source term $\mathbf{f}$ is finally obtained with $\mathbf{f} = -f_n \mathbf{n} - f_t \mathbf{t}$.

6. $\mathbf{f}$ is added to the discrete form of Navier-Stokes equations.

3.2.3 Model of Raschi et al. [124]

In the porous implementation of Raschi et al.'s porous model, the source term $\mathbf{f}$ is given by:

$$\mathbf{f} = -\left(D\mathbf{u} + F||\mathbf{u}||\mathbf{u}\right) . \tag{3.2.3}$$

The porous coefficients C and D, as opposed to Augsburger et al. [7] model, are obtained from pressure drop experimental correlations given by Idelchik [67] across braided screen geometries depicted in Figure 3.8a. More specifically, Idelchik [67] expresses the pressure drop ΔP induced by a screen made of a braided circular metallic wires impacted by an upstream normal velocity u as:

$$\Delta P = \frac{1}{2} \rho u^2 \left(\frac{22}{\mathrm{Re}} + 1.3(1 - \beta) + \left(\frac{1}{\beta} - 1 \right)^2 \right) \tag{3.2.4}$$

with β the porosity of the screen, defined as the ratio of open area over total area subjected to the incoming flow. Interestingly, the Re number in Equation 3.2.4 is not "classically" computed, *i.e.* with the upstream velocity u, but rather with a local velocity u_0 inside the screen such that $\mathrm{Re} = \frac{u_0 D}{\nu}$ with D the wire diameter.

In order to be used for braided endovascular devices geometries that exhibit rhombus cells such as Figure 3.8b, Raschi et al. [124] adapted the previous definitions of β and Re with the geometrical characteristics described in Figure 3.8c. This enabled them to derive the following expressions for C and D:

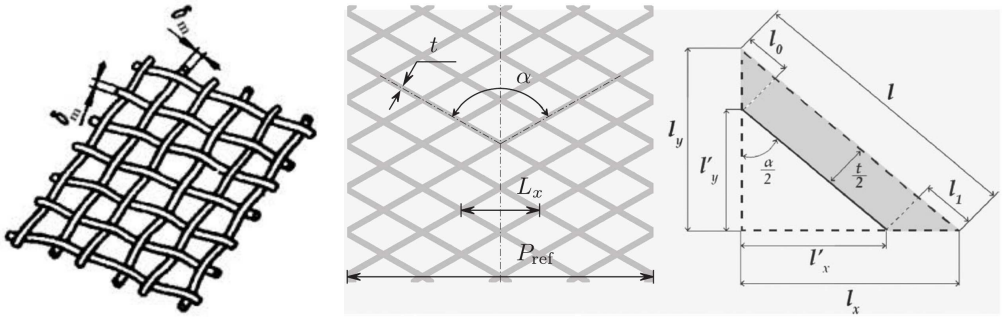

(a) (b) (c)

Figure 3.8: **a:** Wires entanglement studied by Idelchik [67] to derive pressure drop correlations. **b** and **c:** Device geometrical characteristics used by Raschi et al. [124] to compute screen porosity required by Idelchik's formulae.

$$D = \frac{11\mu}{d_h \Delta L} \tag{3.2.5a}$$

$$F = \frac{\rho}{2\Delta L}\left(1.3(1-\beta) + \left(\frac{1}{\beta} - 1\right)^2\right) \tag{3.2.5b}$$

with ΔL the PR width showed in Figure 3.6a. It should be noted that Raschi et al. applied a damping to their coefficients in order to account for an Immersed Body (IB) approach, *i.e.* border fluid nodes not coinciding with the physical border of width ΔL. Therefore, corrected values are given by $D = 0.75D$ and $F = 0.86F$. Since the implementation in YALES2BIO also used the IB approach, as depicted by Figure 3.6a, the correction factors for D and F were also applied.

It is worth mentioning that D and F coefficients only depend onto device geometrical characteristics given in Figure 3.8b,c. More precisely, once the triplet of geometrical parameters (L_x, t, α) is known, porous computations can be performed straightforwardly for any kind of deployed device inside arteries. Raschi et al.'s implementation, and therefore the present one, considers (L_x, t, α) values to be constant along the device surface, meaning that they are obtained by averaging local values of (L_x, t, α) at the aneurysm neck to faithfully account for the device local porosities effect on the flow. In other words, Raschi et al.'s model is homogeneous.

In the remaining of this manuscript, Raschi et al.'s model implementation in YALES2BIO will be referred to as "porous AC" (AC meaning "All Components" for reasons detailed later). In practice, the following steps were implemented. At each fluid iteration, before solving the discrete version of Navier-Stokes equations, and for each fluid grid node:

1. If $\Delta l < \Delta L$, the local fluid velocity vector $\mathbf{u}$ is gathered.
2. Using values of (L_x, t, α) depending on the device deployment geometry, coefficients $0.75D$ and $0.86F$ are computed thanks to Equation 3.2.5
3. The source term $\mathbf{f}$ is finally obtained with Equation 3.2.3.
4. $\mathbf{f}$ is added to the discrete form of Navier-Stokes equations.

Due to its definition in Equation 3.2.3, the source term $\mathbf{f}$ is isotropic, meaning that porous coefficients are multiplying all velocity components equally. However, pressure drop correlations given by Idelchik [67] in Equation 3.2.4, and reused by Raschi et al. [124] to derive their model, were obtained under the strict condition that the upstream velocity is normal to the device. No information regarding the pressure drop behaviour when the upstream flow is not purely normal are given by Idelchik [67], meaning that using porous coefficients isotropically is not physically justified. Therefore, an additional porous model was implemented, further referred to as "porous N" (N for "Normal"), taking into account the normal component of the velocity only. Therefore, the following steps were implemented:

1. If $\Delta l < \Delta L$, the normal of the closest triangle on the device $\mathbf{n}$ as well as the local fluid velocity vector $\mathbf{u}$ are gathered.
2. Using values of (L_x, t, α) depending on the device deployment geometry, coefficients $0.75D$ and $0.86F$ are computed thanks to Equation 3.2.5
3. Velocity vector $\mathbf{u}$ is decomposed into its normal u_n component such that $u_n = \mathbf{u} \cdot \mathbf{n}$. Unit vector $\mathbf{n}$ basis is then reoriented such that $u_n > 0$, as in Augsburger et al.'s implementation (see Section 3.2.2).
4. Normal f_n component of $\mathbf{f}$ is computed following the general expression given by Equation 3.2.3 such that $f_n = (Du_n + Fu_n^2)$.
5. The source term $\mathbf{f}$ is finally obtained with $\mathbf{f} = -f_n\mathbf{n}$.
6. $\mathbf{f}$ is added to the discrete form of Navier-Stokes equations.

3.2.4 Comparisons and limitations

Augsburger et al.'s model usage A model limitation clearly stated by Augsburger et al. is that porous coefficients values, both normal and tangential, must be recomputed each time the stent design differs from the one depicted in Figure 3.7.

Nevertheless, a high number of publications used Augsburger et al.'s model to study the effect of FD inside patient-specific geometries without taking into

account this limitation and modifying the original porous model implementation without proper verification. For example, Zhang et al. [162] showed on 2 FD cases that modifications of porous coefficients values to mimic denser device can be performed to strongly affect intra-saccular velocities and increase treatment efficacy. Nevertheless, Zhang et al. did not demonstrate the exact link between geometrical changes in device deployment, for example a compression of wires to decrease porosity locally or the deployment of a secondary device, and the porous coefficients values. Moreover, Zhang et al. [162] only reported the use of normal coefficients from Augsburger et al. [7]. This throws doubt whether they apply Augsburger et al.'s model on the normal component of the velocity only, or isotropically for all velocity components. The first scenario is not recommended as tangential coefficients are of the same order of magnitude as normal ones, whereas regarding the second, no justification supporting an isotropic implementation are given in [7]. Since no patient-specific conformal computations were performed by Zhang et al. [162], no data supports the fact that their porous implementation is reliable. The exact same issues can be found in another study conducted by the same research group for 8 FD cases [39]. Chong et al. [39] simulated device stretching and double deployment by dividing and multiplying porous coefficients by 2 and 10, respectively. These values were selected so that flow results agreed with DSA follow-up images, which is hardly quantitative.

In an attempt to extend Augsburger et al.'s coefficients to other types of devices, Li et al. [82] used the same methodology described by Augsburger et al. [7], for normal coefficients only, with 4 devices: PED, Silk+, FRED and two PEDs overlaid (same research group as [39]). By performing porous computations using these calibrated coefficients on two patient-specific geometries, they showed that these coefficients influence intra-saccular velocities. They notably demonstrated that the usage of 2 PEDs decreases significantly the flow within the aneurysm compared to using only one device. It is worth mentioning that Li et al. successfully validated their porous model with conformal results in patient-specific geometries for the Silk+ device calibrated porous coefficients in supplementary materials. This means that their porous implementation, either purely normal or isotropic as they only report normal coefficients values, appears to be valid for 2 cases, despite no physical justification to use only normal coefficients is provided. Nevertheless, no such comparisons with conformal results were performed for the other devices, entailing that validity remains speculative for these devices. In a latter study led by the same authors, Li et al. [83] compared CFD porous results with Particle Image Velocimetry (PIV) results for a Silk treated in vitro aneurysm. Despite showing similar flow patterns, porous CFD was overestimating intra-saccular velocities and jets compared to PIV. Moreover, no quantitative comparisons with PIV were performed by Li et al..

Idealized geometries boundary conditions Despite the fact that the procedure to estimate porous coefficients is clearly explained by Augsburger et al., several shortcomings persist. No information regarding side-wall boundary conditions are given by Augsburger et al. [7] for neither normal nor tangential configurations. For the normal one, it appears that due to the fact that the domain is tubular, periodic boundary conditions that could mimic an infinite device were replaced by no-slip boundary condition. Consequently, this adds a supplementary pressure-drop contribution that does not exist for "real" device wires that are immersed in an infinite fluid at the neck, entailing that device effect onto the incoming flow can be overestimated in patient-specific geometries. In addition to that, if no-slip walls were also prescribed for the tangential configuration, as it appears to be the case since an increase of pressure drop was induced by reducing domain size to ease coefficients estimation according to Augsburger et al., the overestimation could be greater than the normal one due to the close presence of surrounding walls. These caveats were identified by latter studies calibrating porous coefficients using the same methodology [45, 82]. To prevent the aforementioned overestimations, Li et al. [82] and Dazeo et al. [45] applied slip-boundary conditions at the walls of the test sections.

Another important aspect which was not discussed by Augsburger et al. is the choice of the number of wires implanted inside the tangential configuration. Indeed, the pressure drop is expected to depend on this number as adding struts inside the domain tends to increase the viscous dissipation occurring at the wires surfaces and consequently to rise the pressure drop across the device. These shortcomings for the tangential configuration were identified and studied by Ohta et al. [109], without providing improvements to obtain tangential coefficients. Dazeo et al. [45] suggested to use velocity profiles for the calibration of tangential coefficients and for validation assessments in this direction.

Coefficients calibrations A benefit of Raschi et al.'s model is that porous coefficients are directly obtained using geometrical properties of the deployed devices. This contrasts with the Augsburger et al.'s model since porous coefficients were obtained for a single device geometry. Therefore, to be applicable to another device type, design or deployment, conformal computations similar to that of Figure 3.7 must be performed, thereby adding a supplementary computational burden. Ideally, for each patient specific device deployment, one should extract a representative set of wires at the neck and immerse it into normal and tangential domains to obtain porous coefficients, as done by Dazeo et al. [46].

Homogeneous limitations As already stated previously, Raschi et al.'s model is homogeneous, meaning that the porous coefficients are the same for each node

inside the PR and are obtained by averaging geometrical (L_x, t, α) values found at the neck. This limitation was clearly identified by Raschi et al. [124] since for one of their validation case, the deployed device exhibited high variations of local porosity due a combination of parent-artery curvature and wide neck size, yielding that hemodynamic differences between porous and conformal results were greater than for all other cases, for which porosities were homogeneous at the neck. Raschi et al. suggested that further improvements of their method should include local device porosities to be interpolated on the nodes of the PR, enabling spatially varying porous coefficients. Such heterogeneous extension of the Raschi et al.'s model was carried out very recently by Li et al. [81] and Dazeo et al. [46], with conformal computations of patient-specific geometries used as reference for comparisons. Interestingly, the heterogeneous version of Raschi et al.'s model did not compared well with conformal results in [81]. Nevertheless, no comparison was performed to investigate if adding heterogeneous properties improves or deteriorates the agreement to conformal results. On the other hand, such comparisons were extensively carried out by Dazeo et al. [46] on a high number of patient-specific FD cases ($N = 14$). Dazeo et al. demonstrated that adding heterogeneity significantly improved homogeneous Raschi et al.'s model, reducing differences with conformal results by 27% compared to the homogeneous model.

Dazeo et al. also showed that despite a proper calibration of Augsburger et al.'s coefficients for each patient-specific deployment, the latter model does not compares well with conformal results. The same authors also stated in [45] that heterogeneous extension of Augsburger et al.'s model is possible but carries a high computational burden, since porous coefficients for each braided section of the device at the neck needs to be calibrated separately using no-slip tangential and normal computations.

Isotropy properties In an extensive study comparing porous models inside simplified geometries similar to Figure 3.7, Dazeo et al. [45] demonstrated that for tangential configurations conformally meshed, varying the inter-wire angle symmetrically around 90° results in asymmetric flow patterns. Dazeo et al. suggested that asymmetries were due to an increase of flow resistance when the incoming flow is aligned with the direction of the smaller angle, and proposed that each three components, 1 normal and 2 tangentials, should have their own porous parameters values. By construction, Augsburger et al.'s model is anisotropic due to different coefficients values for normal and tangential directions, whereas is it not the case for Raschi et al.'s. Thus the tangential flow asymmetries previously identified by Dazeo et al. [45] are expected to be captured by the Augsburger et al.'s model compared to Raschi et al., which is confirmed in [45].

Conclusion All the above limitations of the porous models available in the literature have led many researchers over the last decade to either study and compare each model performances [45, 46], improving them by extending their validity to different device designs [82], or adding sophistications such that introducing coefficients heterogeneity, as done in [46]. In addition to that, rather than improving existing porous models, several researchers decided to create a paradigm shift to enhance computational modelling of endovascular devices. For example, Li et al. [80] introduced a novel methodology based on the framework of screen models that can account for flow deviation. They further validated their method in 2D simplified aneurysms [79] and for 3D in patient-specific cases [81]. More recently, a heterogeneous FD porous method in which velocity gradients at the struts can be reproduced was presented by Yadollahi-Farsani et al. [158] and validated against conformal computations. It should be noted that this model is also applicable to coils, which was its first intended application [157].

These studies and new techniques are indicative of an active research field, where models are intended to evolve towards being more complex and versatile. This adds a supplementary motivation to develop new models, as the one presented in this thesis, since they can be complementary and can address the same challenges in various ways.

3.3 Steady-state validation

To illustrate the capabilities of the proposed model, hemodynamics inside the aneurysm of a patient treated by a commercial flow-diverter was studied. As in Chapter 2, this section was taken from scientific article under favourable review[2].

3.3.1 Numerical setup

Starting from anonymized 3D angiographic medical images coming from CHU Gui de Chauliac, Montpellier, the arterial surface has been reconstructed using the Marching Cubes algorithm [88]. As depicted in Figure 3.9, the arterial geometry consists of a saccular aneurysm (black arrow) located at the ICA (Internal Carotid Artery) portion of the vasculature. The parent artery extends up to two subsequent arterial bifurcations. The surface went through multiple pre-processing steps using the VMTK (Vascular Modelling Tool Kit) library [4]. Smoothing and addition of flow extensions at each opening have been performed. Surface remeshing using distance to centerlines as a meshing size constraint has

[2] A Heterogeneous Model of Endovascular Devices for the Treatment of Intracranial Aneurysms, *International Journal For Numerical Methods in Biomechanical Engineering*, March 2021

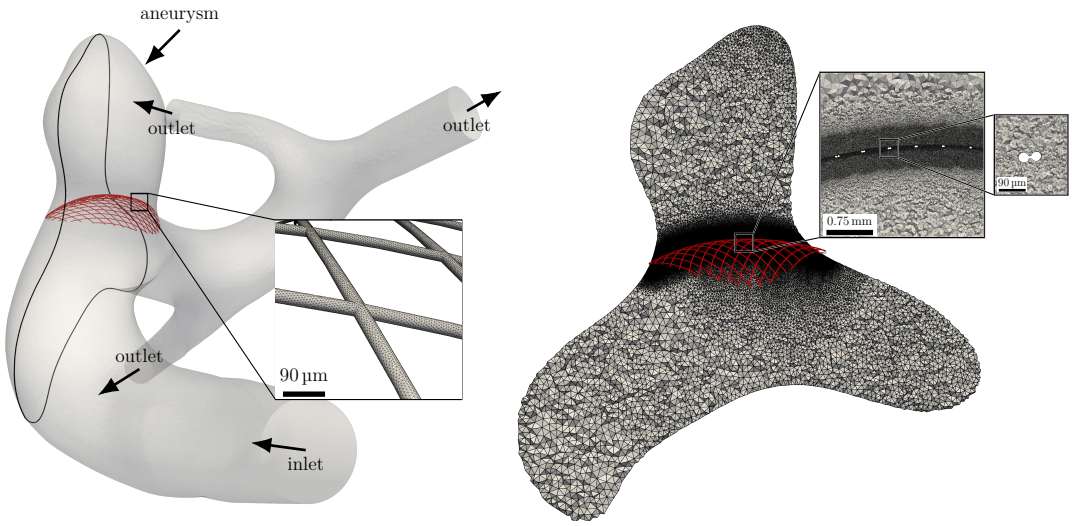

(a) (b)

Figure 3.9: Insights into geometry and meshing characteristics of the aneurysm case. **a:** 3D patient-specific arterial geometry harbouring an intracranial aneurysm treated by a flow-diverter (in red). Note that portions of the device in apposition with the parent artery have been removed. The close-up view shows the surface discretization of the struts. The black line on the arterial surface represents the intersection with the plane used for further analysis. Inlet and outlet sections are denoted with black arrows. **b:** Previously defined plane showing the volume mesh sizes at the aneurysm sac, the parent artery and the neck. Two successive zooms enable to appreciate the smooth mesh size coarsening when moving away from the wires (small white holes).

been carried out. This provides a constant number of elements across all arterial diameters.

Then, the endovascular device was numerically deployed into the previously pre-processed surface. Device length and diameter were chosen in order to start and end into straight arterial sections without occluding the downstream arterial bifurcation. The device consists in 48 wires of 30 µm in diameter with an inter-wire distance $W = 0.335\,\text{mm}$, thus giving a ratio $W/D \approx 11$. Numerical mechanical deployment was performed with the use of beams elements for each wire of the device. The arterial surface was considered to be rigid and static. The LS-DYNA solver [3] was used to solve the mechanical deployment and handle the contact between the device and the arterial wall. The numerical deployment was undertaken by the Sim&Cure company[4].

Three sets of meshes were then built for each of the CFD computations:

[3]http://www.lstc.com/products/ls-dyna
[4]https://sim-and-cure.com/

device-free, conformal and edged-based IBM. The device-free volume mesh inherited grid sizes from the previously pre-processed surface. The grid for the IBM simulations has been obtained by refining the surface and volume of the device-free grid in order to ensure a mesh size $h = w/8$ in the vicinity of the wires. They consist of 3M and 6.5M tetrahedra, respectively.

As opposed to the previous ones, generating the conformal mesh required more steps. First, distal and proximal portions of the device in contact with the arterial walls were removed to save computational costs. Thus only the part immersed in the neck region has been conserved, has depicted by Figure 3.9. Then, circular disks have been extruded along the neutral axis of the wires outputted by LS-DYNA and boolean unions were applied to link all the wires as one surface. This step has been performed using both Gmsh [59] and VTK [131]. The device surface has been discretized with a mesh size $h = \frac{\pi D}{15}$, which is almost an order of magnitude finer that commonly applied in the literature [110]. Next, the device surface was removed from the computational domain using the boolean tool available in the Blender software[5]. Then, surface remeshing and cleaning was performed using VMTK and MeshLab[6], respectively. Finally, a first volume mesh was generated with VMTK and then refined near the struts with MMG3D [44] to provide a smooth transition from fine to coarse regions of the mesh, as depicted by Figure 3.9. It should be noted that a constant mesh size has been specified in a layer around the wires to better capture cylinders wakes. The final mesh consists of 120M tetrahedra.

To reduce the computational burden, only the stationary case was considered when analysing the performance of the heterogeneous model with respect to the conformal case. From a physical point of view, this amounts to considering that the perturbations induced by the network of wires adapt instantly when the outer flow conditions change. This is indeed well justified since the typical time scale of the pulsatile flow rate signal through the parent artery (of order 0.1 s, say) is very large compared to the typical time scale of the flow around each wire (2×10^{-4} s and 5×10^{-5} s for the diffusion and convection times, respectively).

At the inlet, a fully-developed Poiseuille velocity profile has been specified. Peak systolic flow regime was used to simulate a "worst-case scenario", since the maximum velocities are observed during this phase. First, a mean flow rate has been calculated using the ICA diameter as recommended by Valen-Sendstad et al. [143] and Chnafa et al. [36]. Then, it has been plugged onto the generalized flow waveform measured on older adults given by Hoi et al. [66], which resulted in a peak-systolic flow rate of 418.8 ml.min^{-1}. The inlet Reynolds number was equal to $\mathrm{Re} = \frac{UD}{\nu} = 594$, based on the inlet diameter.

[5]https://www.blender.org/
[6]http://www.meshlab.net/

As classically done in cerebral aneurysms hemodynamic simulations, blood was assumed to be an incompressible Newtonian fluid with kinematic viscosity $\nu = 3.5 \times 10^{-6}\,\mathrm{m}^2.\mathrm{s}^{-1}$ and density $\rho = 1.06 \times 10^3\,\mathrm{kg.m}^{-3}$ [37]. Arterial walls (and device surface for the conformal mesh) were assumed to be rigid with a no-slip boundary condition. At the outlets, a convective outflow condition was specified such that

$$\frac{\partial \mathbf{u}}{\partial t} + U_{conv}\frac{\partial \mathbf{u}}{\partial \mathbf{n}} = 0\,, \tag{3.3.1}$$

with $\mathbf{n}$ the outward normal to the outlet surfaces, and U_{conv} the convective velocity adjusted at each outlet. Its value was computed using the ratio of each outlet surface over the sum of the outlet surfaces, which ensures global mass conservation over the entire flow domain.

Qualitative comparisons between conformal and all models results (edge-based IBM and porous) were performed using magnitude velocity contour on the slice depicted in Figure 3.9 and with normal velocities magnitude plotted at the neck. The following quantitative indices were computed to estimate errors with the conformal results:

$$\overline{U}_a = \frac{1}{V_a}\int_{\Omega_a} ||\mathbf{U}||\mathrm{dV} \tag{3.3.2a}$$

$$\overline{\mathrm{WSS}}_a = \frac{1}{S_a}\int_{\partial\Omega_a} ||\mathbf{WSS}||\mathrm{dS} \tag{3.3.2b}$$

$$Q_p = \int_{\Gamma_p} (\mathbf{U}\cdot\mathbf{n})\,\mathrm{dS} \tag{3.3.2c}$$

with Ω_a the aneurysm sac domain of volume V_a and surface S_a manually delineated with ParaView, used to compute spatially-averaged velocity $\mathbf{U}$ and wall-shear-stress vector $\mathbf{WSS}$, respectively $\overline{U}_a$ and $\overline{\mathrm{WSS}}_a$. $\overline{U}_a$ measures the intensity of the flow in the sac [110]. Contrary to the previous intra-saccular quantities, Q_p is defined using the aneurysm neck surface Γ and measures the inflow-rate through the neck domain Γ_p where $\mathbf{U}\cdot\mathbf{n} > 0$, with $\mathbf{n}$ the neck normal. Under pulsatile conditions, reductions of time-averaged Q_p and $\overline{U}_a$ values have been proven to statistically differentiate fast and slow occlusion rate groups [102]. For each index, histograms of local values inside the aneurysm volume, surface and neck were also used to compare modalities, the conformal results being considered as the reference data.

3.3.2 Results

Qualitative comparisons of blood velocities in the vicinity of the aneurysm neck and in the parent artery can be found in Figure 3.10, which displays velocity magnitude contours and 3D-projected fields for all models (no-device, edge-based IBM, porous and conformal). Compared to the no-device case, the conformal figure shows that the jet coming from the parent artery is reduced by the implanted device, yielding a decrease of intra-saccular velocities and a displacement of the center of the recirculating region in the sac. This trend is well captured by both edge-based IBM and porous AC model, despite being less pronounced than in the reference results. Porous AC yields excellent comparisons with the reference velocity field, indicating that this model performs well in that case. Other porous implementations are not correctly reproducing conformal patterns: porous N underestimates the device-induced pressure drop at the neck and yields a velocity field similar to no-device, whereas the velocity reduction with porous A is too high and completely reorganizes the intra-saccular recirculation.

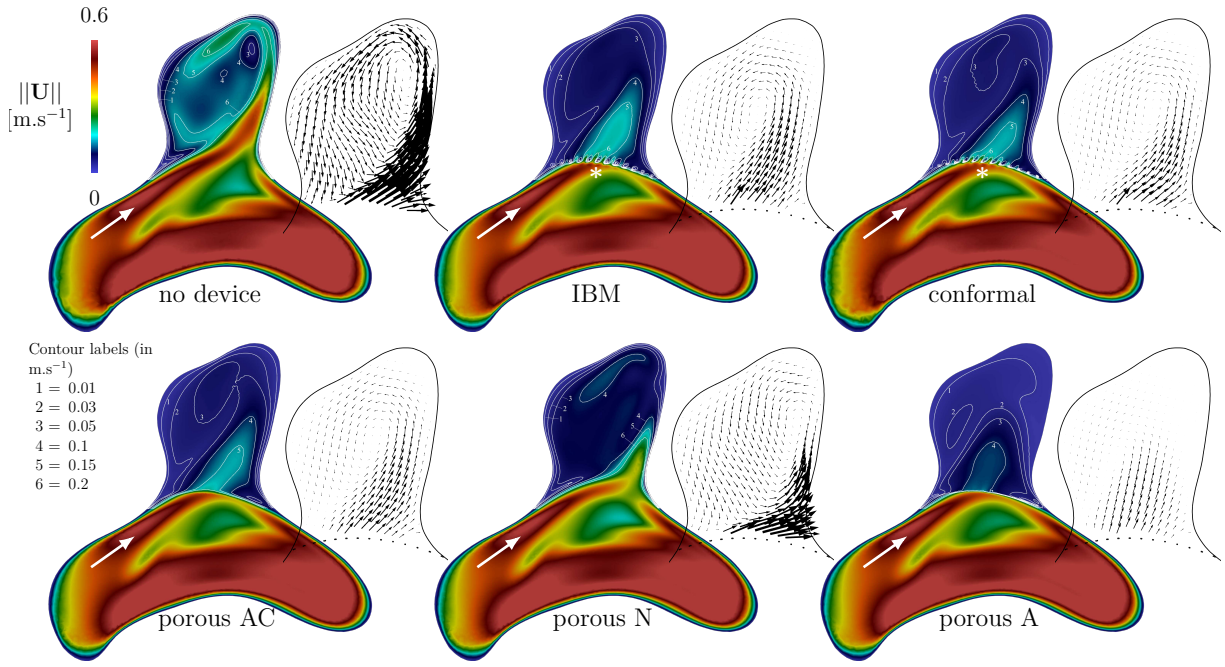

Figure 3.10: Velocity field slices for all studied models. The white arrow shows the main direction of the flow and velocity vectors are projected onto the slice to ease flow visualization on each small right quadrant. The correspondence between contour labels and velocity values is also indicated at the bottom-left corner.

Wakes and jetting-flows between the struts, which are inherently not captured by all porous models, are comparable in the IBM and in the conformal simulations, which demonstrates the robustness of the model when being employed in

a realistic geometry (see the white ∗ symbol in Figure 3.10). It should be noted that the maximum Reynolds number Re reconstructed from the infinity velocity $\mathbf{U}_\infty$ reached 8 in this case, which is in the middle of the intended range of applicability of the proposed method.

Similar conclusions can be drawn from Figure 3.11, which depicts velocities normal to the neck for all presented models. Both IBM and porous AC yield velocity fields similar to the conformal method, on the difference that the proposed model reproduces struts wakes on the positive flow-rate region (see the white ∗ symbol). IBM velocities overestimations compared to either porous AC and conformal are also visible in Figure 3.11 (see the white ◇ symbol). Similarities with the no-device velocity field that were already identified for porous N model are retrieved for normal velocities at the neck. Conversely, porous A model large discrepancies are difficult to visualize in Figure 3.11, owing to two compensating effects: velocity underestimation and over-redirection through the device, causing normal velocities to be similar to conformal. Therefore, Q_p index results should be cautiously interpreted due to such a potential compensation.

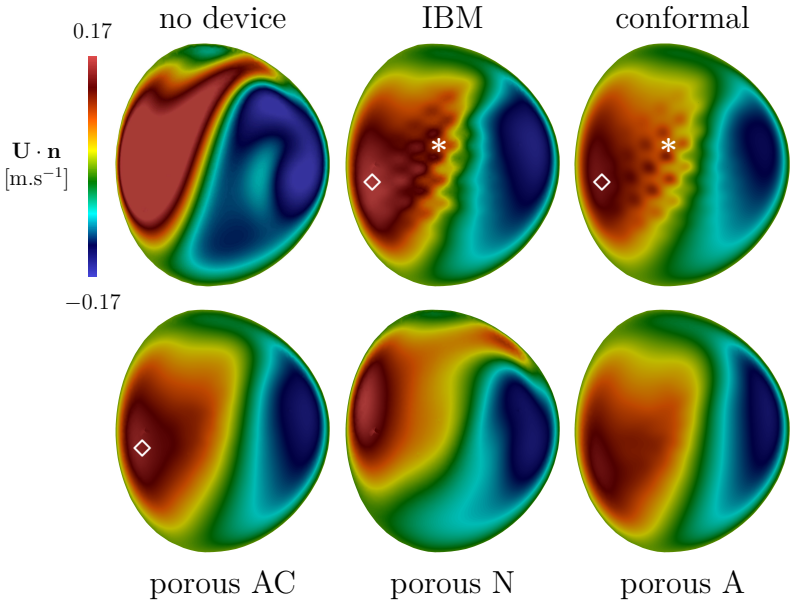

Figure 3.11: Normal velocity maps at the neck for all studied models. The neck normal is oriented towards the aneurysm dome, such that red-colored regions correspond to positive inflow values which are integrated to obtain the Q_p index defined by Equation 3.3.2.

To further study the qualitative performances of the presented model, volume rendering of vorticity magnitude $||\mathbf{\Omega}|| = ||\nabla \times \mathbf{U}||$ is depicted in Figure 3.12. Porous models results are not presented in Figure 3.12 since the major intra-saccular differences highlighted previously in Figure 3.10 were not sufficiently

visible using vorticity magnitude. It should be noted that velocity gradients due to boundary layers close to the arterial wall were automatically removed from the volume fields to enhance flow visualization. Due to the presence of very large vortices, the opacity transfer function was chosen to be a non-linear function (see the black line on the color bar).

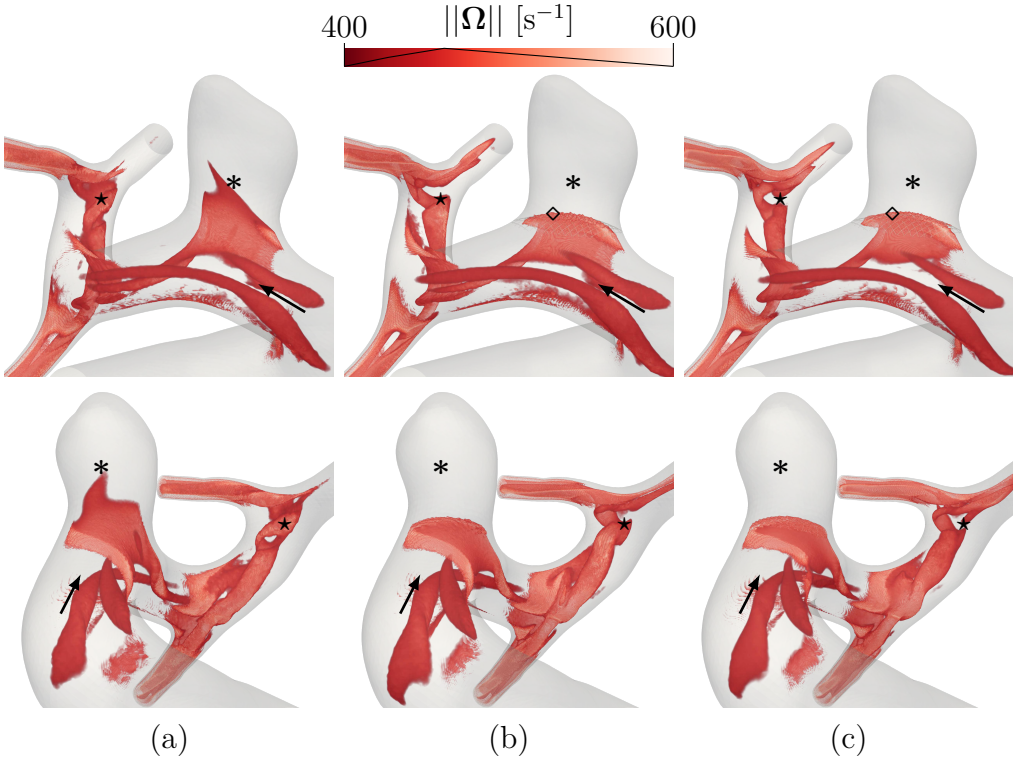

Figure 3.12: Volume rendering of vorticity magnitude $||\mathbf{\Omega}|| = ||\nabla \times \mathbf{U}||$ for **a:** no-device, **b:** edge-based IBM and **c:** conformal configurations for two point of views. The arterial wall is made partially transparent and velocity gradients due to boundary layers at the wall were automatically removed to enhance flow visualization. The opacity transfer function is given directly over the color bar (black line). Black arrows show the main direction of the flow.

As showed by Figure 3.12, two pair of vortices are created in the parent artery, stemming from the upstream curvature in this region. These vortices do not appear to be impacted by the presence of the device. Nevertheless, the struts strongly reduce intra-saccular vorticity compared to the no-device configuration (see the $*$ symbol in Figure 3.12). This behaviour is correctly captured by the proposed model which exhibits velocity gradients due to the wires that are similar to the conformal approach ($\diamond$ symbols). Downstream vortices in the second bifurcation appear to be impacted by the endovascular device, which is also correctly reproduced by the edge-based IBM method ($\star$ symbols).

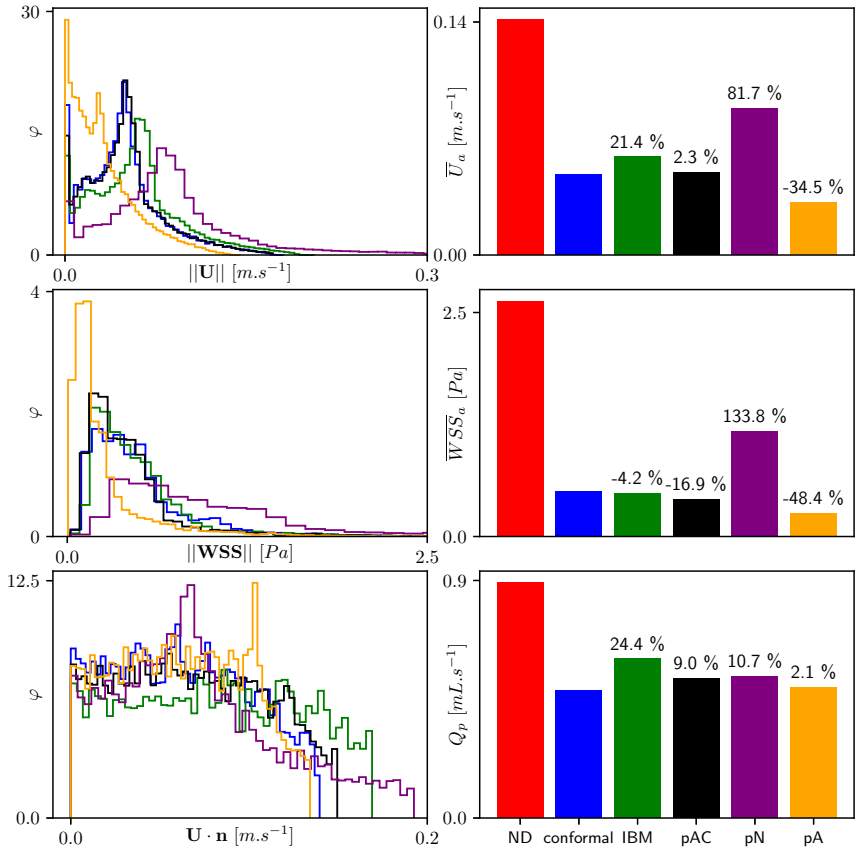

Figure 3.13: Patient-specific quantitative results for all models. **Left**: probability density functions (PDFs) φ for the intra-saccular velocity magnitude (top), wall-shear stress magnitude (middle) and normal positive velocity at the neck (bottom). **Right**: Indices given by Equation 3.3.2 annotated with relative errors E compared to conformal such that $E = \frac{H_{\text{model}} - H_{\text{conformal}}}{H_{\text{conformal}}}$ in percentage, H standing for each hemodynamic index in Equation 3.3.2. Labels pAC, pN and pA corresponds to porous models of Raschi et al. (all-components and normal) and Augsburger et al., respectively. ND stands for "No Device". Colors are the same as for the left part.

Quantitative comparisons between no-device, IBM, porous and conformal modalities can be found in Figure 3.13 where the left column represents Probability Density Functions (PDFs) for the quantitative variables given in Equation 3.3.2, the latter being plotted in the right column of Figure 3.13. The device entails a significant decrease of the velocity magnitude and the two peaks PDF produced by the device is well retrieved by both the edge-based and porous AC models, with $\overline{U}_a$ errors being smaller for porous AC compared to IBM (2% versus 21%). Conversely, other porous models (N and A) over and underestimate velocities, yielding high errors values of 81% and -34%, respectively. This is consistent

with qualitative results presented in Figure 3.10.

The same trends are also found for wall shear stress errors, on the difference that the proposed model yields lower errors compared to porous AC (-4% versus -17%). Interestingly, despite velocities were overestimated for these two models compared to conformal, $\overline{\text{WSS}}_a$ values are underestimated (negative errors). This is partly attributed to the fact that the remaining jet inside the sac is more redirected towards the dome, as depicted in Figure 3.10, causing less parietal friction on the impaction site compared to the conformal simulation. Conformal WSS magnitude PDF is well retrieved by both models (IBM and porous AC). Consistently with previous $\overline{U}_a$ errors, porous models N and A exhibit high $\overline{\text{WSS}}_a$ errors of 130% and -50%, respectively. Contrary to previous findings, these models yield low Q_p errors (10% and 2%), despite the very different velocity fields patterns compared to conformal (see Figure 3.10). As already described in Figure 3.11, normal velocities at the neck can be very similar to conformal due to compensation effects, as exemplified for porous A model. Therefore, interpretation of inflow-rate Q_p errors for other models (IBM and porous AC) has to be performed with caution due to these inconsistencies. From normal velocity histograms in the left of Figure 3.13, one can notice that IBM successively under and overestimates normal velocities, a trend also visible to a lesser extent by porous AC model. Q_p and $\overline{U}_a$ errors are of the same order of magnitude for these two models. It should be emphasized that each model performances with respect to conformal should not be judged solely on Q_p errors but rather by using all quantitative errors as well as qualitative results. To this respect, it can be considered that the proposed edge-based model yields similar performances compared to porous AC, both quantitatively and qualitatively. Other porous models implementations, on the other hand, are not faithfully reproducing intra-saccular hemodynamics compared to conformal.

3.3.3 Computational costs

To enable quantitative comparisons of computational costs between IBM, porous and conformal modalities, the memory used by all the processing units was gathered. Additionally, the two following reduced computational time measures were computed:

$$\begin{cases} \text{RCT}_1 = & \frac{T_{wc} N_p}{N_c N_{it}} \\ \text{RCT}_2 = & T_{wc} N_p \end{cases} \tag{3.3.3}$$

with T_{wc} the wall-clock time, N_p the number of processing units involved in the parallel computation, N_c the total number of cells in the numerical domain

and N_{it} the total number of iterations. RCT_1 enables to study the supplementary cost induced by a model, either porous or the proposed one, compared to a no-model computation. RCT_2 allows comparing two parallel computations when the number of processors, the mesh and the involved numerical models are different, which is the case here. More specifically, it corresponds to the wall-clock computational time needed by a single processor to reach the desired physical time of the simulation. Porous costs were regrouped into a single value since numerical implementations were very similar between all models, yielding negligible differences in computational costs.

The costs summarized in Table 3.3 demonstrate a drastic reduction of both memory usage and RCT_2 by factors of 22 and 5766 respectively for the proposed model. Similar reductions were attained by all porous computations. RCT_2 reduction can be mainly explained by the time-step gain between IBM and conformal, which has been increased by a factor 300 approximately. This reduction is more pronounced for porous models since time-step increased by a factor of 1.7 compared to IBM computations. RCT_1 indicates that the model increases the computational cost per iteration by 12%, which is considered to be acceptable with regards to the RCT_2 and memory usage reductions. Interestingly, increase of RCT_1 is larger for porous compared to IBM (32% versus 12%), probably because porous models implementations were not thoroughly optimized for computational speed.

	Edge-based IBM	Porous	Conformal	Reduction factors	
				IBM	Porous
Total memory usage (in Gb)	10.4	11.1	236.6	22.75	21.3
RCT_1 (in s · Nprocessors/Ncells/Niterations)	4.03×10^{-6}	5.2×10^{-6}	3.56×10^{-6}	0.88	0.68
RCT_2 (in s · Nprocessors)	1.296×10^{6}	1.06×10^{6}	7.473×10^{9}	5766	7050

Table 3.3: Computational costs: memory usage and reduced computational times. The "reduction factors" column stands for conformal over either IBM or porous.

Another computational cost reduction which could not be measurable directly herein originates from the proposed model agility. Performing device shape optimization to enhance intra-saccular hemodynamics, *i.e.* reduce inflow by decreasing device porosity at the jet impaction site as done in [70], is extremely costly and difficult to automatize using a conformal approach due to complex boolean operations and mesh cleaning steps, especially when using open-source codes only such as the ones used herein. Due the fact that the proposed model needs three dimensional mesh refinement using a background metric only, such limitations can be circumvented. This enables to easily change device design characteristics such as braiding angle, wire diameter, number of wires and/or device deployment shapes such as porosity patterns at the neck inexpensively, ushering in a new era

of "low-cost" device optimization both at the design stage, *i.e.* for manufacturers, and during pre-operation steps, *i.e.* for physicians, with minimal losses on accuracy compared to conformal as proven in this section.

3.3.4 Conclusion

This section has seen the successful application of the heterogeneous model introduced in Chapter 2 to a real geometry of FD implanted in a patient-specific case. To reach that conclusion, a high quality conformal computation has been carried-out using mesh number of cells higher by one order of magnitude than classically adopted in the literature [102, 110], this to ensure reliable results. The present model accurately accounts for both intra-saccular and downstream velocity patterns, with an averaged-velocity deviation of 20% compared to conformal. More importantly, no re-adjustments of model constants given in Chapter 2 were necessary to reach such level of agreement with a computational cost reduction by a factor of 5000. Generally, porous and IBM models exhibited similar computational costs gains compared to conformal. Moreover, the presented model qualitative and quantitative errors matched with one of the three porous methods, namely porous AC, whereas other porous implementations (A and N) exhibited large discrepancies.

It has been found that drag forces are underestimated in the patient-specific case since downstream velocities are higher than conformal ones. Although the exact origin for this drag underestimation has not yet be fully investigated, it is hypothesized that it is due to the infinity velocity reconstruction algorithm that was not activated in idealized validations in Chapter 2. Nevertheless, the 20% error with conformal results was considered to be acceptable with regards to drastic gain in computational costs and method agility.

3.4 Pulsatile validation

The heterogeneous model validation presented in Section 3.3 used steady flow conditions for the inlet boundary condition. Nevertheless, intracranial aneurysm hemodynamics is governed by unsteadiness as the heart regularly ejects blood into the circulatory system, thereby increasing flow rate and velocities. Therefore, the goal of this section is two-fold: studying how the present model behaves under these conditions for patient-specific cases and perform comparisons with conformal computations for validation purposes.

Performing unsteady conformal computations with patient-specific geometries is extremely challenging and introduces a high computational burden, as already discussed in previous sections of this thesis. Nevertheless, due to their ability to

capture extremely fine flow details near the devices struts and because they rely on the single assumption of no-slip boundary condition at the wires, this method is considered to be the gold-standard to which any newly introduced model must be compared and validated.

As a matter of fact, all homogeneous models already introduced in the literature have been validated in such a way or with similar methods. The porous model developed by Augsburger et al. [7] used two conformal computations of both shear and inertia-driven[7] aneurysmal geometries containing approximately 8M cells. For the porous model developed by Raschi et al. [124], reference computations cannot be considered as conformal following the definition used in this thesis. Raschi et al. [124] thus used an immersed (or embedded) method (IMM) as reference to compare their porous model results. IMM adaptively refines the mesh in the vicinity of the wires until the grid size can resolve the struts diameter [26]. Despite not being truly conformal, IMM is able to resolve local wakes and jet-inflows and can be considered equal to a conformal computation in terms of flow fidelity. In Raschi et al. [124], a total of three aneurysmal geometries with three devices per case, leading to a number of mesh elements between 2M to 16M approximately, were studied to assess porous-model performances. Side-wall aneurysms were considered with various parent-artery curvatures and device porosities. The screen model validation with patient-specific cases performed by Li et al. [81] also used three conformal computations. The number of cell used in these computations is not given for all cases, but the finest resolution reached 218M nodes for one case.

Since the goal of the heterogeneous model is to be used for any deployed endovascular device and arterial geometry, a high number of patient-specific cases need to be studied to show the versatility of the proposed approach. To prevent performing very costly pulsatile conformal computations, a collaboration has been initiated between our research team and a group of experts in the field of intracranial aneurysms led by the Professor J.R. Cebral from George Mason University[8], which will be further referred to as the "GMU" research group.

Indeed, Pr. Cebral and his team performed over the last years numerical resolved computations of many patient-specific geometries with different endovascular devices types such as flow-diverters [102] and intra-saccular WEBs [32]. This collaboration was intended to compare the proposed method with their resolved results, which are considered in the following of this thesis as the reference. To this end, they selected a set of six FD and four WEB cases from their database. For

[7] Shear-driven refers to the fact that the incoming blood is flowing along the aneurysmal neck tangentially, a condition encountered for side-wall aneurysms located on straight sections of their parent artery. Conversely, the inertia-driven classification stands for aneurysms which are impacted by a jet almost normal to the neck plane, as it is the case for bifurcation aneurysms.
[8] https://cfd.gmu.edu/~jcebral/

each case, our team was provided with the arterial surface, deployed stent geometry and boundary conditions such as the inlet flow rate waveform. Flow-diverter cases came from a database used in a previously published article intended to derive hemodynamic indices predicting treatment outcome [102]. This is also the case for WEB cases which are coming from [32].

3.4.1 Cases description

ID	Aneurysm			Device					Outcome
	Localization	Volume sac mL	Neck surface mm^2	Type	Diameter mm	Number of wires	Wires thickness (µm)	Neck porosity mean ± SD [min-max]	
e10	ICA	0.56	50.6	FD	4	48	48	0.6 ± 0.09 [$0.22 - 0.71$]	fast
e14		0.03	7.14		3.25			0.64 ± 0.02 [$0.53 - 0.67$]	fast
e23R		0.19	33.8		4.75			0.58 ± 0.05 [$0.38 - 0.65$]	fast
e24L		0.28	39.4		4.5			0.65 ± 0.05 [$0.43 - 0.75$]	slow
e32		0.09	23.6		4.5			0.42 ± 0.12 [$0.065 - 0.59$]	slow
e35		0.13	35.5		4.5			0.33 ± 0.14 [$0 - 0.56$]	slow
eweb08	MCA	0.26	17.7	WEB	8	144	25	0.57 ± 0.25 [$0 - 0.83$]	slow
eweb35	MCA	0.20	21.5		8			0.6 ± 0.25 [$0 - 0.85$]	slow
eweb38	MCA	0.21	13.1		6			0.45 ± 0.25 [$0 - 0.77$]	fast
eweb38acom	ACOM	0.16	9.6		7			0.44 ± 0.25 [$0 - 0.78$]	fast

Table 3.4: General characteristics for each patient-specific case

To ease further discussions, each case has been labelled with a unique ID. General characteristics of aneurysms and devices for each case can be found in Table 3.4. All the FD-treated cases harboured a side-wall aneurysm on the ICA portion of the cerebral vascular system. Indeed, FDs have been found to be well adapted to this kind of configurations. WEB-treated aneurysms are located more distally in the vascular system, mostly in the Middle Cerebral Artery (MCA, $n = 3$) and in the Anterior Communicating Artery (ACOM, $n = 1$). All these aneurysms are located at arterial bifurcations, a location prone to aneurysm formation due to increased hemodynamic stresses caused by assymetrical geometries [161].

In order to compute the aneurysm volume reported in Table 3.4, several steps were necessary. First, delineation of the aneurysm sac from its parent artery was performed using user-defined clipping spheres manually placed in a 3D interactive window. At the end of this step, an opened surface consisting of the aneurysmal wall is obtained. This surface was then closed using hole filling tools present in the vmtk C++ library [4]. Finally, the aneurysmal volume was computed by using this enclosed surface. Surface delineation and subsequent aneurysm volume computation were performed thanks to vtk C++ libraries [131].

The neck surface given in Table 3.4 was computed using a triangulated surface also created from a manual delineation by the GMU team. Aneurysm volume and neck surface are illustrated for the e10 case in Figure 3.14a,b. It should be noted

that the surface previously used to close the aneurysm sac was roughly equivalent to the neck area provided by GMU, despite differences in operator delineation and surface reconstruction algorithms.

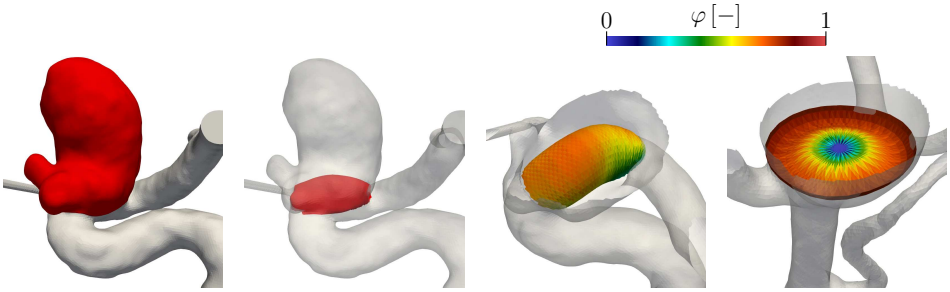

(a) (b) (c) (d)

Figure 3.14: Aneurysmal and device characterizations illustrative examples. **a:** Manual sac isolation in order to compute the aneurysm volume. **b:** Neck surface provided by the GMU team. **c** and **d:** Porosity color-maps for device surface manually clipped at the neck for flow-diverter (case e10) and WEB (case eweb08) devices. The arterial surface is also clipped to ease visualization.

Concerning devices characteristics found in Table 3.4, diameter was chosen for each case by GMU team so as to cope with dimensions of the parent artery (for FDs) and the aneurysm sac (for WEBs), accordingly with in vivo deployed sizes. Benefiting from the surface data-structure needed by the present model to compute local flow rates, the device porosity φ was also available. Porosity measures local wires compaction. For each triangle in the device surface, φ is computed such that:

$$\varphi = \frac{A_{open}}{A_{total}} = 1 - \frac{A_{metal}}{A_{total}}\,, \tag{3.4.1}$$

with A_{metal} the surface area of metal (wires) and A_{total} the underlying triangle area. Porosity patterns for two cases of FD and WEB devices are depicted in Figure 3.14c,d. For FDs, device wires located in inner curvature parts of the parent artery are being compacted, thus decreasing local porosities as exemplified in Figure 3.14c. Conversely for WEBs, porosity patterns are not governed by the arterial surface and are rather induced by a regrouping of wires in the center of the device, as showed in Figure 3.14d. Interestingly, mean porosities are similar for both devices due to the fact that the decrease in number of wires (144 for WEBs, 48 for FDs) is compensated by an increase of wire thickness (25 µm for WEBs, 48 µm for FDs). Nevertheless, porosity ranges found at the neck are smaller by an order of magnitude for FDs than for WEBs, again due to the intra-saccular device design.

For each case, the outcome given in Table 3.4 was defined between occluded after 3 months (fast) and partially permeable after 6 months (slow) during angiographic follow-up.

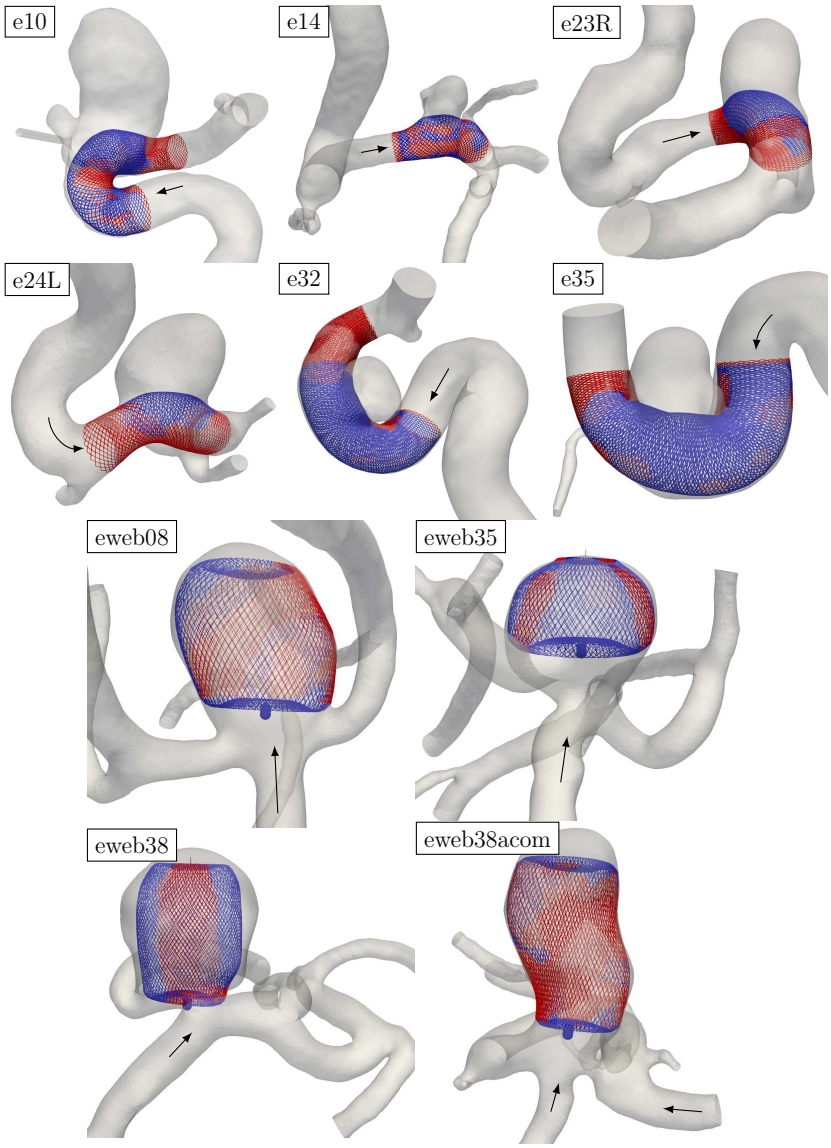

Figure 3.15: Patient-specific GMU cases. The diameter of the wires is on the same scale as the real deployed size. Red wires correspond to parts of the original device (in blue) that were not kept in the YALES2BIO computations since they were either outside or apposed to the parent artery. For WEB devices, the proximal marker volume, *i.e.* the blue cylinders on the inferior part of the devices, was kept in both GMU and YALES2BIO computations. The main incoming flow direction is schematized by black arrows.

Three dimensional views of all the cases arteries going along with the deployed device can be found in Figure 3.15. Red portions of the device correspond to wires

that were not included in IBM computations, either because they were outside the artery or apposed to it. Conversely, the full deployed device was used in GMU computations. The threshold distance to the wall below which a given wire was defined to be apposed to the arterial wall was empirically set to $5D_w$ with D_w the wire diameter ($D_w = 48\,\mu m$ for FDs and $25\,\mu m$ for WEBs). This prevents the model to account for flows in confined regions between the device and the artery, a situation for which the present approach was not fully validated.

Case e10 presents large mal-apposed portions of the device due to the strong curvature of the parent-artery, which causes a wide range of device neck porosity as reported in Table 3.4. This high curvature configuration, associated with a large neck surface, will enable to study a wide variety of flow patterns. As the upstream flow is being pushed to the outer curvature part of the artery, it will encounter large mal-apposed device portions, causing both normal and tangential-longitudinal flow redirections at the wires. This challenges the proposed model to account for non-homogeneous incoming flow directions, making this case very interesting to study. Incoming flow conditions encountered in cases e14, e23R and e24L are less complex than e10 since they are located in low-curved parent-artery sections. It should be noted that e23R and e24L have significant device portions that were removed in IBM computations. As opposed to previous FD cases, e32 and e35 are located on the inner-curvature part of the arterial wall. Therefore, the incoming flow is not expected to be directly pointed towards the aneurysm dome as in other FD cases. In addition to that and for these cases only, there remains large mal-apposed portions of the device upstream to the aneurysm (see Figure 3.16 for e32), again challenging the heterogeneous model to account correctly for many flow conditions. It results that for these cases, it is expected that tangential and longitudinal drag forces components will be more important compared to the normal one.

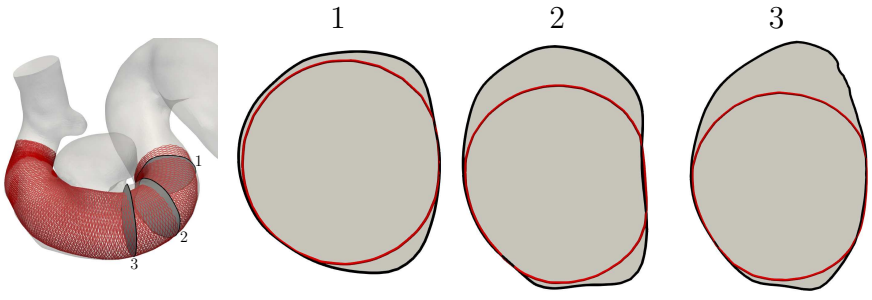

Figure 3.16: e32 device proximal mal-apposition

As already stated previously, WEB cases are found at bifurcation sites. Therefore, these devices are expected to experience incoming flows mostly normal to their neck surface. The eweb38 case is an exception since the aneurysm has de-

veloped on the side-wall of a small bifurcation, as depicted in Figure 3.15. For the eweb38acom case located in the ACOM, two inlets are feeding the aneurysm (left and right arrows). Indeed, it is the location in the circle of Willis where right and left parts are connected together. Significant device parts for cases eweb08 and eweb38acom were removed in YALES2BIO computations since they were either apposed-to or outside the aneurysm wall. Conversely, eweb38 and eweb35 contained large portions of mal-apposed device which were kept. As for FD cases, the full deployed device was used in GMU WEBs computations.

3.4.2 Numerical frameworks

Mesh generation For each case studied, two meshes were created, to compute the flow before treatment and after treatment by the endovascular device, respectively. Pre-treatment volumetric meshes were created by using the arterial surface mesh sizes provided by the GMU team. This entails that the number of elements for these meshes are of the same order of magnitude for both groups, as reported in Table 3.5, with differences mainly due to the use of different meshing tools.

	Pre-treatment		**Post-treatment**	
	GMU	YALES2BIO	GMU	YALES2BIO
e10	1.6	2.3	52	12.8
e14	0.9	1.3	8.9	6.3
e23R	2.1	3	33	8.9
e24L	2.5	3.6	28	9.7
e32	1.3	2.1	60	13.1
e35	1.7	2.4	107	14.8
eweb08	1.9	2.9	147	11
eweb35	1.8	2.4	150	9.8
eweb38	2.8	3.9	163	21
eweb38acom	1.1	1.7	93	7.7

Table 3.5: Number of cells (in million) comparison between YALES2BIO and GMU for each patient-specific case

Concerning post-treatment meshes, removal of apposed and outer device portions is first performed manually using apposition maps rendered in 3D windows using the vtk library. Then, re-meshing of the GMU arterial surface is performed to refine portions of the arterial wall close to the device wires. From this newly re-meshed surface, a first volume mesh is generated, but mesh sizes interpolated from the surface may be too coarse to fully capture the struts wakes for grid elements which are far from the surface and close to the wires. Therefore, an additional volume refinement is carried out under the constraint that mesh size equals $w/8$, with w the inter-crossing distance, inside a region of width 300 µm

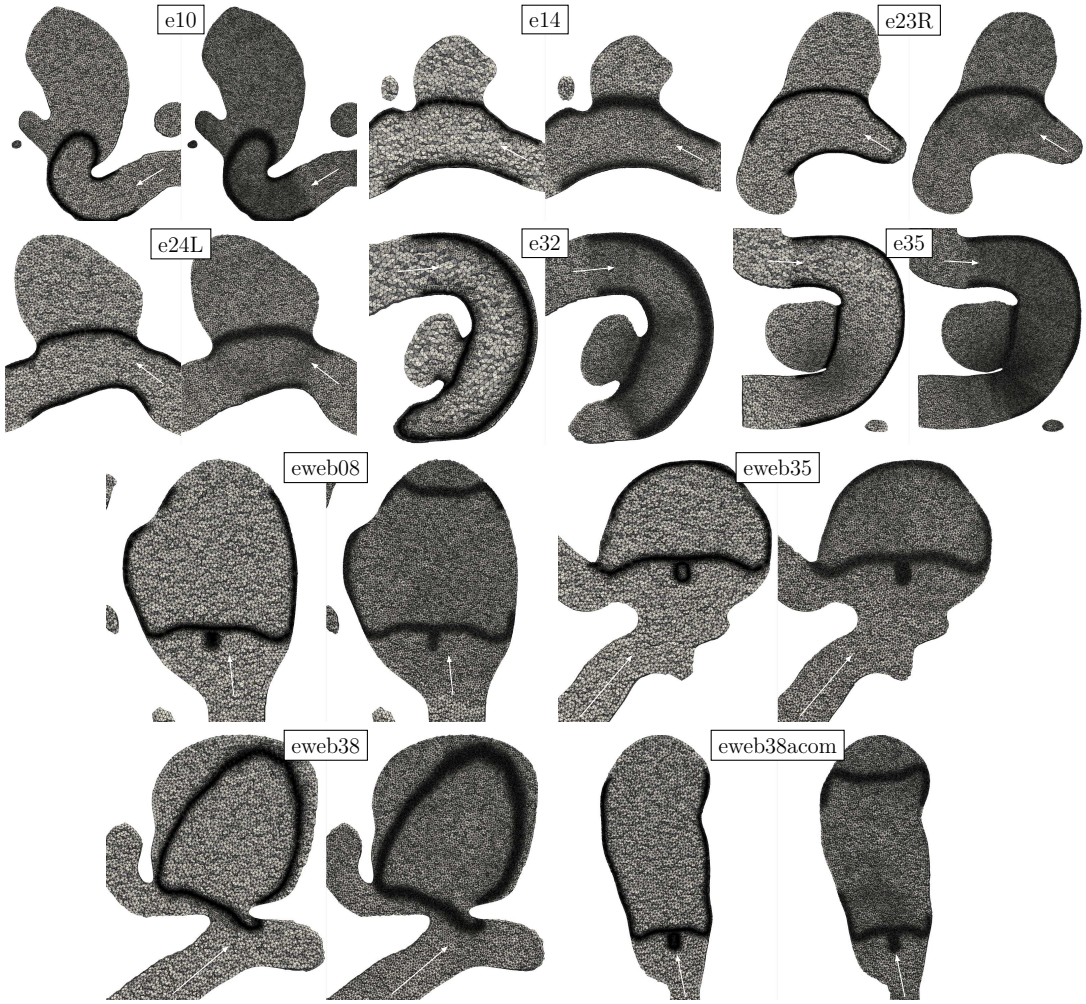

Figure 3.17: Comparison of mesh sizes in the vicinity of the sac for all GMU cases. For each case, the left and right meshes correspond to GMU and YALES2BIO, respectively. White arrows indicate the incoming flow from the parent artery. The number of elements for each case is given in Table 3.5.

around the device surface. This mesh size has proven be adequate for the present model usage in Chapter 3. Finally, mesh quality was enhanced using the mmg library [44], which also produced smooth mesh size gradients. Since GMU meshes are resolving the wires diameter length scale, the number of mesh elements is by an order of magnitude greater compared to YALES2BIO, as reported on the right part of Table 3.5.

Visual comparison of post-treatment meshes is available in Figure 3.17 for all cases. Despite being coarser near the wires compared to GMU, our mesh sizes in the bulk of the aneurysm sac were smaller due to initial surface and volume re-meshing and differences in meshing algorithms. Figure 3.17 enables to appreciate how apposed device portions removal performed manually by our group impacts

the final volume mesh (see cases e23R and eweb38acom for good examples).

Additionally, it is worth remarking that for intra-saccular device cases, distal parts of WEBs kept on YALES2BIO computations were clipped by GMU team to save computational costs. However, this difference is expected to have negligible impacts on the results as explained by an article recently published by GMU team [103]. Comparing numerical computations of 4 WEB cases with two mesh refinement strategies, full and partial (distal removal), Mut et al. [103] demonstrated that the partial strategy yielded differences below 5% for neck inflow rate and time-and-volume averaged velocities inside the sac. Correctly capturing these quantities is essential since they have been proven to be of interest in predicting treatment occlusion rates for endoluminal devices [102]. Other quantities such as kinetic energy and WSS exhibited differences between full and partial refinement from 1% to 25%, with a mean value around 10%. For all hemodynamic variables, these differences decreased when comparing post/pre-treatment reductions.

Fluid properties and boundary conditions At the inlet locations, the flow rate waveform represented in Figure 3.18 was scaled according to the vessel area using a cube law following the principle of minimum work, as advised by measurements performed by Cebral et al. [28]. The shape of the inlet waveform in Figure 3.18 was obtained with measurements from phase contrast magnetic resonance images for normal subjects given by Ford et al. [55]. The pulsatile period T_p was fixed to 1 s. Womersley velocity profiles were prescribed on GMU inlet mesh points, whereas flat profiles were used in YALES2BIO computations. The impact of having different inlet velocity profiles onto aneurysmal velocities is expected to be negligible since inlets were located far upstream aneurysms for all cases, giving the flow a sufficient distance to establish in the tortuous portions of ICA. However, this condition is not met for case eweb38acom where inlet locations are close to the aneurysm, entailing that comparative results conclusions must be taken with great care.

For outlets, zero-pressure boundary conditions were applied for large arteries (MCA and ACA). Conversely, for small branches exiting major parent arteries, the flow rate waveform depicted in Figure 3.18 was scaled in order to obtain a Wall Shear Stress (WSS) value of 1.5 Pa, as for inlets.

For all cases, a Newtonian rheology law was assumed for the fluid with a kinematic viscosity $\nu = 4.0 \times 10^{-6}\,\mathrm{m.s^{-2}}$ and a density $\rho = 1.0 \times 10^{3}\,\mathrm{kg.m^{-3}}$. The total physical-time simulated by both groups was fixed to two cardiac cycles and results from the second cycle were kept for further analysis.

CFD solvers In order to account for wires impact on the flow, post-treatment computations performed by GMU used an adaptative embedded technique, also

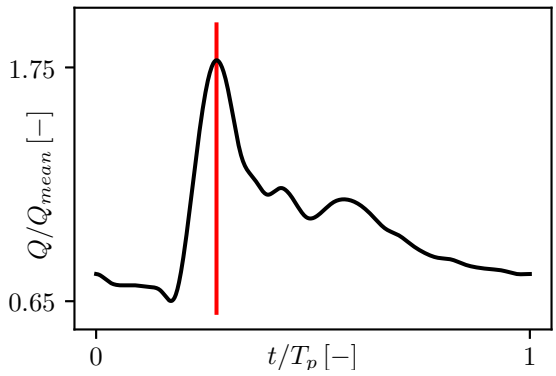

Figure 3.18: Normalized flow rate waveform imposed at the inlets and outflow outlets (*i.e.* small branches) of all patient-specific cases. The red line corresponds to the peak systole for which several comparisons were performed.

referred to as immersed method (IMM), which is extensively described by Cebral and Löhner [26] for endovascular geometries and Löhner et al. [87] for more general applications. This method is not conformal according to the definition used in this thesis, as it does not remove the device volume from the fluid one and does not explicitly applies no-slip boundary conditions on the strut surface nodes. Instead, IMM adaptively refines the mesh in the vicinity of the wires until grid size can resolve struts diameter. Then, fluid elements which are fully immersed inside the wires are deactivated in the linear-system solver by setting to zero coefficients in the edges-matrix. Proper no-slip boundary condition at the wires is ensured via both interpolation from nearest solid nodes and modifications of matrix coefficients to account for fluid cells which are partly immersed in the solid volume. For more details, please refer to [26, 87].

Computations performed with the present model for both FDs and WEBs cases used the numerical framework already described in Chapter 2. Since porous models were not originally developed for and tested with intra-saccular (WEB) cases in the literature, implementations described in Section 3.2 were applied to FDs geometries only.

General solver characteristics from both group is presented in Table 3.6. The main difference concerns temporal advancement handled explicitly in YALES2BIO and implicitly in GMU solver, which makes computational costs comparison difficult to perform.

WEB marker modelling As briefly seen for WEB cases in Figure 3.15 and for an example close-up given in Figure 3.19, intra-saccular devices contain a section at the neck where all the wires are converging into a cylindrical volume

	YALES2BIO	**GMU**
Framework	Finite-Volume	Finite-Element
Pressure strategy	Projection	
Spatial order	4^{th}	2^{nd}
	4^{th}	1^{st}
Temporal scheme	explicit Runge-Kutta	implicit Euler
	30000 iterations per cardiac cycle	100 iterations per cardiac cycle
Parallelism paradigm	MPI	OpenMP

Table 3.6: CFD numerical solver comparisons between GMU and YALES2BIO.

referred to as proximal marker. This volume is crucial for physicians since it is used during the deployment procedure to assess the correct device placement in the aneurysm due to its radio-opacity.

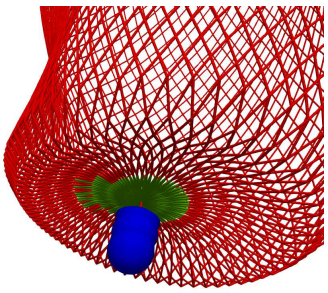

Figure 3.19: The radio-opaque marker volume located on the proximal section of WEB devices is represented in blue. Wires in green were not activated in the heterogeneous model as the packing-density was too high. A penalization method assigning null fluid velocities inside the proximal marker volume and in the vicinity of the closely packed wires was used to model these device parts (more details in the text).

GMU computations model this marker by adding a wire normal to the device with diameter and length roughly equal to 500 µm and 750 µm, thereby refining the mesh a these locations as depicted by Figure 3.17 (see case eweb38acom for example). Since this volume cannot be handled by the heterogeneous model as it uses only edges in rhombus arrangements, additional modelling was needed. To this end, mesh refinement was first performed inside the marker surface so as to correctly capture its effect and a penalization method was applied for internal fluid nodes. Penalization-type methods were first introduced by Arquis E [6] and Angot et al. [2] to model the flow around solid obstacles without explicitly meshing the fluid-structure interface by adding a porous volume source term for the fluid nodes located inside the solid domain. This method can be classified in the family of immersed models. Without going into too much details, a mask

function χ is used to determine whether a given fluid node located at $\mathbf{x}$ belong to the fluid or the solid:

$$\chi(\mathbf{x}) = \begin{cases} 1 & \text{if } \mathbf{x} \in \text{solid}\,, \\ 0 & \text{else}\,. \end{cases} \tag{3.4.2}$$

A source term is then added to the conservation of momentum equation found in the Navier-Stokes system such that:

$$\rho\left(\frac{\partial \mathbf{u}}{\partial t} + \boldsymbol{\nabla}\cdot(\mathbf{u}\otimes\mathbf{u})\right) = -\nabla p + \boldsymbol{\nabla}\cdot\bar{\bar{\tau}} - \chi\frac{\mathbf{u}-\mathbf{u_s}}{\Delta\tau} \tag{3.4.3}$$

with $\mathbf{u_s}$ the solid velocity inside the masked region, in the present case $\mathbf{u_s} = \mathbf{0}$, and $\Delta\tau$ a constant with a dimension of time. In practice, its value is numerically chosen so as to satisfy the constraint $\Delta t/\Delta\tau \gg 1$ which ensures that $\mathbf{u} = \mathbf{u_s} = \mathbf{0}$ on the nodes inside the solid domain. An implicit formulation for the time advancement of this source term was chosen following Berrada [10] to ensure unconditional stability of the numerical method. Additionally, the penalization method was used around struts depicted in green in Figure 3.19 due to the high density of wires that cannot be handled correctly by the heterogeneous model. These wires were removed from the drag force computations under the criterion that $w\sin(\alpha) - D < 0.85h$ with w, α, D and h the inter-wire distance, angle, wire diameter and grid size, respectively. This condition states that jet-inflows occurring inside rhombus cells cannot be represented by the fluid mesh using the present model. A region of width $3h$ around these wires was specified for the mask function χ.

3.4.3 Results

To compare numerical results between GMU, the current proposed IBM approach and porous models, both qualitative and quantitative analysis were performed for each case.

3.4.3.1 Qualitative

Qualitative comparisons of pulsatile velocity fields in intracranial aneurysms is a challenging task as blood flow does not have any preferential direction and exhibits complex patterns due to the curved arteries found upstream to the aneurysm. For example, Raschi et al. [124] used streamlines and wall shear stress surface patterns at three different moment of the cardiac cycle to assess the performances of their porous model. Nevertheless, comparing models with streamlines is difficult since they only give access to general characteristics of the flow inside the aneurysm sac such as main vortical structures, flow impingement and jet

separation. Detailed information regarding local velocity redirection caused by the wires and the device capability to reduce intra-saccular velocities can not be assessed by streamlines. Additionally, WSS patterns do not enable to fully understand the flow inside the sac and to study how well each device model impacts the incoming blood flow at the neck, since it is only a surface quantity.

Li et al. [81] used iso-contours of velocities inside the aneurysm volume to compare their screen model with conformal computations. Despite being representative of global flow behaviours in the sac, iso-velocity surfaces cannot provide access in details to the flow modifications occurring in the close vicinity of the device, which are essential to assess and compare the performances of newly introduced models. Nevertheless, using specific slices inside the aneurysm volume, as it is done by Li et al. [81] and Augsburger et al. [7], can be very valuable since local flow redirection caused by the device and intra-saccular velocities reduction can be assessed and compared, on the condition that the slices are well chosen. Therefore, qualitative assessment was conducted using velocity fields for each case on a single slice which was manually chosen under the criteria that it contains portions of the device and enables to understand the flow structure in the most straightforward manner. Both velocity magnitude contours and projected velocity vectors maps were used. These comparisons were performed at peak-systole, as in Li et al. [81], since it is critical for device models to correctly reduce velocities for this flow condition.

For each FD and WEB case, the peak-systolic velocity field in the second simulated cardiac cycle obtained by using both the current IBM method and porous frameworks detailed in Section 3.2 is compared to results from GMU team, which are considered to be the reference. Porous models were used for FDs cases only as this class of method was not originally built to tackle intra-saccular devices such as WEBs.

Since each geometry used in the current validation step harbours a unique combination of arterial and deployed device geometries, qualitative comparison is performed in the following paragraphs for all the 10 available cases, so as to understand the encountered flow features and better appreciate quantitative comparisons performed later.

Case e10 (Figure 3.20) Colored maps of velocity magnitude along a single slice inside the aneurysm are depicted in Figure 3.20 for both pre-treatment and post-treatment results (IBM, GMU and porous).

Among all intracranial geometries studied in this section, e10 harbours the largest aneurysm in terms of volume and neck surface (see Table 3.4). Its surface shape can be qualified as elongated and harbours multiple irregularities often referred to as blebs in the literature.

The intra-saccular hemodynamic environment has been proven to relate to bleb formation [29]. By virtually removing such irregularities and performing computational simulations, Cebral et al. [29] demonstrated that blebs mostly occur in regions where elevated WSS patterns are present and where inflow and outflow jets impinge the sac surface. Additionally, wall thickness of blebs have been found to correlate well with the presence of jets in their close vicinity, with thin blebs being more common in regions of elevated velocity and WSS, in particular [129].

Such flow conditions are encountered for the bleb depicted in the pre-treatment slice in Figure 3.20. As the inflow jet produced by the upstream curved parent artery enters the aneurysm sac, it splits at the bleb location and forms a local recirculating flow pattern inside the bleb volume. The second part of the jet which was deflected by the bleb further impinges the aneurysm dome and subdivides in two parts which are then diffused in the aneurysm sac before re-entering the arterial circulation.

Flow behaviour after endovascular treatment is completely different from what is described above, as showed by the GMU velocity fields (middle of Figure 3.20). The inflow jet is mostly blocked by non-apposed portions of the device at the aneurysm neck, thereby redirecting the main flow inside the parent artery. No more jet impingement on the aneurysm dome is present and flow is reorganized into an "arch" pattern that starts in the proximal portion of the neck and ends in the distal one (see the contours on the right of the slice for GMU results). Such behaviour is correctly reproduced by the present IBM framework, both in terms of shape and intensity (see the middle-right slice in Figure 3.20.) A slight underestimation of velocities is found for one region in this slice (marked with a white $*$ symbols) and overestimation at the distal position in the neck is obtained where flow re-enters the arterial circulation (white $\diamond$ symbol). This "leak" is due to the fact that some wires are deactivated in this region because some triangles on the device surface lie outside the arterial volume and thus cannot measure infinity velocity, which is a mandatory input to apply drag forces in the IBM framework.

Going into more details, one can notice in the top of Figure 3.20 that velocity redirection caused by the device is overestimated by the IBM framework. Nevertheless, downstream flow patterns does not seem to be affected by this very local overestimation.

As observed on the last line of Figure 3.20, the porous (AC) model underestimates device effect and allows more flow to enter the aneurysm sac, thereby increasing velocities. An opposite trend is found for Augsburger et al. porous (A) model, since velocities are lower than GMU in this slice. Nevertheless, this model yields results which are closer to GMU compared to Raschi et al.'s model.

Porous results using only the normal component of Raschi et al. [124] (see middle image on the last line of Figure 3.20) exhibit a flow which is extremely different to GMU, with a strong remaining jet in the sac and no redirection to the parent-artery.

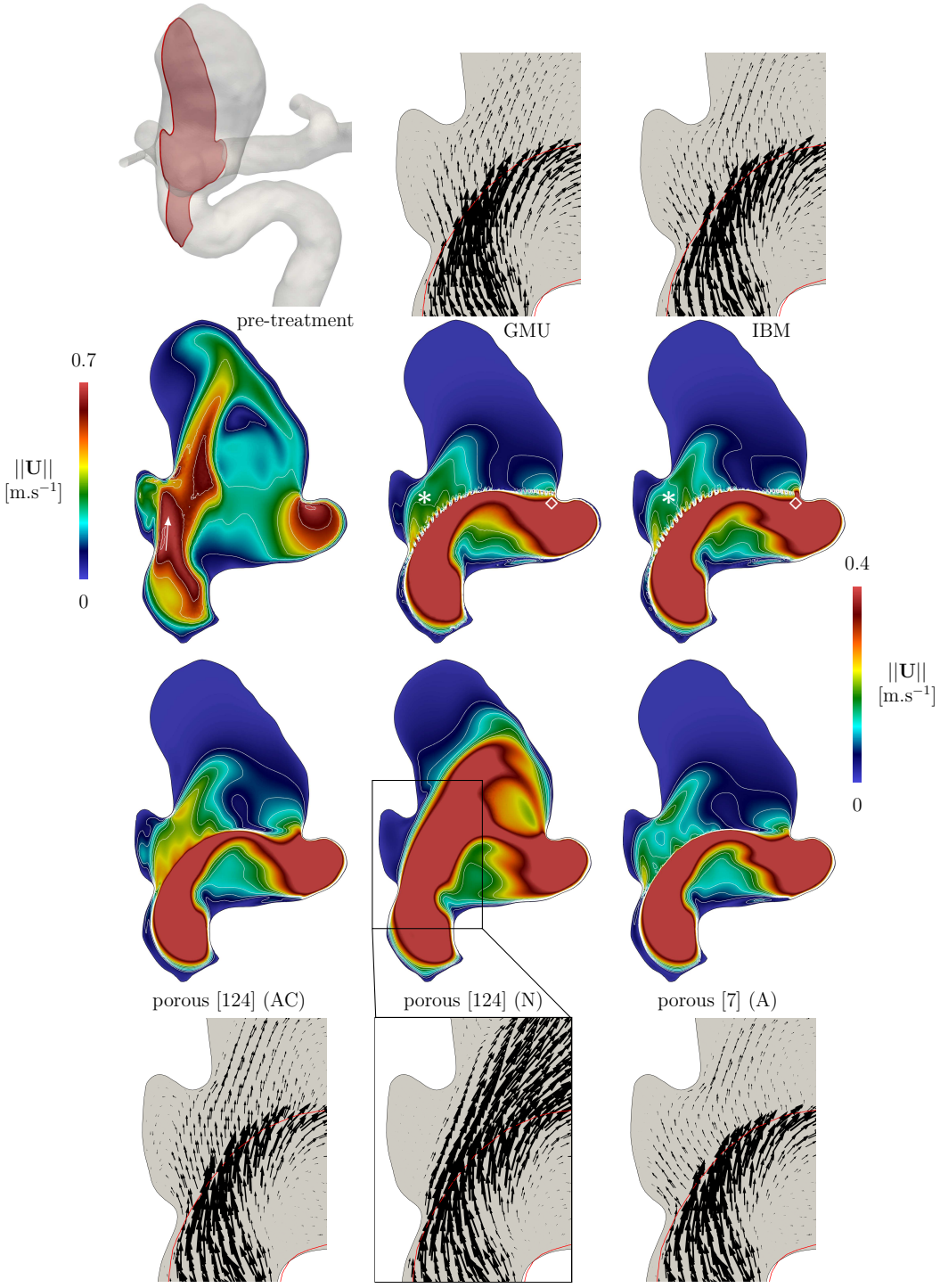

Figure 3.20: e10 qualitative results. Velocity magnitude color maps used different extents compared to pre-treatment to appreciate post-treatment model differences. Velocity vectors are projected onto the slice to ease flow visualization (close-up views with black arrows). The red line represents the device frontier, the white arrow shows the main direction of the upstream flow and the arterial 3D surface is rendered at the top-left corner to appreciate the slice location.

Case e14 (Figure 3.21) Despite being the smallest aneurysm in the whole cohort, pre-treatment upstream velocities are notably high for this case, with values reaching $1.2\,\mathrm{m.s^{-1}}$ in the incoming jet, as showed by the middle-left image in Figure 3.21. The aforementioned strong jet impacts the distal part of the neck and subdivides into two smaller jets: one going through the aneurysm forming a single vortex flow structure inside the sac and another staying in the parent-artery.

It should be noted that due to the neck size being smaller by at least one order of magnitude compared to other cases, only a few device wires interact with the upstream flow. Combined to the small aneurysm volume, this entails that the entire intra-saccular flow depends on a relatively low numbers of wires at the neck, which constraints the different models (porous and IBM) to be realistic for these wires and leaves no room for potential mistakes as they will be propagated directly into the sac. This phenomenon is exemplified by the middle image in Figure 3.21, which shows that the upstream flow is redirected towards the aneurysm sac via mostly two jet-inflows between distal wires at the neck. This behaviour is well reproduced by the IBM velocities as showed on the middle-left of Figure 3.21, despite exhibiting several weaker jet-inflows which are not present in GMU results when moving towards the proximal part of the device (small white $*$ symbols). Nevertheless, these differences seem to have a negligible impact on the intra-saccular velocities as velocity iso-contours are very similar in terms of shape and intensity. One can notice on the top line of Figure 3.21 a slight increase in velocity redirection for IBM velocity vectors very close to the device compared to GMU, but the overall single vortex structure is kept by the proposed model.

As already found for case e10, porous AC overestimates intra-saccular velocities due to a lack of source term at the neck while it is the opposite for porous A [7]. Nevertheless, major intra-saccular flow patterns are correctly reproduced by both approaches compared to GMU results. Porous computation performed with only the normal component of Raschi et al. [124] does not sufficiently reduce intra-saccular velocities and underestimates device impact onto the flow, as already found for case e10.

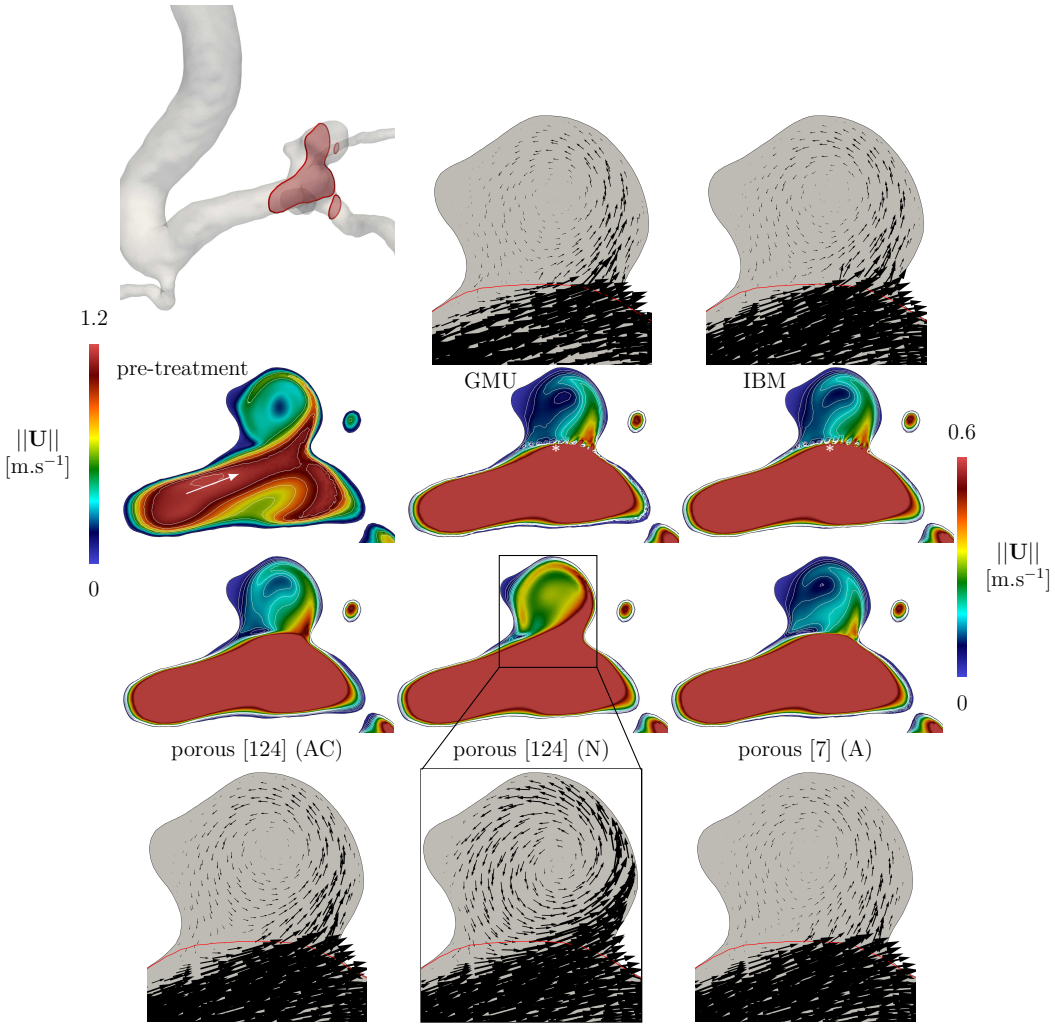

Figure 3.21: e14 qualitative results. Velocity magnitude color maps used different extents compared to pre-treatment to appreciate post-treatment model differences. Velocity vectors are projected onto the slice to ease flow visualization (close-up views with black arrows). The red line represents the device frontier, the white arrow shows the main direction of the upstream flow and the arterial 3D surface is rendered at the top-left corner to appreciate the slice location.

Case e23R (Figure 3.22) Case e23R harbours an aneurysm which is the mean range in terms of volume and neck surface. It should be noted that the device was extremely well apposed to the arterial wall in both distal and proximal regions. Therefore, manual device trimming performed by our team only left wires at the neck of the aneurysm, as depicted in blue in Figure 3.15.

A sudden parent artery diameter decrease upstream to the aneurysm, at the location of the black arrow in Figure 3.15, causes a jet filling most of the artery and directly impinging the lateral proximal side of the aneurysm wall with velocities reaching $0.8\,\mathrm{m.s^{-1}}$. This creates a single vortex type of intra-saccular flow.

The flow-diverter deployed in this case completely prevents the aforementioned jet from entering the sac, as described in the middle of Figure 3.22, but still conserves the single vortex structure but with less intensity compared to pre-treatment. Many jetting-flows between wires are present in the device close proximity, which cause a high velocity redirection as showed by velocity vectors on top of Figure 3.22. Since the device porosity is relatively low compared to other FD cases (0.58), wires are densely and regularly packed along the device surface, inducing that velocities inside the sac are low and are entirely governed by the many jetting-flows found at the neck. Thereby, local flow redirection patterns are propagated inside the whole sac volume.

Such flow characteristics are captured by the IBM framework, although some discrepancies exist compared to GMU model both in terms of velocity redirection and magnitude. As showed on the middle-right of Figure 3.22, the effect of the device on the flow is overestimated by the present model, which creates lower fluid velocities in the sac compared to GMU. In addition, while the jetting-flows are captured by the IBM framework, local redirection is too pronounced and generates a flow which goes on the opposite direction to the upstream jet, as detailed in the top-right image in Figure 3.22 (see white $*$ symbols). Since this case was proved to be sensible to flow patterns found at the neck, as already discussed previously for GMU results, the redirection overestimation produced by IBM destabilizes the whole intra-saccular flow and creates a vortex structure which is similar in shape but different in direction to the GMU results.

As for previous cases, porous AC model [124] overestimates intra-saccular velocities. Nevertheless, velocity redirection at the device is correctly reproduced by this model and in a better way compared to IBM results. This is also true for porous A [7], for which velocity magnitude reduction compare wells to conformal results.

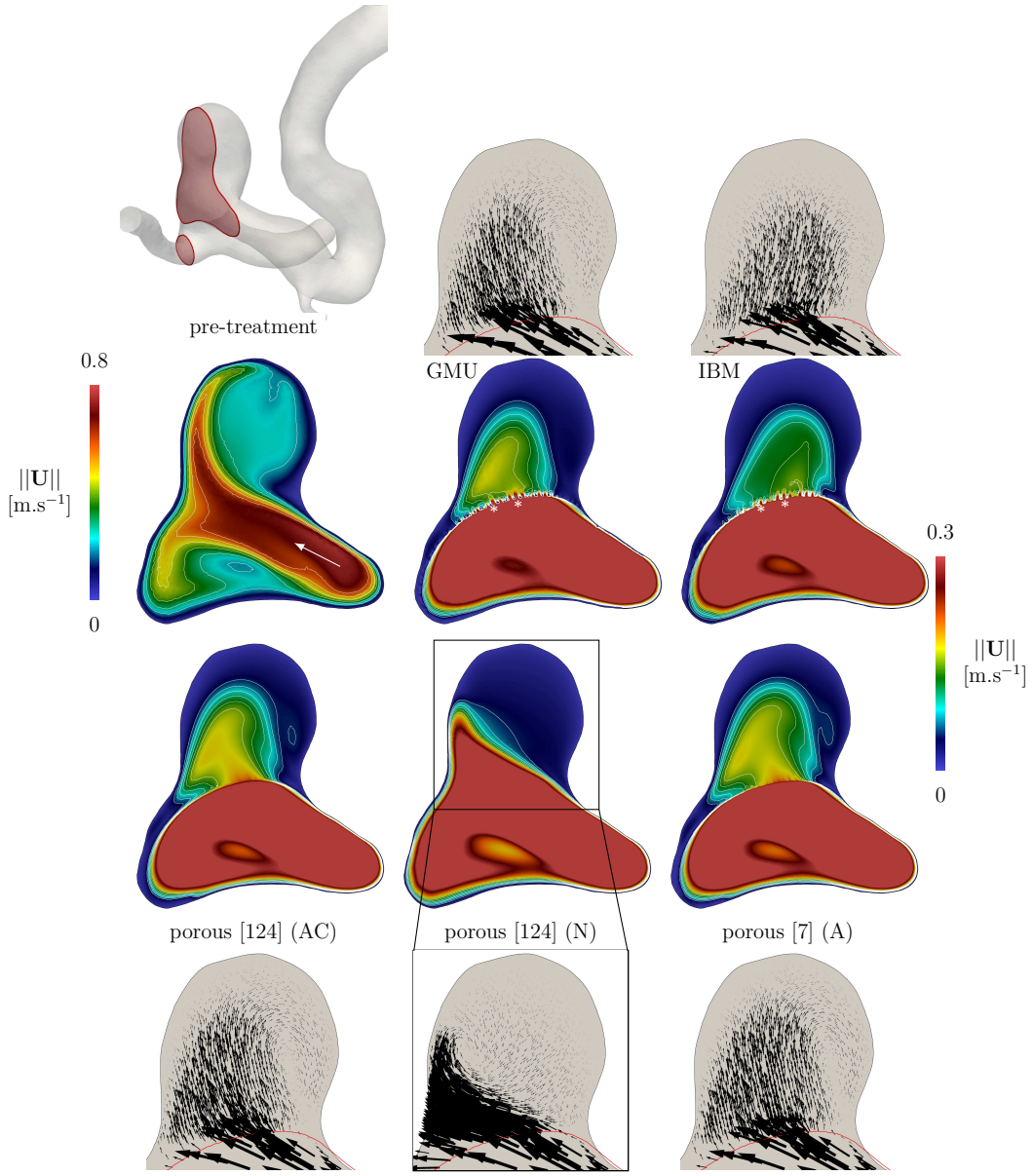

Figure 3.22: e23R qualitative results. Velocity magnitude color maps used different extents compared to pre-treatment to appreciate post-treatment model differences. Velocity vectors are projected onto the slice to ease flow visualization (close-up views with black arrows). The red line represents the device frontier, the white arrow shows the main direction of the upstream flow and the arterial 3D surface is rendered at the top-left corner to appreciate the slice location.

Case e24L (Figure 3.23) Case e24L presents some similarities with e23R in terms of aneurysm shape and size and also in terms of device apposition since most distal and proximal portions were removed from YALES2BIO computations. Nevertheless, wires packing is less important for this case compared to e23R, with a device porosity of 0.65. Due to the strong curvature found upstream to the aneurysm, the jet found at the neck has already been separated into two parts, the above one impacting the aneurysm wall distally and close to the aneurysm dome (see the long white arrow in Figure 3.23).

As for previous cases, device deployment strongly reduce intra-aneurysmal hemodynamic by preventing the jet from entering the sac, creating a low flow region with velocities being decreased to approximately $0.1\,\mathrm{m.s^{-1}}$ (see middle of Figure 3.23). Many jet wakes are found at the neck and strongly redirect the flow towards the aneurysm dome, as showed by the vectors in the top-middle image of Figure 3.23.

Both velocity magnitude reduction and redirection are well reproduced by the IBM framework, despite slight overestimations of jetting-flow angles (see small white $*$ symbols). Nevertheless, this redirection difference between GMU and IBM models does not seem to impact the flow structure inside the sac, as showed by velocity vectors on top of Figure 3.23.

Consistently with previous cases, porous AC [124] and porous A [7] under and overestimates the device effect onto the flow compared to conformal results, respectively. As showed on the bottom line of Figure 3.23, both porous modalities correctly reproduce velocity iso-contours inside the sac, contrary to the porous N model which fails to reduce the upstream jet.

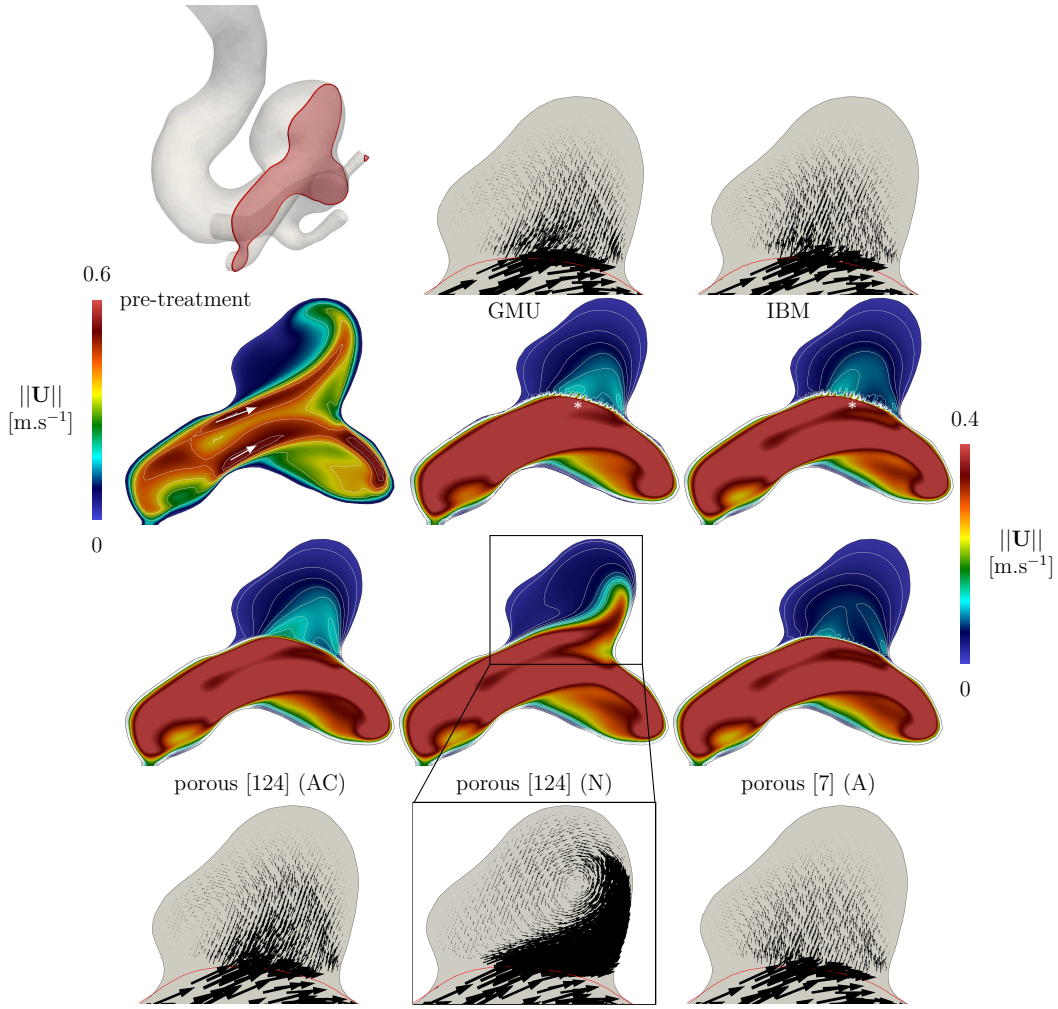

Figure 3.23: e24L qualitative results. Velocity magnitude color maps used different extents compared to pre-treatment to appreciate post-treatment model differences. Velocity vectors are projected onto the slice to ease flow visualization (close-up views with black arrows). The red line represents the device frontier, the white arrow shows the main direction of the upstream flow and the arterial 3D surface is rendered at the top-left corner to appreciate the slice location.

Case e32 (Figure 3.25) As already stated previously, case e32 presents some differences in terms of shape and device apposition compared to other cases. The first specificity lies in the fact that large portions of the device are not apposed to the arterial wall, especially in the proximal section as briefly detailed in Figure 3.16. This proximal mal-apposition challenges both porous and heterogeneous models to correctly account for flow separation at this location, which will impact downstream velocities in the aneurysm sac. Moreover, some wires located in the inner part of the parent artery curvature are densely packed due to device compression, which produces non homogeneous porosity patterns throughout the device surface with minimal values reaching almost zero in this region.

The second specificity concerns the localization of the aneurysm sac which is placed on the inner curvature of the parent-artery, as depicted in the top-left image in Figure 3.25. This entail that the incoming flow does not directly impinge the neck or the aneurysm dome but rather follows the parent-artery curvature before crossing the neck plane laterally to the aneurysm, as depicted by the velocity magnitude iso-contour on the left of Figure 3.24.

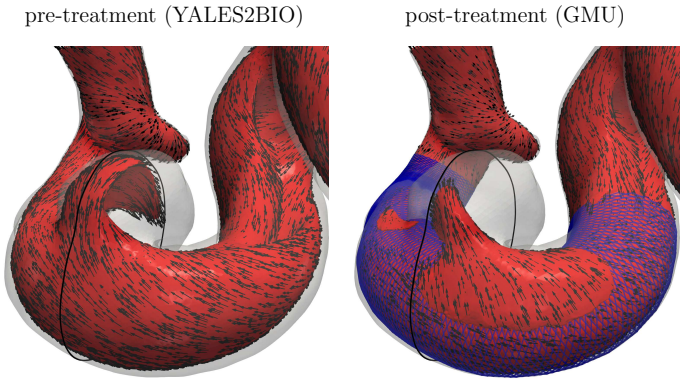

Figure 3.24: Iso-surface of velocity magnitude for case e32 near the sac, showing the complex structure arising from the aneurysm location on the inner-curved part of the parent artery. It should be noted that chosen values for velocity iso-surfaces are different between pre and post-treatment results. The slice used in Figure 3.25 is depicted on the surface as a black line.

The device deployment and its subsequent mal-apposition introduce drastic changes in the flow structure compared to the pre-treatment velocity field, since two distinct and not-communicating regions are created: inside and outside the device, as showed by GMU results on the right of Figure 3.24. The remaining jet present outside the device on the slice of Figure 3.25 stems from the upstream flow being pushed towards the external curvature side of the parent artery, going through the device and not being able to return back to the parent artery. This phenomenon is represented by the image on the right of Figure 3.24, which clearly

shows the region where the flow goes through the device to form a jet going inside the aneurysm. One can also appreciate how the device reduces the angle between the neck plane normal and the incoming flow in Figure 3.24.

This clear flow structure distinction between external and internal regions of the device is well reproduced by the IBM model. In addition to that, the agreement on the persistent intra-saccular jet shape and intensity between GMU and IBM results is good, as showed by the velocity vectors on top of Figure 3.25. Conversely, no porous model is able to sufficiently separate internal and external flows, thereby greatly overestimating intra-saccular velocities.

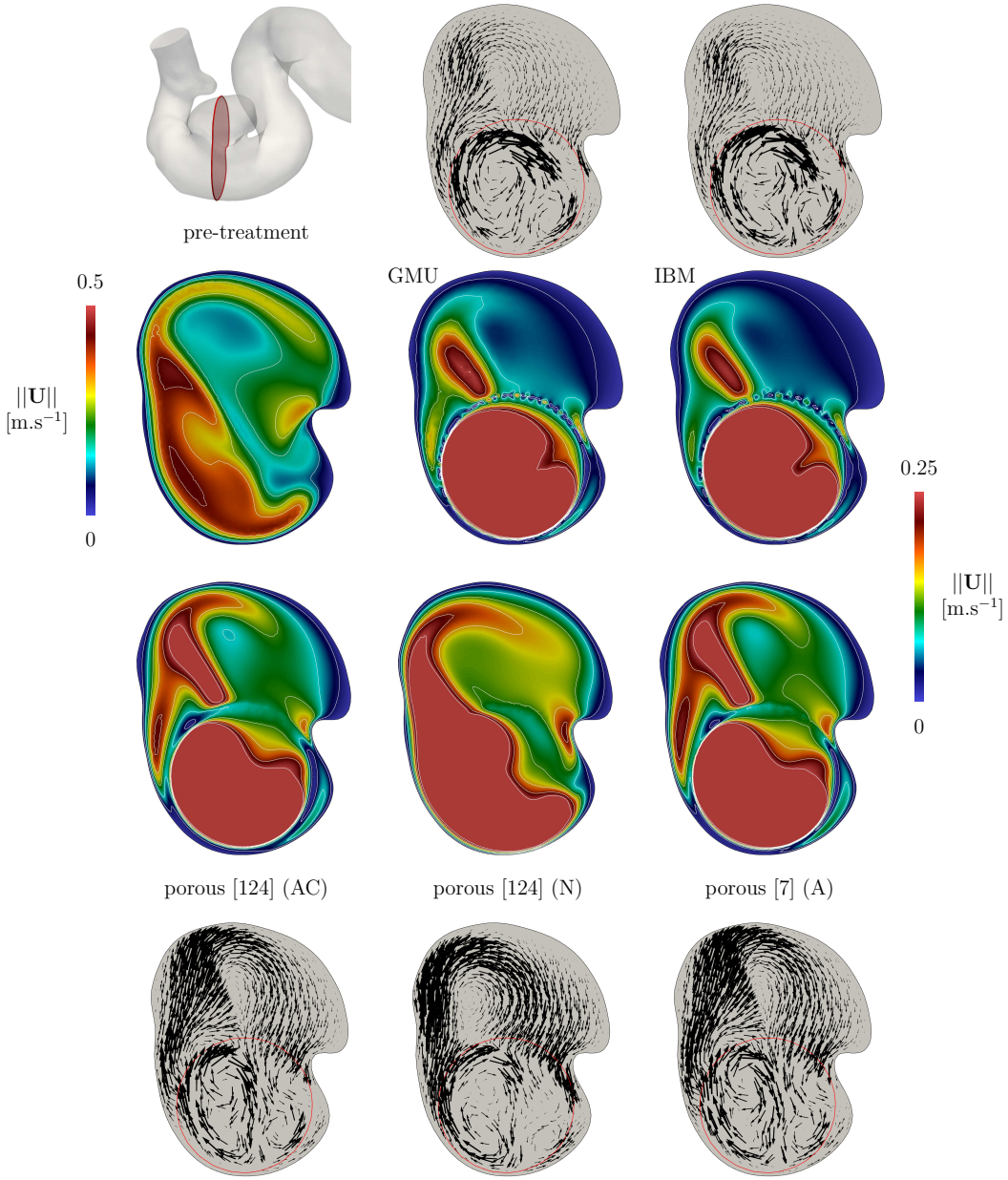

Figure 3.25: e32 qualitative results. Velocity magnitude color maps used different extents compared to pre-treatment to appreciate post-treatment model differences. Velocity vectors are projected onto the slice to ease flow visualization (views with black arrows). The red line represents the device frontier and the arterial 3D surface is rendered at the top-left corner to appreciate the slice location.

Case e35 (Figure 3.26) Despite being slightly larger, the aneurysm found on case e35 exhibits several similarities with the one harboured by case e32. It is located in the inner curvature region of its parent artery and the device is mal-apposed proximally, entailing a high number of elements for both GMU and YALES2BIO meshes (107 and 14 million respectively).

Pre-treatment flow structure is very close to e32 as the parent-artery curvature creates a region of higher velocities projected onto the arterial wall which further goes through the aneurysm neck laterally as showed by Figure 3.26. The distinct flow separation caused by the device between inner and outer regions is also present for this case but to a lesser extent compared to e32 as intra-saccular velocities only reach approximately $0.1\,\mathrm{m.s^{-1}}$. The agreement between GMU and the present model is very good for this case, even if the remanent intra-saccular jet is underestimated in YALES2BIO computations (see the white $*$ symbol in Figure 3.26). The single vortex flow structure inside the sac is correctly captured by IBM as showed by velocity vectors on the top of Figure 3.26.

Interestingly, the all-components porous model by Raschi et al. [124] compares well with GMU results and contrary to all previous cases, it underestimates intra-saccular velocities. Conversely, the porous model by Augsburger et al. [7] does not sufficiently reduces the flow inside the sac and yields an overestimation of the remanent jet. Nevertheless, these two models are able to capture the in-out distinction, which was not the case for previous case e32.

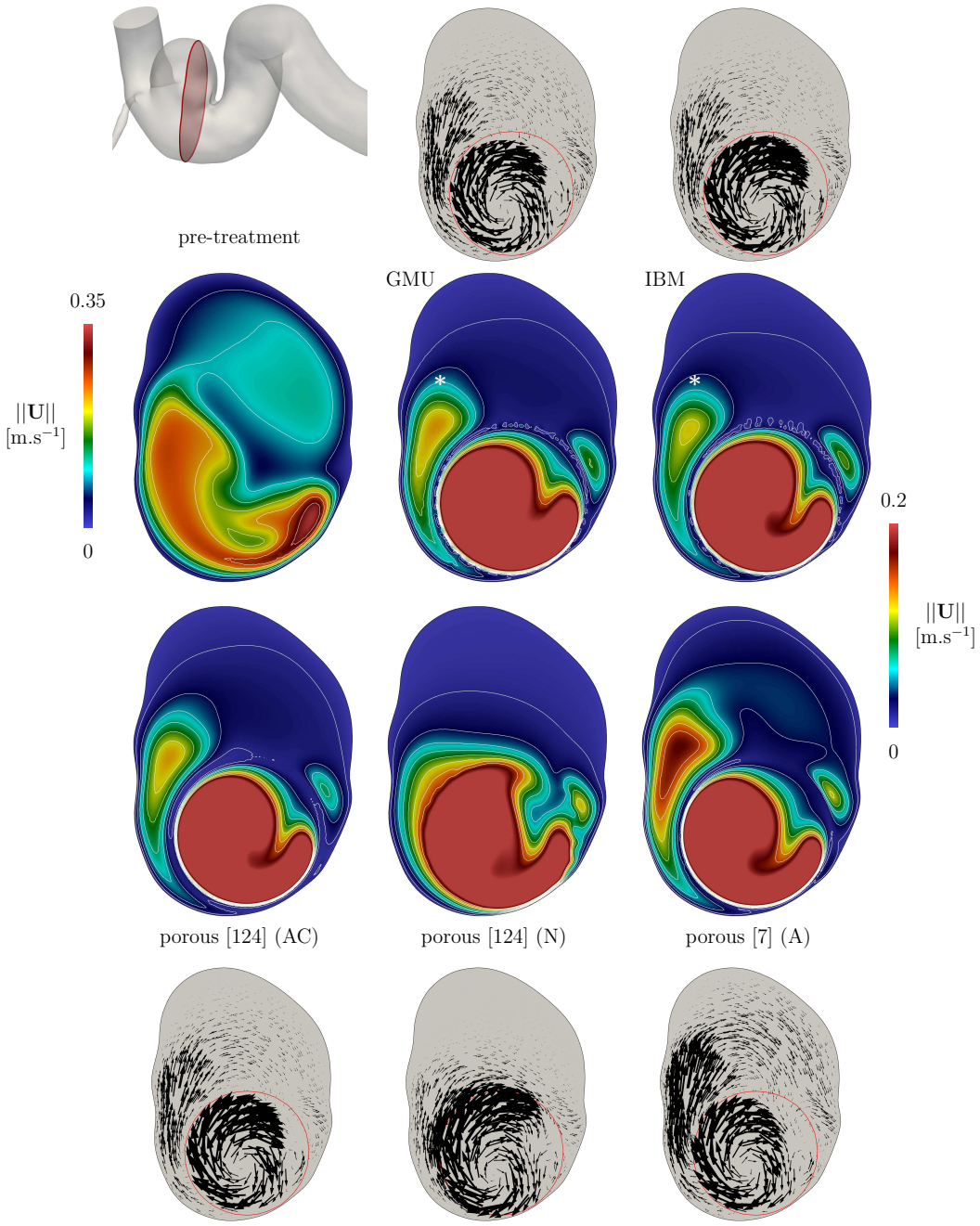

Figure 3.26: e35 qualitative results. Velocity magnitude color maps used different extents compared to pre-treatment to appreciate post-treatment model differences. Velocity vectors are projected onto the slice to ease flow visualization (views with black arrows). The red line represents the device frontier and the arterial 3D surface is rendered at the top-left corner to appreciate the slice location.

WEB cases (Figure 3.27) Peak-systolic qualitative comparisons for WEB cases are available in Figure 3.27. As opposed to FD cases, pre-treatment velocity patterns are different since WEB devices are used to treat bifurcating aneurysms. Post-treatment computations were conducted with the present IBM model only, since porous frameworks were not developed for and tested with intra-saccular cases in the literature.

For eweb08, a strong jet with velocities as high as $1\,\mathrm{m.s^{-1}}$ impacts the aneurysm dome and further diffuses inside the sac. Some instabilities appear at the tip of the jet, due to the presence of shear layers isolated inside the sac of high length, as depicted on the top-left image of Figure 3.27. Post-treatment results indicate that the aforementioned jet is completely blocked by the high density of wires at the proximal marker of the device, thereby forming a vortex on the left side of the marker as showed by GMU velocity field in Figure 3.27. Several struts wakes and jetting-flows are present but they are in minority along the device surface at the neck due to the density of wires. No substantial flow exists in the sac far downstream of the neck, indicating that the device is efficiently excluding the aneurysm from its parent artery flow. These flow patterns are well reproduced by the heterogeneous model as the left vortex is clearly visible on the side of the proximal marker, the latter being also accurately captured by the penalization method. However, it appears that both struts jetting-flows and velocity redirection are overestimated (see the white $*$ symbol) by IBM. This can be explained using drag forces considerations. Since the flow at these location is mostly normal to the device surface, longitudinal and tangential drag force components are less significant than the normal one, the latter model underestimating forces compared to conformal results as already indicated in Section 2.4.2. Therefore, this underestimation of the normal component does not sufficiently impede the incoming jet from entering the aneurysm, thereby overestimating intra-saccular velocities. In addition to that, wires patterns in this region exhibit a low $\tilde{W}/D \approx 4$ ratio for which the heterogeneous model have not been built for and fully validated. Nevertheless, this normal force underestimation does not have any noticeable effect onto downstream velocities as they are very similar to that of GMU.

Case eweb38acom exhibits similar pre-treatment velocity patterns to that of eweb08, on the difference that jet instabilities are not present due to lower velocities reaching only $0.5\,\mathrm{m.s^{-1}}$ at the neck. In addition to that, no impaction zone is found at the aneurysm dome as the jet rapidly diffuses inside the sac. Post-treatment results indicate that similarly to eweb08, the upstream jet is entirely blocked by the device at the neck, inducing downstream velocities to approach zero. No significant wakes produced by the wires are present due to the high density of struts at the impacting region. These trends are remarkably well captured by IBM, as well as the impact of the proximal marker volume onto the flow

thanks to the penalization method.

Compared to other WEB cases, the eweb38 aneurysm cannot be qualified as bifurcating since it has grown on the lateral side of its parent artery, close to a bifurcation, see the third line in Figure 3.27. Nevertheless, pre-treatment velocities show a strong jet ($0.8\,\mathrm{m.s^{-1}}$) originating from the separation of another one at the bifurcation site. No instabilities are found at the tip of the jet, which impacts the lateral side of the sac before further diffusing and returning back to the arterial circulation via the artery harboured by the aneurysm sac. Due to the numerical deployment procedure from GMU, some device wires are protruding in the parent artery through the bifurcation site, which prevents the aforementioned pre-treatment jet separation and completely reorganizes the flow near the neck. It should also be pointed out that the deployed device configuration near the bifurcation is not realistic, as a non-negligible portion of the wires are found outside the artery (visible in Figure 3.17 and more clearly in Figure 3.40). As the jet impacts these protruding wires, it is completely deflected on both sides of the device surface and goes through the bifurcation via a small section enclosed by the device and the arterial wall, inside which velocities are increased due to conservation of mass. It should be noted that the flow is almost parallel to the device in this section due to the high density of wires. A residual jet originating from jetting-flows inside protruding wires is formed on the other side of the device and induces a slow recirculation region that is confined inside the device before returning to the arterial circulation similarly to pre-treatment. The major impact of device protrusion at the bifurcation site is correctly captured by the heterogeneous model, except that the intra-saccular jet is more deflected than GMU. Consequently, as remaining portions of the sac contain very low velocities, downstream recirculation is majorly impacted by the jet deflection, leading to important discrepancies compared to GMU. Nevertheless, jet magnitude is very similar to that of GMU, meaning that the intensity to which the device blocks the flow is correctly captured by the present model. In addition to that, the recirculation confinement inside the device is also reproduced with fidelity by the proposed model.

The device in case eweb35 is located very far from the neck plane due to its size and orientation with respect to the aneurysm, as depicted in Figure 3.15, which was not the case for previous devices. In addition to that, the upstream jet does not directly impact the dome but is rather tangential to the aneurysm wall all along the sac before returning to the arterial circulation (see the left artery on the bottom line of Figure 3.27). Since the location to which this jet encounters the device has a low density of wires, this entails that strong redirection and flow blockage identified on all previous cases are not predominant for this case. This yields intra-saccular post-treatment velocity field slower but similar in shape to

pre-treatment, with several jetting-flows between device struts. These qualitative characteristics are well reproduced by the heterogeneous model with an overestimation of downstream-to-the-device velocities, which has to be put in perspective with the differences in upstream jet shape and magnitude (see white ∗ symbol in Figure 3.27) between GMU and YALES2BIO IBM results.

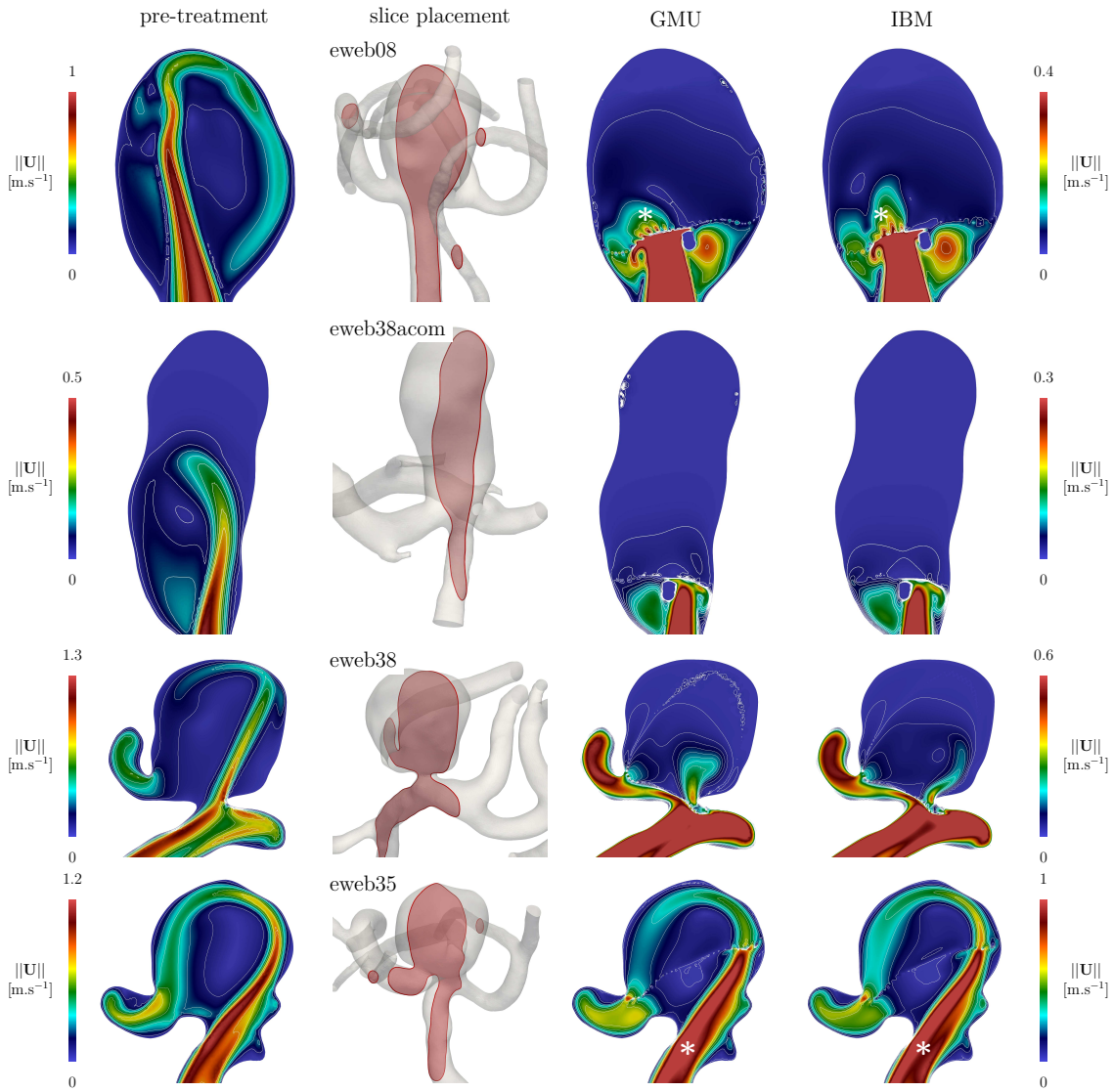

Figure 3.27: Qualitative results for WEB cases. As for FDs, pre and post-treament velocity maps color extents are different to distinguish model performances. Exact 3D slice locations with respect to the aneurysm are given to ease flow comprehension.

Overall qualitative conclusions As demonstrated in previous paragraphs, the heterogeneous model developed in this thesis qualitatively reproduced gold-

standard results from GMU team. Most notably, jetting-flows between struts as well as intra-saccular velocity reductions and redirections are captured, both for FD and WEB cases. In addition to that, the model has demonstrated its versatility, compared to porous models, to account for both mal-apposed device portions and distinctive characteristics such as inward parent artery curvature. Moreover, model applicability was successfully further extended to other type of braided device, namely intra-saccular WEBs, without any model modifications other than the penalization implementation for extremely dense wires found at the recess, confirming again model versatility.

3.4.3.2 Quantitative

In order to quantitatively assess the performances of the IBM model compared to conformal and porous frameworks, multiple indices and criteria were computed so as to provide an extensive validation. Two types of quantitative comparisons were performed: macroscopic and local.

Macroscopic comparisons The first type of comparison can be qualified as macroscopic since quantities averaged in space and/or in time are used. The first macroscopic index is spatial and time-averaged intra-saccular velocity defined as:

$$U_a = \frac{1}{V_a} \int_{\Omega_a} || < \mathbf{U} > ||\mathrm{d}V \tag{3.4.4}$$

with V_a being the aneurysm volume reported in Table 3.4 such that $V_a = \int_{\Omega_a} \mathrm{d}V$, Ω_a the computational domain labelled as the aneurysm sac, $< \mathbf{U} >$ the component-wise time-averaged velocity and $\mathrm{d}V$ the fluid grid points volume.

Assessing the reproducibility of this quantity for the different models is crucial since its has been put forward by many publications as a potential treatment success predictor for flow-diverters by Mut et al. [102], Ouared et al. [110] and for intra-saccular devices [32]. Comparisons were performed for post-treatment results but also for pre-treatment fields so as to study the agreement between different CFD codes without device modelling. This is intended to highlight to which extent numerical solver and mesh resolutions differences impact intra-saccular flow.

Figure 3.28 presents the comparison of GMU and YALES2BIO U_a results for the pre and post-treatment FD cases with different models. Comparisons in Figure 3.28 show that the agreement between pre-treatment velocities are very good for all FD cases except for e14 in which our solver overestimates velocities by approximately $0.02\,\mathrm{m.s^{-1}}$. Since this case presents the higher pre-treatment velocities among all FD cases inside the impacting jet at the neck, as described

by Figure 3.21, this difference might be caused by differences in spatial and temporal discretization orders along with different mesh sizes. Indeed, as the GMU solver has lower discretization orders compared to YALES2BIO (see Table 3.6), numerical diffusion is expected to be higher and thus reduce the velocity of the upstream jet at the aneurysm neck. This phenomenon can be amplified as blood flows inside curved artery sections upstream, since velocity gradients can be underestimated by GMU at these locations, thus producing a different velocity field entering the aneurysm.

In accordance with the qualitative results presented in Section 3.4.3.1, one can see that the reduction of intra-saccular velocities due to the device is high, with values never exceeding 40% (blue bars in the bottom plot of Figure 3.28). Most notably, cases e32 and e35 have their velocities reduced by 85% and 90% respectively, due to their particular parent-artery curvature environment.

The bottom-right quadrant of Figure 3.28 shows the post-treatment error E defined as $E = \frac{U_a^{\text{model}} - U_a^{\text{GMU}}}{U_a^{\text{GMU}}}$ in percentage. Since over and underestimations are needed to be captured by this index, no absolute value was used. Figure 3.28 confirms qualitative findings for the normal porous model, which is not able to sufficiently impede velocities at the neck for all cases. Among all models (IBM and porous) and FD cases, intra-saccular velocities are systematically overestimated, except for the IBM results for case e32. On average for all cases, porous A produces less errors than porous AC (except for e32 and e35). Interestingly, one can notice that the variations of the porous AC model errors are low and around a mean value of 20%, except for case e32, for which the error reached more than 100%. The same phenomenon is also observed for the porous A model: even if the errors are of the same order as those obtained with IBM for 3 cases (e14, e10 and e24L), very high values are observed for cases e32 and e35, with errors going up to 130%. This is not observed for the IBM method, as a maximum error of 5% only was reached for cases e14 and e35, thereby demonstrating both the robustness of the proposed approach to correctly reproduce intra-saccular mean velocities and its versatility to be used in any geometries and device deployment. Moreover, this highlights the fact that despite the porous A and AC models produce errors which are of the same order of magnitude to IBM ones for 4/6 cases, these models fail to capture the complex flow features found on cases e32 and e35, probably due to both the strong curvature of the parent artery and the device mal-apposition in these cases.

Since the presence of Flow-Diverter apposed portions have been proven to correlate with treatment outcome by Rouchaud et al. [128], it is crucial for CFD models to accurately account for mal-apposed devices configurations in order to further study changes in the hemodynamics for these cases. This has been confirmed by Mut et al. [102] for one illustration case that was not occluded at

follow-up. In the case reported in [102], even if the device is present at the neck, intra-saccular flow is sustained via a strong inflow jet originating from several upstream gaps between the parent-artery and the device.

Figure 3.28 demonstrates that porous models cannot be used for such cases since they yield large errors, especially AC and A models. On the contrary, due to its inherent versatility, Figure 3.28 shows that the heterogeneous model developed in this thesis can be used to study how device apposition influences hemodynamics inside the aneurysm sac.

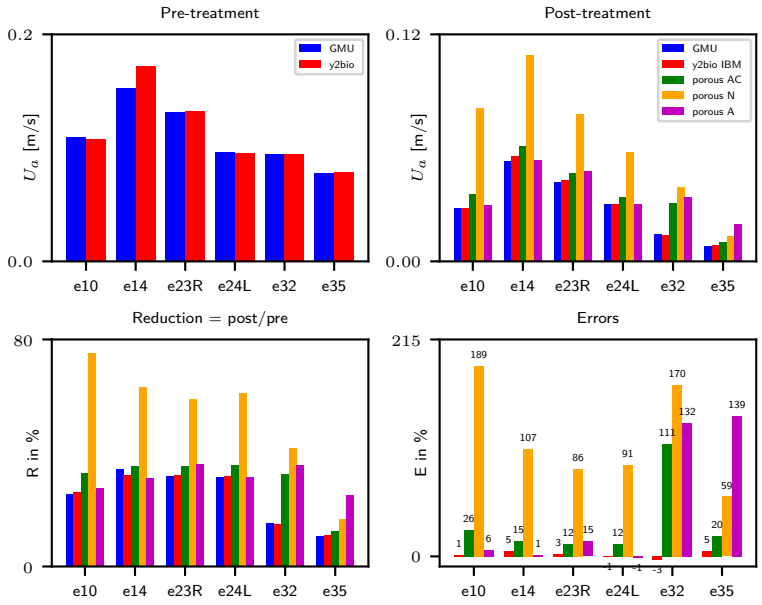

Figure 3.28: Flow-Diverters quantitative results for the U_a macroscopic metric, for both pre and post-treatment results with all models (GMU, IBM and porous). Post-treatment relative errors at the bottom-right corner use GMU results for reference value.

Figure 3.29 compares pre and post-treatment U_a values between GMU and IBM for all the WEB cases. As for Flow-Diverter cases, the agreement of pre-treatment mean velocities for WEBs is excellent as showed by the top-left graph in Figure 3.29, with a maximum difference of $-5 \times 10^{-3}\,\mathrm{m.s^{-1}}$ reached by case eweb08, which is smaller by an order of magnitude than for FD case e14 (recall $0.02\,\mathrm{m.s^{-1}}$). The values of pre-treatment U_a predicted by YALES2BIO tend to be lower than those of the GMU group for all cases except eweb38, a trend that was not clearly identified previously in FD cases. Reductions between post and pre-treatment velocities are of the same order of magnitude compared to FD, with averages of 33% and 25% for WEBs and FDs, respectively. This similar reductions values could be explained by similarities in device porosity mean values

between WEBs and FDs (see Table 3.4). Errors between GMU and the heterogeneous model are below 10% for all cases, consistently with previous qualitative results, with a maximum error of 8% reached by case eweb38. This confirms that the jet direction discrepancy previously found quantitatively for eweb38 does not induce a drastic increase of intra-saccular velocities, entailing that occlusion predictions based on U_a would not have been changed by using either GMU or the heterogeneous model. These errors are in the same range as for FDs, which confirms the ability of the proposed heterogeneous model to correctly capture mean intra-saccular velocities.

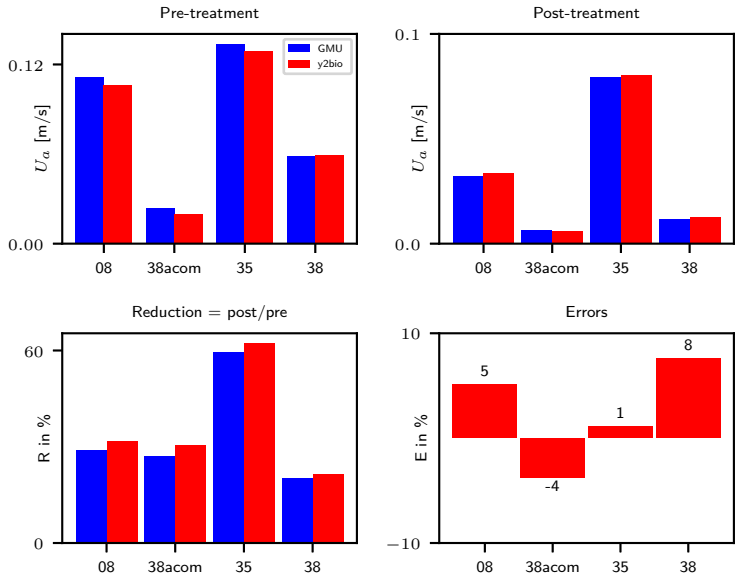

Figure 3.29: WEBs quantitative results for the U_a macroscopic metric, for both pre and post-treatment results. Post-treatment relative errors at the bottom-right corner use GMU results for reference value.

The second macroscopic index used to assess model performances is related to the positive flow-rate at the neck Q_p defined as:

$$Q_p = \int_{\Gamma_n^p} \mathbf{U} \cdot \mathbf{n} \mathrm{d}S \tag{3.4.5}$$

with $\mathbf{n}$ the neck normal, $\mathbf{U}$ the fluid velocity, $\mathrm{d}S$ the infinitesimal neck surface and Γ_n^p the neck surface domain where $\mathbf{U} \cdot \mathbf{n} > 0$. It measures the extent to which the parent artery communicates with the aneurysm sac. As for the U_a index, inflow rate Q_p has been found to correlate with treatment success and predict outcome, in particular with WEB type of devices [32]. This trend has also been recently confirmed for FDs in a meta-analysis including 5 studies correlating

hemodynamics with treatment outcome [160]. Consequently, reproducing this quantity is crucial for CFD models to correctly predict aneurysm occlusion.

Nevertheless, and for model comparison purposes only, the present inflow rate definition slightly differs from above references as we chose to study it at peak systole only, whereas it is classically time-averaged over one cardiac cycle. In addition to that, the neck plane used to compute inflow rate was manually placed downstream of the device in order to better capture the differences between models, which would not have been noticeable if the averaging plane was placed upstream. This entails that for some cases, the neck surface given by GMU team and previously described in Figure 3.14 differs drastically from the neck plane manually placed. This is particularly true for WEBs, as some deployments yielded a device located far from the aneurysm entrance (see for example cases eweb08 and eweb35 in Figure 3.15). For each case, the plane parameters (normal and origin) were chosen under the constraints it was not crossing the device (for FDs) and was as much as possible parallel to the "original" neck already delineated by GMU. Then, velocities were interpolated onto the neck plane and values for Q_p were obtained by discretization of Equation 3.4.5.

Figure 3.30 compares pre and post-treatment Q_p values between GMU, porous and IBM for all the FD cases. Results given on the top-left quadrant of Figure 3.30 show that the agreement between GMU and YALES2BIO for pre-treatment inflow rates is excellent, with slight systematic overestimations for our solver, except for case e23R. Device implantation induces reductions of inflow rate going from 57% (e14) to 24% (e35) as showed by the bottom-left quadrant of Figure 3.30. These reductions are higher than those found for U_a, probably because the inflow rate is instantaneous whereas U_a is averaged in time. Nevertheless, global tendencies are similar and the smallest reductions are found for cases e32 and e35.

Errors given on the bottom-right quadrant of Figure 3.30 were computed the same way as for U_a, namely $E = \frac{Q_p^{\text{model}} - Q_p^{\text{GMU}}}{Q_p^{\text{GMU}}}$ in percentage. Consistent with previous findings, the normal porous model (porous N) is not able to capture inflow rate correctly. Nevertheless, this is not true for case e23R for which the error is of the same order of magnitude as other models. Figure 3.31 presents a comparison between porous N and GMU velocities on the neck plane for case e23R. One can notice in Figure 3.31 that despite the velocity maps are extremely different between GMU and porous N, the normal component is conserved, thereby producing low Q_p errors. This phenomenon results from an ideal combination between neck placement and flow redirection and was not observed for other cases. This indicates that conclusions regarding model performances using only inflow-rate must be taken with great care and have to be combined with results from other indices such as U_a to be relevant.

The same tendency previously identified for U_a is found, namely that porous

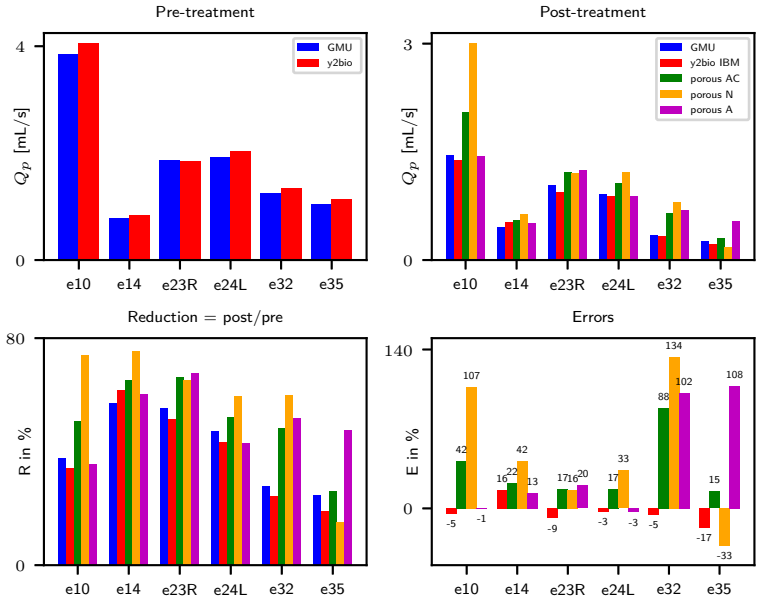

Figure 3.30: Flow-Diverters quantitative results for the Q_p macroscopic metric, for both pre and post-treatment results with all models (GMU, IBM and porous). Post-treatment relative errors at the bottom-right corner use GMU results for reference value.

AC and porous A errors are of the same order of magnitude as IBM ones for 4/6 cases and large discrepancies begin to appear for case e32 (both models) and e35 (porous A). In addition to that, porous A seems to better reproduce Q_p than porous AC as the mean error among cases (except e32 and e35) is smaller for this model. Interestingly, it is seen that the IBM framework systematically underestimates Q_p and thus produces negative errors, except for case e14. Nevertheless, the versatility of the method is demonstrated by the robustness of the results compared to porous models.

Figure 3.32 depicts Q_p results for WEB cases. Pre-treatment inflow rate Q_p values for WEBs are greater than FDs due to differences in hemodynamic environment consisting of jets for bifurcating aneurysms. As for FDs, both pre and post-treatment agreement is very good, with a maximum error reaching -20% for case eweb38acom. This high underestimation must be put in perspective by the fact that case eweb38acom exhibits the smallest post-treatment inflow value, meaning that the use of a relative error expression is sensible to small absolute changes. Contrary to FDs, the present model tends to overestimate Q_p as 3/4 errors are positive, which can be partly explained by the underestimation of normal drag forces reported in Section 2.4.2, that prevents the device from sufficiently reducing the incoming jet found in bifurcation aneurysms.

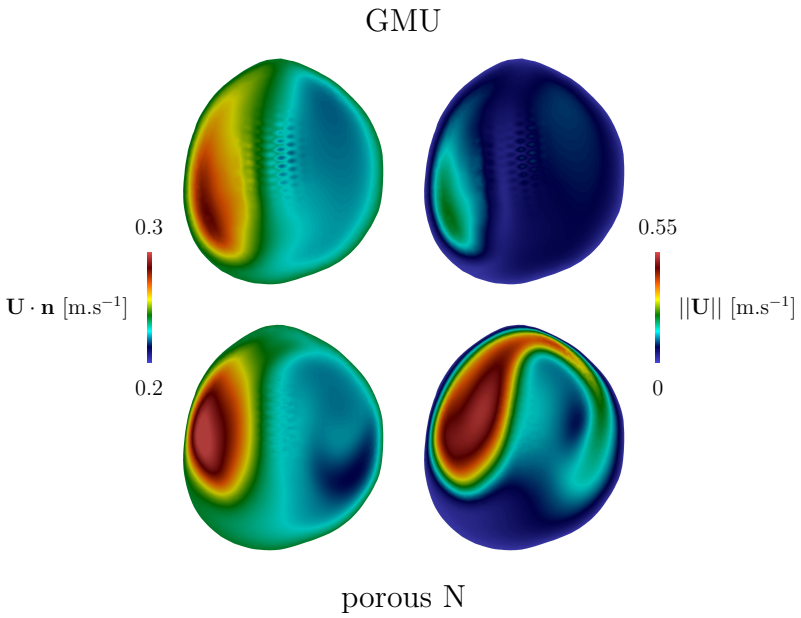

Figure 3.31: Comparison of neck-related quantities between GMU (first line) and porous N (second line) for case e23R. **Left column:** $\mathbf{U} \cdot \mathbf{n}$ map with $\mathbf{n}$ the plane normal. **Right column:** velocity magnitude.

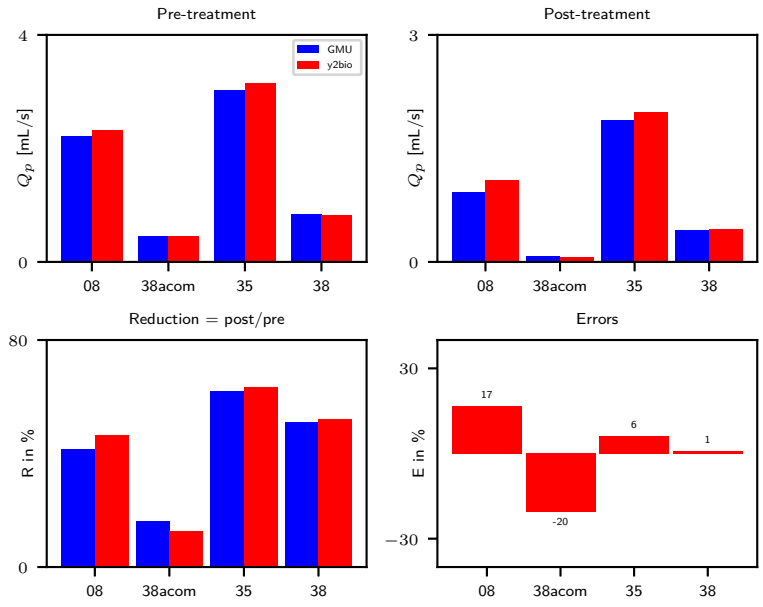

Figure 3.32: WEBs quantitative results for the Q_p macroscopic metric, for both pre and post-treatment results. Post-treatment relative errors at the bottom-right corner use GMU results for reference value.

Local comparisons During the ASME 2012 Summer Bioengineering CFD challenge [137], several CFD research groups were provided with the same arterial geometry, flow rates and fluid properties to assess variability in CFD solutions. It has been demonstrated that although the agreement between groups for pressure patterns was excellent, a high variability in flow instabilities inside the sac was identified, owing to differences in numerical solver settings and discretization schemes. This trend has been confirmed and extended on 12 aneurysmal geometries by Valen-Sendstad and Steinman [142], who demonstrated that solver settings alter significantly flow unsteadiness and advocated the use of high resolution strategies to understand aneurysm rupture mechanisms.

As GMU and YALES2BIO flow solvers present some numerical differences, most notably in the time-integration numerical schemes (see Table 3.6), it has been decided to perform local comparisons using time-averaged velocities instead of instantaneous ones. To perform point-to-point local comparisons, velocities for each model (GMU, IBM and porous) must be located on the same mesh. As YALES2BIO grids were finer than the GMU ones inside the aneurysm sac (see Figure 3.17), velocities were interpolated on GMU mesh for each case and model (porous and IBM). Interpolating from finer to coarser grid prevents oversampling and extrapolation potential errors, a situation that was unfortunately not avoided for the very fine grid elements located inside the wires envelops for GMU meshes. Interpolation between grids was performed using the vtk filter vtkResampleWithDataSet[9]. Local comparisons were performed both with and without nodes located inside the wires on GMU mesh to show the effect of interpolation oversampling.

To compare interpolated velocities, the first method that was used is linear regression, also referred to as Pearson's product moment correlation between two samples x (the reference) and y (the model). Linear regression was performed for intra-saccular values of $|| < \mathbf{U}_{\text{GMU}} > ||$ as x and $|| < \mathbf{U}_{\text{model}} > ||$ as y for each model and case. Pre-treatment velocity fields were also compared via linear regression to give an insight into numerical solver differences without any device model. The choice to study velocity magnitude rather than each component was motivated by the fact that there is no preferential direction for the flow inside intracranial geometries as they are extremely tortuous and orientated differently for each patient, and to decrease the number of quantities to compare. Linear regression is notably used to compare velocity fields between PC-MRI and CFD [119]. One of the most important index used in this method is r^2 and is given as:

$$r^2 = \left(\frac{\sigma_{xy}}{\sigma_x \sigma_y} \right)^2 \tag{3.4.6}$$

[9]https://vtk.org/doc/nightly/html/classvtkResampleWithDataSet.html

with $\sigma_x = \sqrt{\frac{1}{N}\sum_{i=1}^{N}(x_i - \overline{x})^2}$ and $\sigma_{xy} = \frac{1}{N}\sum_{i=1}^{N}(x_i - \overline{x})(y_i - \overline{y})$ the standard deviation of x and covariance of (x, y) respectively. r^2 measures the proportion of variance of y that can be explained by a linear function in the form $y = ax + b$. Therefore and in the present case, $r^2 = 1$ indicates a perfect correlation between GMU and the studied model (IBM and porous) whereas $r^2 = 0$ means that the velocity magnitude fields are completely different. Studying r^2 only is not self-sufficient since the value of a also give important informations. Notably, it enables to determine if velocities are systematically under- ($a < 1$) or overestimated ($a > 1$). Nevertheless, linear regression results must be interpreted with great care as they are very sensitive to the data distribution around the fitted line. This is referred to as the homoscedasticity assumption, which states that the variance of the errors must be constant for linear regression to provide reliable results, the error being defined as the vertical spread around the fitted line at each point [24]. Therefore, evaluating both r^2 and a values along with raw data on scatter plots is required to make relevant conclusions regarding model performances.

Figure 3.33 depicts correlations metrics (r^2, slope and intercept) for all models and FD cases, along with scatter plots comparing post-treatment intra-saccular velocities between GMU and either porous or IBM. Pre-treatment correlations are excellent for all the cases with minimum and maximum values of r^2 equal to 0.943 (e10) and 0.999 (e35), as given in Figure 3.33. The same observation is true for the slope a with 0.90 (e10) and 1.02 (e35) for minimum and maximum. This means that for equivalent mesh sizes, numerical solver differences do not seem to impact time-averaged velocities inside the sac. Studying pre-treatment correlations enables to fix a maximum value that post-treatment correlations would reach if device models were to be equivalent between our respective solvers.

Post-treatment r^2 values reported on the top line of Figure 3.33 were obtained without the nodes located inside the device wires. They correspond to the green linear fit on the scatters plots, whereas the red line represents the linear regression with all available nodes inside the aneurysm sac. For all cases and models, it has been found that removing device internal nodes from correlations computations increased r^2, indicating that oversampling has a non negligible effect on model comparisons (mean r^2 increase of 0.05 for IBM). For all cases, IBM provides both higher correlation coefficients r^2 and slopes compared to porous models A and AC. Visually inspecting scatter plots for all cases except e32 and e35 highlights the fact that porous AC underestimates velocities, which is systematic for case e23R since the linear fit is rather correct ($r^2 = 0.69$) but with a slope equals to 0.56. To a lower extent, the same behaviour is find for porous A. Concerning cases e32 and e35, high discrepancies are found for all porous models as correlations coefficients r^2 and a are very low, which is consistent with the previous quantitative results. To a smaller extent, the proposed heterogeneous model also yield low correlations

for these cases, as velocities are underestimated for e32. Conclusions regarding case e35 must be interpreted carefully as the homoscedasticity assumption is not fulfilled, as depicted by the scatter plot. In addition to that, the underestimation identified by the IBM correlation coefficients for this case is only valid for low velocities, entailing that higher velocities are correctly captured (see the scatter plot). This is essential since these velocities drive the whole flow in the aneurysm sac.

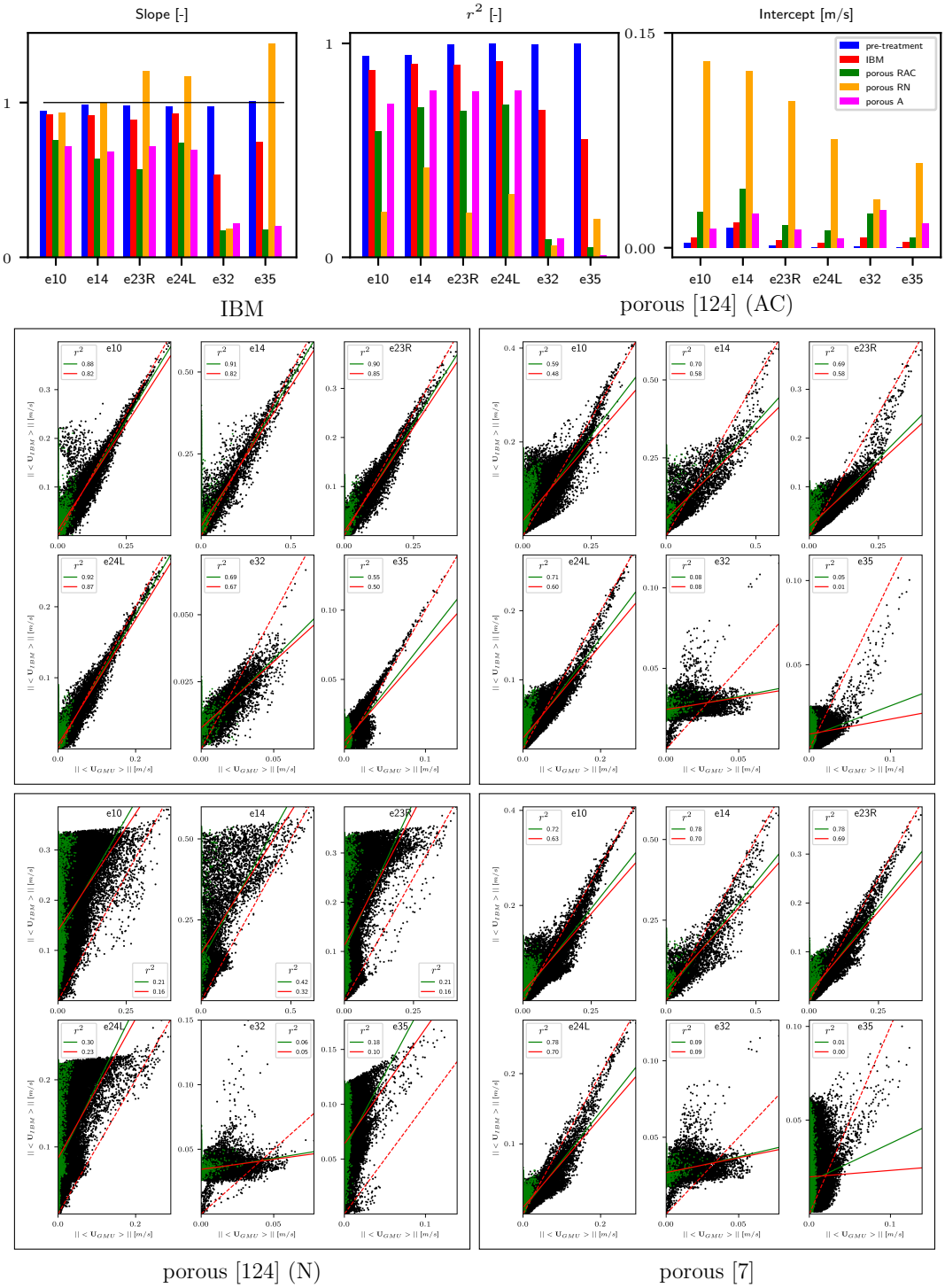

Figure 3.33: Flow-Diverters local quantitative comparisons using correlations metrics. **Top line**: correlations coefficients for each case and model. **Middle and bottom lines**: Each quadrant represent scatter plots of post-treatment velocities inside the sac. Only 1/50 of the mesh points are represented to lighten representation, red and green lines represent linear correlation fit using all the nodes inside the sac or by excluding internal wire nodes (in green), respectively. The red dashed line is the $y = x$ ideal correlation.

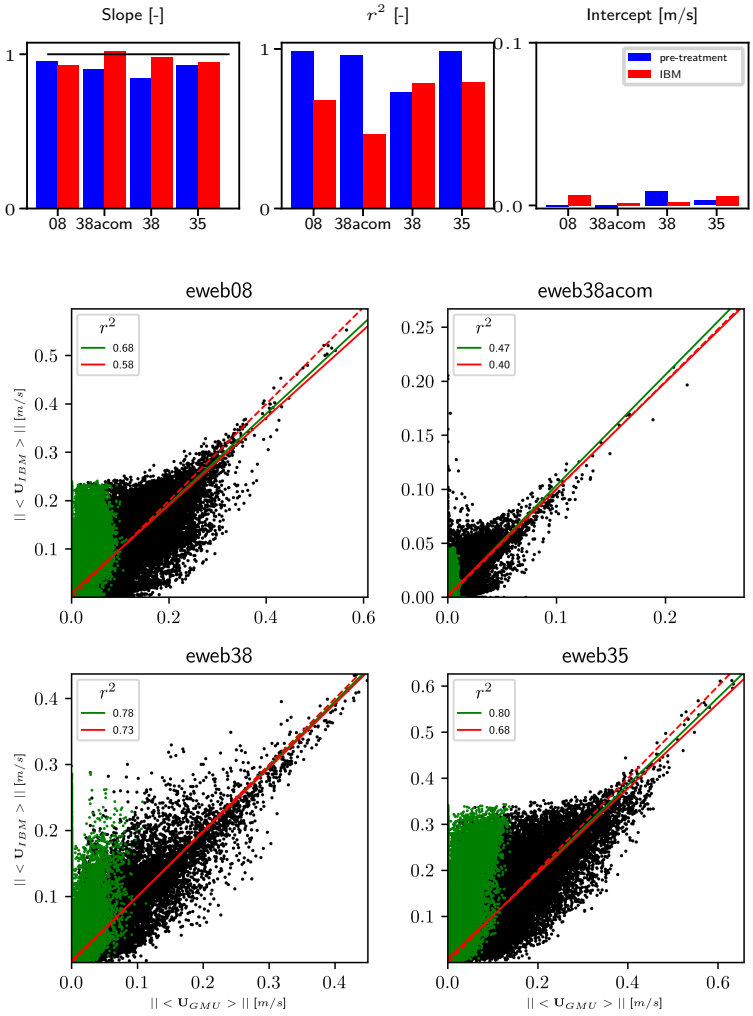

Figure 3.34: WEBs local quantitative comparisons using correlations metrics. **Top line**: correlations coefficients for each case and model. **Middle and bottom lines**: Each quadrant represent scatter plots of post-treatment velocities inside the sac. Only 1/50 of the mesh points are represented to lighten representation, red and green lines represent linear correlation fit using all the nodes inside the sac or by excluding internal wire nodes (in green), respectively. The red dashed line is the $y = x$ ideal correlation.

Figure 3.34 depicts correlations metrics (r^2, slope and intercept) for all WEB cases, along with scatter plots comparing post-treatment intra-saccular velocities between GMU and IBM. From Figure 3.34, one can see that pre-treatment correlations for WEBs are very high except for case eweb38, with $r^2 = 0.73$. Figure 3.35 presents pre-treatment correlations results and colored maps of intra-saccular velocities inside the sac of case eweb38. As depicted in Figure 3.35, velocity patterns indicate that the angle to which the parent artery jet enters

the aneurysm is underestimated for YALES2BIO results compared to GMU for this case. When interpolated and compared on the same mesh, this creates two areas: one inside which YALES2BIO velocities are high compared to GMU and vice-versa for the other area. The exact origin for these differences are yet unclear since many parameters vary between solvers such as boundary conditions (flat vs Womersley profiles, despite sufficient distance was left for the flow to establish itself), mesh number of cells and numerical discretization schemes. Nevertheless, differences in discretization order are put forward as a plausible cause. Indeed, as velocity gradients are expected to be high at the impaction site on the wall, the spatial order to which they are numerically approximated is rather important and it is hypothesized that these gradients dictate the downstream flow behaviour significantly.

WEBs post-treatment correlations r^2 values found in Figure 3.34 are lower than FDs, especially for cases eweb08 and eweb38acom (0.68 and 0.47). Nevertheless, slope values are found to be very close to 1 and the visual agreement found on scatter plots is rather good for these cases. These low values for r^2 are similar to case e35 and are induced by an inhomogeneous distribution of velocities inside the sampling interval, as most points lie in the low velocities part. Such patterns are not found for cases eweb38 and eweb35, as r^2 values are higher, 0.78 and 0.8 respectively, and distributions are more homogeneous (see the scatter plots). It should be noted that the mean increase of r^2 values due to internal device points removal is higher than for FDs cases (0.085 compared to 0.05), due to the fact that the aneurysm delineation step kept a high proportion of mesh points internal to intra-saccular device wires.

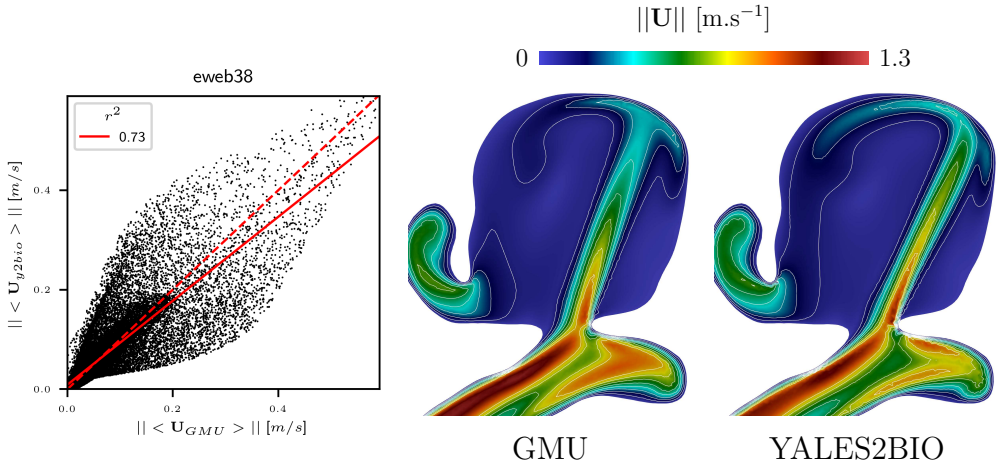

Figure 3.35: Pre-treatment correlation results for case eweb38. **Left**: Scatter plot of time-averaged intra-saccular velocities. **Right**: Peak-systolic velocity field for both GMU and YALES2BIO solvers.

Despite being useful to show tendencies, estimating errors between models with linear regression is tedious as r^2 cannot be considered as an error measurement. Therefore, and to complement the above correlations conclusions, the relative error E between each model for interpolated velocities inside the aneurysm was computed as:

$$E = \frac{1}{V_a} \int_{\Omega_a} \frac{|| < \mathbf{U}_{\text{model}} > - < \mathbf{U}_{\text{GMU}} > ||}{U_a^{\text{GMU}}} \text{d}V \times 100 \tag{3.4.7}$$

with V_a and Ω_a defined as in Equation 3.4.4. It should be noted that the nodes located inside the wires were removed from post-treatment errors computations in an attempt to reduce uncertainties due to interpolation oversampling at these locations. Compared to linear regression that used velocity magnitude as metrics, E is expected to be more sensitive to differences in speed direction as it directly compares velocity vectors component-wise. Velocity U_a^{GMU} serves to normalize the absolute error and was computed using post-treatment velocities for post-treatment errors, and vice-versa for pre-treatment comparisons. Nevertheless, it remains questionable to use GMU results as reference for pre-treatment computations, for which the terminology "error" might be changed to "difference" in an attempt to emphasize that no solver can be considered as the reference.

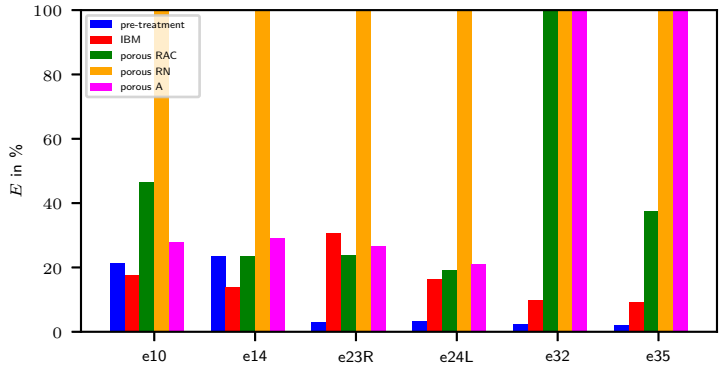

Figure 3.36: Flow-Diverters local quantitative comparisons using error metric E Equation 3.4.7 for each case and model, compared to GMU results.

Figure 3.36 presents the error E given by Equation 3.4.7 for all FD cases and computational models (porous and IBM). From Figure 3.36, the first finding is that the errors for pre-treatment velocities are very low (below 4%) for all cases except for e10 and e14, with errors reaching 21% and 23% respectively. Looking more carefully into contours for case e10 provided in Figure 3.37, it appears that this large error is caused by differences in the angle to which the incoming jet enters the aneurysm. Compared to GMU, the upstream jet obtained with

YALES2BIO is less deflected by the arterial wall located near the bleb. Therefore, this creates an area of high velocities that does not exist in GMU velocity field, thereby increasing errors locally (see the right image in Figure 3.37). These differences in jet angles are very similar to the ones already identified in pre-treatment velocities for case eweb38 (see Figure 3.35) and for which differences in spatial numerical order were identified to be a plausible cause. The exact same phenomenon was observed for case e14 due to a high jet magnitude (the highest in the whole FD cohort) that separates at the aneurysm neck (see Figure 3.21), creating an area of high gradients in this region that are not predicted similarly between solvers. Nevertheless, no further investigations were performed for these cases as velocity patterns and mean values inside the sac were very similar for both solvers. This emphasizes that the error E is extremely sensitive to differences in jets, which are greatly reduced by devices. Therefore, it is expected that post-treatment errors will be mostly located in jetting-flows between the struts, which are intended to be captured by the heterogeneous model.

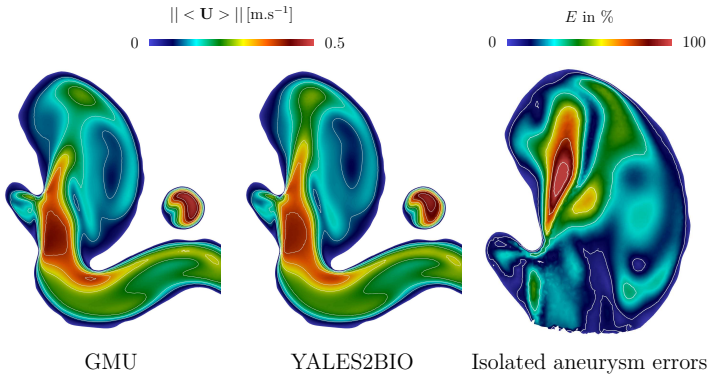

Figure 3.37: Pre-treatment errors and magnitude of time-averaged velocity for case e10.

Figure 3.36 also displays the errors associated with the porous models. Porous A and AC errors are roughly equivalent for all cases, except for case e10 where porous A outperforms porous AC (27% vs 46%) and for case e35 where it is the opposite (157% vs 37%). This trend is consistent with both U_a and Q_p errors given by Figure 3.28 and Figure 3.30, respectively. Apart from case e23R, the IBM framework introduced in this thesis yields errors smaller than 20%, which are below all porous models. IBM errors are particularly low for cases e32 and e35 (below 10%) which is not the case for all porous models as velocities discrepancies are high for these cases.

Qualitative discrepancies in case e23R for the IBM model, which were already detected at peak-systole in Figure 3.22, are recovered quantitatively in Figure 3.36 with an error going up to 30%. Interestingly, these differences were not detected

by neither U_a and Q_p errors nor by linear regression as IBM outperformed all porous models according to these metrics, for this case. Only a metric comparing directly velocity vectors and not norms and projections identifies this discrepancy. Therefore, this stresses the need to use multiple metrics to compare velocity fields between numerical methods, as some of them might be of interest but could hide important differences due to their definition and usage.

IBM qualitative results for case e23R showed that local velocity redirection caused by the device is overestimated, meaning that planar drag forces are too high and straighten struts jetting-flows more than GMU. This is coherent with findings from Section 2.4.2, *i.e.* that both tangential and longitudinal drag force components are overestimated compared to forces in conformal simulations. This redirection overestimation is present for all other cases, but e23R harbours several differences that magnify this overestimation. First, wires density is relatively high at the neck (0.58 of porosity), thereby increasing the errors at the neck. Second, the impacting jet is almost parallel to the device on wide areas of the neck. This means that both tangential and longitudinal drag force components, which suffer from overestimations compared to conformal, are predominant for these locations. Finally, since velocities are low inside the sac, the downstream flow is highly impacted by the local velocity patterns created when the jet crosses the device struts. Therefore, when combined, all these factors induce that despite IBM reproduces well the velocity magnitude, velocity direction is different from that of GMU. Unlike IBM, porous model errors, which are of the same order of magnitude as IBM ones (porous AC 23% and porous A 26%) are attributed to velocity magnitude differences compared to GMU, as redirection seemed to be well captured by these models (see Figure 3.22).

Nevertheless, conclusions regarding errors for case e23R must be taken with great care as there exists significant velocity differences upstream of the aneurysm and the device. As showed in the top of Figure 3.38 for the YALES2BIO (IBM) solution, the jet impacting the device contains lower velocities compared to that of GMU (small white $*$ symbols). For the same inter-wire distance and angle of attack, it has been found in Section 3.1.2 that the local redirection angle is increasing as the upstream Reynolds number decreases (see Figure 3.4). Therefore, this can partly explain why IBM wires, which are subjected to a lower incoming flow compared to GMU, redirect more the jetting-flows towards the aneurysm dome. Upstream differences were also found for pre-treatment velocities in case e23R. To a lesser extent, this trend is present for case e24L as showed on the bottom of Figure 3.38 (small white $*$ symbols), with less impact on post-treatment IBM error (16%).

The exact origins for these upstream discrepancies are still not completely understood. They are probably caused by differences in solver numerical schemes

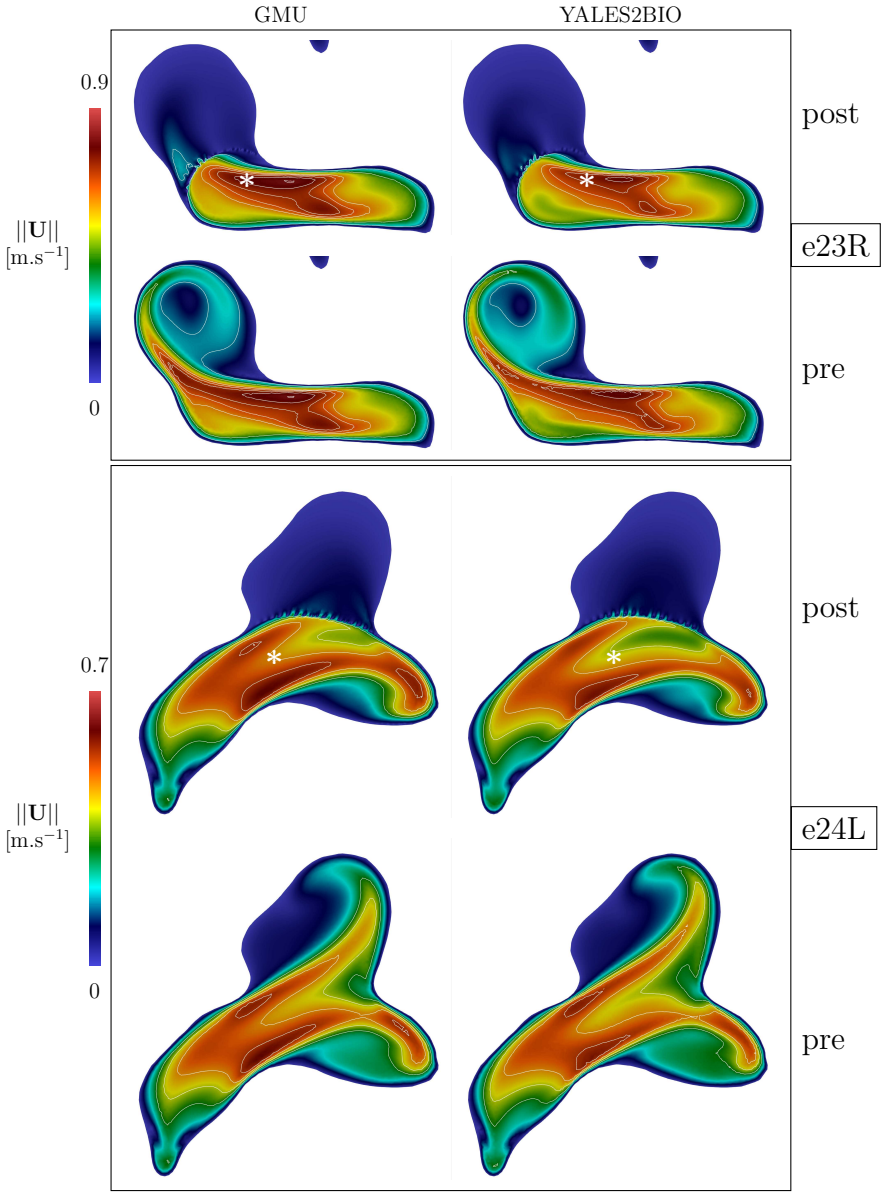

Figure 3.38: Upstream differences at peak systole between GMU and YALES2BIO results for 2 specific FD cases.

and/or inflow boundary condition (flat vs Womersley for GMU) despite a long distance was left for the flow to establish through tortuous artery sections. This emphasize that the terminology "error" might not be adequate as we are comparing two different solvers, and could be replaced by "difference" to mitigate comparisons. It should also be pointed out that "real" conformal computations performed by both teams could discriminate errors coming from solver differences and those coming from device model, but this was not further considered as it would require too much computational resources and since post-treatment errors

were judged to be acceptable between our respective models.

Figure 3.39 presents the error E given by Equation 3.4.7 for all WEB cases. The analysis is going to be conducted without considering case eweb38 for now, which will be dealt with later. Pre-treatment errors are of the same order of magnitude as FDs, with a maximum value of 25% reached for case eweb38acom, which is attributed to inlet velocity profiles differences (flat vs Womersley) since the inlet location is close to the aneurysm sac for this case, yielding a difference in jet diffusion inside the sac. Qualitative differences found for case eweb08 in Figure 3.27, namely an overestimation of velocity redirection inside the sac close to the device, are recovered here with a post-treatment error reaching 23%. Post-treatment errors for cases eweb38acom and eweb35 are either smaller or roughly equal to pre-treatment ones and confirm the correct agreement trends already identified in previous sections.

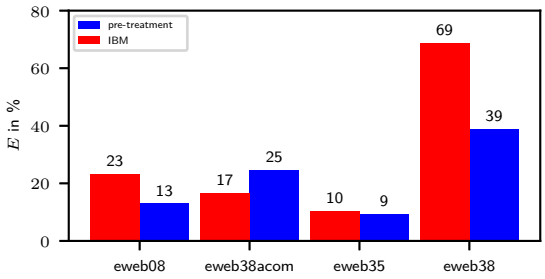

Figure 3.39: WEBs local quantitative comparisons using error metric E Equation 3.4.7 for each case and model, compared to GMU results.

As already discussed previously, pre-treatment errors found for case eweb38 are caused by jet angle differences between flow solvers, which induce an error as high as 39%. Nevertheless, post-treatment errors are also elevated (69%) as the jet originating from protruding wires is inducing a different flow recirculation inside the sac compared to GMU, with area of high errors where the jets do not coincide (see Figure 3.27). These errors can be attributed to multiple factors. First, the error definition Equation 3.4.7 uses the GMU averaged velocity to obtain a relative number, the latter being extremely low ($0.01\,\mathrm{m.s^{-1}}$) which magnifies small absolute differences. Secondly, it has been proven that heterogeneous model performances for densely packed wires are low, the latter situation being found at the protruding wires where the jet originates (see Figure 3.40). Third, device deployment yields unrealistic wires positioning out of the artery that further re-enter through the bifurcation section, as depicted by Figure 3.40. This entails that some underlying hypotheses used to build the model, most notably hypothesis H1 and H3, are not satisfied (see Section 2.2.1). H1 stated that device curvature can be neglected, which is not possible as the angle between wires approaches 90°

near protruding wires (see the white $*$ symbol in Figure 3.40). H3 claimed that wires are immersed and isolated at the neck, a situation not met due to wires proximity with both the bifurcation site and parent artery wall. In addition to that, undisturbed velocity reconstruction hypotheses are also violated since wires local curvature was not taken into account when building the reconstruction algorithm in Section 3.1. Finally, respective meshing strategies yield a decrease in mesh sizes near the bifurcation site for the heterogeneous model (see the black $*$ symbol on the bottom of Figure 3.40), a location which has already been proven to induce near-wall gradients differences between our respective CFD codes without any device (see Figure 3.35).

In conclusion, we do not recommend to use the heterogeneous model for such kind of extreme situations, which could have been avoided using more realistic numerical deployment algorithms that prevent major wires protrusion outside both the aneurysm and the parent artery. Nevertheless, a reassuring point is that despite the jet direction is different inside the sac, its intensity is similar and produces low errors for both Q_p and U_a metrics, inducing that occlusion predictions using these indices coming from the present model would not have been changed compared to GMU ones.

3.5 Conclusion

This chapter presented extensive patient-specific validations with steady conformal results coming from our team in Section 3.3 and pulsatile from GMU team in Section 3.4. Good qualitative and quantitative comparisons were obtained for all GMU flow-diverter cases and the model has proven to be better or equivalent to all porous model implementations. More importantly, model versatility and robustness has been demonstrated for two FDs cases (e32 and e35), as porous models exhibited high errors and bad qualitative agreement for these cases, which was not true for the heterogeneous framework as errors were of the same order of magnitude compared to other FDs samples. This is of importance since these two FDs geometries are representative of typical non-apposed situations that proved to be associated to bad outcomes in both in vivo [128] and in silico studies [102], entailing that the present model is able to both predict and potentially provide understanding of mechanisms leading to bad outcome status as opposed to porous models.

We have also demonstrated that performing comparisons between two different CFD codes (GMU and YALES2BIO) and device models is challenging since flow discrepancies can be found upstream to the region of interest, *i.e.* the aneurysm, and induce differences that can be amplified due to very low post-treatment velocities. Nevertheless, investigating the exact mechanisms responsi-

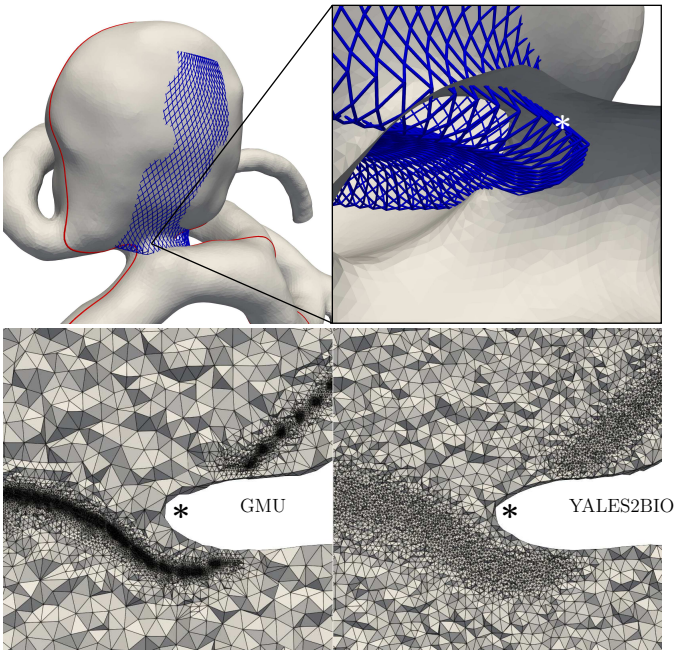

Figure 3.40: Case eweb38 specificities that have most probably induced high errors for the heterogeneous model. **Top:** device deployment protrusion outside the aneurysm and ostium containing high curvature device portions (see the white $*$ symbol), yielding that some heterogeneous model building hypotheses collapse (namely H1 and H3 in Section 2.2.1). **Bottom:** differences in mesh resolutions near the bifurcation ostium. The slice location used to compare mesh sizes is depicted in red on the arterial surface on the top-left corner.

ble for these upstream discrepancies has not been conducted as it proved to be unnecessary to achieve satisfactory comparisons. This stresses the need, when comparing two CFD solvers, to eliminate as much as possible variabilities that are not of primary interest, for example differences in numerical scheme orders, to focus on the only variability source of concern, in the present case the numerical handling of endovascular device and its effect on the flow. Moreover, we also emphasized that comparisons between solutions from different solvers must not rely on a single index, *i.e.* preventing that all your eggs are in the same basket, as some discrepancies were not detected by "classical" macroscopic measures such as mean intra-saccular velocity.

Finally, as one of the motivations for building the heterogeneous model was computational costs reduction, the latter was assessed for the steady validation only in Section 3.3, demonstrating drastic decrease in both memory consumption and effective computational time, the latter originating from time-step increase in the present model. Computational cost comparison was not conducted for pulsatile validation. However, we expect that the drastic reduction in number of

cells for the present framework, as reported in Table 3.5, by almost an order of magnitude would reduce random access memory consumption as well as storage burden.

This chapter has also seen the successful application of the heterogeneous model to a novel type of endovascular device that was not tackled in the literature by no other means than conformal computations due to its complex design: intra-saccular Woven EndoBridge (WEB). Despite excellent comparisons were found for 3/4 WEB geometries, one case (eweb38) demonstrated that when being used outside its building hypothesis framework, the proposed model produces large errors. Therefore, we recommend to use it only when "realistic" device deployment is obtained, which was not the case for case eweb38. This further emphasizes that when being used under its hypotheses, the heterogeneous model versatility is able to correctly account for various device types. This builds confidence in model usage for this type of devices, which is conducted in the next chapter.

Chapter 4

Heterogeneous model application to intrasaccular device

Chapter contents

Previous chapters introduced and validated the heterogeneous model developed during this thesis, demonstrating its versatility to capture very detailed flow features for various patient-specific geometries and more importantly, for different types of braided devices, *i.e.* flow-diverters (FDs) and intra-saccular (WEBs). In this chapter, the model aims at being used for a concrete application: retrospectively studying how intra-saccular WEB affect hemodynamics inside bifurcating

aneurysms and attempting to predict angiographic outcome using both geometrical and flow indices for a wide variety of cases.

To the knowledge of the authors, there exists only one CFD study in the literature dedicated to outcome prediction for WEB-treated aneurysms with $N = 36$ cases, owing both to the recency of the WEB device and their complex shape [32]. Therefore, this work is here as a further exploration: the number of cases is of the same order and constitutes a pilot study calling for adding more cases. This limitation, among others, is discussed later. Consequently, this chapter is dedicated to the description of flow features captured by the model in such geometries and devices rather than finding robust correlations between occlusion score and hemodynamic parameters in this context.

4.1 Introduction

The last decade has seen the emergence of a new kind of braided device intended to treat wide-neck bifurcation aneurysms (WNBAs): the Woven EndoBridge (WEB) device (MicroVention/Sequent Medical, Aliso Viejo, California, USA). Broadly speaking, its design consists of a short flow-diverter whose wires have been regrouped at both ends using a radio opaque marker cylinder (red circles in Figure 4.2), referred to as the recess region. It is inserted inside a catheter and delivered inside the aneurysm sac, as depicted in the right of Figure 4.1. A major advantage of such devices is that once fully deployed, the proximal marker is still attached to the catheter (see Figure 4.1), providing that re-sheathing is possible to either correct the apposition or elect another device size.

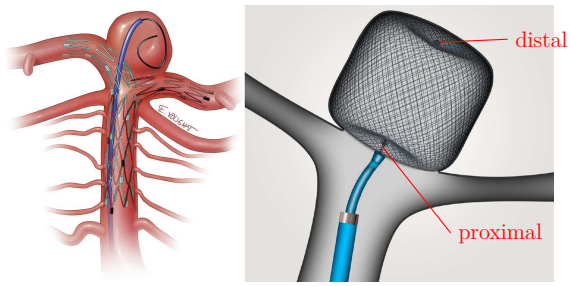

Figure 4.1: Treatment options for WNBAs: stent assisted coiling and intrasaccular WEB (left and right respectively). Images taken and modified from [1, 51].

The first design of WEB consisted of a superposition of two braiding layers and was referred to as Double Layer (DL, see the left of Figure 4.2). To enhance catheter navigability through the arterial network and subsequent delivery, single-layered versions (SL and SLS for spherical shape) were introduced in 2013 in

Europe, containing from 144 to 216 wires of approximately 20 µm in diameter [22]. The exact number of wires for each device size, as well as the exact value for strut width, were not communicated by the manufacturer. Therefore, it has been chosen to fix these values to 144 wires of 20 µm in diameter in following sections. Due to the high concentration of wires at the proximal recess, these devices are likely to disrupt blood flow at this location, which is not possible with FDs as porosity values slightly vary across the aneurysm neck.

It should be noted that single layered WEB versions (SL and SLS) are majorly used nowadays since they provide equal safety results compared to Dual Layers [22, 89] but with easier navigability and delivery characteristics, especially for distal aneurysms that require small catheters. On the contrary to endoluminal devices such as FDs and stents, WEBs are deployed inside the aneurysm sac, entailing that anti-platelet therapy is not mandatory for these devices due to a lower risk of thromboembolism [49]. Nevertheless, Caroff et al. [22] reported that anti-platelet treatment was prescribed for 67% of patients due to device protrusion inside the parent artery, *i.e.* proximal sections of the device emerging from the aneurysm sac, which were either corrected with balloon remodelling or stent placement or closely monitored, depending on the degree of protrusion judged by the clinician.

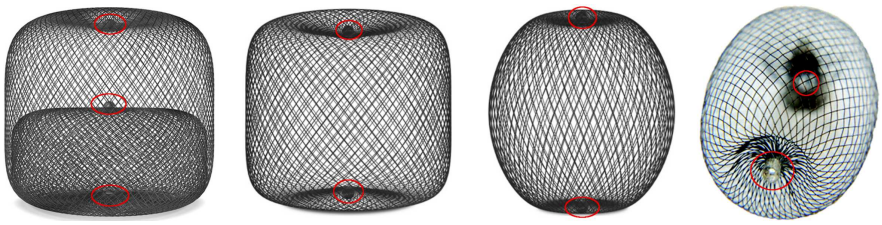

Figure 4.2: WEB device close-up views for each design. Images have been taken and modified from [22, 49, 84].

Despite complete occlusion rates were found to be approximately equal to 80% [20, 89] with very low procedure-related complications (13% according to Caroff et al. [22]), it has been noticed in the earliest stages of WEB usage that approximately 50% of WEB treated aneurysms exhibited a shape modification, denoted as WSM for WEB Shape Modification [40]. WSM consists of either a deepening or a spacing of device radio-opaque markers, and is clearly visible in follow-up medical images as exemplified in Figure 4.3a. Very recently, Ding et al. [48] demonstrated with rabbits as animal model that aneurysms treated by WEBs that WSM was closely linked to the presence of organized thrombus inside the sac (see Figure 4.3b). More specifically, Ding et al. showed that intra-saccular levels of smooth muscle actin and fibrosis were positively correlated with WSM,

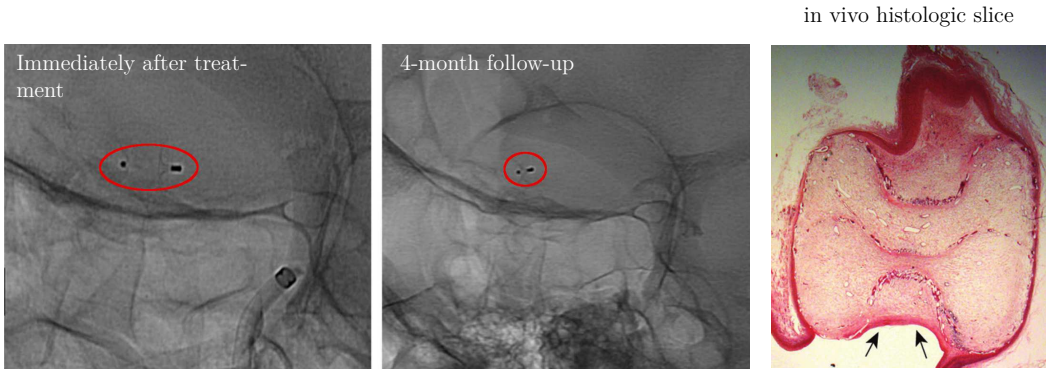

(a) (b)

Figure 4.3: WEB shape modification examples. **a:** Medical follow-up images showing radio opaque markers getting closer togther after 4 months. Taken and modified from [40]. **b:** Histologic slice inside an rabbit aneurysm treated by a DL WEB, demonstrating the thrombus organization inside the sac as well as the WEB compression of recess sections. Taken and modified from [48].

irrespectively of device type (DL, SL and SLS). In addition to that, no correlations between WSM and follow-up occlusion score were found by Ding et al., a finding recently confirmed by Cagnazzo et al. [20] who also found that shape modifications were more likely to occur for aneurysms containing irregularities (blebs or multilobular shape) and large ostium dimensions, confounder variables being taken into account.

In the first in silico CFD study dedicated to outcome prediction for WEBs, Caroff et al. [23] reported that WSM can be predicted via the use of CFD simulations without any virtual device implantation, *i.e.* only with pre-treatment velocity fields. They notably found that the inflow ratio, *i.e.* the ratio of inflow rate between parent and ostium surfaces, was significantly higher for cases harbouring WSM. Caroff et al.'s conclusions entail that hemodynamics might have a crucial role in inducing such shape modifications but most authors point out that the mechanisms underlying WSM are complex and multifactorial.

In an attempt to predict outcome for WEB treated aneurysms, several studies have been conducted using either in vivo or in silico data. For example, Cagnazzo et al. [20] used follow-up images on 86 cases to demonstrate that similarly to WSM, occlusion rates were significantly lower for irregular aneurysms and wide ostium cases. To quantify in vivo the hemodynamics impact of WEBs, Gölitz et al. [60] recently conducted a series of measurements of the intensity of contrast material flowing through the sac region of interest (ROI) manually delineated, both before and after treatment. By analysing time-density curves (TDC), they managed to quantify macroscopic hemodynamics variables such as

inflow and outflow wash-in/out inside the ROI. Despite noticing a significant decrease of TDC-derived indices between pre and post-treatment groups, no flow parameter differences were found to effectively dichotomize complete and incomplete occlusion groups.

In addition to show that WSM was linked to hemodynamics neck derived quantities, Caroff et al. [23] observed a tendency for smaller inflow ratios between occluded and non occluded groups, despite not reaching statistically significance probably due to the low number of cases ($N = 19$). Nevertheless, hemodynamics alterations caused by WEBs are not reported by Caroff et al. [23] since they only used pre-treatment velocity fields, entailing that a full comprehension of the link between hemodynamics and occlusion is not entirely possible using their results.

A very recent in silico study conducted by Cebral et al. [32] on 36 WEB treated aneurysms demonstrated, using both hemodynamics results from CFD computations and geometrical measurements, that outcome score varies significantly with aneurysm and ostium sizes, similarly as in Cagnazzo et al. [20] for the latter. More importantly, Cebral et al. discovered that incomplete occlusion can also be predicted by hemodynamics neck related quantities such as post-treatment inflow rate and its reduction compared to pre-treatment. Interestingly, hemodynamics significant variables were found to be of equally importance to geometrical ones (neck and aneurysm size) to efficiently predict aneurysm occlusion with WEBs.

Previous paragraphs indicate that the exact underlying mechanisms responsible for either WSM or correct occlusion are not fully understood yet, on the one hand because such devices have been recently introduced, and on the other hand because performing in silico modelling with such devices is extremely complex due to their design that induce both tedious deployment strategies and high computational resources needed to resolve the high number of wires at the recess [32, 103]. These concerns act as supplementary motivations to develop faithful computational strategies at reduced costs such as the one developed in this thesis, which is why it has been decided to illustrate the model capabilities in situations were it is most needed.

4.2 Methods

4.2.1 Patient-specific database

A collaboration between our research group and Dr. Daniel Eduardo Mantilla García, interventional neuroradiologist from FOSCAL Clinic, Bucaramanga, Colombia was established. Between 2014 and 2017, Dr. Mantilla treated intracranial aneurysms using WEBs at the neuro-interventional radiology service of CHU Gui-de-Chauliac, Montpellier and provided us access to an anonymised database

of cases. Only Dr. Mantilla, under the authority of CHU Gui-de-Chauliac, had access to the database containing non-anonymised data. Our research group received and manipulated only anonymised and transformed data such as arterial surfaces reconstructed from raw imaging and 3D geometries of deployed devices. The present study was observational and retrospective: no modification of the clinical protocol was induced and the selection of the implanted device was unchanged. Among all cases available in the database, the following inclusion criteria were applied:

- patients of age above 18 years old
- patients harbouring an intracranial aneurysm
- patients treated by a single WEB device
- DICOM 3D series data available in the database
- angiographic follow-up available
- unruptured and ruptured aneurysms

Cases with poor image quality, either follow-up ones or 3D DICOM, were discarded by visual inspections. To focus onto hemodynamics effects caused by WEBs alone and to prevent any bias, cases harbouring other deployed medical devices such as FDs, stents or coils were excluded from this study. For each case extracted from the database, the following data were retrieved:

- DICOM 3D series data before WEB implantation
- DSA follow-up score (BOSS, described in Section 4.3.2)
- age and sex of the patient
- deployed WEB parameters: diameter and height
- aneurysm location (ICA, MCA, basilar, vertebral)
- if available, hypertension and smoking comorbidities
- if available, interventional details such as the size of deployed but not detached WEB devices

Among all cases present in the database, a total of 27 arterial geometries were included in the present study. Implanted device characteristics as well as aneurysm location and occlusion score are given in Table 4.1 for each case. A wide majority (60%) of treated aneurysms were found in the Middle Cerebral

Artery (MCA), a location known to be prone to bifurcation aneurysms [161]. Only Single-Layered WEB versions (SL and SLS) were used during all surgical procedures and 70% of patients were women. The proportion of incomplete occlusion observed in the present cohort is 22%, which is line with results found in the litterature [20]. Therefore, due to the relatively low number of cases and the imbalance in number of patients inside each occlusion group, statistical conclusions must be taken with great care.

Case id	Aneurysm location	WEB type and size	Patient sex	Patient age	Follow-up delay	Outcome	Hypertension	Smoking
2	MCA	SL 8x4	M	55	9	c	0	0
3	MCA	SL 7x4	F	85	3	c	1	1
4	ICA	SL 7x5	M	50	4	c	1	1
6	ACOM	SL 9x4	M	56	12	d	N/A	N/A
10	ICA	SL 6x4	M	74	12	b	1	1
12	MCA	SLS 10	F	69	13	b	1	1
14	MCA	SL 10x6	F	35	15	f	1	1
15	MCA	SL 11x6	F	53	5	c	1	1
16	ICA	SL 9x7	F	72	15	b	1	1
17	ACOM	SL 7x4	F	69	19	c	1	1
18	MCA	SL 7x5	F	70	5	c	1	1
20	MCA	SL 7x5	M	59	10	c	0	1
21	BA	SLS 7	F	55	12	c	0	1
23	BA	SLS 9	F	44	4	f	N/A	N/A
24	BA	SL 7x3	F	83	13	b	1	1
25	ICA	SL 7x5	M	59	6	b	0	1
26	MCA	SL 8x6	F	57	26	f	1	1
27	MCA	SL 10x6	F	44	12	f	1	1
31	MCA	SL 10x7	F	62	8	b	0	1
35	MCA	SL 7x3	M	53	9	b	1	1
37	ACOM	SL 4x3	F	62	13	b	1	1
38	MCA	SL 5x3	M	56	13	c	1	1
39	MCA	SL 7x3	F	54	10	b	1	0
41	MCA	SL 6x3	F	60	14	c	1	1
43	BA	SL 6x3	F	74	26	b	1	1
44	MCA	SL 4x3	F	69	21	b	1	1
46	MCA	SL 9x4	F	51	12	d	1	1

Table 4.1: Device and aneurysm characteristics extracted from the database. **ACOM**: Anterior Communicating artery. **ICA**: Internal Carotid Artery. **MCA**: Middle Cerebral Artery. **BA**: Basilar Artery. Device size is expressed as Diameter x Height in mm and follow-up time is in months. Occlusion score were chosen according to the BOSS classification detailed later in Section 4.3.2.

4.2.2 Numerical device deployment

Retrospectively using 3D DICOM images obtained during the surgical intervention, Dr. Mantilla numerically deployed the same WEB reference implanted inside the patient using the Sim&Size® software (Sim&Cure, Montpellier, France), which major steps are depicted in Figure 4.4. Arterial surface reconstruction using the Marching Cubes technique [88] is performed by the software, and the

threshold value used to determine if a given voxel is lying either inside, across or outside the artery is manually chosen by the operator until visual satisfaction with grey-scale levels is reached. This step is illustrated in Figure 4.4a.

Then, a centerline from the neck-center to the user-defined dome is created and the device reference is manually placed along that path, see Figure 4.4b. Accordingly to clinical recommendations, initial position for numerical deployment was chosen to be close to the neck surface. Numerical deployment is then performed using the internal Sim&Size® mechanical solver that resolves the solid contact between wires and arterial surface. Solver verification and validation was performed by comparing in vivo and in silico deployments. Results and conclusions can be found in the technical file used to obtain both the FDA clearance and CE mark.

Finally, visual inspection of the deformed device with arterial apposition colormap is available in the software GUI to qualitatively assess the deployment and redo it until satisfaction is reached (see Figure 4.4c). It should be stressed that the final position of the in silico device given by Sim&Size® was not directly compared to in vivo data in the present cohort, which is very difficult to quantitatively perform using medical images. Nevertheless, this issue was thought to be mitigated by the fact that the agreement with in vivo data observed during solver validation and verification was correct and by the fact that clinical recommendations followed during interventional procedures (*i.e.* initial release close to the neck) were also used during the in silico deployment.

According to Caroff et al. [22], the total number of wires inside WEBs is increasing with device size from 144 to 216 wires of 20 µm in diameter. Nevertheless, as the exact number of wires per reference was not communicated by the manufacturer, we decided to use 144 wires irrespectively of device size for each deployment in an attempt to homogenize conclusions. The choice to use the lowest number of wires (144) among references was motivated by the intent to reduce computational costs, but more importantly to prevent artificial hemodynamics overestimations caused by a simulated number of wires that could potentially be greater than the one which was really implanted inside the patient.

4.2.3 Arterial surface pre-processing

For each case, the arterial surface used by the mechanical solver as well as the final step of device deformation were outputted by Sim&Size® to be used as inputs to the following CFD computations. Semi-automatic cleaning of the arterial surface mesh was carried out using custom python scripts based onto the vmtk library [4]. Small adjacent arteries as well as surface fusions due to imaging artefacts were firstly manually removed. Then, holes filling as well as addition of inlet and outlet extensions were automatically performed. Finally, two surface remeshing steps

a: Threshold value choice for surface reconstruction

b: Device placement along neck-to-dome centerline

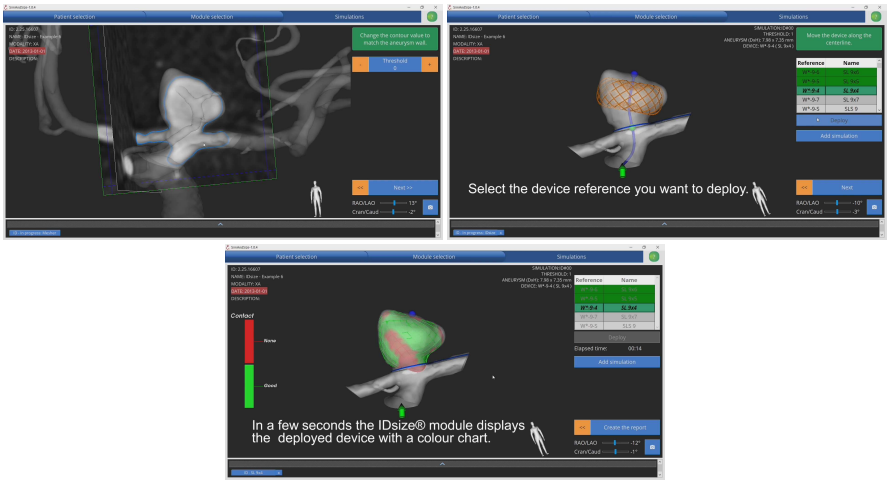

c: Apposition and deformation visualization

Figure 4.4: Sim&Size® steps for WEB device deployment. Taken from https://sim-and-cure.com/.

were carried-out: a first one intended to refine the full surface towards a single value of approximately 0.2 mm, and a second one using distance to centerlines as mesh size constraint to keep a constant number of elements across arterial diameters. During the second step, computation of the mesh size scalar field was constrained with a minimum function using the first step value sizes in order to prevent any mesh coarsening at the aneurysm surface, since portions at the dome of the aneurysm are far from centerlines locations. These successive remeshing steps entail that the mesh size at the aneurysm surface is kept at the value previously prescribed in the first step (0.2 mm), a value which has been found to be sufficient for high-order solvers to yield realistics results [72]. Nevertheless, in the case of small aneurysm dimensions, visual inspection of the surface mesh was done to determine if a subsequent refining step was necessary on a case-by-case basis. Finally, surface smoothing was carried-out, visually checked and potentially redone until satisfaction was reached.

Arterial cleaned surfaces as well as deployed device are depicted in Figure 4.5 for all cases included in this study. Several cases, such as n14, n27 and n15 exhibit a device compression due to an oversizing while others such as n20, n35 and n44 are not filling the entire aneurysm sac due to either an elongated shape (n20, n35) or a sac constriction (n44). Pronounced proximal device protrusion is found in cases n12, n16, n23, n26, n37, and n46 and all cases contain irregularities on the aneurysm sac surface.

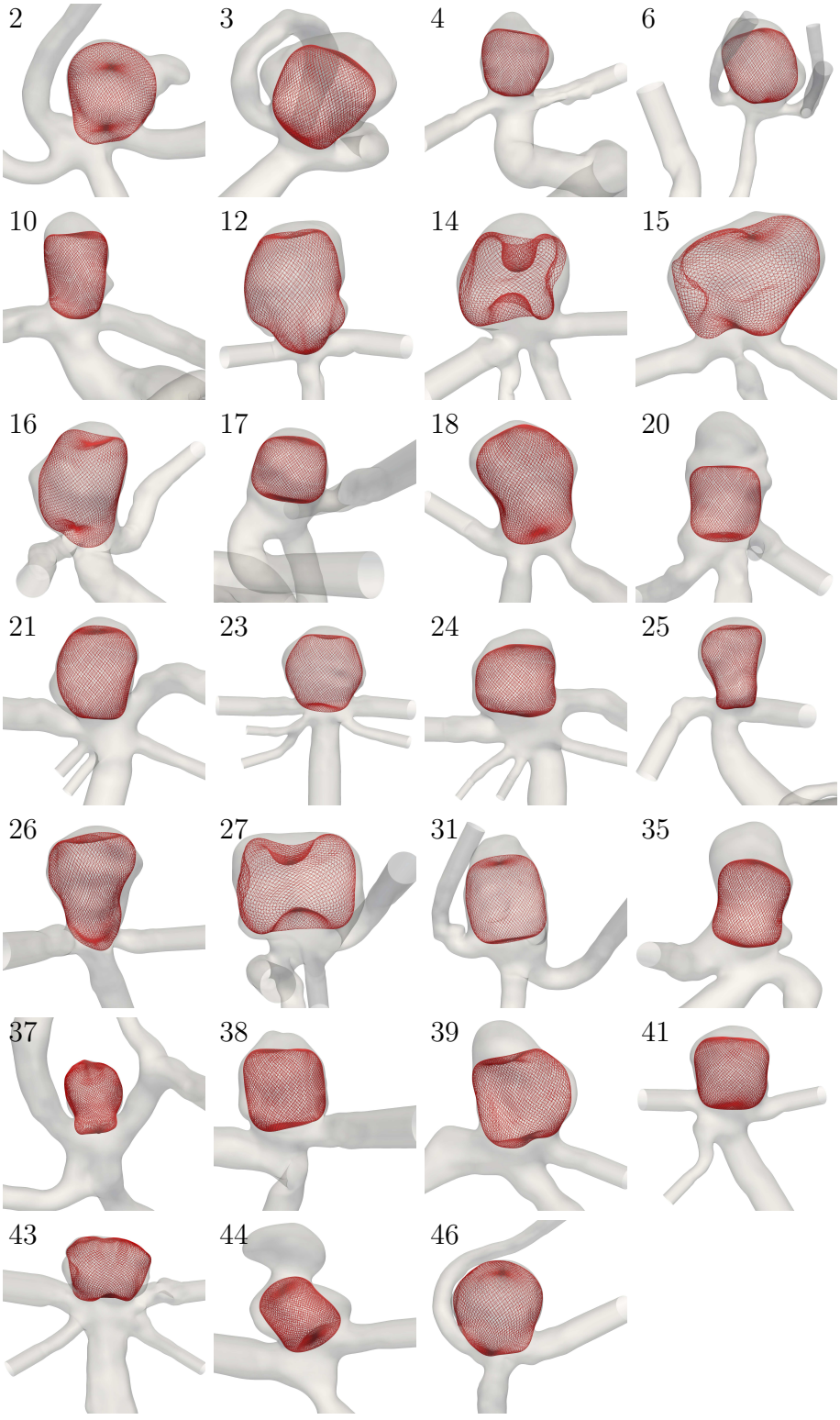

Figure 4.5: Illustrations of all the WEB deployments and arterial geometries used in this chapter.

In order to extract intra-saccular hemodynamics quantities as well as geometrical ones such as aneurysm volume and neck surface, a semi-automatic isolation procedure was used and is illustrated in Figure 4.6. Using the previously pre-processed surface, successive manual clippings using a sphere are carried out by the user to isolate the aneurysm surface from its parent artery (see the red surface on the right of Figure 4.6). Then, a warping of length 0.1 mm along surface normals is applied to the previously clipped open surface, which is subsequently closed using the VMTK surface capper with the smooth option activated at a value of 0.6 (see the grey surface on the right of Figure 4.6). Surface warping is performed to ensure that volume mesh points are effectively inside the surface, thereby preventing loss of nodes, especially at the aneurysm frontier. It should be noted that the warping constant was manually adjusted for several cases since surrounding arteries were very close to the aneurym sac (see n46 and n3 for example).

This final surface served two purposes: identifying both the intra-saccular surface and volume nodes to perform spatial averaging, and extracting the neck surface for further post-processing computations such as positive flow rate (see the blue surface on the right of Figure 4.6). In practice, neck surface obtention was carried-out by intersecting computational volumes (pre and post) with the aforementioned closed surface thanks to a combination of vtkCutter[1] and vtkImplicitPolyDataDistance[2] filters. This entails that the blue surface discretization (see Figure 4.6) is different from the original surface used to perform the cut. The same neck delineation procedure was followed between pre and post-treatment results to ensure consistent comparisons.

It should be noted that this isolation procedure was not the only one used in this study. A first version used the combination of a clipping sphere and a plane, but we noticed that it was impossible for some cases to effectively delineate the neck using such procedure, which is why the second procedure was developed a-posteriori. Nevertheless, we do not expect that these differences in neck delineation strategies to have a major impact onto computational results as the number of cases using strategy 1 (plane + sphere) is low (6/27) and the corresponding neck surfaces for these cases were well adapted to arterial geometries, *i.e.* the neck was not "complex" to delineate.

4.2.4 Device pre-processing

As already stated in Chapter 3, the heterogeneous model requires to compute flow rate across device pores, which necessitates to reconstruct a surface from the

[1]https://vtk.org/doc/nightly/html/classvtkCutter.html
[2]https://vtk.org/doc/nightly/html/classvtkImplicitPolyDataDistance.html

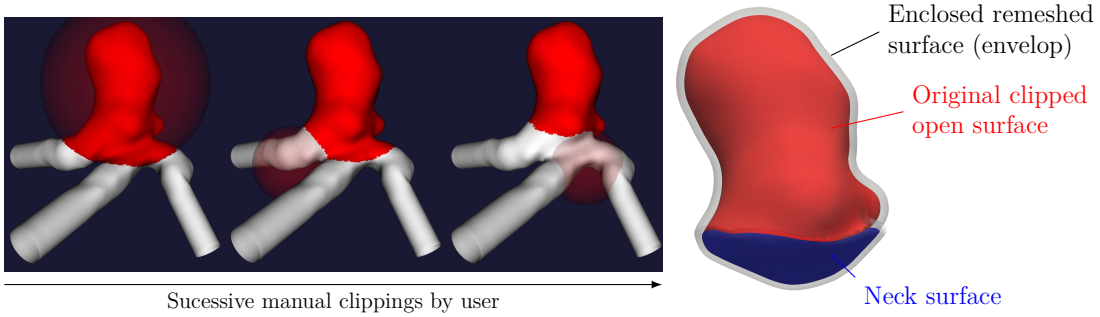

Figure 4.6: Manual aneurysm isolation steps and automatic neck surface creation. The enclosing surface (grey) aims at identifying surface and volume mesh points to compute spatially averaged quantities such as mean velocity inside the sac. The neck surface (blue) serves to compute both local inflow rate for example.

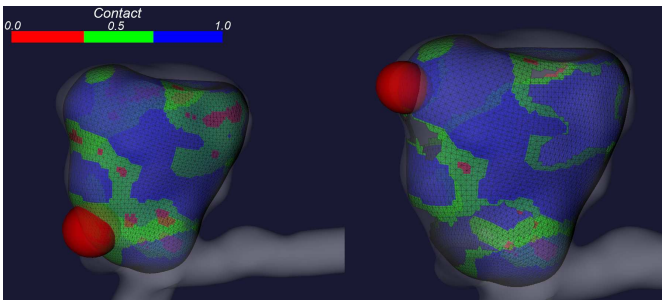

a: Initial surface b: Final trimmed surface

Figure 4.7: Device trimming GUI example for case n26. The contact apposition map values are defined as: 0 = outside the surface, 0.5 = inside and at a distance less than $5D$ and 1 = inside at a distance greater than $5D$.

neutral-fibre wires given by Sim&Size®. Therefore, an automatic device surface reconstruction was performed using wires connectivity. This step connects the 4 rhombus cell points using their barycenter, as exemplified for FDs in Figure 3.1. Special care was taken at the recess location since all wires are merged together, which is different from the FD surface data-structure seen in Figure 3.1.

Then, a graphical user-interface was created in order to successively remove apposed to the artery device portions thanks to a manually-placed clipping sphere, as depicted in red in Figure 4.7a. The threshold below which apposition was judged to be correct was arbitrarily fixed to $5D$ with D the wire diameter (for WEBs, $D = 20\,\mu m$). As the agreement between the previous numerical results for WEBs, which also followed this $5D$ threshold for device apposition cropping, and GMU computations, who did not remove apposed portions, was found to be very good in Chapter 3, this gave us confidence to apply such threshold in subsequent

computations. Both surface reconstruction and GUI were made possible thanks to custom python-vtk scripts. An example of final device shape after manual trimming is given in Figure 4.7b for case n26.

At recess locations, the high density of wires was modelled using the same procedure already described in Section 3.4.2, namely a penalization source term inside a region of width $3h$ around the device surface ensuring a zero fluid velocity.

4.2.5 Volume meshing

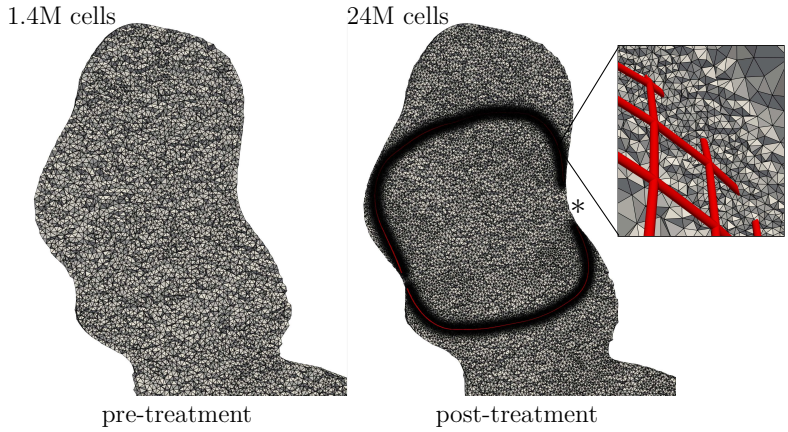

Figure 4.8: Volume slices showing pre and post-treatment mesh sizes for case n35. A close-up view enable to appreciate both the number of cells between rhombus cells and the smooth mesh coarsening. Wires diameter (in red) is at the same scale as real device, *i.e.* 20 µm.

Starting from the pre-processed arterial surface already described, two sets of volume meshes were created: pre-treatment (without device) and post-treatment (with device immersed), both with the VMTK library relying onto the Tetgen tetrahedral mesh generator [132]. Volume grid sizes for the pre-treatment mesh were interpolated from the surface triangulation, entailing an homogeneous mesh size inside the aneurysm while arterial branches contained a constant number of elements across their diameter thanks to the previous distance-to-centerline mesh size constraint. Among all pre-treatment meshes, the minimum, maximum and mean number of cells reached 1M, 5.6M and 2.2M respectively, which is line with values commonly reported in the literature [31, 72, 110, 142]. Pre-treatment mesh size for case n35 is exemplified in the left of Figure 4.8.

Concerning post-treatment mesh, several steps were necessary to produce grid of sufficient quality around the device wires. First, surface regions close to remaining apposed device portions were refined and an initial volume mesh was created using this refined surface. This entails that if the previous device trimming step kept large apposed portions, mesh size inside the volume would be

drastically reduced due to mesh size interpolation from surface to volume. As the first volume mesh generation might have "missed" internal device portions, volume refinement was carried to ensure a grid size of $h = w/8$ inside a region of width $8D$ around device surface, with w the mean inter-wire distance. This means that the number of cells is dependent on the device size, as inter-wire distance increases with device size. Final mesh cleaning and quality improvements were performed with the MMG3D library [44]. The choice for mesh size value prescribed in this chapter was judged to be sufficient as it proved to produce good quantitative comparisons with conformal results presented in Chapter 3.

Minimum, maximum and mean number of cells reached 14M, 33M and 21M respectively for post-treatment meshes. The number of cells for meshes found in the sole in silico WEB study found in the literature [32] is greater to ours by an order of magnitude. Nevertheless, mesh comparisons must be taken with caution as Cebral et al. [32] mostly focused onto DL devices, which contain a very high density of wires compared to the SL types used in this study, and since numerical handling of endovascular device resolves the wires, similarly as in Chapter 3.

Representative mesh sizes for case n35 are depicted in the right of Figure 4.8 as an example. One can appreciate the effect of device trimming onto volume mesh size ($*$ symbol), as well as the smooth transition from fine to coarse regions when moving away from the wires. In addition to that, it is seen on the right of Figure 4.8 that mesh size does not resolve the wires diameter but are still capable of capturing potential jetting-flows inside rhombus cells, which was the intended goal for the development of the heterogeneous model.

4.2.6 Fluid and boundary conditions

As commonly done in the field of CFD for intracranial aneurysms, blood was assumed to be incompressible and Newtonian, with a density $\rho = 1060\,\mathrm{kg.m^{-3}}$ and kinematic viscosity $\nu = 3.5 \times 10^{-6}\,\mathrm{m.s^{-2}}$ [37]. No-slip boundary condition was applied at the arterial wall and convective outflows were specified for all outlet sections using Equation 3.3.1. Since patient-specific flow rates were not available, the pulsatile waveform depicted in Figure 4.9, which is representative of ICA measurements performed by Hoi et al. [66] from an older adult population, was prescribed at the inlet surfaces along with a fully developed Poiseuille velocity profile. The only difference in waveform shape concerns MCA inlets, for which Fourier coefficients were damped by 30% to account for the decrease in pulsatility found at these locations [142].

To correctly account for the various inlet locations present in the present cohort (ICA, MCA and BA), different strategies were used to scale the previous flow rate waveform mean value. For ICA inlets, mean flow rate was computed such that it results in a mean velocity of $0.27\,\mathrm{m.s^{-1}}$ as recommended by [143].

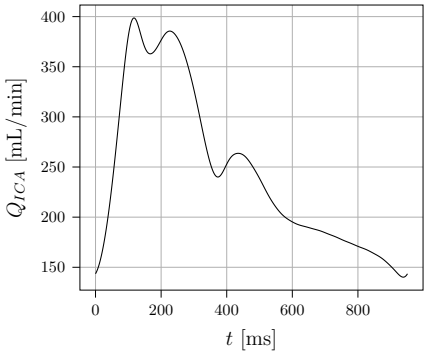

Figure 4.9: ICA flow rate representative of an older adult from [66], with a cardiac cycle period of $T_p = 0.951\,\mathrm{s}$.

The same procedure was followed for MCA inlets with a mean velocity value of $0.37\,\mathrm{m.s^{-1}}$ following [142]. In other words, MCA and ICA mean inlet flow rates were scaled according to a square law using the inlet diameter. For inlets located in the posterior circulation, *i.e.* Basilar Artery, measurements performed by Cebral et al. [28] and later re-analysed by Valen-Sendstad and Steinman [142] suggest that a mean flow rate cube law is appropriate for Vertebral Arteries that feed the basilar one. Therefore, following [30, 37], mean flow rate Q for BA inlets was computed such that it produces a mean WSS of 1.5 Pa such that:

$$Q = \frac{\mathrm{WSS}\pi}{32\mu} D^3 \tag{4.2.1}$$

with D the inlet diameter and μ the dynamic viscosity. Simulations were performed for 4 and 3 cardiac cycles for pre and post-treatment configurations, this to ensure that the zero-velocity initial condition was flushed and that flow periodicity was reached. Only the last simulated cardiac cycle was kept to perform qualitative and quantitative analysis, especially for time-averaging quantities.

4.2.7 Quantities of interest

Quantitative analysis using hemodynamics, anatomical and deployed device characteristics was performed in an attempt to dichotomize complete and incomplete occlusion groups. All quantities have been summarized in Table 4.2 and Table 4.3 for hemodynamics and anatomical/device-related indices, respectively. For hemodynamics indices, pre and post-treatment values are computed, as well as the ratio defined as post/pre.

[3]https://vtk.org/doc/nightly/html/classvtkSelectEnclosedPoints.html
[4]https://vtk.org/doc/nightly/html/classvtkMassProperties.html
[5]https://vtk.org/doc/nightly/html/classvtkPolyDataNormals.html
[6]https://vtk.org/doc/nightly/html/classvtkCellLocator.html

Quantity	Definition	Unit	Description
ICI	$< \frac{Q_i/Q_p}{A_i/A_{neck}} >$	[−]	The Inflow Concentration Index (ICI) measures how much the flow entering the aneurysm through the neck is concentrated, but also compares to which extent the aneurysm is fed by its parent artery [101]. Q_i is the positive flow rate at the neck with its associated area A_i. Q_p and A_{neck} are parent artery flow rate and neck area, respectively. The neck normal was orientated towards the aneurysm sac to compute Q_i.
Q^+	$< Q_i >$	[$m^3.s^{-1}$]	Positive flow-rate Q^+ is the time-averaged inflow Q_i trough the neck surface [101].
FN	$\frac{T_p Q^+}{V_a}$	[−]	The flushing Number (FN) compares the total blood volume that entered through the neck during one cardiac cycle of period T_p with the aneurysm volume V_a. It is a measure of blood exchange amount between the parent artery and the aneurysm and is introduced in this study.
U_a	$\frac{1}{V_a}\int_{\Omega_a} \|\| < \mathbf{U} > \|\| dV$	[$m.s^{-1}$]	U_a, which was already defined in Equation 3.3.2, is the spatial and time-averaged velocity inside the aneurysm sac [110].
SR_a	$\frac{1}{V_a}\int_{\Omega_a} 2\sqrt{< S_{ij} >< S_{ij} >} dV$	[s^{-1}]	The shear rate spatially averaged inside the aneurysm (SR_a) [101], with S_{ij} the symmetrical part of the velocity gradient tensor $G_{ij} = \frac{\partial u_i}{\partial x_j}$ such that $\bar{\bar{\mathbf{S}}} = \frac{1}{2}(\bar{\bar{\mathbf{G}}} + \bar{\bar{\mathbf{G}}}^T)$. G_{ij} components are computed via the high-order numerical gradient reconstruction available in the yales2bio code and time-averaged component-wise.
VO_a	$\frac{1}{V_a}\int_{\Omega_a} \|\| < \nabla \times \mathbf{U} > \|\| dV$	[s^{-1}]	The vorticity spatially averaged inside the aneurysm (VO_a) [101]. The same numerical gradient reconstruction as $SR_a$was used, as well as component-wise time integration.
MATT	$\frac{V_a}{U_a A_{neck}}$	[s]	Mean Aneurysm Transient Time (MATT) is representative of a convective time inside the aneurysm [102], and can be termed as an averaged intra-saccular residence time.
TAWSS	$\frac{1}{S_a}\int_{\Gamma_a} \|\| < \boldsymbol{\tau}_\mathbf{w} > \|\| dS$	[Pa]	Time-Averaged Wall Shear Stress (TAWSS) spatially averaged on the aneurysm surface Γ_a [101]. $\boldsymbol{\tau}_\mathbf{w}$ is the wall shear stress vector computed such as $\boldsymbol{\tau}_\mathbf{w} = 2\mu\bar{\bar{\mathbf{S}}} \cdot \mathbf{n}_\mathbf{w}$ with $\mathbf{n}_\mathbf{w}$ the wall outward normal vector.

Table 4.2: Hemodynamic quantities of interest. The $< \bullet >$ notation denotes last cardiac cycle time-averaging operator such that $< \bullet >= \frac{1}{T_p}\int_{T_p} \bullet \, dt$. Time-averaging was performed on-the-fly for aneurysm-related parameters, *i.e.* at each time-step, while quantities that needed the neck surface such as Q^+ were computed posterior to computations using 30 regularly outputted solutions during the last cardiac cycle.

Quantity	Definition	Unit	Description
Anatomical			
V_a	$\int_{\Omega_a} \mathrm{d}V$	[mL]	The total aneurysm volume. In practice, all volume points lying inside the previously described surface Figure 4.6 are first extracted using the vtkSelectEnclosedPoints filter [3]. Then, nodal volume scalar field is computed and further numerical integration is performed.
S_{neck}	$\int_{\Gamma_n} \mathrm{d}S$	[mm^2]	The total neck surface (see the blue surface in Figure 4.6).
R_a	$\frac{\sqrt[3]{V_a}}{\sqrt{S_{\text{neck}}}}$	[–]	The volume to neck surface ratio, which measures the aneurysm elongation.
Device-related			
R_d	$\frac{V_{\text{device}}}{V_a}$	[–]	The ratio between the aneurysm volume V_a and the device one V_{device}. Measures how well the device fills the aneurysm cavity. In practice, the device trimming step depicted in Figure 4.7 also outputs the entire unclipped surface, from which V_{device} was computed using the vtkMassProperties filter [4]. Since vtkMassProperties makes uses of the divergence theorem, device cell normals must be oriented outwards and consistently across the surface, which was ensured with the vtkPolyDataNormals[5] filter.
D_{neck}	$\frac{1}{S_{\text{neck}}} \int_{\Gamma_n} \lvert\lvert\mathbf{X}_{\text{neck}}^{\text{device}}\rvert\rvert \mathrm{d}S$	[mm]	D_{neck} measures the averaged distance between neck and device. In practice, for each point on the neck surface Γ_n, its closest neighbour on the device is obtained via the vtkCellLocator[6] filter, $\mathbf{X}_{\text{neck}}^{\text{device}}$ being the vector between these two points.
ApR	$\frac{S_{\text{apposed}}}{S_{\text{device}}}$	[–]	The Apposition Ratio (ApR) measures to which extent the device is apposed to the arterial surface. Threshold distance for apposition was fixed to $5D$ in accordance with previous sections. Proximal and distal apposition of FDs was proved to be associated to aneurysm occlusion by Rouchaud et al. [128], but no similar studies have been conducted for WEBs to date.

Table 4.3: Anatomical and device-related quantities of interest. An illustrative example with corresponding indices values is available in Figure 4.10.

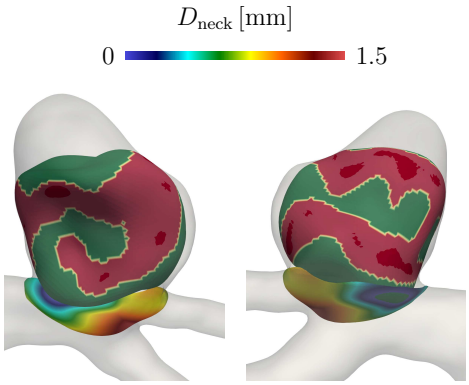

Case n39:

- $R_d = 0.65$
- $D_{\text{neck}} = 0.62\,\text{mm}$
- ApR $= 0.45$
- $V_a = 0.15\,\text{mL}$
- $S_{\text{neck}} = 19.2\,\text{mm}^2$
- $R_a = 1.2$

Figure 4.10: Case n39 example for distance to device D_{neck} and contact apposition ratio ApR maps. Red portions on the device surface are apposed to the aneurysm sac and summed for the computation of S_{apposed} in Table 4.3.

4.3 Results

4.3.1 Hemodynamics

This section entails to quantitatively and qualitatively describe hemodynamics for all cases in the present database. To ease discussions and organization, this section is divided into several questions that we considered to be of interest in order to understand hemodynamics inside WEB treated aneurysms both before and after treatment.

What are the main flow characteristics encountered inside bifurcation aneurysms without any device? A distinctive feature of bifurcating aneurysm is that they exhibit jet-like flow structures that further disperse and divide inside the sac, as opposed to most sidewall aneurysms for which a large main vortex fills the entire sac volume. For example, Cebral et al. [27] noticed that despite all aneurysm geometries are different, and so as hemodynamics, a classification based on qualitative features can be performed by dividing intra-saccular flow patterns into 4 categories depending on the number of vortices inside the sac and their stability in time during the cardiac cycle. In a later similar study led by the same group with an enlarged database of cases ($N = 210$), Cebral et al. [30] demonstrated that unstable flow features such as small jets through the neck and concentrated impingement regions were significantly associated with aneurysm rupture, as well as flow complexity which was measured by means of

flow separations and/or the presence of multiple vortex inside the sac. Similar quantitative analysis and conclusions were found for ACOM aneurysms in [25], for which aneurysms are mainly located at bifurcations similarly to the present database. Using knowledge and experiences from previous references, flow classification was performed by visually inspecting time-averaged velocity fields for all cases, which led to the identification of 4 flow types:

Type I The parent-artery jet is tangential to the aneurysm sac and does not separate at the neck entry,

Type II When going through the neck, the jet is separated at an arterial junction with a branching vessel and is further oriented tangentially to the aneurysm sac,

Type III The incoming jet directly impinges the aneurysm dome and subsequently separates,

Type IV No clear flow organization inside the sac.

As given by Table 4.4, most aneurysms flows are of types I and II (37% each). It is worth remarking that the distinction between these groups is expected to be subjected to high inter-observer variability as they exhibit very similar flow patterns.

	Cases ids
Type I	n4, n15, n16*, n20, n25, n31, n38, n41, n43, n46
Type II	n2, n3, n12, n21, n24, n26, n27, n35*, n39, n44
Type III	n6*, n14, n17, n18, n23
Type IV	n10, n25, n37*

Table 4.4: Flow type classification results for the present database, with * denoting illustrative examples depicted in Figure 4.11.

Velocity contours as well as TAWSS maps for one illustrative example per flow-type are depicted in Figure 4.11, where we can see that Type I flows create an homogeneous distribution of parietal friction all over the aneurysm sac, blebs and irregularities aside. The same observation is true for Type II, which in addition exhibits an elevated region of parietal friction at the neck bifurcation location due to jet separation. For Type III, jet impingement on the dome region creates a very high TAWSS region compared to other types ($\approx 25\,\mathrm{Pa}$) that rapidly disperse on

the sac. The absence of intra-saccular flow organization for Type IV aneurysms can be attributed to the sac location with respect to the parent artery. Indeed, for cases n37 and n25, the local bifurcation angle induces that most of the proximal flow is directed towards either one or both downstream arteries, thus leaving the aneurysm sac without any entering jet. Regarding the last reported Type IV case (n10), the combination of aneurysm elongation and upstream parent artery curvature does not create a clear jet inside the sac as blood flows directly to the distal arteries.

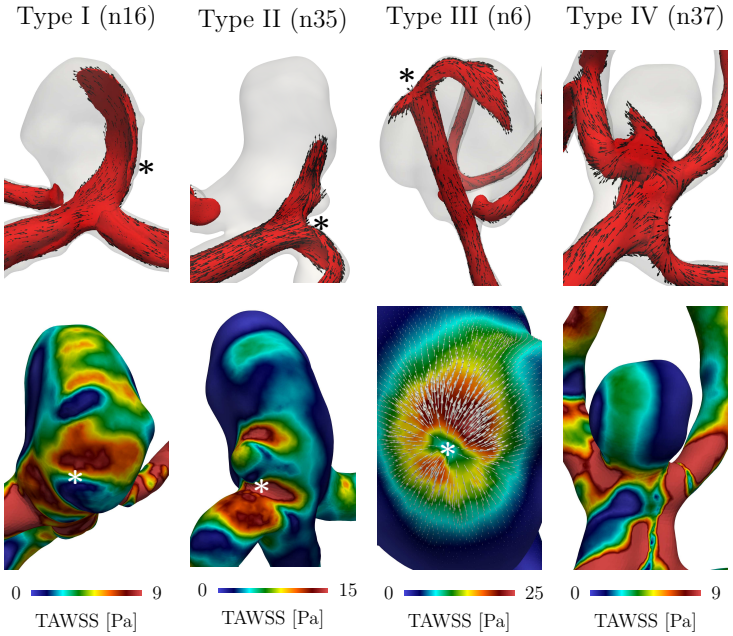

Figure 4.11: Main pre-treatment flow types for the present hemodynamics database. Since views are different between top and bottom rows, $*$ symbols have been placed to ease 3D correspondence between views. TAWSS vectors for Type III are oriented negatively to better illustrate the flow separation.

What is the hemodynamics impact of device apposition? To study how device apposition affects intra-saccular hemodynamics, the median value (30.18%) of the apposition ratio (ApR) index was used to dichotomize between good and bad apposition groups. In each group, the presence of a jet between the arterial sac and the device frontier (referred to as "near wall jet presence") was visually assessed using time-averaged velocity field.

Contingency table was computed and is available in Table 4.5. Each subgroup was labelled with a unique id to ease discussion. Several interesting observations can be made from Table 4.5. The first one is that a correct device apposition systematically implies the absence of a near-wall jet (groups with superscripts (1)

		Degree of apposition	
		good (ApR > 0.3)	**bad** (ApR < 0.3)
Near wall jet presence	yes	**1**$^{(1)}$ (n4)	**6**$^{(2)}$ (n3, n15, n16, n20, n35, n44)
	no	**12**$^{(3)}$ (n6, n10, n12, n18, n21, n26, n37, n38, n39, n41, n43, n46)	**8**$^{(4)}$ (n2, n14,n17, n23, n24, n25, n27, n31)

Table 4.5: Contingency table for device apposition and near-wall jet presence. Each subgroup is labelled with a superscript for further in-text referencing.

and (2)), which is not true for one case (n4) illustrated in Figure 4.12. Indeed, despite the device is correctly apposed on the "right" part of the sac, parent artery curvature induces the creation of a jet that impacts the "left" side of the neck, a location where the device is not apposed. The jet flow is therefore similar to pre-treatment until it encounters the top part of the device where it is deflected and reduced in magnitude. It is worth noticing that a recirculating cell similar to a lid-driven cavity flow is found near the bottom recess at the neck (see the white $*$ symbol). Nevertheless, the ApR index value for this case (30.42%) is the forthcoming value to the median (30.18%), meaning that its apposition classification into the correct group is debatable.

The second interesting conclusion that can be drawn from Table 4.5 is that bad device apposition is not associated with the presence of a near-wall jet, and this for a non-negligible portions of cases in the present cohort (30%). These cases have been gathered under the subgroup (4) label and an internal supplementary subdivision based upon hemodynamics qualitative features identified 5 scenarios, labelled as "(4.1)" and so on. One case example per scenario is available in Figure 4.12 (red quadrant).

Scenario (4.1), depicted by case n2, represents a situation where the incoming jet impacts a region of the device with both low wires density and correct neck apposition, leaving no space for the jet to enters near-wall regions. This induces that the downstream-to-the-device remaining jet stays further confined inside the device volume despite encountering non-apposed device portions when recirculating in the sac. A similar flow configuration is found for scenario (4.2), depicted by case n24, on the difference that device protrusion strongly deviates the jet towards both downstream arteries and that no remaining jet is present inside the device due to the high density of wires near the impaction site. Scenario (4.3), see case n25, can be considered as a mirror of subgroup (1) flow, since the device is correctly apposed on the region where the jet impacts the device whereas low apposition is present in other regions. Scenario (4.4), see case n14, is very special since the device over-sizing entailed severe compressions and reorientations of device portions, which causes a low ApR value of 21%. Since the jet impacts

tangentially a re-oriented and compressed device portion, it is deflected towards downstream arteries without being able to reach near-wall regions. A similar type of flow was identified for case n27 who also suffered from device over-sizing and compression (see Figure 4.5). Finally, scenario (4.5) is characterized by a complete blockage of the jet since it directly impacts the recess location where the density of wires is very high, entailing an absence of remaining internal jets. In addition to that, device protrusion causes the flow to be effectively deviated towards downstream branches, despite not being very clear in Figure 4.12.

The last interesting result from Table 4.5 is that the proportion of cases which harbour near-wall jets is relatively low (26%) in the present cohort. As exemplified on the subgroup (2) green quadrant in Figure 4.12, these cases contain a deployed device which is either close to the neck, as intended when being deployed, but not apposed to the sac portion where the pre-treatment incoming jet enters the aneurysm (see n20), or disoriented, thus leaving spaces for blood to circulate between the sac and the device (see n44). These cases also highlights an important point concerning the use of pre-treatment computations to potentially provide treatment guidelines to physicians. Indeed, they deploy intra-saccular devices so as to both fill the sac while not being too far from the neck to prevent potential aneurysm recanalization (see on-line appendix of [20]). Nevertheless, accurately measuring device apposition as well as its exact positioning inside the sac is hardly feasible during the deployment procedure. Simulation tools such as Sim&Size® allow to estimate such quantities before proceeding to the intervention, whereas VasoCT images only provide a rough estimate after deploying the device. Therefore, pre-treatment computations could be analysed prior to the surgery to identify regions where device should be absolutely deployed to effectively block the entering jet, in order to prevent situations such as the ones found in subgroup (2). Added to deployment recommendations already existing, *i.e.* device filling and minimal neck distance, such hemodynamic criterion could be added to clinical routine to potentially increase treatment efficacy if proven to be relevant in retrospective and prospective studies. With this presented method, this would be possible for elective cases only due to the time needed to perform numerical computations, which usually took a couple of hours for pre-treatment simulations in the present cohort (surface cleaning and pre-processing are not included in this timing estimation).

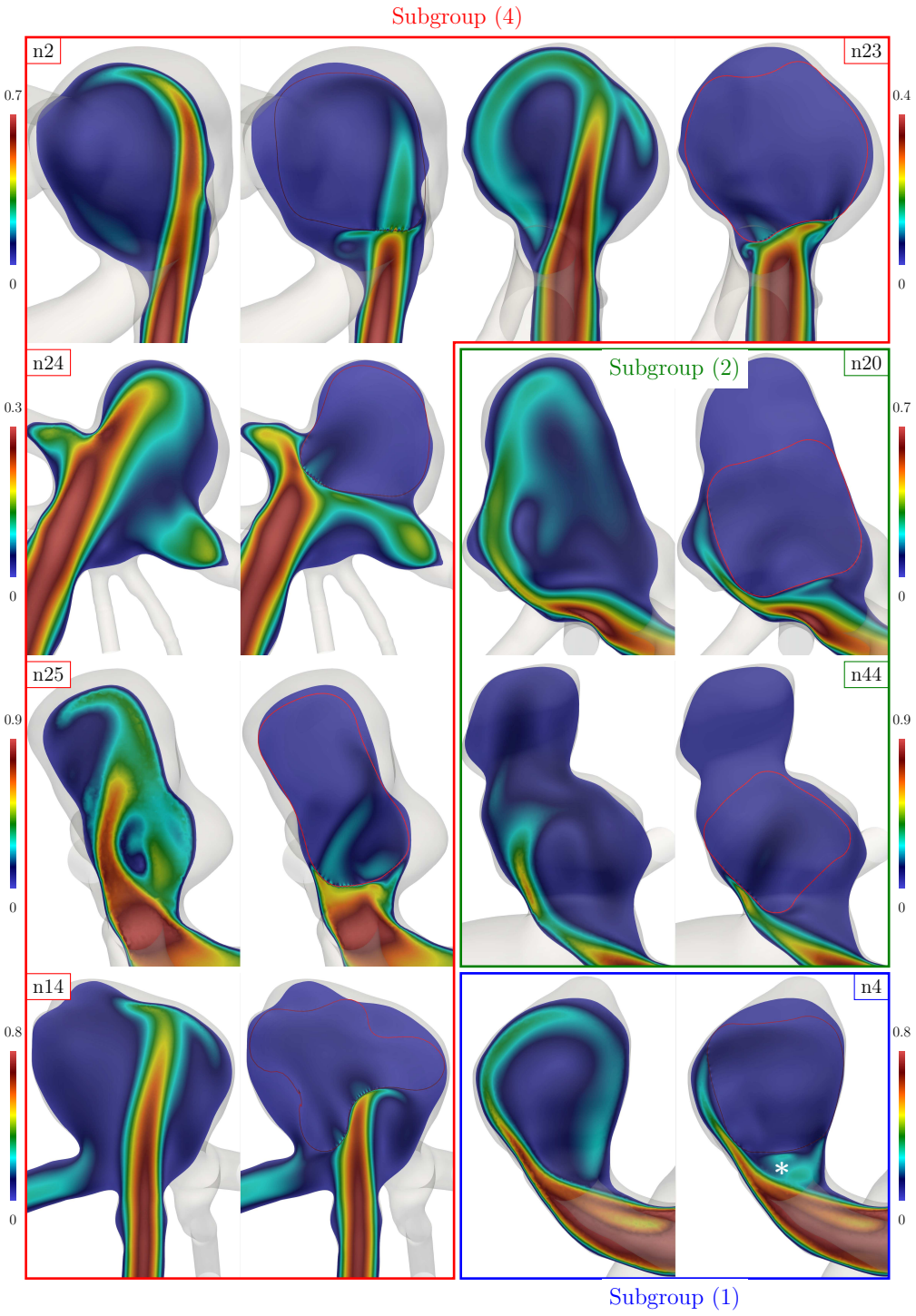

Figure 4.12: Device apposition impact onto hemodynamics. Subgroups labelling correspond to those in Table 4.5 and time-averaged $< \mathbf{U} >$ velocity fields are represented for each case.

What is the impact of the device protrusion on the hemodynamics? Since WEBs are deployed inside the aneurysm sac, the use of antiplatelet therapy was first hypothesized to be not mandatory in early publications using such devices [49], as opposed to endoluminal devices such as FDs due to thromboembolism risks. Nevertheless, WEB device protrusion, *i.e.* proximal marker emerging from the sac at the bifurcation, which has been reported in 47% of cases by Caroff et al. [22], induces that additional surgical acts such as stent placement, balloon remodelling and clot removal may be needed, but also that the use of anti-platelet therapies is mandatory for these cases.

Therefore, we decided to analyse how device protrusion affects hemodynamics in the device vicinity. Visual presence of device portions crossing through the neck surface was used to dichotomize between absence and presence of device protrusion in the present cohort. In addition to that, visual inspection of the neck inflow Q^+ ratio ($Q^+_{\text{post}}/Q^+_{\text{pre}}$) through all cases revealed the presence of two groups, qualified as high and low. The Q^+ ratio threshold between these groups was arbitrary set to 0.5 (see Figure A.2).

		Q^+ **ratio group**	
		high	low
Device protrusion	yes	**2** (n16,n44)	**10** (n10, n12, n21, n23, n24, n25, n26, n37, n43, n46)
	no	**15** (n2, n3, n4, n6, n14, n15 ,n17, n18, n20, n27, n31, n35, n38, n39, n41)	**0**

Table 4.6: Protrusion contingency table

If the device were to protrude at the neck, a low Q^+ ratio is expected, reflecting an effective flow blockage by the device. From Table 4.6, we can see that this statement is true for all cases except two for which device protrusion was not automatically inducing a low neck-inflow ratio; these two cases (n16 and n44) are depicted in Figure 4.13.

For these cases, the classification in the high inflow ratio group can be explained by device positioning with respect to both the neck and the impacting jet. Indeed for case n16, device protrusion at the neck, represented by the intersection between green and red lines in Figure 4.13, does not majorly affects the incoming jet since the latter is oriented towards the "left" part of the device that is not apposed to the aneurysm sac and rotated, thus leaving a non negligible gap for blood to flow tangentially to the device in this region (see the black $*$ symbol in Figure 4.13). Therefore, post-treatment neck inflow does not significantly decrease compared to pre-treatment situation, as seen in the left of Figure 4.13, entailing an inflow ratio classification into the high group for this

case. Concerning case n44, the situation is rather similar to n16: the combination of mal-apposition and device orientation with respect to the jet does not impede the latter to create an area at the neck surface with high projected velocities, on the difference that another phenomenon is at stake compared to n16. Indeed, a region with velocities oriented more normally to the neck compared to pre-treatment appears due to the device proximity that locally redirects the flow (see white $*$ in Figure 4.13) and thus keeps this case in the high inflow ratio group. It should be noted that these cases were previously classified in the "near-wall jet presence" group (see Table 4.5).

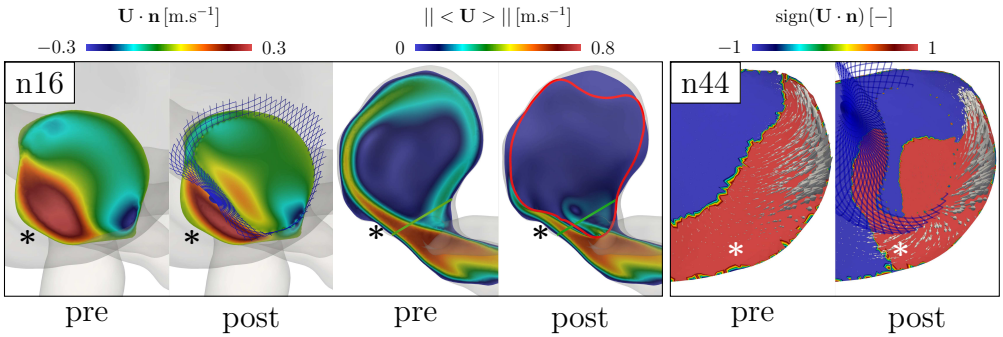

Figure 4.13: Device protruding cases that are still classified in the high Q^+ ratio group. **Case n16:** The left view represents pre and post-treatment projected velocity at the neck surface for the last instant of the cardiac cycle. The device (in blue) has been clipped to enhance flow visualization. On the right view, green and red lines correspond to neck and device surfaces, respectively. **Case n44:** The sign of the projected velocity at the neck is represented, along with velocity vectors in white to appreciate how the device protrusion modifies the local hemodynamics environment.

Interestingly, device protrusion was found for a vast majority of cases in the present cohort (44%). However, this number cannot be compared to medical research references since protocols to identify and measure protrusion are likely to be different than ours. In addition to that, it also highly depends onto operator experience with WEBs, sizing and mechanical manipulation during intervention, and by consequence onto which clinical center was used to gather data in medical studies. For example in 2015, Caroff et al. [22] identified a proportion of 47% cases harbouring device protrusion, while this number goes to 0% in a very recent study performed by Cagnazzo et al. [20] in 2019. As already stated, differences between these studies can be explained by medical experience gains over the years during WEB deployment procedures, which are likely to be higher for Cagnazzo et al. than Caroff et al. (2019 vs 2015), but this might not be the only factor at stake. Indeed, for aneurysms treated posterior to 2017 in [20], the simulation software Sim&Size® was used for a non-negligible portion of cases (64%). This entails that

device protrusion could have been anticipated using such software, since it gives access to the final deployed shape of the device, and might be another factor explaining the absence of protruded devices in Cagnazzo et al. [20] compared to Caroff et al. [22].

As it could have been expected, cases with pronounced device protrusion exhibit major flow redirection towards downstream arteries, as exemplified by case n12 in Figure 4.14 for which high density of wires prevents any circulation inside the aneurysm. The same redirection is also present for case n26 (bottom view), on the difference that a residual jet subsists inside the sac due to a low pore density near the impaction site on the device (top view). Nevertheless, such redirection is not restricted to protruding cases, as exemplified by n38 in Figure 4.14, for which an upstream arterial constriction focuses the jet into the device recess section, entailing a clear separation towards downstream arteries. However, due to the absence of device protrusion and subsequent flow constriction, the widths of separated jets are not as low as for protruding cases n12 and n26 (see white $*$ symbols).

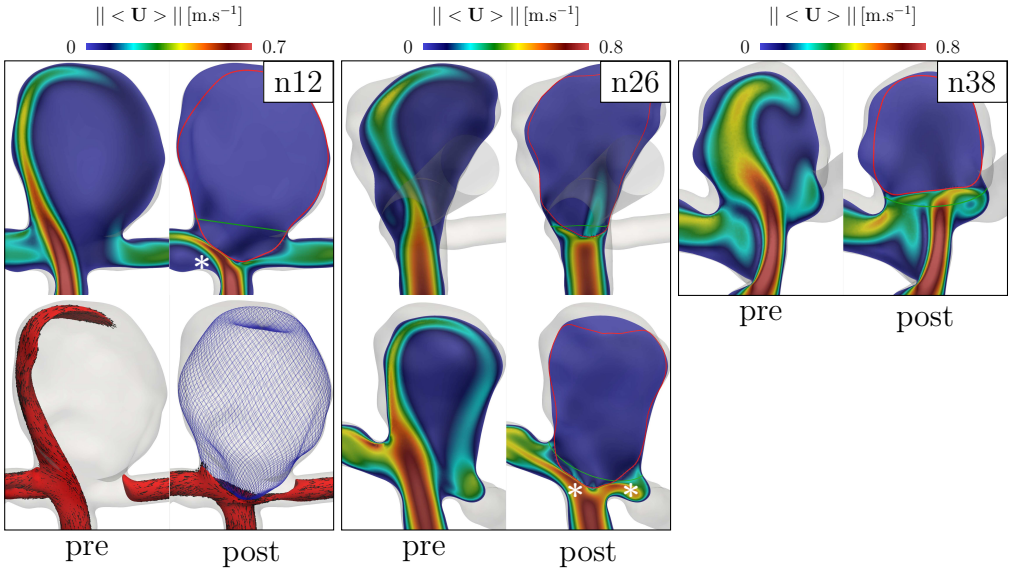

Figure 4.14: Hemodynamic impact of device protrusion. Cases n12 and n26, which have been classified in the positive device protrusion group, exhibit a major flow redirection due to device presence beyond the neck and inside the parent arterial bifurcation. The same phenomenon is found for several non-protruding cases such as n38, but to a lesser extent compared to n12 and n26. Red and green lines correspond to device and neck surfaces, respectively.

Can hemodynamic indices provide counter-intuitive conclusions? When studying hemodynamic indices, one could expect that the ratio post/pre should

be smaller than one, reflecting the ability of the device to effectively impede velocities inside the sac (ratio close to zero) or not (ratio close to one). Therefore, the presence of hemodynamic ratios greater than one should never be possible following this principle. Despite this statement was found to be correct in the present cohort for all spatially averaged quantities inside the sac (U_a, SR_a, VO_a, MATT) and also at the aneurysm wall (TAWSS), we found that for three cases over the 27, neck-related indices such as ICI, Q^+ and FN do not obey this rule (see raw data available in Figure A.3 and Figure A.2).

In particular, case n6 exhibited Q^+ and FN ratios of 1.17 and 1.13 respectively. From case n6 velocity field depicted on the left of Figure 4.15, one can see that an upstream constriction creates an area of high velocities ($1.1\,\mathrm{m.s}^{-1}$) very localized at the aneurysm neck (in green). When the device is deployed, this strong jet is majorly blocked at the recess location, leaving only a small persistent intra-saccular jet and entailing jet separation upstream to the device. Consequently, as the neck is very close to the device, this separation creates regions at the neck with higher normal velocity components that were not existing pre-operatively, thereby increasing the positive flow-rate globally (see the left-bottom line of Figure 4.15). For the last two cases n31 and n15, an ICI ratio of 1.3 each was reached, which can be explained by looking at the right of Figure 4.15. As opposed to most cases in the present cohort, pre-treatment velocities at the neck for case n31 induce two distinct areas with positive normal components: one at the jet entrance near the parent artery bifurcation, which is "classical" and found for all other cases, and another one near the downstream artery on the "left". This second region is created by the combination of a major recirculation inside the sac and a large neck size of $45\,\mathrm{mm}^2$ (the largest in the cohort) that induces a re-entry of blood through the neck before exiting the aneurysm, as depicted by velocity streamlines. Device presence inside the aneurysm majorly reorganizes intra-saccular flow, the large pre-treatment recirculation is absent and prevents flow re-entry through the neck. Therefore, the second region is missing at the neck and decreases the A_i value in the ICI expression in Table 4.2, inducing an increase of ICI value. In addition to that, potential compensation of ICI increase by reduction of positive inflow Q_i is not possible since the device is located far from the jet entrance at the bifurcation (see top-right of Figure 4.15).

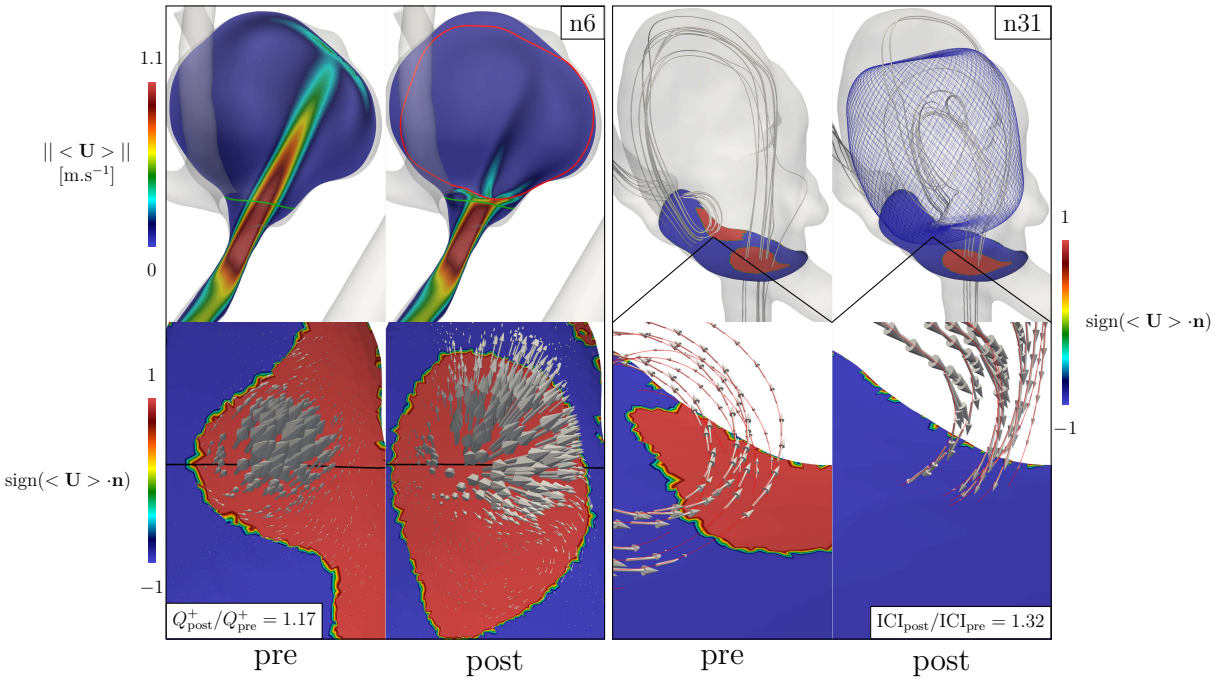

Figure 4.15: Counter-intuitive ratio values for neck-related indices Q^+ and ICI. **Case n6:** Arterial constriction and neck proximity with the device entail a jet separation that creates higher normal velocity components compared to pre-operatively (see white velocity vectors at the neck). Lines in red, green and black represent the device, neck and location of the plane use to visualize flow in the top row, respectively. **Case n31:** A complete flow-reorganization inside the sac due to the device presence removes an area of positive flow-rate, thereby increasing ICI_{post} value. Streamlines have been computed with temporally averaged velocities using the same source of points at the neck, and velocity vectors are overlaid on these streamlines to ease flow visualization.

4.3.2 Link with medical outcome

This section presents preliminary analysis intended to link both hemodynamic and geometrical indices in the present cohort with medical outcome that was gathered retrospectively, in an attempt to predict outcome and provide insights into mechanisms potentially involved in occlusion success or failure.

Occlusion at follow-up was assessed by Dr Mantilla with visual inspection of DSA images using the Beaujon Occlusion Scale Score (BOSS) [22], which divides occlusion in 6 scores: a, b, c, d and e (see Figure 4.16A). Score a is not used in practice since it corresponds to device absence. Score b represents a situation where the complete absence of contrast material circulation inside the aneurysm is due to both correct device apposition and neck-coverage. Score c is very similar to b, with the difference that the proximal marker is hidden by contrast material. Previous scores (b and c) were judged as complete outcome and referred to as "success" in subsequent sections. In contrary to b and c, score d exhibits a non-negligible amount of contrast material inside the device, despite the latter is correctly apposed to the aneurysm: it is referred to as "intra device opacification". Score e is representative of a situation in which the device is too distal inside the aneurysm and creates a region between the neck surface and the proximal recess where contrast material is freely circulating: it is referred to as "neck remnant". Finally, score f depicts both a device mal-apposition as well as a proximal misplacement, leaving gaps between the aneurysm wall and the device for the contrast material to flow in. Cases with score d, e or f were qualified as incomplete outcome and referred to as "failure" in following sections.

As depicted by Figure 4.16B, follow-up time is not homogeneous in the cohort, going from 3 to 26 months after the surgical act. Nevertheless, no significant difference is found regarding the follow-up time between success and failure groups ($p = 0.6$, statistical technique described later). This finding is important since time plays an important role in the healing process of treated aneurysms due to thrombosis reactions, and examining case occlusions at different timings in a given cohort can induce potential biases. Interestingly, we noticed that cases treated before or during 2014 (blue dots in Figure 4.16B) were monitored significantly earlier compared to more recent cases ($p = 0.0009$). This is due to a shift in intervention follow-up protocols since long-term treatment efficacy was better understood after 2014, as WEB-SL devices were introduced in 2013 in Europe.

In an attempt to study the individual impact of each hemodynamic and geometric parameter onto occlusion status, univariate two-sided Mann-Whitney rank-sum tests were performed automatically using scipy[7]. Choosing the right statistical test can be cumbersome and can lead to erroneous conclusions; therefore, we enumerate here the reasons that motivated our choice:

[7]https://docs.scipy.org/doc/scipy/reference/generated/scipy.stats.mannwhitneyu.html

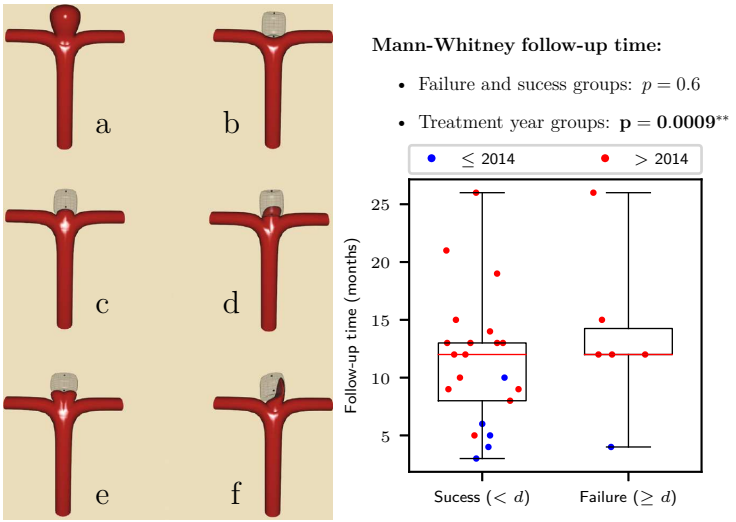

(A) (B)

Figure 4.16: Follow-up descriptors and results. **A:** Beaujon Occlusion Scale Score, taken and modified from [22]: a: No device implanted b: Complete occlusion c: Proximal recess opacification d: Intra device opacification e: Neck remnant f: Aneurysm remnant: contrast agent both inside the device and gaps with the arterial wall. Scores a and b are regrouped as complete outcome ("success"), the other ones being considered as incomplete ("failure"). **B:** Follow-up time box-plots found in the present cohort, for correct and incorrect occlusion scores. The median, first and third quartiles are represented as red and black lines, respectively, as well as minimum and maximum values using bars. Blue and red distinction is based onto the year at which the surgical act was performed (before or after 2014), recalling that WEB SL types were available in Europe from 2013.

1. Success and failure groups are internally and externally independent, meaning that one case outcome does not impact another one, irrespectively of occlusion group classification.

2. Geometrical and hemodynamic indices are continuous and non-parametric variables, *i.e.* not normally distributed in each group. Latter statement was verified using Shapiro-Wilk test and visual inspection of raw data histograms.

3. Sample sizes are small, 21 and 6 for success and failure groups, respectively, making the Mann-Whitney test a preferred approach.

Mann-Whitney test compares rank-sums and tests if, for two samples X and Y, the probability of X being greater (or smaller) than Y equals the probability of Y being greater (or smaller) than X. A p-value smaller than 0.05 was considered to depict a statistical difference between groups.

Outcome score statistics for patient data Since smoking usage and hypertension data were not available for all cases (see Table 4.1), statistics were not performed for these variables. Nevertheless, it is found that age has a significant impact on outcome: younger patients are more likely to harbour unfavourable outcome compared to older ones ($p = 0.005$). This finding is interesting but was not confirmed in large in vivo WEB cohorts such as Cagnazzo et al. [20].

Outcome score statistics for device and geometrical data (Table 4.7) Aneurysm volume V_a is significantly higher for non-occluded cases, as seen in Table 4.7. This finding is in line with Cebral et al. [32] for their aneurysm size index Asize. Nevertheless, comparisons with the present V_a index must be performed with great care as Asize measures the maximum sac diameter. Concerning in vivo studies, no such significant difference was found by Cagnazzo et al. [20] for the index which definition is the closest to ours: aneurysm dome size. This lack of significance might be caused by differences in measurement method compared to in silico: points manually placed vs automatic measures. Interestingly, Cagnazzo et al. [20] demonstrated that higher aneurysm domes significantly promoted WEB shape modifications. Neck-size (max diameter) was also found to be systematically higher in the failure group by Cebral et al. [32], a behaviour not recovered in the cohort for the similar index S_{neck}. Nevertheless, the ratio between aneurysm volume and neck surface R_a, measuring aneurysm elongation, was significantly higher in the non-occluded group, a finding confirmed by Cebral et al. [32] only before adjustments for multiple testing.

Concerning device-related indices R_d, D_{neck} and ApR, no significant differences were found. Since these measures were introduced in this study, it is difficult to know if this finding is coherent and consistent with other studies. This lack of significance stresses the need to develop other device-related measures or combine the ones presented here. For example, one could normalize distance to the neck D_{neck} by aneurysm size or parent-artery diameter. In addition to that, the apposition ratio ApR index suffers from a major drawback, since it does not discriminate device portions that have a chance of being in contact with the aneurysm (lateral side and distal recess) with the ones that will never be in contact to any wall (the proximal recess), thereby introducing a bias proportional to device size.

Outcome score statistics for hemodynamic data (Table 4.8) Interestingly, pre-treatment inflow concentration index (ICI) showed a statistical difference between outcome groups, with non-occluded ICI values being higher. Using steady CFD computations on 19 WEB cases without any device deployed and measuring an index similar to ICI denoted as inflow ratio (neck inflow divided

Index	Success	Failure	p-value
V_a	0.25 ± 0.18	0.39 ± 0.09	$\mathbf{0.025}^{**}$
S_{neck}	21.12 ± 8.43	22.72 ± 4.65	0.502
R_a	1.32 ± 0.17	1.54 ± 0.14	$\mathbf{0.021}^{**}$
R_d	0.75 ± 0.15	0.76 ± 0.13	0.884
D_{neck}	0.61 ± 0.39	0.88 ± 0.71	0.705
ApR	0.34 ± 0.15	0.29 ± 0.11	0.466

Table 4.7: Geometrical and devices related statistical differences. Values are expressed as mean $\pm$ SD and p-values less than 0.05 are labelled with **.

by parent-artery flow rate), Caroff et al. [23] showed that complete occlusion group presented lower inflow ratios, similarly to our conclusions based upon ICI. However, this trend did not reach statistical significance in [23].

From Table 4.8, one can notice that no statistical difference were found for "pure" hemodynamic indices measured at the neck: Q^+ for all scenarios (pre, post and ratio) and ICI (post and ratio). The "pure" qualifying adjective stands for indices that do not contain geometrical parameters, as it is not the case for the flushing number FN. This finding is at odds with those of Cebral et al. [32], who identified reduction and post Q^+ as well as ICI reduction to be of significance between occlusion groups. This discrepancy with the present results might originate from multiple factors:

1. 80% of devices used in Cebral et al. [32] are Double-Layered WEBs, which comprise a higher density of wires at the proximal recess (see the left of Figure 4.2), entailing potentially higher flow-blockage and thus reducing neck-inflow values.

2. Cebral et al. cohort of patients exhibits a perfect balance of occluded and non-occluded cases (18/18), which increases statistical reliability compared to the present study.

3. The database contains a non-negligible number of protruding devices crossing the neck surface (44%), entailing the creation of two distinct groups of inflow ratio (high and low) as already stated previously (see Figure A.2). This separation creates a bias when analysing post-treatment neck-related quantities since measurements are highly dependent onto neck-placement with respect to the device. Despite being feasible in principle, performing inflow subgroups statistical analysis, *i.e.* comparing occlusion status for cases in the high inflow ratio group and doing likewise for the low inflow group, was not possible due to a substantial reduction of non-occluded cases in each inflow group (3 high, 3 low), de facto inducing a loss of statistical

Index	Success	Failure	p-value
Q^+			
pre	1.55 ± 1.31	1.28 ± 0.45	0.930
post	1.24 ± 1.46	0.81 ± 0.33	0.793
ratio	0.70 ± 0.32	0.73 ± 0.35	0.620
U_a			
pre	0.13 ± 0.08	0.09 ± 0.03	0.232
post	0.05 ± 0.05	0.02 ± 0.01	0.096*
ratio	0.31 ± 0.14	0.25 ± 0.11	0.540
ICI			
pre	2.12 ± 1.31	3.14 ± 0.93	**0.029****
post	1.80 ± 2.03	2.27 ± 1.68	0.398
ratio	0.72 ± 0.40	0.63 ± 0.36	0.838
SR_a			
pre	409.86 ± 228.40	258.14 ± 101.04	0.122
post	197.81 ± 221.29	80.02 ± 45.25	**0.044****
ratio	0.41 ± 0.20	0.33 ± 0.15	0.466
VO_a			
pre	297.17 ± 167.71	187.06 ± 73.55	0.109
post	131.58 ± 151.28	52.64 ± 32.04	0.051*
ratio	0.38 ± 0.19	0.30 ± 0.15	0.431
TAWSS			
pre	2.69 ± 2.29	1.66 ± 0.77	0.307
post	0.90 ± 1.15	0.27 ± 0.16	0.058*
ratio	0.30 ± 0.15	0.18 ± 0.07	0.051*
MATT			
pre	0.11 ± 0.07	0.25 ± 0.19	**0.011****
post	0.69 ± 1.23	1.02 ± 0.46	**0.006****
ratio	4.92 ± 4.64	5.13 ± 3.00	0.540
FN			
pre	7.56 ± 5.92	3.35 ± 1.51	**0.018****
post	5.34 ± 5.89	1.99 ± 0.83	**0.021****
ratio	0.69 ± 0.32	0.71 ± 0.33	0.540

Table 4.8: Hemodynamic related statistical differences. Values are expressed as mean ± SD and p-values less than 0.05 are labelled with **, while marginal significance p-values in $]0.05, 0.1]$ are labelled with *.

reliability and power. In addition to that, device protrusion rate is not reported by Cebral et al. [32], meaning that using their inflow rate results for comparisons with ours would be akin to compare apples and oranges.

A striking and counter-intuitive result from the present database is that post-treatment shear rates are significantly lower in non-occluded cases. Such trend is also found for U_a, VO_a and TAWSS with marginal significance. These findings are at odds with previous knowledge for FDs, as Mut et al. [102] demonstrated a significant increase of mean velocities and shear rates when going from fast to slow occlusion groups, owing to a proximal device mal-apposition that creates a leak feeding the aneurysm as exemplified for one presented case. This was also confirmed by Ouared et al. [110] who found mean velocity ratios to be higher in non-occluded groups and identified a minimum threshold of 0.65

velocity ratio to predict occlusion with 99% and 67% sensitivity and specificity, respectively. Nevertheless, care should be exercised when comparing with Ouared et al. [110] statistics since their cohort contained only 3/12 cases non-occluded. In vivo 3D-PCMRI results for FDs presented by Brina et al. [15] showed an almost significant trend towards lower systolic velocity reduction ratio PVRR in cases presenting late or no thrombosis at 12 months. Since PVRR is defined as $1-(U_a^{\text{post}}Q_{\text{ICA,pre}})/(U_a^{\text{pre}}Q_{\text{ICA,post}})$ with U_a being aneurysm velocity spatially averaged and Q_{ICA} parent artery flow rate, this means that the ratio $U_a^{\text{post}}/U_a^{\text{pre}}$ is greater for cases in the late thrombosis group, similarly to Ouared et al. [110] (the dependence on parent artery flow rate being neglected, as demonstrated in [15]). Interestingly, Brina et al. [15] found no statistical difference for time averaged PVRR, which was hypothesized by Brina et al. to be caused by time-averaging procedure containing low velocities for which 3D-PCMRI limitations might be at stake. Similar conclusions regarding U_a reduction were found for the sole in silico WEB study conducted by Cebral et al. [32], despite showing marginal levels of significance before adjustments for multiple comparisons. Nevertheless, care must be exercised when comparing the present results with those of Cebral et al. [32] for reasons detailed previously.

Such inverse statistical differences are also found for the MATT index for both pre and post scenarios, indicating that non-occluded aneurysms are more likely to harbour longer residence times, which is also counter-intuitive since thrombosis reactions needed to stabilize aneurysm sac and promote correct outcome are favoured by larger residence time that let these reactions to occur. The same counter-intuitive result is obtained for FN, since cases in non-occluded group exhibit a lower volume of blood flowing through the neck inside the sac, both before and after treatment. However, it is not yet clear if these statistical differences are caused by the fact that these variables (MATT and FN) contain an already significant geometrical index, aneurysm volume V_a, or if hemodynamic brings a significant weight.

In an attempt to understand these counter-intuitive results compared to FDs already existing correlations, we propose the following causes. On the one hand, intra-saccular hemodynamic alterations caused by the implantation of FDs and WEBs are different. First ones exhibit large recirculation regions inside the sac due to their lateral positioning with respect to the parent artery, and potential remanent jets caused by device proximal mal-apposition. In addition to that, the relative device proximity with neck surface and parent artery can induce neoendothelialisation on device surface starting from apposed device regions [71, 128], thereby isolating the aneurysm progressively. On the contrary, since WEBs are mostly indicated for bifurcating aneurysms, they are more likely to be subjected to strong impacting jets, a rare flow condition encountered by lateral aneurysms

treated with FDs. Moreover, WEBs porosity distribution across the neck is different to FDs. Therefore, comparing FDs and WEBs occlusion scores using different occlusion metrics for different flow topologies might not be relevant.

On the other hand, thrombosis mechanisms favouring occlusion are likely to be different for each device type. Indeed, levels of intra-saccular thrombosis were proven to be correlated to WEB shape modifications, causing the device to compress itself inside the sac [48]. Therefore, deployed WEB device positioning inside the sac can evolve during the healing process, leading to potential changes in occlusion score over time since it has been depicted in previous sections that hemodynamic environment is sensible to WEB positioning inside the sac, a situation which is not possible with FDs as they are static at the neck.

We thus propose the following mechanism to explain the link, previously identified in the cohort, between lower velocities, shear rates and higher MATT values in the non-occluded group compared to occluded one. Due to lower velocities and higher residence time, thrombosis reactions develop more rapidly for cases in the non-occluded group compared to the occluded one. Therefore, this gives rise to the formation of a thrombus inside the device and sac, which in turns can slightly modify WEB shape. Since the neck might not be correctly covered by the WEB due to previous shape modification, an intra-device opacification (score d) is therefore possible thanks to gaps at the neck for blood to flow inside the sac, or a neck remanent (score e) due to device retraction, or both (score f). Since thrombus formation is delayed in occluded cases due to higher velocities and lower residence times, changes in occlusion score due to WEB shape modifications are less likely to occur. However, several counter-arguments can call into question the present reasoning. Firstly, WSM has not been associated with clinical outcome in previous studies [20, 48]. Secondly, significant WSMs were only reported for 3 cases: 2 in the occluded and 1 in the non-occluded group, making this phenomenon the exception rather than the rule in the present cohort. However, we demonstrated in previous section that hemodynamic alterations are very sensible to device positioning inside the sac, meaning that a pronounced and visible WSM might not be needed to induce important hemodynamic changes.

Apart from [32] and to the knowledge of the authors, no other in silico studies intended to predict WEB outcomes based on hemodynamic have been performed in the literature, entailing that there is no means to cross-validate our counter-intuitive results and either refute or confirm the presented mechanism hypothesis. In addition to that, the only in vivo study comparing hemodyamic-like indices with WEB outcome found recently no statistical differences between occlusion groups [60].

Unravelling the exact mechanisms responsible for intra-saccular thrombus initiation, evolution and its link with medical outcome for WEB treated aneurysms

would enable to confirm or refute our previous reasoning. Answering these questions is feasible with very controlled in vitro experiments inside silicone models, as done recently by Gester et al. [58] for FDs. Gester et al. showed that although thrombus initiation was similar between two FD sizes deployed in the same geometry, thrombus composition evolved in time and resulted in two different scenarios: one size exhibited larger amounts of erythrocyte-rich regions compared to fibrin and platelet-rich areas, inducing an unstable thrombus that collapsed after silicone removal, while the other size harboured a more organized and stable thrombus with a higher proportion of fibrin-rich regions than the other size. Performing such kind of experiments with WEBs would be highly desirable and to date, no studies devoted to that topic were found in the literature to the authors' knowledge.

4.4 Limitations

This study harbours several important limitations, which have been empirically classified according to their importance:

1. Treatment outcome was assessed between 3 to 26 months after deployment in the present cohort. Nevertheless, CFD computations reflect flow conditions encountered seconds to minutes after device detachment, entailing that flow modifications induced by the potential presence of a thrombus inside the sac, or by device shape modifications, are not taken into account in the present modelling. This is best exemplified by Ding et al. [50] for dual-layers only and by the same team in [48]: angiograms obtained five minutes after device detachment resulted in different grading scores than those obtained three months later (see figure 3 in [50] for example). At the time of writing this study, angiographic control images after device deployment were not available. Therefore, comparisons with such images should be seriously investigated to make sure that angiographic qualitative features such as intra-saccular jets and recirculations are qualitatively recovered numerically. Despite CFD computations are not able to model the full development of a thrombus inside the sac, performing such comparisons would build confidence that the numerical hemodynamic starting point environment after device deployment is similar to the one found in vivo.

2. The "true" in vivo device positioning inside the sac was not directly compared to simulations, which is difficult to perform quantitatively using control images. However, this limitation can be mitigated by the fact that all WEB numerical deployments followed the same recommendations used

by physicians during procedure, namely to minimize the distance to the neck while preventing protrusion and filling the sac as much as possible, since R_d and D_{neck} medians are high and low in the present cohort (0.8 and 0.5 mm, see Figure A.1), respectively. To measure the impact of this limitation without knowing a priori the "true" in vivo device position inside the sac, one could numerically deploy the same device size multiple times by changing for example the neck-to-dome centerline (see Figure 4.4b) and perform CFD computation for each placement. This would allow to study hemodynamic variability with respect to device positioning and assess if previous statistical differences are impacted. It is expected that performing such study would be more relevant for non-apposed device cases, since apposed ones have no room for manoeuvre inside the sac.

3. An imbalance between occluded and non-occluded groups was present in the cohort, inducing low statistical reliability. In addition to that, we only performed univariate statistical analysis due to the low number of available cases, thus setting aside potential interactions between indices that could have been detected with multi-variate analysis for more cases.

4. We have not performed inter and intra-observer agreement for the occlusion score we used (BOSS), which could build confidence in the present results if it were to be realized. Moreover, the use of multiple occlusion gradation scores could promote a deeper understanding of occlusion patterns and initiate a fruitful discussion on the link between hemodynamic and occlusion.

5. The exact number of wires per device size was not communicated by the manufacturer and was fixed to 144 for all computations. Conducting a comparative study using the same geometry and device size by varying the number of wires from 144 to the exact value (if known) would reveal this parameter importance with respect to statistical results.

6. Idealized boundary conditions were used at arterial inlets since patient-specific flow rates were not available. In addition to that, rigid walls and Newtonian fluid hypothesis were prescribed, as classically done in the field of aneurysmal CFD. Despite taking into account more complex phenomenon such as wall motion and blood shear thinning is of course needed to provide more faithful computations, Steinman and Pereira [136] recently identified that their impact is lower compared to segmentation and imaging modalities for example.

4.5 Conclusion

In this chapter, the heterogeneous model was applied to a "real-world" application involving many different patient-specific geometries treated with WEB devices. A collaboration with an interventional neuroradiologist was conducted (Dr. Mantilla) in order to have access to a patient-specific database of cases treated with WEBs and for which follow-up scores were available. Specific semi-automatic and as intuitive as possible numerical tools were developed for pre and post-processing of numerical computations, with the intention to be used by non-CFD users (as it was the case for Dr. Mantilla). This allowed Dr. Mantilla to prepare 70% of the cases presented in this chapter, and post-processing steps were entirely automatized.

This chapter can be considered as a pilot study answering the following questions:

- "Can we build a hemodynamic database of WEB treated aneurysms at low computational costs with non-CFD experts?"
- "Using this database, is it possible to have first insights into occlusion mechanisms and their link with hemodynamic and geometrical parameters?"

Answers to the first question were given in Section 4.3.1, where we showed that the hemodynamics database contained a wide variety of pre-treatment flow patterns owing to various parent-artery geometries and that a classification was possible. Moreover, post-treatment velocity fields were analysed, revealing that important questions regarding device apposition and protrusion impact onto hemodynamics could be answered using the database.

Concerning the second question, addressed in Section 4.3.2, several geometrical and hemodynamics indices were found to be correlated to occlusion status. Nevertheless, and specifically for hemodynamics, several counter-intuitive results were found. Due to literature scarcity on hemodynamic with WEB treated aneurysms, both in silico and in vivo, no confirmation nor refutation of the mechanisms proposed in this chapter to explain these counter-intuitive results was possible. In addition to that, several important limitations were identified and should be considered when analysing the statistical results presented herein. Therefore, this chapter can be considered as a first step towards understanding WEB occlusion and hemodynamics, and that many more steps are necessary to build entire confidence in the present results and proposed mechanisms.

Chapter 5

Conclusions and perspectives

Chapter contents

5.1 Heterogeneous model enhancements

Model development and idealized validation presented in Chapter 2 showed that drag force models planar to the device, *i.e.* tangential and longitudinal, are overestimated compared to conformal computations, especially at low $\tilde{W}/D$ values and when the incoming flow is tangential to the device surface. Despite this overestimation was found to have limited consequences in the patient specific validation in Chapter 3, flow redirection at the neck for one case (e23R) was greater than GMU results, causing large errors downstream in the sac. Therefore, enhancing models for planar drag forces is needed to improve heterogeneous results and further establish the present model versatility. This would need to take into account more complex phenomena that have been neglected so far such that longitudinal and extra-family interactions between cylinders. On the other hand, patient-specific validation for WEBs demonstrated that the normal component drag model underestimates conformal forces, as the remaining jet intensity downstream to the device was larger in heterogeneous results compared to GMU. Including crossings effects, that have only been modelled by a simple superposition of cylinder forces coming from each family, should be considered to mitigate the aforementioned issue.

In addition to that, including diffusive regimes, *i.e.* low Reynolds number, in the proposed approach operating range would be beneficial to increase its versatility. However, this is considered to be a second order improvement as no significant impact of this lack in the proposed model has been noticed in the patient-specific validation.

The unperturbed upstream velocity $\mathbf{U}_\infty$ reconstruction procedure presented in Section 3.1 makes use of multiple hypothesis that can be relaxed once a greater comprehension of the interactions between local flow patterns and upstream ones is achieved. Moreover, the procedure fitted the angular redirection law at $\mathrm{Re} = 5$ only and summarized local flow patterns with one averaged angle value only. This could be overcome by implementing more complex techniques such as Machine Learning (ML). Algorithm inputs could be for example geometricals (*i.e.* the relative distance between interpolation points and wires locations) and fluid-related (*i.e.* flow rate and local velocity angle with respect to the local wire orientation), whereas the output would be the reconstructed $\mathbf{U}_\infty$ vector. Such ML algorithm could be trained and tested using 3D conformal computations described in Section 2.2.3 and should be envisioned for future developments as drag models highly depends on the quality of this input data.

The aforementioned potential enhancements highlight one major advantage of the current proposed approach compared to homogeneous methods: sub-models such as drag force models (tangential, longitudinal and normal) can be revisited and improved once the general implementation is carried-out in a given numerical solver.

5.2 Validation improvements

The patient-specific validation presented in Chapter 3 was based on comparisons with three porous models to assess the benefits brought by the current approach. Nevertheless, several other homogeneous strategies have been developed recently and should be implemented in YALES2BIO to be compared on the same FDs cases. For example, the screen model developed by Li et al. [81] which is intended to reproduce local flow redirection induced by the device and account for device porosity inhomogeneities at the neck should be considered of interest for implementation in our CFD code. Moreover, the recent heterogeneous model introduced by Yadollahi-Farsani et al. [158] that resulted from similar observations and motivations as those emphasized in the present thesis, namely the ability to reproduce local struts-induced flow heterogeneities while keeping low computational costs, should be compared with the current work. Implementing such models in the same CFD code, *i.e.* YALES2BIO, would enable to study in details models performances by keeping other potential sources of differences such as

boundary conditions, spatial and temporal numerical orders in the background. This would also allow to compare computational efficiency thoroughly.

When introducing a novel model, reference data coming from gold-standard frameworks is needed to assess its accuracy. As commonly done in CFD for treated IAs, such data was considered to be conformal results in the present thesis, *i.e.* in silico. Nevertheless, there is growing evidence from the literature that CFD for FD-treated aneurysm can be accurately compared to Particle Image Velocimetry (PIV) results, as carried-out by Bouillot et al. [12, 13], Liou and Li [85]. Moreover, 4D Flow MRI has proven to provide reliable measurements of intra-saccular velocities for endovascularly treated IAs [15, 56, 114]. Therefore, being able to compare the current numerical model with experimental measurements from PIV and/or 4D Flow MRI would provide invaluable validation, on the condition that comparisons are carried-out carefully as stated recently by Puiseux et al. [119] for 4D Flow MRI.

5.3 Thrombosis

Hemodynamics alone cannot predict thrombus formation and more importantly, clot composition and its long-term stability, as recently noticed by Sarrami-Foroushani et al. [130]. These authors successfully managed to numerically reproduce clot composition and shape in two FD treated idealized geometries coming from an in vitro study by Gester et al. [58]. Despite both FD configurations harboured similar favourable outcome results based solely on hemodynamics criteria, clot composition and quality varied between unorganized red thrombi and stable platelet-rich. Therefore, among all potential perspectives, adding thrombosis models to the current hemodynamics framework would be invaluable in outcome prediction, as envisioned recently by Ngoepe et al. [107]. This would notably need to develop a multi-scale methodology able to handle the wide time scales involved in thrombosis, as clot initiation and maturation can take between days to months to develop whereas current hemodynamics computations only represent a few seconds. Moreover, a delicate balance between thrombosis models complexity, computational costs and usability in clinically relevant context should be found to ensure that such a tool is useful to the clinical community, wherein short time frames are the rule rather than the exception. Sensitivity analysis and model reduction for numerical coagulation cascade models are necessary in order to reach such balance and were recently carried-out by Méndez Rojano et al. [95], whose model have been implemented in YALES2BIO. Computational models intended to reproduce clot development in patient-specific IAs such as the ones presented by Ngoepe and Ventikos [105], Peach et al. [111] or Sarrami-Foroushani et al. [130] could be good starting points to a future framework implementation

in YALES2BIO, alongside with specifically designed device-related thrombosis models already available in the current CFD solver (see Méndez Rojano et al. [94]).

Appendix

Heterogeneous model application to intrasaccular device

Chapter contents

A.1 Correlations results

Raw data used to produce correlations with medical outcome results presented in Section 4.3.2 are available here. For each graph, aneurysm location as well as occlusion score are given, along with median, first and third quartiles values in solid and dotted lines, respectively.

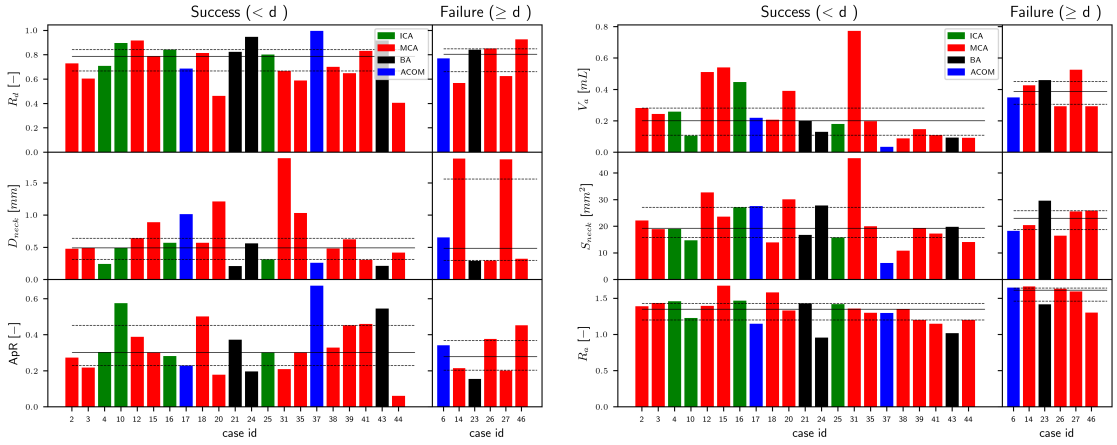

Figure A.1: Geometrical and device-related indices

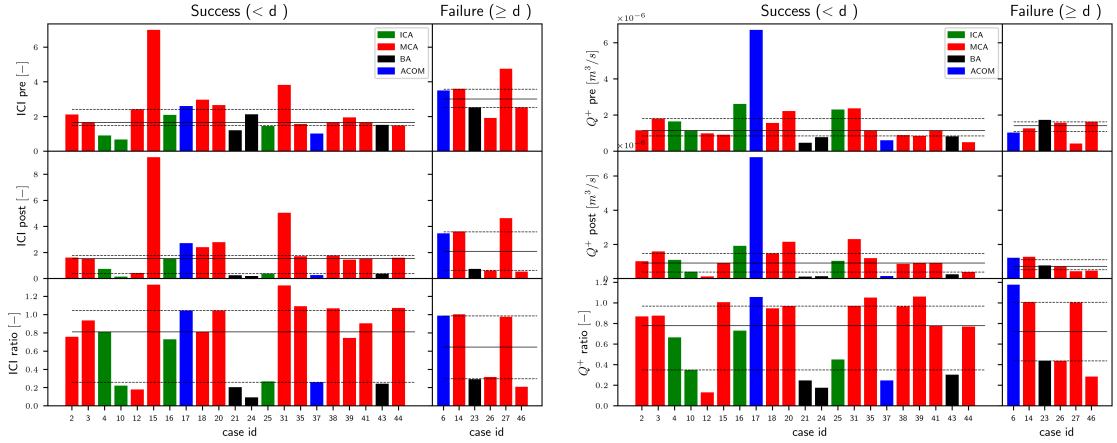

Figure A.2: ICI and Q^+

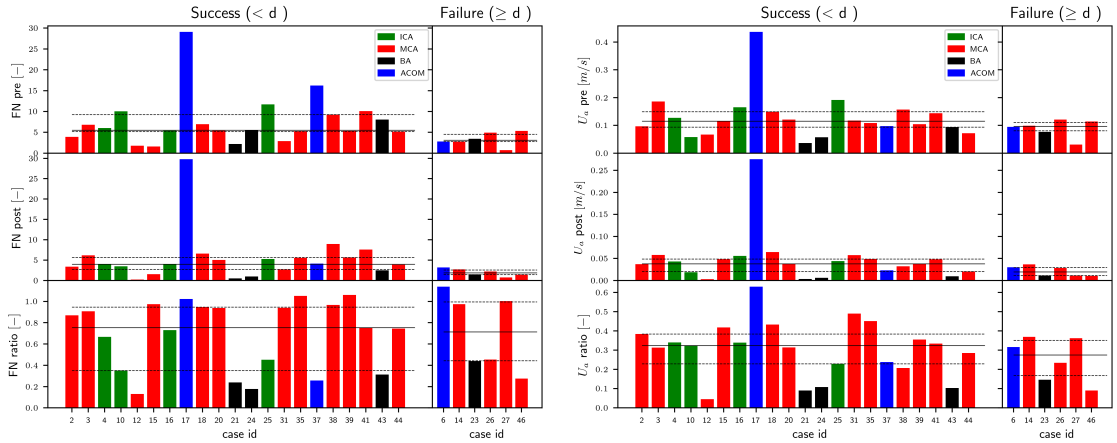

Figure A.3: FN and U_a

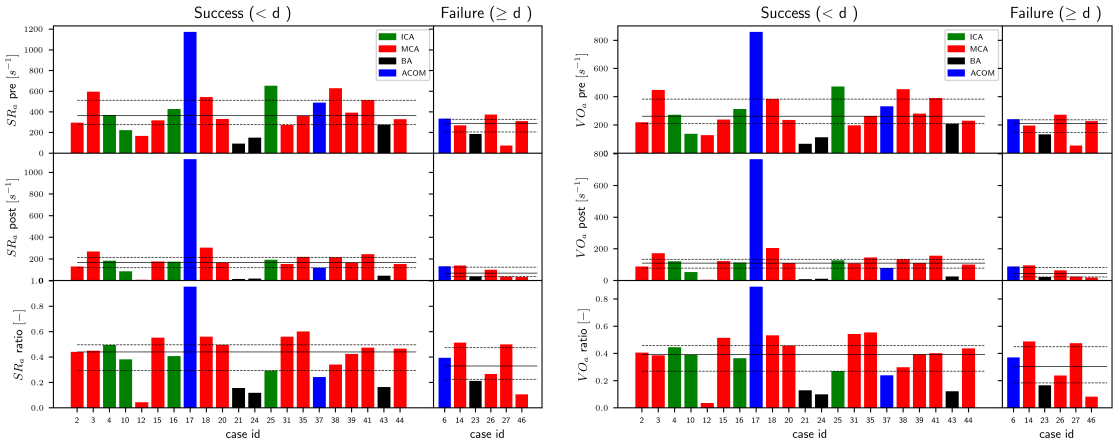

Figure A.4: SR_a and VO_a

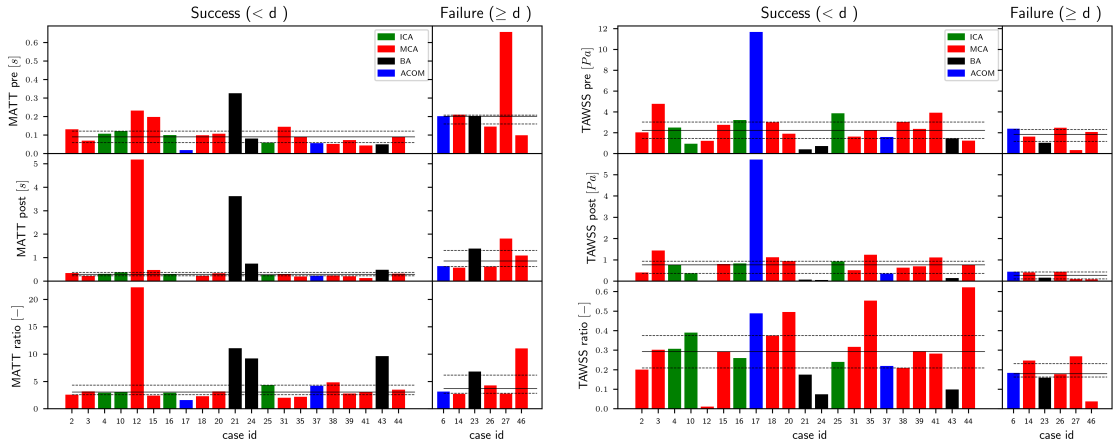

Figure A.5: MATT and TAWSS

Nomenclature

ACA Anterior Carotid Artery

ACOM Anterior Communicating artery

ADPKD Autosomal Dominant Polycystic Kidney Disease

BA Basilar Artery

BOSS Beaujon Occlusion Scale Score

CE Conformité Européenne

CFD Computational Fluid Dynamics

CoW Circle of Willis

CS Cardiovascular System

CT Computed Tomography

EC Endothelial Cells

FD Flow-Diverter

FDA Food and Drug Administration

FIAs Familial Intracranial Aneurysms

GMU George Mason University

IA Intracranial Aneurysm

IBM Immersed Boundary Method

ICA Internal Carotid Artery

ISUIA International Study of Unruptured Intracranial Aneurysm

MCA Middle Carotid Artery

PCOM Posterior Communicating artery

PED Pipeline Embolization Device

RBC Red Blood Cell

RKPM Reproducing Kernel Particle Methods

ROI Region Of Interest

SAH Subarachnoid Haemorrhage

UIAs Unruptured Intracranial Aneurysms

VMTK Vascular Modelling Toolkit

VTK Visualization Toolkit

WBC White Blood Cell

WEB Woven EndoBridge

WNBAs Wide-Neck Bifurcation Aneurysms

WSM WEB Shape Modification

YALES2 Yet Another LES Solver

Bibliography

[1] M. I. Chaudry A. M. Spiotta, R. D. Turner and A. S. Turk. *Management of Cerebrovascular Disorders*. Springer International Publishing, 2019. doi: 10.1007/978-3-319-99016-3. URL https://www.springer.com/gp/book/9783319990156#aboutBook.

[2] P. Angot, C.-H. Bruneau, and P. Fabrie. A penalization method to take into account obstacles in incompressible viscous flows. *Numerische Mathematik*, 81(2):497–520, 1999. doi: http://dx.doi.org/10.1007/s002110050401.

[3] S. Ansari, M. Dadmehr, B. Eftekhar, D. J. McConnell, S. Ganji, H. Azari, S. Kamali-Ardakani, B. L. Hoh, and J. Mocco. A simple technique for morphological measurement of cerebral arterial circle variations using public domain software (osiris). *Anatomy & Cell Biology*, 44:324, 2011. doi: http://dx.doi.org/10.5115/acb.2011.44.4.324.

[4] L. Antiga, M. Piccinelli, L. Botti, B. Ene-Iordache, A. Remuzzi, and D. A. Steinman. An image-based modeling framework for patient-specific computational hemodynamics. *Medical & Biological Engineering & Computing*, 46(11):1097–1112, November 2008. doi: 10.1007/s11517-008-0420-1. URL http://link.springer.com/10.1007/s11517-008-0420-1.

[5] T. Aoki, M. Nishimura, T. Matsuoka, K. Yamamoto, T. Furuyashiki, H. Kataoka, S. Kitaoka, R. Ishibashi, A. Ishibazawa, S. Miyamoto, R. Morishita, J. Ando, N. Hashimoto, K. Nozaki, and S. Narumiya. Pge2-ep2 signalling in endothelium is activated by haemodynamic stress and induces cerebral aneurysm through an amplifying loop via nf-κb. *British Journal of Pharmacology*, 163(6):1237–1249, 2011. doi: http://dx.doi.org/10.1111/j.1476-5381.2011.01358.x.

[6] Caltagirone JP. Arquis E. Sur les conditions hydrodynamiques au voisinage d'une interface milieu fluide-milieu poreux: application à la convection naturelle. *Comptes rendus de l'Académie des sciences*, 299:1–4, 1984.

[7] L. Augsburger, P. Reymond, D. A. Rufenacht, and N. Stergiopulos. Intracranial stents being modeled as a porous medium: Flow simulation in stented cerebral aneurysms. *Annals of Biomedical Engineering*, 39(11):850–863, 2010. doi: http://dx.doi.org/10.1007/s10439-010-0200-6.

[8] Barbour. *Computational and Experimental Investigation into the Hemodynamics of Endovascularly Treated Cerebral Aneurysms*. PhD thesis, University of Washington, 2018. URL https://digital.lib.washington.edu/researchworks/handle/1773/41820.

[9] T. Becske, D. F. Kallmes, I. Saatci, C. G. McDougall, I. Szikora, G. Lanzino, C. J. Moran, H. H. Woo, D. K. Lopes, A. L. Berez, D. J. Cher, A. H. Siddiqui, E. I. Levy, F. C. Albuquerque, D. J. Fiorella, Z. Berentei, M. Marősfoi, S. H. Cekirge, and P. K. Nelson. Pipeline for uncoilable or failed aneurysms: Results from a multicenter clinical trial. *Radiology*, 267(6): 858–868, 2013. doi: http://dx.doi.org/10.1148/radiol.13120099.

[10] Yassine Berrada. Penalization in a fourth order code for incompressible flows to handle fixed and moving immersed bodies. Master's thesis, Ecole polytechnique de Louvain, 2019.

[11] J. G. Betts, P. Desaix, E. Johnson, J. E. Johnson, O. Korol, D. Kruse, B. Poe, J. A. Wise, M. Womble, and K. A. Young. *Anatomy & Physiology*. 2013.

[12] P. Bouillot, O. Brina, R. Ouared, K.-O. Lovblad, M. Farhat, and V. M. Pereira. Particle imaging velocimetry evaluation of intracranial stents in sidewall aneurysm: Hemodynamic transition related to the stent design. *PLoS One*, 9(12):e113762, 2014. doi: http://dx.doi.org/10.1371/journal.pone.0113762.

[13] P. Bouillot, O. Brina, R. Ouared, H. Yilmaz, K.-O. Lovblad, M. Farhat, and V. Mendes Pereira. Computational fluid dynamics with stents: quantitative comparison with particle image velocimetry for three commercial off the shelf intracranial stents. *Journal of NeuroInterventional Surgery*, 8:309–315, 2015. doi: 10.1136/neurintsurg-2014-011468.

[14] P. Bouillot, O. Brina, R. Ouared, H. Yilmaz, M. Farhat, G. Erceg, K.-O. Lovblad, M. I. Vargas, Z. Kulcsar, and V. M. Pereira. Geometrical deployment for braided stent. *Medical Image Analysis*, 30(5):85–94, 2016. doi: http://dx.doi.org/10.1016/j.media.2016.01.006.

[15] O. Brina, P. Bouillot, P. Reymond, A. S. Luthman, C. Santarosa, M. Fahrat, K. O. Lovblad, P. Machi, B. M. A. Delattre, V. M. Pereira, and M. I. Vargas. How flow reduction influences the intracranial aneurysm occlusion: A prospective 4d phase-contrast mri study. *American Journal of Neuroradiology*, (11), 2019. doi: http://dx.doi.org/10.3174/ajnr.A6312.

[16] W. Brinjikji, M. H. Murad, G. Lanzino, H. J. Cloft, and D. F. Kallmes. Endovascular treatment of intracranial aneurysms with flow diverters: A meta-analysis. *Stroke*, 44(2):442–447, 2013. doi: http://dx.doi.org/10.1161/STROKEAHA.112.678151.

[17] J. L. Brisman, J. K. Song, and D. W. Newell. Cerebral aneurysms. *New England Journal of Medicine*, 355(8):928–939, 2006. doi: http://dx.doi.org/10.1056/NEJMra052760.

[18] J. P. Broderick, R. D. Brown, L. Sauerbeck, R. Hornung, J. Huston, D. Woo, C. Anderson, G. Rouleau, D. Kleindorfer, M. L. Flaherty, I. Meissner, T. Foroud, E. Charles, J. Moomaw, and E. S. Connolly. Greater rupture risk for familial as compared to sporadic unruptured intracranial aneurysms. *Stroke*, 40(6):1952–1957, 2009. doi: http://dx.doi.org/10.1161/STROKEAHA.108.542571.

[19] R. D. Brown, J. Huston, R. Hornung, T. Foroud, D. F. Kallmes, D. Kleindorfer, I. Meissner, D. Woo, L. Sauerbeck, and J. Broderick. Screening for brain aneurysm in the familial intracranial aneurysm study: frequency and predictors of lesion detection. *Journal of Neurosurgery*, 108(6):1132–1138, 2008. doi: http://dx.doi.org/10.3171/JNS/2008/108/6/1132.

[20] F. Cagnazzo, R. Ahmed, R. Zannoni, C. Dargazanli, P.-H. Lefevre, G. Gascou, I. Derraz, C. Riquelme, A. Bonafe, and V. Costalat. Predicting factors of angiographic aneurysm occlusion after treatment with the woven endobridge device: A single-center experience with midterm follow-up. *American Journal of Neuroradiology*, (9), 2019. doi: http://dx.doi.org/10.3174/ajnr.A6221.

[21] J. K. Campos, B. Cheaney II, B. V. Lien, D. A. Zarrin, C. D. Vo, G. P. Colby, L.-M. Lin, and A. L. Coon. Advances in endovascular aneurysm management: flow modulation techniques with braided mesh devices. *Stroke and Vascular Neurology*, 5(3):1–13, 2020. doi: http://dx.doi.org/10.1136/svn-2020-000347.

[22] J. Caroff, C. Mihalea, J. Klisch, C. Strasilla, A. Berlis, T. Patankar, W. Weber, D. Behme, E. A. Jacobsen, T. Liebig, S. Prothmann, C. Cognard, T. Finkenzeller, J. Moret, and L. Spelle. Single-layer webs: Intrasaccular flow disrupters for aneurysm treatment—feasibility results from a european study. *American Journal of Neuroradiology*, 36(7):1942–1946, 2015. doi: http://dx.doi.org/10.3174/ajnr.A4369.

[23] J. Caroff, C. Mihalea, V. Da Ros, T. Yagi, M. Iacobucci, L. Ikka, J. Moret, and L. Spelle. A computational fluid dynamics (cfd) study of web-treated

aneurysms: Can cfd predict web "compression" during follow-up? *Journal of Neuroradiology*, 44(7):262–268, 2017. doi: http://dx.doi.org/10.1016/j.neurad.2017.03.005.

[24] R. J. Casson and L. D. Farmer. Understanding and checking the assumptions of linear regression: a primer for medical researchers: Assumptions of linear regression. *Clinical & Experimental Ophthalmology*, 42(6):590–596, 2014. doi: http://dx.doi.org/10.1111/ceo.12358.

[25] M. A. Castro, C. M. Putman, M. J. Sheridan, and J. R. Cebral. Hemodynamic patterns of anterior communicating artery aneurysms: A possible association with rupture. *American Journal of Neuroradiology*, 30(1):297–302, 2009. doi: http://dx.doi.org/10.3174/ajnr.A1323.

[26] J. R. Cebral and R. Löhner. Efficient simulation of blood flow past complex endovascular devices using an adaptive embedding technique. *IEEE Transactions on Medical Imaging*, 24(4):468–476, 2005. doi: http://dx.doi.org/10.1109/TMI.2005.844172.

[27] J. R. Cebral, M. A. Castro, J. E. Burgess, R. S. Pergolizzi, M. J. Sheridan, and C. M. Putman. Characterization of cerebral aneurysms for assessing risk of rupture by using patient-specific computational hemodynamics models. *American Journal of Neuroradiology*, 26(10):2550–9, 2005. URL https://www.ncbi.nlm.nih.gov/pubmed/16286400.

[28] J. R. Cebral, M. A. Castro, C. M. Putman, and N. Alperin. Flow–area relationship in internal carotid and vertebral arteries. *Physiological Measurement*, 29(5):585–594, 2008. doi: http://dx.doi.org/10.1088/0967-3334/29/5/005.

[29] J. R. Cebral, M. Sheridan, and C. M. Putman. Hemodynamics and bleb formation in intracranial aneurysms. *American Journal of Neuroradiology*, 31(10):304–310, 2009. doi: http://dx.doi.org/10.3174/ajnr.A1819.

[30] J. R. Cebral, F. Mut, J. Weir, and C. M. Putman. Association of hemodynamic characteristics and cerebral aneurysm rupture. *American Journal of Neuroradiology*, 32(11):264–270, 2011. doi: http://dx.doi.org/10.3174/ajnr.A2274.

[31] J.R. Cebral, M. Raschi, F. Mut, Y.-H. Ding, D. Dai, R. Kadirvel, and D. Kallmes. Analysis of flow changes in side branches jailed by flow diverters in rabbit models. *International Journal for Numerical Methods in Biomedical Engineering*, 30:988–999, 2014. doi: 10.1002/cnm.2640.

[32] J.R. Cebral, B.J. Chung, F. Mut, J. Chudyk, C. Bleise, E. Scrivano, P. Lylyk, R. Kadirvel, and D. Kallmes. Analysis of flow dynamics and outcomes of cerebral aneurysms treated with intrasaccular flow-diverting devices. *American Journal of Neuroradiology*, 2019. doi: https://doi.org/10.3174/ajnr.A6169.

[33] N. Chalouhi, B. L. Hoh, and D. Hasan. Review of cerebral aneurysm formation, growth, and rupture. *Stroke*, 44(12):3613–3622, 2013. doi: http://dx.doi.org/10.1161/STROKEAHA.113.002390.

[34] C. Chnafa, S. Mendez, and F. Nicoud. Image-based large-eddy simulation in a realistic left heart. *Computers and Fluids*, 94:173–187, 2014.

[35] C. Chnafa, S. Mendez, and F. Nicoud. Image-based simulations show important flow fluctuations in a normal left ventricle: What could be the implications? *Annals of Biomedical Engineering*, 44(11):3346–3358, 2016.

[36] C. Chnafa, P. Bouillot, O. Brina, B. M. A. Delattre, M. I. Vargas, K. O. Lovblad, V. M. Pereira, and D. A. Steinman. Vessel calibre and flow splitting relationships at the internal carotid artery terminal bifurcation. *Physiological Measurement*, 38(11):2044–2057, 2017. doi: http://dx.doi.org/10.1088/1361-6579/aa92bf.

[37] C. Chnafa, P. Bouillot, O. Brina, M. Najafi, B. M. A. Delattre, M. I. Vargas, V. M. Pereira, and D. A. Steinman. Errors in power-law estimations of inflow rates for intracranial aneurysm cfd. *Journal of Biomechanics*, 80 (10):159–165, 2018. doi: http://dx.doi.org/10.1016/j.jbiomech.2018.09.006.

[38] K. J. Chodzyǹski, P. Uzureau, V. Nuyens, A. Rousseau, G. Coussement, and K. Zouaoui Boudjeltia. The impact of arterial flow complexity on flow diverter outcomes in aneurysms. *Scientific Reports*, 10(6), 2020. doi: http://dx.doi.org/https://doi.org/10.1038/s41598-020-67218-9.

[39] W. Chong, Y. Zhang, Y. Qian, L. Lai, G. Parker, and K. Mitchell. Computational hemodynamics analysis of intracranial aneurysms treated with flow diverters: Correlation with clinical outcomes. *American Journal of Neuroradiology*, 35(11):136–142, 2013. doi: http://dx.doi.org/10.3174/ajnr.A3790.

[40] C. Cognard and A. C. Januel. Remnants and recurrences after the use of the web intrasaccular device in large-neck bifurcation aneurysms. *Neurosurgery*, 76(2):522–530, 2015. doi: http://dx.doi.org/10.1227/NEU.0000000000000669.

[41] D. G. Crowdy. Uniform flow past a periodic array of cylinders. *European Journal of Mechanics - B/Fluids*, 56(3):120–129, 2016. doi: http://dx.doi.org/10.1016/j.euromechflu.2015.10.003.

[42] R. J. Damiano, V. M. Tutino, N. Paliwal, D. Ma, J. M. Davies, A. H. Siddiqui, and H. Meng. Compacting a single flow diverter versus overlapping flow diverters for intracranial aneurysms: A computational study. *American Journal of Neuroradiology*, 38(1):603–610, 2017. doi: http://dx.doi.org/10.3174/ajnr.A5062.

[43] W. E. Dandy. Intracranial aneurysm of the internal carotid artery: cured by operation. *Annals of Surgery*, 107(5):654–659, 1938. doi: http://dx.doi.org/10.1097/00000658-193805000-00003.

[44] C. Dapogny, C. Dobrzynski, and P. Frey. Three-dimensional adaptive domain remeshing, implicit domain meshing, and applications to free and moving boundary problems. *Journal of Computational Physics*, 262(4):358–378, 2014. doi: http://dx.doi.org/10.1016/j.jcp.2014.01.005.

[45] N. Dazeo, J. Dottori, G. Boroni, and I. Larrabide. A comparative study of porous medium cfd models for flow diverter stents: Advantages and shortcomings. *International Journal for Numerical Methods in Biomedical Engineering*, 34(9):e3145, 2018. doi: http://dx.doi.org/10.1002/cnm.3145.

[46] N. Dazeo, J. Dottori, G. Boroni, A. P. Narata, and I. Larrabide. Stenting as porous media in anatomically accurate geometries. a comparison of models and spatial heterogeneity. *Journal of Biomechanics*, 110(9):109945, 2020. doi: http://dx.doi.org/10.1016/j.jbiomech.2020.109945.

[47] N. K. de Rooij, F. H. H. Linn, J. A. van der Plas, A. Algra, and G. J. E. Rinkel. Incidence of subarachnoid haemorrhage: a systematic review with emphasis on region, age, gender and time trends. *Journal of Neurology, Neurosurgery & Psychiatry*, 78(12):1365–1372, 2007. doi: http://dx.doi.org/10.1136/jnnp.2007.117655.

[48] Y. Ding, D. Dai, A. Rouchaud, K. Janot, S. Asnafi, D. F. Kallmes, and R. Kadirvel. Web device shape changes in elastase-induced aneurysms in rabbits. *American Journal of Neuroradiology*, 42(12):334–339, 2020. doi: http://dx.doi.org/10.3174/ajnr.A6899.

[49] Y. H. Ding, D. A. Lewis, R. Kadirvel, D. Dai, and D. F. Kallmes. The woven endobridge: A new aneurysm occlusion device. *American Journal of Neuroradiology*, 32(2):607–611, 2011. doi: http://dx.doi.org/10.3174/ajnr.A2399.

[50] Y.-H. Ding, D. Dai, D. Schroeder, R. Kadirvel, and D. F. Kallmes. Experimental testing of the dual-layer woven endobridge device using an elastase-induced aneurysm model in rabbits. *Interventional Neuroradiology*, 22(2): 299–303, 2016. doi: http://dx.doi.org/10.1177/1591019916628202.

[51] A. A. Dmytriw, M. M. Salem, V. X. D. Yang, T. Krings, V. M. Pereira, J. M. Moore, and A. J. Thomas. Endosaccular flow disruption: A new frontier in endovascular aneurysm management. *Neurosurgery*, 86(3):170–181, 2019. doi: http://dx.doi.org/10.1093/neuros/nyz017.

[52] S. D'Souza. Aneurysmal subarachnoid hemorrhage:. *Journal of Neurosurgical Anesthesiology*, 27(7):222–240, 2015. doi: http://dx.doi.org/10.1097/ANA.0000000000000130.

[53] D. B. Ellegala and A. L. Day. Ruptured cerebral aneurysms. *New England Journal of Medicine*, 352(1):121–124, 2005. doi: http://dx.doi.org/10.1056/NEJMp048301.

[54] N. Etminan and G. J. Rinkel. Unruptured intracranial aneurysms: development, rupture and preventive management. *Nature Reviews Neurology*, 12(11):699–713, 2016. doi: http://dx.doi.org/10.1038/nrneurol.2016.150.

[55] M. D. Ford, N. Alperin, S. H. Lee, D. W. Holdsworth, and D. A. Steinman. Characterization of volumetric flow rate waveforms in the normal internal carotid and vertebral arteries. *Physiological Measurement*, 26(4):477–488, 2005. doi: http://dx.doi.org/10.1088/0967-3334/26/4/013.

[56] S. V. Frolov, S. V. Sindeev, J. S. Kirschke, P. Arnold, S. Prothmann, D. Liepsch, A. Balasso, A. Potlov, I. Larrabide, and S. Kaczmarz. Cfd and mri studies of hemodynamic changes after flow diverter implantation in a patient-specific model of the cerebral artery. *Experiments in Fluids*, 59(11), 2018. doi: http://dx.doi.org/10.1007/s00348-018-2635-8.

[57] D. Gallo, D. A. Steinman, P. B. Bijari, and U. Morbiducci. Helical flow in carotid bifurcation as surrogate marker of exposure to disturbed shear. *Journal of Biomechanics*, 45(9):2398–2404, 2012. doi: http://dx.doi.org/10.1016/j.jbiomech.2012.07.007.

[58] K. Gester, I. Lüchtefeld, M. Büsen, S. J. Sonntag, T. Linde, U. Steinseifer, and G. Cattaneo. In vitro evaluation of intra-aneurysmal, flow-diverter-induced thrombus formation: A feasibility study. *American Journal of Neuroradiology*, 37(10):490–496, 2015. doi: http://dx.doi.org/10.3174/ajnr.A4555.

[59] C. Geuzaine and J.-F. Remacle. Gmsh: A 3-d finite element mesh generator with built-in pre- and post-processing facilities. *International Journal for Numerical Methods in Engineering*, 79(9):1309–1331, 2009. doi: http://dx.doi.org/10.1002/nme.2579.

[60] P. Gölitz, H. Luecking, P. Hoelter, F. Knossalla, and A. Doerfler. What is the hemodynamic effect of the woven endobridge? an in vivo quantification using time-density curve analysis. *Neuroradiology*, 62(3):1043–1050, 2020. doi: http://dx.doi.org/10.1007/s00234-020-02390-3.

[61] J. P. Greving, M. J. H. Wermer, R. D. Brown, A. Morita, S. Juvela, M. Yonekura, T. Ishibashi, J. C. Torner, T. Nakayama, G. J. E. Rinkel, and A. Algra. Development of the phases score for prediction of risk of rupture of intracranial aneurysms: a pooled analysis of six prospective cohort studies. *The Lancet Neurology*, 13(1):59–66, 2014. doi: http://dx.doi.org/10.1016/S1474-4422(13)70263-1.

[62] Lola Guedot. *Développement de méthodes numériques pour la caractérisation des grandes structures tourbillonnaires dans les brûleurs aéronautiques : application aux systèmes d'injection multi-points.* PhD thesis, INSA de Rouen, 2015.

[63] K. A. Hackenberg, D. Hänggi, and N. Etminan. Unruptured intracranial aneurysms: Contemporary data and management. *Stroke*, 49(9):2268–2275, 2018. doi: http://dx.doi.org/10.1161/STROKEAHA.118.021030.

[64] C. Hahn and M. A. Schwartz. Mechanotransduction in vascular physiology and atherogenesis. *Nature Reviews Molecular Cell Biology*, 10(1):53–62, 2009. doi: http://dx.doi.org/10.1038/nrm2596.

[65] T. Hashimoto, H. Meng, and W. L. Young. Intracranial aneurysms: links among inflammation, hemodynamics and vascular remodeling. *Neurological Research*, 28(6):372–380, 2006. doi: http://dx.doi.org/10.1179/016164106X14973.

[66] Y. Hoi, B. A. Wasserman, Y. J. Xie, S. S. Najjar, L. Ferruci, E. G. Lakatta, G. Gerstenblith, and D. A Steinman. Characterization of volumetric flow rate waveforms at the carotid bifurcations of older adults. *Physiological Measurement*, 31(3):291–302, March 2010. doi: 10.1088/0967-3334/31/3/002. URL http://stacks.iop.org/0967-3334/31/i=3/a=002?key=crossref.d0c2fda4d23842496e89dc93a8607322.

[67] I. E. Idelchik. *Handbook of Hydraulic Resistance*. BHB, fourth 4th edition, 2008. URL https://www.begellhouse.com/ebook_platform/5877598576b05c67.html.

[68] C. Iss, D. Midou, A. Moreau, D. Held, A. Charrier, S. Mendez, A. Viallat, and E. Helfer. Self-organization of red blood cell suspensions under confined 2d flows. *Soft Matter*, 15:2971–2980, 2019.

[69] G. Janiga, C. Rössl, M. Skalej, and D. Thévenin. Realistic virtual intracranial stenting and computational fluid dynamics for treatment analysis. *Journal of Biomedical Optics*, 46:7–12, 2013. doi: 10.1016/j.jbiomech.2012.08.047.

[70] G. Janiga, L. Daróczy, P. Berg, D. Thévenin, M. Skalej, and O. Beuing. An automatic cfd-based flow diverter optimization principle for patient-specific intracranial aneurysms. *Journal of Biomedical Optics*, 48(14):3846–3852, 2015. doi: 10.1016/j.jbiomech.2015.09.039.

[71] R. Kadirvel, Y.-H. Ding, D. Dai, I. Rezek, D. A. Lewis, and D. F. Kallmes. Cellular mechanisms of aneurysm occlusion after treatment with a flow diverter. *Radiology*, 270(2):394–399, 2014. doi: http://dx.doi.org/10.1148/radiol.13130796.

[72] M. O. Khan, K. Valen-Sendstad, and D. A. Steinman. Narrowing the expertise gap for predicting intracranial aneurysm hemodynamics: Impact of solver numerics versus mesh and time-step resolution. *American Journal of Neuroradiology*, 36(3):1310–1316, 2015. doi: http://dx.doi.org/10.3174/ajnr.A4263.

[73] R. Kleinloog, N. de Mul, B. H. Verweij, J. A. Post, G. J. E. Rinkel, and Y. M. Ruigrok. Risk factors for intracranial aneurysm rupture: A systematic review. *Neurosurgery*, 82(5):431–440, 2017. doi: http://dx.doi.org/10.1093/neuros/nyx238.

[74] J. Krejza, M. Arkuszewski, S. E. Kasner, J. Weigele, A. Ustymowicz, R. W. Hurst, B. L. Cucchiara, and S. R. Messe. Carotid artery diameter in men and women and the relation to body and neck size. *Stroke*, 37(4):1103–1105, 2006. doi: http://dx.doi.org/10.1161/01.STR.0000206440.48756.f7.

[75] Z. Kulcsár, E. Houdart, A. Bonafé, G. Parker, J. Millar, A. J. P. Goddard, S. Renowden, G. Gál, B. Turowski, K. Mitchell, F. Gray, M. Rodriguez, R. van den Berg, A. Gruber, H. Desal, I. Wanke, and D. A. Rüfenacht. Intraaneurysmal thrombosis as a possible cause of delayed aneurysm rupture

after flow-diversion treatment. *American Journal of Neuroradiology*, 32 (11):20–25, 2011. doi: http://dx.doi.org/10.3174/ajnr.A2370.

[76] L. Lanotte, J. Mauer, S. Mendez, D. A. Fedosov, J.-M. Fromental, V. Claveria, F. Nicoud, G. Gompper, and M. Abkarian. Red cells' dynamic morphologies govern blood shear thinning under microcirculatory flow conditions. *Proceedings of the National Academy of Sciences USA*, 113(47): 13289–13294, 2016. doi: 10.1073/pnas.1608074113.

[77] I. Larrabide, A. J. Geers, H. G. Morales, M. L. Aguilar, and D. A. Rüfenacht. Effect of aneurysm and ica morphology on hemodynamics before and after flow diverter treatment. *Journal of NeuroInterventional Surgery*, 7:272–280, 2014. doi: http://dx.doi.org/10.1136/neurintsurg-2014-011171.

[78] M. R. Levitt, C. Mandrycky, A. Abel, C. M. Kelly, S. Levy, V. K. Chivukula, Y. Zheng, A. Aliseda, and L. J. Kim. Genetic correlates of wall shear stress in a patient-specific 3d-printed cerebral aneurysm model. *Journal of NeuroInterventional Surgery*, pages 1–6, 2019. doi: http://dx.doi.org/10.1136/neurintsurg-2018-014669.

[79] S. Li, J. Latt, and B. Chopard. The application of the screen-model based approach for stents in cerebral aneurysms. *Computers and Fluids*, 172(8): 651–660, 2018. doi: http://dx.doi.org/10.1016/j.compfluid.2018.02.007.

[80] S. Li, J. Latt, and B. Chopard. Model for pressure drop and flow deflection in the numerical simulation of stents in aneurysms. *International Journal for Numerical Methods in Biomedical Engineering*, 34(3):e2949, 2018. doi: http://dx.doi.org/10.1002/cnm.2949.

[81] S. Li, B. Chopard, and J. Latt. Continuum model for flow diverting stents in 3d patient-specific simulation of intracranial aneurysms. *Journal of Computational Science*, 38(11):101045, 2019. doi: http://dx.doi.org/10.1016/j.jocs.2019.101045.

[82] Y. Li, M. Zhang, D. I. Verrelli, W. Chong, M. Ohta, and Y. Qian. Numerical simulation of aneurysmal haemodynamics with calibrated porous-medium models of flow-diverting stents. *Journal of Biomechanics*, 80(10):88–94, 2018. doi: http://dx.doi.org/10.1016/j.jbiomech.2018.08.026.

[83] Y. Li, D. I. Verrelli, W. Yang, Y. Qian, and W. Chong. A pilot validation of cfd model results against piv observations of haemodynamics in intracranial aneurysms treated with flow-diverting stents. *Journal of Biomechanics*, 100 (2):109590, 2020. doi: http://dx.doi.org/10.1016/j.jbiomech.2019.109590.

[84] T. Liebig, C. Kabbasch, C. Strasilla, A. Berlis, W. Weber, L. Pierot, T. Patankar, X. Barreau, J. Dervin, A. Kuršumović, S. Rath, B. Lubicz, and J. Klisch. Intrasaccular flow disruption in acutely ruptured aneurysms: A multicenter retrospective review of the use of the web. *American Journal of Neuroradiology*, 36(7):1721–1727, 2015. doi: http://dx.doi.org/10.3174/ajnr.A4347.

[85] T.-M. Liou and Y.-C. Li. Effects of stent porosity on hemodynamics in a sidewall aneurysm model. *Journal of Biomechanics*, 41(6):1174–1183, 2008. doi: http://dx.doi.org/10.1016/j.jbiomech.2008.01.025.

[86] W. K. Liu, S. Jun, and Y. F. Zhang. Reproducing kernel particle methods. *International Journal for Numerical Methods in Fluids*, 20:1081–1106, 1995.

[87] R. Löhner, J. D. Baum, E. Mestreau, D. Sharov, C. Charman, and D. Pelessone. Adaptive embedded unstructured grid methods. *International Journal for Numerical Methods in Engineering*, 60(3):641–660, 2004. doi: http://dx.doi.org/10.1002/nme.978.

[88] W. E. Lorensen and H. E. Cline. Marching cubes: A high resolution 3d surface construction algorithm. *ACM SIGGRAPH Computer Graphics*, 21 (8):163–169, 1987. doi: http://dx.doi.org/10.1145/37402.37422.

[89] B. Lubicz, J. Klisch, J.-Y. Gauvrit, I. Szikora, M. Leonardi, T. Liebig, N. P. Nuzzi, E. Boccardi, F. D. Paola, M. Holtmannspötter, W. Weber, E. Calgliari, V. Sychra, B. Mine, and L. Pierot. Web-dl endovascular treatment of wide-neck bifurcation aneurysms: Short- and midterm results in a european study. *American Journal of Neuroradiology*, 35(1):432–438, 2014. doi: http://dx.doi.org/10.3174/ajnr.A3869.

[90] M. Malandain, N. Maheu, and V. Moureau. Optimization of the deflated conjugate gradient algorithm for the solving of elliptic equations on massively parallel machines. *Journal of Computational Physics*, 238:32–47, 2013.

[91] N. Marheineke and R. Wegener. Modeling and application of a stochastic drag for fibers in turbulent flows. *International Journal of Multiphase Flow*, 37(3):136–148, 2011. doi: http://dx.doi.org/10.1016/j.ijmultiphaseflow.2010.10.001.

[92] J. Mauer, S. Mendez, L. Lanotte, F. Nicoud, M. Abkarian, G. Gompper, and D. A. Fedosov. Flow-induced transitions of red blood cell shapes under shear. *Physical Review Letters*, 121(118103), 2018.

[93] S. Mendez, E. Gibaud, and F. Nicoud. An unstructured solver for simulations of deformable particles in flows at arbitrary Reynolds numbers. *Journal of Computational Physics*, 256(1):465–483, 2014.

[94] R. Méndez Rojano, S. Mendez, and F. Nicoud. Introducing the procoagulant contact system in the numerical assessment of device-related thrombosis. *Biomechanics and Modeling in Mechanobiology*, 17(3):815–826, 2018.

[95] R. Méndez Rojano, S. Mendez, D. Lucor, A. Ranc, M. Giansily-Blaizot, J.-F. Schved, and F. Nicoud. Kinetics of the coagulation cascade including the contact activation system: Sensitivity analysis and model reduction. *Biomechanics and Modeling in Mechanobiology*, 18(4):1139–1153, 2019.

[96] H. Meng, V. M. Tutino, J. Xiang, and A. Siddiqui. High wss or low wss? complex interactions of hemodynamics with intracranial aneurysm initiation, growth, and rupture: Toward a unifying hypothesis. *American Journal of Neuroradiology*, 35(4):1254–1262, 2013. doi: http://dx.doi.org/10.3174/ajnr.A3558.

[97] T. Miyagi. Viscous flow at low reynolds numbers past an infinite row of equal circular cylinders. *Journal of the Physical Society of Japan*, 13(5):493–496, 1958. doi: http://dx.doi.org/10.1143/JPSJ.13.493.

[98] U. Morbiducci, A. M. Kok, B. R. Kwak, P. H. Stone, D. A. Steinman, and J. J. Wentzel. Atherosclerosis at arterial bifurcations: evidence for the role of haemodynamics and geometry. *Thrombosis and Haemostasis*, 115:484–492, 2016. doi: http://dx.doi.org/10.1160/TH15-07-0597.

[99] A. Morita, T. Kirino, Hashi K., N. Aoki, S. Fukuhara, N. Hashimoto, T. Nakayama, M. Sakai, A. Teramoto, S. Tominari, and T. Yoshimoto. The natural course of unruptured cerebral aneurysms in a japanese cohort. *New England Journal of Medicine*, 366(6):2474–2482, 2012. doi: http://dx.doi.org/10.1056/NEJMoa1113260.

[100] V. Moureau, P. Domingo, and L. Vervisch. Design of a massively parallel CFD code for complex geometries. *Comptes Rendus Mécanique*, 339(2-3):141–148, 2011.

[101] F. Mut, R. Löhner, A. Chien, S. Tateshima, F. Viñuela, C. Putman, and J. R. Cebral. Computational hemodynamics framework for the analysis of cerebral aneurysms. *International Journal for Numerical Methods in Biomedical Engineering*, 27(12):822–839, 2010. doi: http://dx.doi.org/10.1002/cnm.1424.

[102] F. Mut, M. Raschi, E. Scrivano, C. Bleise, J. Chudyk, R. Ceratto, P. Lylyk, and J. R. Cebral. Association between hemodynamic conditions and occlusion times after flow diversion in cerebral aneurysms. *Journal of NeuroInterventional Surgery*, 7:286–290, 2015. doi: 10.1136/neurintsurg-2013-011080.

[103] F. Mut, B. J. Chung, J. Chudyk, P. Lylyk, R. Kadirvel, D. F. Kallmes, and J. R. Cebral. Image-based modeling of blood flow in cerebral aneurysms treated with intrasaccular flow diverting devices. *International Journal for Numerical Methods in Biomedical Engineering*, 2019. doi: 10.1002/cnm.3202. URL https://onlinelibrary.wiley.com/doi/abs/10.1002/cnm.3202.

[104] T. Müller, J. Meyer, and G. Kasper. Low reynolds number drag and particle collision efficiency of a cylindrical fiber within a parallel array. *Journal of the Aeronautical Sciences*, 77:50–66, 2014. doi: 10.1016/j.jaerosci.2014.07.007. URL http://dx.doi.org/10.1016/j.jaerosci.2014.07.007.

[105] M. N. Ngoepe and Y. Ventikos. Computational modelling of clot development in patient-specific cerebral aneurysm cases. *Journal of Thrombosis and Haemostasis*, 14(2):262–272, 2016.

[106] M. N. Ngoepe, A. F. Frangi, J. V. Byrne, and Y. Ventikos. Thrombosis in cerebral aneurysms and the computational modeling thereof: A review. *Frontiers in Physiology*, 9(306):1–22, 2018.

[107] M. N. Ngoepe, A. F. Frangi, J. V. Byrne, and Y. Ventikos. Thrombosis in cerebral aneurysms and the computational modeling thereof: A review. *Frontiers in Physiology*, 9:306, 2018.

[108] D. J. Nieuwkamp, L. E. Setz, A. Algra, F. H. Linn, N. K. de Rooij, and G. J. Rinkel. Changes in case fatality of aneurysmal subarachnoid haemorrhage over time, according to age, sex, and region: a meta-analysis. *The Lancet Neurology*, 8(7):635–642, 2009. doi: http://dx.doi.org/10.1016/S1474-4422(09)70126-7.

[109] M. Ohta, H. Anzai, Y. Miura, and T. Nakayama. Parametric study of porous media as substitutes for flow-diverter stent. *Biomaterials and Biomedical Engineering*, 2(6):111–125, 2015. doi: http://dx.doi.org/10.12989/bme.2015.2.2.111.

[110] R. Ouared, I. Larrabide, O. Brina, P. Bouillot, G. Erceg, H. Yilmaz, K. O. Lovblad, and V. Mendes Pereira. Computational fluid dynamics analysis of flow reduction induced by flow-diverting stents in intracranial aneurysms: A patient-unspecific hemodynamics change perspec-

tive. *Journal of NeuroInterventional Surgery*, 8:1288–1293, 2016. doi: 10.1136/neurintsurg-2015-012154.

[111] T. W. Peach, M. Ngoepe, K. Spranger, D. Zajarias-Fainsod, and Y. Ventikos. Personalizing flow-diverter intervention for cerebral aneurysms: from computational hemodynamics to biochemical modeling. *International Journal for Numerical Methods in Biomedical Engineering*, 30:1387–1407, 2014. doi: 10.1002/cnm.2663.

[112] T. W. Peach, D. Ricci, and Y. Ventikos. A virtual comparison of the eclips device and conventional flow-diverters as treatment for cerebral bifurcation aneurysms. *Cardiovascular Engineering and Technology*, (7), 2019. doi: http://dx.doi.org/10.1007/s13239-019-00424-3.

[113] V. M. Pereira, O. Bonnefous, R. Ouared, O. Brina, J. Stawiaski, H. Aerts, D. Ruijters, A. P. Narata, P. Bijlenga, K. Schaller, and K.-O. Lovblad. A dsa-based method using contrast-motion estimation for the assessment of the intra-aneurysmal flow changes induced by flow-diverter stents. *American Journal of Neuroradiology*, 34(11):808–815, 2012. doi: http://dx.doi.org/10.3174/ajnr.A3322.

[114] V. M. Pereira, O. Brina, B. M. A. Delattre, R. Ouared, P. Bouillot, G. Erceg, K. Schaller, K.-O. Lovblad, and M.-I. Vargas. Assessment of intra-aneurysmal flow modification after flow diverter stent placement with four-dimensional flow mri: a feasibility study. *Journal of NeuroInterventional Surgery*, 7(10):913–919, 2014. doi: http://dx.doi.org/10.1136/neurintsurg-2014-011348.

[115] R. D. Perrone, A. M. Malek, and T. Watnick. Vascular complications in autosomal dominant polycystic kidney disease. *Nature Reviews Nephrology*, 11(8):589–598, 2015. doi: http://dx.doi.org/10.1038/nrneph.2015.128.

[116] C. S. Peskin. The immersed boundary method. *Acta Numerica*, 11:479–517, 2002.

[117] L. Pierot and A. K. Wakhloo. Endovascular treatment of intracranial aneurysms: Current status. *Stroke*, 44(7):2046–2054, 2013. doi: http://dx.doi.org/10.1161/STROKEAHA.113.000733.

[118] A. Pinelli, I. Z. Naqavi, U. Piomelli, and J. Favier. Immersed-boundary methods for general finite-difference and finite-volume Navier–Stokes solvers. *Journal of Computational Physics*, 229:9073–9091, 2010.

[119] T. Puiseux, A. Sewonu, O. Meyrignac, H. Rousseau, F. Nicoud, S. Mendez, and R. Moreno. Reconciling PC-MRI and CFD: an in-vitro study. *NMR in Biomedicine*, 2019.

[120] Thomas Puiseux. *Simulations numériques pour l'Imagerie par Résonance Magnétique à contraste de phase*. PhD thesis, Université de Montpellier, 2019. URL http://theses.fr/2019MONTS109.

[121] L. N. Sekhar R. G. Ellenbogen, S. I. Abdulrauf. *Principles of Neurological Surgery*. Saunders, 3 edition, 2012. URL https://www.elsevier.com/books/principles-of-neurological-surgery/9781437707014.

[122] A. T. Rai, J. P. Hogg, B. Cline, and G. Hobbs. Cerebrovascular geometry in the anterior circulation: an analysis of diameter, length and the vessel taper. *Journal of NeuroInterventional Surgery*, 5(4):371–375, 2012. doi: http://dx.doi.org/10.1136/neurintsurg-2012-010314.

[123] A. T. Rai, D. Rodgers, E. A. Williams, and J. P. Hogg. Dimensions of the posterior cerebral circulation: an analysis based on advanced non-invasive imaging. *Journal of NeuroInterventional Surgery*, 5(11):597–600, 2012. doi: http://dx.doi.org/10.1136/neurintsurg-2012-010549.

[124] M. Raschi, F. Mut, R. Löhner, and J. R. Cebral. Strategy for modeling flow diverters in cerebral aneurysms as a porous medium. *International Journal for Numerical Methods in Biomedical Engineering*, 30(3):909–925, 2014. doi: http://dx.doi.org/10.1002/cnm.2635.

[125] K. Ravindran, M. M. Salem, A. Y. Alturki, A. J. Thomas, C. S. Ogilvy, and J. M. Moore. Endothelialization following flow diversion for intracranial aneurysms: A systematic review. *American Journal of Neuroradiology*, 40 (1):295–301, 2019. doi: http://dx.doi.org/10.3174/ajnr.A5955.

[126] G. J. E. Rinkel, M. Djibuti, A. Algra, and J. van Gijn. Prevalence and risk of rupture of intracranial aneurysms: A systematic review. *Stroke*, 29(1): 251–256, 1998. doi: http://dx.doi.org/10.1161/01.STR.29.1.251.

[127] A. Ronkainen, J. Hernesniemi, M. Puranen, L. Niemitukia, R. Vanninen, M. Ryynänen, H. Kuivaniemi, and G. Tromp. Familial intracranial aneurysms. *The Lancet*, 349(2):380–384, 1997. doi: http://dx.doi.org/10.1016/S0140-6736(97)80009-8.

[128] A. Rouchaud, C. Ramana, W. Brinjikji, Y.-H. Ding, D. Dai, T. Gunderson, J. Cebral, D. F. Kallmes, and R. Kadirvel. Wall apposition is a key factor for aneurysm occlusion after flow diversion: A histologic evaluation in 41

rabbits. *American Journal of Neuroradiology*, 37(7):2087–2091, 2016. doi: http://dx.doi.org/10.3174/ajnr.A4848.

[129] S. F. Salimi Ashkezari, F. Mut, B. J. Chung, A. K. Yu, C. J. Stapleton, A. P. See, S. Amin-Hanjani, F. T. Charbel, B. Rezai Jahromi, M. Niemelä, J. Frösen, S. Maiti, A. M. Robertson, and J. R. Cebral. Hemodynamics in aneurysm blebs with different wall characteristics. *Journal of NeuroInterventional Surgery*, (10):neurintsurg–2020–016601, 2020. doi: http://dx.doi.org/10.1136/neurintsurg-2020-016601.

[130] A. Sarrami-Foroushani, T. Lassila, S. M. Hejazi, S. Nagaraja, A. Bacon, and A. F. Frangi. A computational model for prediction of clot platelet content in flow-diverted intracranial aneurysms. *Journal of Biomechanics*, 91(6):7–13, 2019. doi: http://dx.doi.org/10.1016/j.jbiomech.2019.04.045.

[131] Wi. Schroeder, K. Martin, and B. Lorensen. *The Visualization Toolkit: An Object-Oriented Approach To 3D Graphics*. Kitware Inc., 4.1 edition, July 2018.

[132] H. Si. Tetgen, a delaunay-based quality tetrahedral mesh generator. *ACM Transactions on Mathematical Software*, 41(2):1–36, 2015. doi: http://dx.doi.org/10.1145/2629697.

[133] J. Sigüenza, S. Mendez, D. Ambard, F. Dubois, F. Jourdan, R. Mozul, and F. Nicoud. Validation of an immersed thick boundary method for simulating fluid-structure interactions of deformable membranes. *Journal of Computational Physics*, 322:723–746, 2016.

[134] J. Sigüenza, S. Mendez, and F. Nicoud. How should the optical tweezers experiment be used to characterize the red blood cell membrane mechanics? *Biomechanics and Modeling in Mechanobiology*, 16:1645–1657, 2017.

[135] T. Steiner, S. Juvela, A. Unterberg, C. Jung, M. Forsting, and G. Rinkel. European stroke organization guidelines for the management of intracranial aneurysms and subarachnoid haemorrhage. *Cerebrovascular Diseases*, 35: 93–112, 2013. doi: http://dx.doi.org/10.1159/000346087.

[136] D. A. Steinman and V. M. Pereira. How patient specific are patient-specific computational models of cerebral aneurysms? an overview of sources of error and variability. *Neurosurgical Focus*, 47(7):E14, 2019. doi: http://dx.doi.org/10.3171/2019.4.FOCUS19123.

[137] D. A. Steinman, Y. Hoi, P. Fahy, L. Morris, M. T. Walsh, N. Aristokleous, A. S. Anayiotos, Y. Papaharilaou, A. Arzani, S. C. Shadden, P. Berg,

G. Janiga, J. Bols, P. Segers, N. W. Bressloff, M. Cibis, F. H. Gijsen, S. Cito, J. Pallarés, L. D. Browne, J. A. Costelloe, A. G. Lynch, J. Degroote, J. Vierendeels, W. Fu, A. Qiao, S. Hodis, D. F. Kallmes, H. Kalsi, Q. Long, V. O. Kheyfets, E. A. Finol, K. Kono, A. M. Malek, A. Lauric, P. G. Menon, K. Pekkan, M. Esmaily Moghadam, A. L. Marsden, M. Oshima, K. Katagiri, V. Peiffer, Y. Mohamied, S. J. Sherwin, J. Schaller, L. Goubergrits, G. Usera, M. Mendina, K. Valen-Sendstad, D. F. Habets, J. Xiang, H. Meng, Y. Yu, G. E. Karniadakis, N. Shaffer, and F. Loth. Variability of computational fluid dynamics solutions for pressure and flow in a giant aneurysm: The asme 2012 summer bioengineering conference cfd challenge. *Journal of Biomechanical Engineering*, 135(2):021016, 2013. doi: http://dx.doi.org/10.1115/1.4023382.

[138] P. Taraconat, J.-P. Gineys, D. Isèbe, F. Nicoud, and S. Mendez. Numerical simulation of deformable particles in a Coulter counter. *International Journal for Numerical Methods in Biomedical Engineering*, 35(11):e3243, 2019. doi: 10.1002/cnm.3243.

[139] Pierre Taraconat. *Application of numerical simulation for a better characterization of red blood cells by impedance measurement*. PhD thesis, Université de Montpellier, 2020. URL http://theses.fr/2020MONTS006.

[140] S. Tominari, A. Morita, T. Ishibashi, T. Yamazaki, H. Takao, Y. Murayama, M. Sonobe, M. Yonekura, N. Saito, Y. Shiokawa, I. Date, T. Tominaga, K. Nozaki, K. Houkin, S. Miyamoto, T. Kirino, K. Hashi, and T. and Nakayama. Prediction model for 3-year rupture risk of unruptured cerebral aneurysms in japanese patients: Cerebral aneurysm rupture risk. *Annals of Neurology*, 77(4):1050–1059, 2015. doi: http://dx.doi.org/10.1002/ana.24400.

[141] A. Utkarsh. *The ParaView Guide: Community Edition*. Kitware Inc., June 2017.

[142] K. Valen-Sendstad and D. A. Steinman. Mind the gap: Impact of computational fluid dynamics solution strategy on prediction of intracranial aneurysm hemodynamics and rupture status indicators. *American Journal of Neuroradiology*, 35:536–543, 2014.

[143] K. Valen-Sendstad, M. Piccinelli, R. KrishnankuttyRema, and D. A. Steinman. Estimation of inlet flow rates for image-based aneurysm cfd models: Where and how to begin? *Annals of Biomedical Engineering*, 43(6):1422–1431, june 2015. doi: 10.1007/s10439-015-1288-5. URL http://link.springer.com/10.1007/s10439-015-1288-5.

[144] J. van Gijn, R. S. Kerr, and G. J. Rinkel. Subarachnoid haemorrhage. *The Lancet*, 369(1):306–318, 2007. doi: http://dx.doi.org/10.1016/S0140-6736(07)60153-6.

[145] Stijn Vantieghem. *Numerical simulations of quasi-static magnetohydrodynamics using an unstructured finite volume solver: development and applications*. PhD thesis, Université Libre de Bruxelles, 2011.

[146] C. Vega, J. V. Kwoon, and S. D. Lavine. Intracranial aneurysms: Current evidence and clinical practice. *American Family Physician*, 66(4):601–608, 2002. URL https://www.aafp.org/afp/2002/0815/p601.html.

[147] J. P. Villablanca, G. R. Duckwiler, R. Jahan, S. Tateshima, N. A. Martin, J. Frazee, N. R. Gonzalez, J. Sayre, and F. V. Vinuela. Natural history of asymptomatic unruptured cerebral aneurysms evaluated at ct angiography: Growth and rupture incidence and correlation with epidemiologic risk factors. *Radiology*, 269(10):258–265, 2013. doi: http://dx.doi.org/10.1148/radiol.13121188.

[148] M. H. Vlak, A. Algra, R. Brandenburg, and G. J. Rinkel. Prevalence of unruptured intracranial aneurysms, with emphasis on sex, age, comorbidity, country, and time period: a systematic review and meta-analysis. *The Lancet Neurology*, 10(7):626–636, 2011. doi: http://dx.doi.org/10.1016/S1474-4422(11)70109-0.

[149] M. H. Vlak, G. J. Rinkel, P. Greebe, and A. Algra. Independent risk factors for intracranial aneurysms and their joint effect: A case-control study. *Stroke*, 44(4):984–987, 2013. doi: http://dx.doi.org/10.1161/STROKEAHA.111.000329.

[150] M. J. Wermer, I. C. van der Schaaf, A. Algra, and G. J. Rinkel. Risk of rupture of unruptured intracranial aneurysms in relation to patient and aneurysm characteristics: An updated meta-analysis. *Stroke*, 38(4):1404–1410, 2007. doi: http://dx.doi.org/10.1161/01.STR.0000260955.51401.cd.

[151] M. J. H. Wermer, I. C. van der Schaaf, B. K. Velthuis, A. Algra, E. Buskens, and G. J. E. Rinkel. Follow-up screening after subarachnoid haemorrhage: frequency and determinants of new aneurysms and enlargement of existing aneurysms. *Brain*, 128(7):2421–2429, 2005. doi: http://dx.doi.org/10.1093/brain/awh587.

[152] D. O. Wiebers. Unruptured intracranial aneurysms: natural history, clinical outcome, and risks of surgical and endovascular treatment. *The Lancet*, 362(7):103–110, 2003. doi: http://dx.doi.org/10.1016/s0140-6736(03)13860-3.

[153] L. N. Williams and R. D. Brown. Management of unruptured intracranial aneurysms. *Neurology Clinical Practice*, 3(4):99–108, 2013. doi: http://dx.doi.org/10.1212/CPJ.0b013e31828d9f6b.

[154] H. R. Winn, J. A. Jane, J. Taylor, D. Kaiser, and G. W. Britz. Prevalence of asymptomatic incidental aneurysms: review of 4568 arteriograms. *Journal of Neurosurgery*, 96(1):43–49, 2002. doi: http://dx.doi.org/10.3171/jns.2002.96.1.0043.

[155] J. Xiang, D. Ma, K. V. Snyder, E. I. Levy, A. H. Siddiqui, and H. Meng. Increasing flow diversion for cerebral aneurysm treatment using a single flow diverter. *Neurosurgery*, 75:286–294, 2014. doi: 10.1227/NEU.0000000000000409.

[156] H. W. Xu, S. Q. Yu, C. L. Mei, and M. H. Li. Screening for intracranial aneurysm in 355 patients with autosomal-dominant polycystic kidney disease. *Stroke*, 42(1):204–206, 2011. doi: http://dx.doi.org/10.1161/STROKEAHA.110.578740.

[157] H. Yadollahi-Farsani, M. Herrmann, D. Frakes, and B. Chong. A new method for simulating embolic coils as heterogeneous porous media. *Cardiovascular Engineering and Technology*, 10(10):32–45, 2018. doi: http://dx.doi.org/10.1007/s13239-018-00383-1.

[158] H. Yadollahi-Farsani, E. Scougal, M. Herrmann, W. Wei, D. Frakes, and B. Chong. Numerical study of hemodynamics in brain aneurysms treated with flow diverter stents using porous medium theory. *Computer Methods in Biomechanics and Biomedical Engineering*, 22(5):961–971, 2019. doi: http://dx.doi.org/10.1080/10255842.2019.1609457.

[159] M. Zhang, Y. Li, X. Zhao, D. I. Verrelli, W. Chong, M. Ohta, and Y. Qian. Haemodynamic effects of stent diameter and compaction ratio on flow-diversion treatment of intracranial aneurysms: A numerical study of a successful and an unsuccessful case. *Journal of Biomechanics*, 58:179–186, 2017. doi: 10.1016/j.jbiomech.2017.05.001.

[160] M. Zhang, S. Tupin, H. Anzai, Y. Kohata, M. Shojima, K. Suzuki, Y. Okamoto, K. Tanaka, T. Yagi, S. Fujimura, and M. Ohta. Implementation of computer simulation to assess flow diversion treatment outcomes: systematic review and meta-analysis. *Journal of NeuroInterventional Surgery*, (10):neurintsurg–2020–016724, 2020. doi: http://dx.doi.org/10.1136/neurintsurg-2020-016724.

[161] X.-J. Zhang, W.-L. Hao, D.-H. Zhang, and B.-L. Gao. Asymmetrical middle cerebral artery bifurcations are more vulnerable to aneurysm formation. *Scientific Reports*, 9(10):15255, 2019. doi: http://dx.doi.org/10.1038/s41598-019-51734-4.

[162] Y. Zhang, W. Chong, and Y. Qian. Investigation of intracranial aneurysm hemodynamics following flow diverter stent treatment. *Medical Engineering and Physics*, 35(5):608–615, 2013. doi: http://dx.doi.org/10.1016/j.medengphy.2012.07.005.

[163] V. Zmijanovic, S. Mendez, V. Moureau, and F. Nicoud. About the numerical robustness of biomedical benchmark cases: Interlaboratory FDA's idealized medical device. *International Journal for Numerical Methods in Biomedical Engineering*, 33(1):e02789:1–17, 2017.

Abstract

Hemodynamics of endovascularly treated intracranial aneurysms has been proven to be one of the essential mechanisms driving treatment success due to its intimate relationship with processes involved in thrombosis and leading to a stable clot inside the aneurysm. Giving access to hemodynamics, patient-specific computational fluid dynamics (CFD) simulations have been actively performed during the last decade in an attempt to both enhance existing devices and predict the chances of success beforehand to the surgical act. Nevertheless, "classical" CFD simulations, referred to as *conformal*, yield high computational and meshing costs due to the heterogeneity of length scales between the dense weave of the fine struts of the device and the arterial volume. Homogeneous strategies recently developed to circumvent this issue substitute local dissipations due to the wires with a global effect in the form of a pressure-drop across the device surface. However, these methods cannot accurately reproduce the flow-patterns encountered near the struts, despite the fact that the latter strongly dictates the downstream intra-saccular flow environment.

This thesis aims at developing a computational model correctly reproducing local wires-induced flow heterogeneities while keeping memory consumption, meshing and computational times as low as possible. A framework based on the Immersed Boundary Method (IBM) is introduced and validated on both idealized and patient-specific geometries treated with endovascular devices. It is shown that the present model compares qualitatively and quantitatively well with conformal results for flow-diverters (FDs) but more importantly, it yields results that are either comparable or better than homogeneous methods with gains of one and three orders of magnitude for memory and computational time compared to conformal, respectively. Moreover, the proposed approach has proven its versatility to correctly account for other braided endovascular devices such as intra-saccular WEBs.

Finally, a database of numerical computations using the present model has been built using 27 patient-specific geometries treated with WEBs and for which the treatment outcome is known. Semi-automated numerical tools used to build this database and intended to non-CFD specialists are presented. Preliminary results from a study dedicated to treatment outcome prediction with both geometrical and hemodynamics indices derived from this database are given and discussed. Several important limitations are drawn and should be considered in future works.

Keywords : hemodynamics, Computational Fluid Dynamics, intracranial aneurysm, endovascular treatment, flow-diverter, heterogeneous modelling, drag model, Immersed Boundary Method

---

Résumé

L'hémodynamique présente dans les anévrismes intracrâniens traités par voie endovasculaire s'est avérée être l'un des mécanismes essentiels à la réussite du traitement en raison de sa relation étroite avec les processus impliqués dans la thrombose et conduisant à la formation d'un caillot stable à l'intérieur de l'anévrisme. Donnant accès à l'hémodynamique, la mécanique des fluides numériques (MFN) utilisée sur des géométries réelles de patients a été largement utilisée au cours de la dernière décennie afin d'améliorer les dispositifs existants et de prédire les chances de succès en amont de l'acte chirurgical. Néanmoins, les simulations CFD "classiques", dites *conformes*, entraînent des coûts de calcul et de maillage élevés en raison de l'hétérogénéité des échelles de longueur entre le tressage dense des fils fins composant le dispositif et le volume artériel. Les stratégies homogènes récemment développées pour contourner ce problème substituent les dissipations locales dues aux fils par un effet global sous la forme d'une perte de charge à travers la surface du dispositif. Cependant, ces méthodes ne peuvent pas reproduire avec précision l'écoulement local au niveau des fils, en dépit du fait que ce dernier dicte fortement l'hémodynamique intra-sacculaire en aval.

Cette thèse vise à développer un modèle de calcul reproduisant correctement les hétérogénéités d'écoulement locales induites par les fils tout en maintenant la consommation de mémoire, le maillage et les temps de calcul aussi bas que possible. Une approche basée sur la méthode des frontières immergées (IBM) est introduite et validée sur des géométries à la fois idéalisées et réelles de patients traités avec des dispositifs endovasculaires. Il est démontré que le modèle actuel se compare qualitativement et quantitativement bien aux résultats conformes pour les diverteurs de flux (FDs) mais, plus important encore, il donne des résultats qui sont soit comparables soit meilleurs que les méthodes homogènes, avec des gains respectivement d'un et trois ordres de grandeur en mémoire vive et temps de calcul par rapport à la méthode conforme. De plus, l'approche proposée a prouvé sa polyvalence à modéliser fidèlement d'autres dispositifs endovasculaires tressés tels que les WEBs intra-sacculaires.

Enfin, une base de données de calculs numériques utilisant le modèle actuel a été construite à partir de 27 géométries réelles de patients traités avec des WEBs et pour lesquels le résultat du traitement est connu. Des outils numériques semi-automatiques utilisés pour construire cette base de données et destinés aux non-spécialistes de la MFN sont présentés. Les résultats préliminaires d'une étude consacrée à la prédiction du résultat du traitement en utilisant à la fois des indices géométriques et hémodynamiques dérivés de cette base de données sont donnés et discutés. Plusieurs limites importantes sont soulignées et doivent être prises en compte dans des travaux futurs.

Mots-clefs : hémodynamique, Mécanique des Fluides Numérique, anévrisme intracrânien, traitement endovasculaire, diverteur de flux, modélisation hétérogène, modèle de traînées, Méthode des Frontières Immergées